An investigation of CO_2-brine interactions using North Sea oil well data with respect to Geological Storage of Carbon Dioxide and Enhanced Oil Recovery

By

Luc Thomas Steel

Thesis submitted to Heriot-Watt University for the

Degree of Doctor of Philosophy in Chemical Engineering

Institute of Mechanical, Process and Energy Engineering

School of Engineering and Physical Sciences

April 2017

Abstract

Geochemical trapping, comprising mineral and solubility trapping, is the most secure and permanent trapping mechanism for CO_2 geological storage. CO_2 dissolution in brine is also an important mechanism for CO_2 enhanced oil recovery, as it improves sweep efficiency and increases oil displacement. This study aims to address current knowledge gaps that relate to how brine composition affects CO_2 geochemical trapping mechanisms and the effect that CO_2-saturated brine has on the permeability and porosity of host rock. Several different geochemical models that can be used to predict geochemical trapping potentials were reviewed and the importance of selecting the correct equation of state (EoS) was addressed. The geochemical modelling software, HydraFLASH was selected to calculate CO_2 solubility in brine and PHREEQC was chosen to predict mineral trapping potentials. Hydrothermal experiments were performed to investigate the importance of well selection within a field, concluding that geochemical trapping potentials can vary within the same field as a consequence of brine compositional changes, in particular changes in SO_4^{2-} concentrations due to seawater flooding, at individual wells.

Further experiments were performed to assess the potential for calcite, which overlays many potential aquifer stores, to buffer brine and promote mineral trapping, as well as to investigate the potential effect that CO_2-saturated brine has on the permeability and porosity of local host rock. The addition of calcite resulted in a significant increase in brine pH, but not sufficient enough to promote mineral trapping. In addition, CO_2-saturated brine reacting with host rock resulted in the dissolution of Ca, Mg and S bearing minerals within the rock. However, an overall decrease of rock porosity and permeability was observed, due to the formation of clays and Na-micas and the mobilisation of fines.

Acknowledgements

I would first like to thank my supervisors, Professor Mercedes Maroto-Valer and Professor Eric Mackay, for their continuous support and guidance throughout the entire PhD process. My gratitude also extends to the rest of the CICCS team for their support and especially to Dr Qi Liu who acted as an unofficial supervisor but treated me as a colleague. I would also like to thank Dr Jim Buckman, Dr Lorna Eades and Dr Georgina Rosair for the analysis work they did for me throughout the PhD. I would like to convey special gratitude to Richard Kinsella, a technician, who one every occasion went above and beyond to help me, without whom I would not have completed my PhD.

I would never have had this opportunity to obtain a PhD if it hadn't been for my father. Who always put my needs before his own and without whom none of this would have been possible. Finally, I would like to thank my fiancé, Catriona. Who has been through 7 years of my University ups and downs and never lost faith in me for a second. Both her and my father made this possible and for that they both have my eternal gratitude.

ACADEMIC REGISTRY
Research Thesis Submission

Name*:*			
School/PGI:			
Version: *(i.e. First, Resubmission, Final)*		Degree Sought (Award **and** Subject area)	

Declaration

In accordance with the appropriate regulations I hereby submit my thesis and I declare that:

1) the thesis embodies the results of my own work and has been composed by myself
2) where appropriate, I have made acknowledgement of the work of others and have made reference to work carried out in collaboration with other persons
3) the thesis is the correct version of the thesis for submission and is the same version as any electronic versions submitted*.
4) my thesis for the award referred to, deposited in the Heriot-Watt University Library, should be made available for loan or photocopying and be available via the Institutional Repository, subject to such conditions as the Librarian may require
5) I understand that as a student of the University I am required to abide by the Regulations of the University and to conform to its discipline.

* *Please note that it is the responsibility of the candidate to ensure that the correct version of the thesis is submitted.*

Signature of Candidate*:*		Date:	

Submission

Submitted By *(name in capitals):*	
Signature of Individual Submitting:	
Date Submitted:	

For Completion in the Student Service Centre (SSC)

Received in the SSC by *(name in capitals):*

Method of Submission

(Handed in to SSC; posted through internal/external mail):

*E-thesis Submitted (**mandatory for final theses)***

Signature: Date:

Table of Contents

List of Figures

List of Tables

List of Boxes

Abbreviations

API	American Petroleum Institute
BET	Brunauer, Emmett and Teller
BPR	Back Pressure Regulator
CCGT	Combined-Cycle Gas Turbines
CDIAC	Carbon Dioxide Information Analysis Centre
CCS	Carbon Capture and Storage
CCSM	Carbon Capture and Storage by Mineralisation
CHP	Combined Heat and Power
DOE	U.S. Department of Energy
ECBM	Enhanced Coal Bed Methane
EDS	Energy Dispersive X-ray Spectrometer
EGR	Enhanced Gas Recovery
ETI	Energy Technologies Institute
EOR	Enhanced Oil Recovery
EoS	Equation of State
ESEM	Environmental Scanning Electron Microscope
GIIP	Gas Initially in Place
GWP	Global Warming Potential
ICDD	International Centre Diffraction Data
ICP-OES	Inductively Coupled Plasma - Optical Emission Spectroscopy
IEA	International Energy Agency
IPCC	Intergovernmental Panel on Climate Change

IPE	Heriot Watt University Institute of Petroleum Engineering
Micro-CT	Micro Computed Tomography
Mtoe	Million tonnes of oil equivalent
NDD	Non-Density Dependant
NETL	U.S. National Energy Technology Laboratory
OOIP	Original Oil in Place
PC-SAFT	Perturbed Chain for of the Statistical Associating Fluid Theory
PDS	Particle Size Distribution
PR	Peng-Robinson
PRV	Pressure Relief Valve
PTFE	polytetrafluoroethene
PVT	Pressure-Volume-Temperature
sCPA	Simplified Cubic Plus Association
SEM	Scanning Electron Microscopy
SR	Saturation Ratio
SRK	Soave-Relich-Kwong
UKCS	United Kingdom Continental Shelf
USEPA	United States Environmental Protection Agency
USGS	United States Geological Survey
VdW	Van der Waals
VPT	Valderrama-Patel-Teja
WAG	Water Alternating Gas
XRD	X-ray Diffraction

Publications

L. Steel, Q. Liu, E. Mackay and M. M. Maroto-Valer, "CO_2 Solubility measurements in brine under reservoir conditions: A comparison of experimental and geochemical modeling methods", Greenhouse Gases: Science and Technology, 2016, 6, 197-217. DOI: 10.1002/ghg.1590

Chapter 1 Introduction

The International Energy Agency's (IEA) recent "Key World Energy Statistics 2016" report has estimated that in 2014, 11,110 Mtoe (Million tonnes of oil equivalent) of global total primary energy supply came directly from fossil fuels [1]. This is only expected to increase by 2030, where fossil fuels are expected to account for 12,500 Mtoe of total primary energy supply [2]. As a result, reliance on fossil fuels will only increase over the coming decades which will lead to two significant issues. Firstly, increased reliance on fossil fuels will result in more rapid depletion of reserves as fossil fuels are not an infinite resource. As of 2015 the renewable energy sector only accounted for 2.8% of global power consumption [3]. Therefore, it is vital that the lifetime of fossil fuel reserves are prolonged until renewable energy technologies can take over as the dominant global energy supplier. Secondly, the resulting higher CO_2 emissions, which are a direct consequence of increased burning of fossil fuels, will have further detrimental effects on our environment. In fact, CO_2 emissions associated with energy consumption in 2015 were at a record high of 33.5Gt [3]. Therefore, strategies need to be employed to increase fossil fuel reserves and reduce CO_2 emissions. Two such strategies are Enhanced Oil Recovery (EOR) and Carbon Dioxide Capture and Storage (CCS).

During its lifetime, an oil field goes through three stages of production, namely primary, secondary and tertiary [4]. During the primary stage, the natural pressure in the reservoir forces the oil to flow to the surface. Once the pressure has dropped to a point where there is not enough natural drive to force the oil to the surface, the field enters the secondary stage whereby water and/or gas is injected. The injected water and/or gas increase the reservoir pressure and displace the oil. However, upon competition of the secondary stage there can still potentially be 55-88% of the original oil in place (OOIP) remaining [5]. It is at this point where the field enters the tertiary stage and EOR technologies are employed to further increase recovery. One such EOR technology which is widely employed, especially in the U.S., is CO_2-EOR.

CO_2-EOR has been prevalent in the U.S. since 1972 when the first large scale CO_2-EOR project was established in the Permian Basin in West Texas [6]. Since then the application of CO_2-EOR has expanded to 136 projects across the U.S., producing 300,000 barrels of oil per day [7]. The CO_2-EOR process involves injecting supercritical CO_2 into the reservoir, where it comes into contact with oil [8]. Once the CO_2 and oil come into contact, the CO_2 becomes miscible with the oil, which is known as the miscible zone. The CO_2 that dissolves in the oil causes it to swell, forming a concentrated oil bank which is

then pushed towards the production well, allowing the oil to be extracted. CO_2-EOR is one of the most effective EOR technologies and will contribute to increasing fossil fuels recovery. However, although increasing fossil fuel reserves is vital to meeting future global energy demands, increased burning of these fuels will result in more CO_2 emissions which need to be appropriately dealt with. It is for this reason that CCS technologies are necessary.

The first stage of CCS involves removing CO_2 from a flue gas through pre-combustion, post-combustion or oxy-fuel combustion [9]. Once the CO_2 has been captured it needs to be stored in a safe and permanent manner. At present, CO_2 storage within depleted oil and gas fields or deep saline aquifers is the most effective means of storing CO_2. This is due to their integrity and safety, as well as their large storage capacities and the fact that most of the infrastructure needed for CO_2 injection is already in place as a result of the oil and gas industry [10]. Global storage capacities for CO_2 are expected to be in the range of 400-10,000Gt for deep saline aquifers and 920Gt for depleted oil and gas fields [11]. Comparing these values with global annual CO_2 emissions in 2015 of 33.5Gt, it is clear that these storage options have the potential to significantly reduce CO_2 emissions entering the atmosphere [3].

When injecting CO_2 into deep geological formations, such as saline aquifers and depleted oil and gas fields, it is important to understand how the CO_2 will be stored via trapping mechanisms. There are two different mechanisms by which CO_2 can be trapped: physical trapping and geochemical trapping [12]. The former is split into three separate mechanisms; static (structural and stratigraphic), hydrodynamic and residual gas trapping, whereas the latter consists of mineral and solubility trapping. Upon injection, CO_2 is generally trapped by physical trapping mechanisms, as geochemical trapping occurs over a considerable time period [13]. Geochemical trapping is preferred as it does not depend on the integrity of the cap rock unlike physical trapping and so is a more secure method of storage.

Solubility trapping involves CO_2 dissolving in the local brine and becoming trapped [14]. The dissolved CO_2 then reacts with water to form carbonic species. After solubility trapping, the CO_2 is no longer in a separate phase and so the CO_2 fluid is not subject to the buoyant forces that drive it upwards, as CO_2 saturated brine is denser than unsaturated brine [15]. Consequently, the CO_2 is now securely stored within the geological formation. CO_2 solubility in brine is not only fundamental to solubility trapping but it also affects

CO_2-EOR. When CO_2 dissolves in brine, the sweep efficiency improves, and the CO_2 may mobilise residually trapped oil contacted by the CO_2 saturated brine, and therefore, increase oil displacement.

Due to the formation of solid insoluble carbonates, mineral trapping is the safest and most permanent means of CO_2 geological storage. Mineral trapping in these deep formations usually takes place at temperatures between 313K and 473K and pressures ranging from 7MPa to 28MPa [16]. Previous studies have shown that higher pressure and temperature conditions result in an increase in the formation of mineral carbonates, with temperature having a greater effect than pressure [17]. The contribution of pressure and temperature are, however, minor in comparison with the effect that brine pH has on mineral trapping [17].

The optimal pH level for the formation of mineral carbonates is over 9.0 due to the large quantity of carbonate (CO_3^{2-}) ions being present [18]. Brine pH in deep formations usually ranges from 2-7 and at pH <7, formation of mineral carbonates is unlikely due to too few or no carbonate ions being present [19]. The brine pH, however, does increase with the injection of CO_2 due to geochemical reactions between the host rock and the injected CO_2 [20]. When CO_2 dissolves in brine, it forms a weak acid. This acid will then react with calcite contained within the host rock, resulting in an overall loss of calcite and the formation of bicarbonate (HCO_3^-) which is alkaline [20]. Consequently, the pH of the brine will increase. Therefore, as more CO_2 is injected and dissolves the local calcite, the brine pH will further increase due to the increased levels of HCO_3^- ions. As a result, calcite should act as a buffer and may promote mineral carbonation [21]. Buffering of acid brine in chalk formations due to calcite dissolution and any resulting changes in porosity will be of interest in carbonate formations where there are chalk intervals overlying many of potential aquifer stores.

When CO_2-saturated brine reacts with local host rock it can lead to the dissolution and precipitation of minerals within the rock. This can have a significant effect on the porosity and permeability of the rock [22]. The effect of CO_2 saturated brine on porosity and permeability of local host rock is important when selecting a site for CO_2 injection. Consequently, this may have positive impacts in regards to CO_2 storage security, as the reduced flow capacity will in turn reduce the extent of CO_2 migration [22]. Conversely, reduced porosity and permeability will mean that greater injection pressure will be needed

to displace CO_2 into the formation. Therefore, the impact of long term exposure of host rock to CO_2-saturated brine is an important avenue of research.

1.1 Current knowledge gaps

There has been extensive work on measuring CO_2 solubility in brine, especially in trying to achieve an accurate experimental procedure for measuring CO_2 solubility in brine under reservoir conditions [23]. However, a review of recent experimental work is needed to assess the evolution of experimental methods over recent years and if the associated changes in experimental procedure and equipment have resulted in more accurate measurements of CO_2 solubility under reservoir conditions. In addition, although a number of different geochemical modelling software packages have been used to calculate CO_2 solubility in brine, the importance of selecting the correct equation of state (EoS) has yet to be discussed in previous literature. This EoS, along with the associated geochemical modelling software, can be used to ascertain the validity of the published experimental results and confirm whether the accuracy of CO_2 solubility measurements has improved over recent years.

Geochemical trapping potentials are affected by a number of different factors, such as pressure, temperature, salinity and brine pH [17, 24]. Previous work has investigated how these conditions can affect geochemical trapping potentials and there has also been studies showing the effect of certain brine ions on pH. However, brine composition changes with location and there has yet to be a study focused on how changes in brine composition within the same field can result in different geochemical trapping potentials [25]. This could mean that some locations are better suited for geochemical trapping than others which would be an important factor when selecting a site for CO_2 geological storage.

There is also a lack of experimental work that focuses on the effect that CO_2-saturated brine has on local host rock over extended periods of time. The presence of calcite in the rock could lead to a buffering effect. When CO_2 dissolves in brine, it forms a weak acid which will react with the calcite to form HCO_3^- which is alkaline [20]. Over time this could lead to an overall increase in pH which may promote mineral trapping. In addition, the continued exposure of host rock to CO_2-satured brine could result in significant changes in porosity and permeability which in turn affect CO_2 storage security [22]. Therefore, further experimental work into the consequences of exposure of host rock to

CO_2-saturtred brine over an extended (9 month) period of time is an important avenue of research.

1.2 Aim and research objectives

The most permanent and secure CO_2 storage mechanisms within deep geological formations are solubility and mineral trapping. Furthermore, CO_2 solubility in brine plays an important role in EOR, as it improves sweep efficiency and increases oil displacement. Brine composition varies with location and can alter over time, usually as a result of seawater injection into the reservoir. In addition, the interactions between CO_2-saturated brine and host rock can lead to changes in permeability and porosity due to dissolution and precipitation of minerals, that in turn can significantly affect CO_2 storage security. **Therefore, the aim of this study is to investigate how brine composition affects CO_2 geochemical trapping mechanisms and the effect that CO_2-saturated brine has on the permeability and porosity of host rock.** This will be achieved through a combination of experimental work and geochemical modelling, using real brine data from North Sea oil wells to produce synthetic brines. The experimental work will be performed under reservoir conditions to best simulate the interactions between CO_2 and brine in a real reservoir.

The main objectives of this study are:

Objective 1: To select geochemical modelling software that can assess geochemical trapping mechanisms on a geological timescale and validate experimental data.

Objective 2: To develop a range of synthetic brines with varying compositions using North Sea oil well data. The different brines created will be used to investigate:

- ✓ Compositional changes in brine within the same field
- ✓ Brine composition before and after seawater flooding
- ✓ Brine salinity and composition between different fields
- ✓ The importance of well selection within a field

Objective 3: To measure CO_2 mineral trapping potentials under reservoir conditions, using a high pressure rig and appropriate analytical techniques.

Objective 4: To asses calcite's potential to buffer brine and promote mineral carbonation, as well as how the dissolution and precipitation of minerals can affect the properties of the host rock, such as porosity.

Objective 5: To assess the potential effect that CO_2-saturated brine has on the permeability and porosity of local host rock over an extended period of time.

1.3 Thesis structure

This thesis is divided into eight distinct chapters. Chapter 1 is an introduction to the topic, highlighting the knowledge gaps and the aim and objectives of the study. Chapter 2 consists of an in-depth literature review on recent research and developments in both the CCS and EOR industries, mainly focusing on CO_2 geochemical trapping mechanisms and CO_2-EOR. Chapter 3 provides a detailed description on how the experimental work was performed. Chapter 4 discusses the selection of geochemical modelling software used to measure geochemical trapping potentials on a geological timescale and describes how the geochemical modelling work was performed (Objective 1). Objectives 2 and 3 are addressed in Chapter 5 which focuses on the importance of well selection through the development of synthetic brines and the measurement of geochemical trapping potentials through experimental and geochemical modelling work. Chapter 6 studies calcite's potential to buffer brine and promote mineral trapping, as well as how the dissolution and precipitation of minerals can affect the properties of host rock (Objective 4). Objective 5 is addressed in Chapter 7, where a typical North Sea host rock was subjected to CO_2-saturated brine under reservoir conditions for up to 9 months. Finally, Chapter 8 presents the conclusions of this study and also suggests future studies to compliment and expand on the work presented here.

Chapter 2 Literature Review

This chapter provides an in-depth analysis of the need for both CO_2 Capture and Storage (CCS) and Enhanced Oil Recovery (EOR) technologies and the development of said technologies. The purpose of this literature review is to provide the necessary background information for this study and offer an insight into why this research was undertaken.

2.1 Global energy demand

The International Energy Agency (IEA) has predicted that global total primary energy supply will rise to an estimated 16,500 Mtoe (Million tonne of oil equivalent) by 2030 with fossil fuels accounting for 75% of this value (approximately 12,500 Mtoe), while in 2014 fossil fuels accounted for roughly 11,110 Mtoe [2, 1]. Consequently, global reliance on fossil fuels is only likely to increase over the next few decades. This presents two significant issues. The first being that fossil fuels are not an infinite resource and so increased reliance on fossil fuels will put major strain on reserves. Furthermore, increased burning of fossil fuels will result in higher CO_2 emissions which were already at a record high in 2015, where global CO_2 emissions resulting from energy consumption were approximately 33.5Gt [3].

2.1.1 Fossil fuels and CO_2 emissions

According to the "BP Statistical Review of World Energy June 2016" the proven* reserves of oil, natural gas and coal are at present 1,698 thousand million barrels, 186.9 trillion cubic meters and 891,531 million tonnes, respectively [3]. Taking into account current extraction rates, coal supplies are estimated to last at least another century, whereas oil and natural gas reserves may be depleted within the next 60 years. Hydraulic fracking, for instance, which involves injecting millions of gallons of water, chemicals and sand at high pressure into shale deposits in order to break it up and release oil and shale gas, is receiving wide scale implementation in the U.S [26]. Hydraulic fracking in the U.S. alone is estimated to produce 13.6 trillion cubic meters of shale gas. Although there are concerns about environmental damage caused by fracking, which has resulted in hydraulic fracking not being implemented on a large scale in Europe, fracking does have the potential to increase fossil fuel reserves. Regardless, it does appear evident that oil and natural gas reserves will be the first to run out. This is a major concern as oil

*Proven reserves are those quantities of petroleum which, by analysis of geological and engineering data, can be estimated with reasonable certainty to be commercially recoverable, from a given date forward, from known reservoirs and under current economic conditions, operating methods, and government regulations [188]

accounted for almost one third (32.9%), and natural gas one quarter (23.8%) of the total primary energy consumption in 2015 [3].

In addition to the concerns attributed to diminishing fossil fuel reserves, there is also major concern with the effect that burning these fuels has on the Earth's climate. The combustion of fossil fuels release several greenhouse gases, such as carbon dioxide (CO_2), nitrous oxides, methane and aerosols into the Earth's atmosphere, which have an adverse effect on both humans and wild life. Of these greenhouse gases, CO_2 is considered to be the main culprit behind climate change as it absorbs photons in the infrared [27]. This results in CO_2 acting as a shield, trapping solar energy in the atmosphere that was absorbed by the Earth's surface and re-emitted. As levels of CO_2 in the atmosphere increase, so does the amount of energy trapped which in turn can lead to global warming, increased evaporation/precipitation and amplified winds. CO_2 is a relatively weak greenhouse gas compared to other gases such as methane and nitrous oxide. It has a Global Warming Potential (GWP), which is a measure of the contribution that a greenhouse gas has on global warming over a particular period of time, of 1 over a 100 year period [27]. In comparison, methane and nitrous oxide have GWP values of 28-36 and 265-298, respectively. The reason that CO_2 is considered to be responsible for climate change is hence not due to its GWP but due to the large quantities of CO_2 that are being produced.

In 2015, global CO_2 emissions resulting from energy consumption were approximately 33.5Gt [3]. Taking into account the IEA's total primary energy supply predictions for 2030 this value is only likely to rise. Levels of CO_2 emissions could in fact increase more rapidly over the next decade as new markets emerge, such as India and China, relying on substantial quantities of coal. For example, in 2015 China and India accounted for more than half of the global consumption of coal [3]. Coal is not only the most abundant fossil fuel but the largest producer of CO_2, where 1t of coal can produce 2.86t of CO_2 assuming that complete combustion is achieved. The IEA has predicted that as new markets emerge and oil and gas reserves are depleted, the global reliance on coal is likely to increase substantially [28].

2.1.2 Strategies to reduce CO_2 emissions and reliance on fossil fuels

With the knowledge that fossil fuel reserves may very well run out in just over a century and the potentially permanent damage that the increasing levels of CO_2 are doing to the Earth's climate, new strategies need to be implemented for both global energy security

and for the health of our environment. At present, there are several different strategies being taken in regards to this problem. For instance, increasing the efficiency of coal and gas-fired power plants would result in less fossil fuels being consumed and a reduction in CO_2 emissions. This can be done using several different technologies, such as combined heat and power (CHP), combined-cycle gas turbines (CCGT) and cofiring, as described below [29]. CHP involves rejected heat being passed through a heat exchanger so as to provide direct heat for space heating, water heating and process heating. This process reduces the large amount of heat rejection associated with power-only generation, which in turn means less fuel being needed and lower CO_2 emissions.

CCGT power plants use both a gas and steam turbine in tandem so that the exhaust gas from the gas turbine can be used to heat the steam. This can result in a thermal efficiency 10% greater than conventional steam plants (which usually have a maximum efficiency of 36%) [29]. Cofiring is used to adapt coal-fired power stations to fire coal with biomass to a fuel mix percentage of 10-25% on a mass basis. The cofiring method does not actually increase power plant efficiency, however, it does result in a reduction in the amount of coal needed and CO_2 emissions. Cofiring plants not only require less coal, but approximately 50,000-150,000 tons of CO_2 can be saved in a cofiring project each year [29].

The three aforementioned methods are effective in terms of reducing CO_2 emissions and the reliance on fossil fuels. However, they are not a solution to the problem. There is a potential solution which would result in almost zero CO_2 emissions and end our reliance on fossil fuels: renewable energies. The renewable energy sector has grown considerably over the past decade, accounting for 2.8% of global energy consumption in 2015, compared with 0.8% a decade ago [3]. This large increase has been due to the development of new technologies and increased investments by many governments. The Scottish government for instance has plans to generate 100% of its electricity via renewable sources by the year 2020. For this to be achieved an installed capacity of 15-16GW will be required [30]. However, according to the "Scottish Renewables Briefing – November 2015", this target will not be achieved by 2020, as predicted installed capacity will generate approximately 87% of electricity against the target of 100% [31]. Large scale renewable projects are being planned and undertaken by governments in many different countries. However, as previously stated, the renewable industry accounted for only 2.8% of global power consumption in 2015 and many renewable targets set by governments, such as in Scotland, are not being met [3, 31].

However, a recent report by Heuberger et al. (2016) suggests that intermittent renewable energies (such as wind and solar) must be implemented alongside Carbon Dioxide Capture and Storage (CCS) and not instead of, if global CO_2 reduction targets are to be met [32]. The reason being is that, although power generation from renewable energies such as wind are emission free, the fact that the power generation is intermittent means that they require fossil fuel power plants to generate back-up capacity to meet electricity demands. This means that the implementation of wind power can reduce CO_2 emission from 0.78 to 0.38 t_{CO2}/MWH, but when combined with CCS technologies this can be reduced to 0.05-0.1 t_{CO2}/MWH. The Intergovernmental Panel on Climate Change (IPCC) predict that without the implementation of CCS power plants, the global mitigation costs for CO_2 are 138% higher and per the Low Carbon Innovation Coordination Group, if the UK's energy sector does not fully integrate CCS then the costs between 2010 and 2050 will be £100-500 billion higher [33, 34].

Consequently, renewable energies cannot, at present, be relied on for global energy security or to have a significant effect on the reduction of CO_2 emissions without being implemented alongside CCS. Therefore, strategies need to be employed until renewable energy technologies are at the stage where they can take over as the dominant global energy supplier. These should involve trying to prolong the lifetime of fossil fuel reserves and dealing with the current CO_2 levels being produced. In addition to increasing power plant efficiency and using alternative fuels (such as biomass), two such strategies that are currently being employed are Enhanced Oil Recovery (EOR) and the aforementioned CCS, that are described in Sections 2.2 and 2.4, respectively.

2.2 Enhanced oil recovery technologies

An oil field goes through three different production stages throughout its lifetime, namely primary, secondary and tertiary [4]. During the primary stage, when the oil field is first put into production, the reservoir pressure forces the oil to flow to the surface naturally. This stage accounts for an original oil in place (OOIP) recovery of only 6-15% [5]. Once the pressure of the reservoir drops and there is no longer the required natural pressure to extract the oil, the field enters the secondary stage and either water or natural gas is injected to increase the reservoir pressure and displace the oil. The OOIP recovery at this stage is approximately 6-30%, depending on the specifics of the reservoir geology. A further 8-20% of the OOIP can still be recovered during the tertiary stage which refers to the use of Enhanced Oil Recovery (EOR) technologies [5]. This does however still leave 35-80%, of the OOIP remaining, and therefore, it is clear that further development

of EOR technologies is needed and that doing so could substantially increase the remaining lifetime of oil reserves.

2.2.1 Secondary stage of oil recovery

As mentioned above, during the primary stage, the initial reservoir pressure provides enough force to push the oil to the surface without any additional intervention. As oil is extracted, the pressure in the reservoir drops which reduces, and eventually halts production [4]. Therefore, fluids need to be injected so as to maintain the pressure in order for oil production to continue. This is the secondary stage and involves the injection of water and/or natural gas. The injected water and gas is usually recycled from the reservoir itself, reducing costs. The purpose of the injected water/gas is two-fold. The first is to maintain the reservoir pressure so that production can continue and the second is to sweep the reservoir oil towards the production wells which further increases production [4]. In many cases the Water Alternating Gas (WAG) method is used to increase sweep efficiency. This is due to the injected gas being less dense than the oil and the water being denser. Individually, the gas would only sweep the top part of the reservoir whereas the water would sweep the bottom. By combining water and gas injection using the WAG method the area of the reservoir that is swept is maximised. However, not all the oil that has come into contact with the injected water/gas will be displaced due to viscosity, well spacing and general rock characteristics (some of the oil may be trapped) [4]. As a result, this residual oil will remain in the porous media. To recover this oil EOR technologies are needed.

2.2.2 Overview of different EOR technologies

EOR technologies are employed to increase both macroscopic and microscopic displacement efficiencies compared with those achieved during the secondary stage. Macroscopic efficiency is increased by reducing the mobility ratio between the displacing and displaced fluids, whereas increasing microscopic efficiency is achieved by reducing the interfacial tension between the two fluids. There are four main categories of EOR technologies; namely, thermal recovery, chemical flooding, microbial flooding and gas miscible recovery [35]. The focus of this study is on gas miscible recovery, namely CO_2-EOR; however, a brief description of the four categories involved is also provided here.

As can be seen from Figure 2.1, thermal recovery results in the highest production rate of all the EOR technologies producing approximately 2 million barrels of oil per day as of 2010. Along with miscible gas recovery, it is the most widely implemented method of

EOR. Thermal recovery is generally used for the extraction of heavy, viscous crudes and consists of steam injection or in-situ combustion. It can be used to stimulate individual wells or flood the entire field. Steam injection is used to recover heavy viscous oil, as the heat from the steam thins the oil, which along with the increased pressure associated with the introduction of the steam, allows the oil to be produced [36]. The less economically viable thermal recovery process is in-situ combustion. During this process oil is recovered by burning a fraction of it within the reservoir. This is done by injecting oxygen or air. The produced combustion gases provide the necessary gas drive to displace the oil [36].

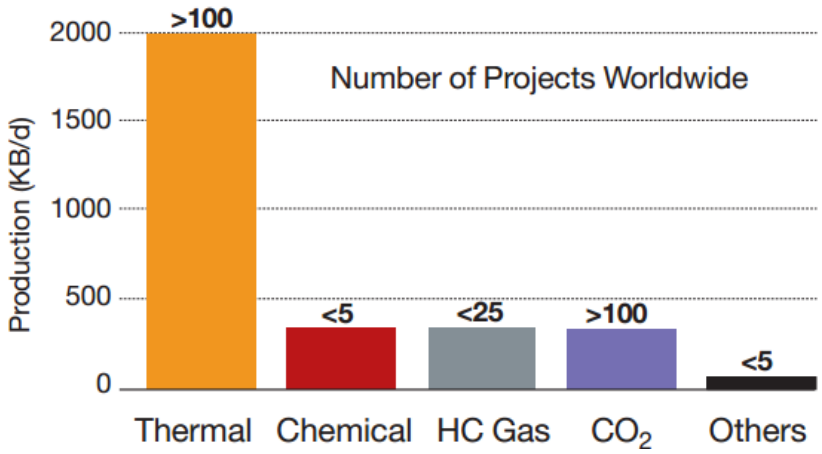

Figure 2.1: Worldwide EOR production rates as of 2010 in thousand barrels per day [37]

Chemical recovery comes in two forms, namely polymer flooding and surfactant flooding. The former increases macroscopic displacement efficiency, whereas the latter increases microscopic displacement efficiency. During polymer flooding, water-soluble polymers with high molecular weight are added to the injection water. The two most common polymers used are partially hydrolyzed polyacrylamide and xanthan [38]. The introduction of these polymers improves the water's mobility ratio which in turn reduces oil bypassing and raises the yield [35]. Surfactant flooding on the other hand, involves injecting a surfactant solution (that reduces interfacial tension) into the reservoir. This is usually followed by the injection of polymer thickened water and finally brine. The overall result is a large increase in microscopic displacement efficiency. However, high costs associated with the amount of chemicals needed and the fact that they are not recoverable seriously hinders the wide-spread application of this process [35]. This is backed up by the data in Figure 2.1 which shows that as of 2010 there were less than 5 EOR projects worldwide that implemented chemical recovery.

Microbial recovery involves introducing microbes to the oil which induce several changes, such as a reduction in viscosity and interfacial tension. There are two main mechanisms in microbial recovery. The first breaks down and metabolises the oil at the oil-water contact which increases the oils mobility. The second mechanism forces water into new channels by blocking the existing water channels located within the reservoir. This in turn provides the driving force for the oil to reach the surface [39]. At present, microbial recovery is still in the development stage and has only been field tested.

The final and most important EOR technology, in regards to this study, is gas miscible recovery. As can be seen from Figure 2.1, gas miscible recovery (shown as HC Gas and CO_2) has had wide scale implementation and the vast majority of EOR projects either use gas miscible recovery or thermal recovery. Although thermal recovery results in a higher production rate, gas miscible recovery is used for the extraction of light crudes and can be used in both carbonate and sandstone reservoirs [37]. During gas miscible recovery a solvent is injected into the reservoir which usually consists of nitrogen, flue gas, natural gas (which can be enriched) or CO_2. Miscible flooding consists of three different processes; first contact miscible flooding, vaporising gas drive and condensing gas drive [35].

2.2.3 Miscible flooding processes

First contact miscible flooding is the most direct method of miscible displacement, where the injected solvent mixes completely with the oil to form a single phase. For this to be achieved, the pressure must be above the cricondenbar, which is defined as the maximum pressure at which two phases can exist in equilibrium [4]. When a single phase is formed, the interfacial tension effectively disappears, which allows the miscible gas to displace the oil and force it to the surface [35]. This process, however, generally requires expensive hydrocarbon solvents (C_{3+}) such as natural gas. Flue gas and CO_2 are not first contact miscible. They instead form two-phase regions when mixed with reservoir fluids, where miscibility is attained via the mass transfer of components which is a result of multiple contacts between the solvents and the oil throughout the reservoir. This is known as dynamic miscible displacement and can be achieved by either vaporising or condensing gas drive [35].

Vaporising gas drive involves the vaporisation of intermediate reservoir oil components. The creation of a miscible transition zone and the high injection pressure allows for the extraction of hydrocarbons C_2 to C_6. This process displaces almost all the oil in the contact

area, but this area may be small due to reservoir heterogeneities and poor flow conditions [35]. During the injection of a rich gas, the gas and oil are at first immiscible. When the fresh solvent meets the reservoir oil, a miscible bank is formed as a result of condensation. This is the basis behind condensation gas drive. Once the miscible bank has formed a process analogous to vaporising drive develops and causes the oil located behind the front to become lighter. Due to swelling, this lighter oil will occupy a considerably larger volume in the rock pores than that of the original oil. The result will be the formation of a mobile oil bank situated behind the gas zone which has been stripped of its intermediate components [35].

In terms of dynamic miscible displacement, CO_2 has proven to be one of the most effective solvents. This is due to the fact that the pressure required to achieve dynamic miscibility is considerably lower when using CO_2 over other solvents and it also allows for the extraction of higher molecular weight hydrocarbons up to C_{30} [35]. As a result, CO_2 flooding is not only the most effective means of gas miscible recovery, but also considered to be one of the most effective methods of EOR. CO_2-EOR is discussed in the following section.

2.3 CO_2-enhanced oil recovery

The first large scale CO_2-EOR project known as the SACROC Unit was established back in 1972 in the Permian Basin located in West Texas [6]. The CO_2 used in this project came from natural gas processing facilities. It later became apparent that large quantities of CO_2 could be produced from naturally occurring CO_2 fields which was a far cheaper option. As a result, in the early 1980s extensive pipeline networks were constructed so as to connect the CO_2 fields located in New Mexico, Colorado and Mississippi to the growing number of CO_2-EOR projects in West Texas [6]. This cheap source of CO_2 led to the construction of CO_2-EOR projects in other regions of the U.S. such as the Gulf Coast and Rocky Mountains, leading to a large growth in U.S. projects from 1986 onwards, which is shown in Figure 2.2.

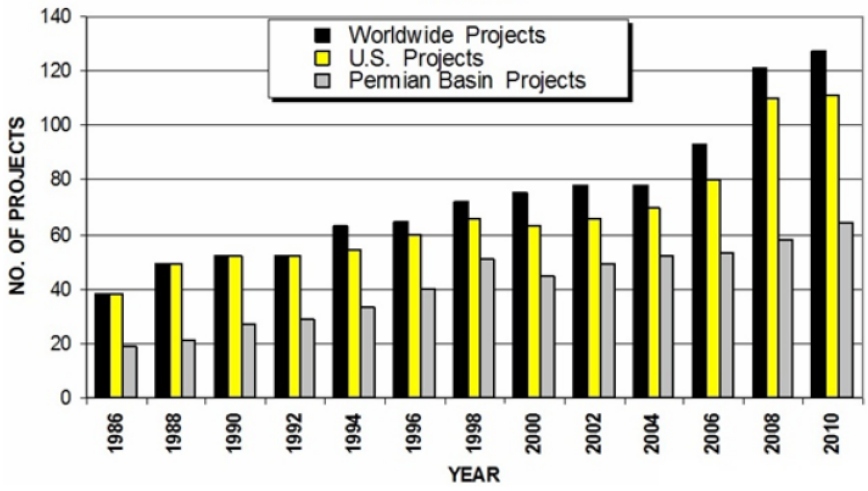

Figure 2.2: Expansion of CO_2-EOR industry from 1986-2010 [40]

2.3.1 Scale of CO_2-EOR in the United States

As of 2014, there were 136 CO_2-EOR projects in operation across the U.S., producing 300,000 barrels per day and requiring over 3,000 miles of pipeline to transport the CO_2 from its source to the oil fields [7, 41]. This industry has shown significant growth over the past four decades and now includes over 20 participating companies that are developing new practices and technologies to further boost CO_2-EOR efficiency [8]. It is estimated that these current projects could potentially produce 26-61 billion barrels of additional oil over their lifetime and with additional research into new technologies the overall production potential could reach 67-137 billion barrels [42]. With the U.S. consuming 7.08 billion barrels of oil in 2015, CO_2-EOR has the potential to significantly increase the lifetime of remaining oil reserves [43]. This will allow more time for technologies such as renewable energies to reach maturity and take over as the global primary energy source.

2.3.2 Proposed CO_2-EOR in the North Sea

Although the vast majority of CO_2-EOR projects are located in the U.S., there are many other locations worldwide, where CO_2-EOR is being considered. For instance, since 1999 there have been proposals for CO_2-EOR in the North Sea. It is estimated that CO_2-EOR could potentially produce 2.4 billion barrels of oil in 19 oilfields located in the UK Continental Shelf (UKCS) and a further 3 billion barrels in 11 oilfields located in the Danish and Norwegian sectors [44]. This does not take into account smaller oilfields which could increase these values significantly. It is clear that CO_2-EOR in the North Sea has huge potential but there is unwillingness for companies to invest. The main barrier for these proposals has been the difficulties associated with offshore CO_2-EOR.

In the U.S., all CO_2 injection is onshore and in fact the only location where offshore CO_2-EOR has been explored is of the coast of Brazil at the Lula oil and gas field [44]. Pilot projects for offshore oil production are far more expensive compared with onshore and so core sampling must be conducted prior to production. Core testing can take several months to complete, after which a detailed model of the reservoir must be produced. The core samples, as well as the reservoir models, may be unrepresentative for specific reservoirs and hence produce uncertainties in the data [44]. Other factors such as topology, capacity, pressure management, phasing, role of shipping and entry specifications also need to be taken into account as they all affect offshore CO_2-EOR. What makes the Lula field project the exception is that it was only discovered in 2006 and was specifically developed with the intention of CO_2-EOR [45]. In addition, the solution gas in the Lula field has a high CO_2 content of 8-15%. This CO_2 is separated from the produced natural gas and used for re-injection, meaning that it does not require an external supply of CO_2.

In addition to the North Sea oilfields being offshore, their characteristics are far different from those in the Permian Basin in the U.S. [44]. For instance, North Sea oilfields are located within deep sandstones with steeply dipping beds, lots of fault blocks, high API gravity oil (i.e. light crudes) and have high permeability. Conversely, the oilfields in the Permian Basin used for CO_2-EOR consist of carbonates with low permeability, few faults and low API gravity oil. Said differences have raised concerns surrounding the performance of CO_2-EOR in the North Sea [44]. Another major barrier associated with CO_2-EOR in the North Sea is CO_2 supply. As previously stated, in the U.S. there is already a huge infrastructure in place to connect the large CO_2 fields to CO_2-EOR projects. These fields account for 83% of the CO_2 used in EOR and provide a low cost and reliable supply [6]. At present, a reliable source of CO_2 is not available for potential CO_2-EOR projects in the North Sea and until this is rectified, it is unlikely that CO_2-EOR will be implemented in the North Sea [44]. However, there is a potential solution to this problem, in the form of CCS and this will be discussed in Section 2.8.

2.3.3 CO_2 injection process

The principles of how gas miscible recovery works have already been discussed in Section 2.2.3. However, the injection process itself has yet to be discussed. CO_2 is transported to the site via pipeline under the conditions that it will be used in when it reaches the injection wells i.e. under supercritical conditions [8]. A fluid that is heated above its critical temperature and compressed above its critical pressure is defined as a

supercritical fluid. CO_2 is in a supercritical state above its critical temperature of 304.128K and critical pressure of 7.377MPa [46]. Under these conditions, a fluid has density akin to a liquid, with the viscosity and diffusivity similar to that of a gas [47]. Having a high density but low viscosity makes supercritical CO_2 ideal for transportation through pipelines. In addition, supercritical fluids have a faster rate of diffusion through a solid matrix than their liquid counterparts, but retain a high solvent strength so as to extract solutes contained within the solid matrix [47]. These properties maximises the effectiveness of CO_2 at displacing residual oil. Upon reaching the injection wells, the CO_2 is injected into the reservoir, moving through the rocks pore spaces where it comes into contact with droplets of oil and becomes miscible with the oil. At this point a concentrated oil bank is formed and pushed towards production wells [8].

As the bank reaches the production wells, oil and water are forced to the surface, where they are collected in a centralised facility. The fluids are then separated and the gas stream produced must then undergo further processing. This is due to the fact that the gas stream may contain CO_2 which must be separated from the natural gas. Upon separation, the CO_2 is recompressed and re-injected to start the process over. In many cases the water produced at the wells is treated and undergoes reinjection, alternating with the CO_2 injection so as to improve the sweep efficiency [8]. This process is known as Water Alternating Gas (WAG) and an outline of the process can be seen in Figure 2.3. The combination of CO_2 and water maximises the sweep area and once the CO_2 comes in contact with the oil, it becomes miscible with the oil (miscible zone). As previously stated, the CO_2 that dissolves in the oil causes it to swell, increasing the volume that it occupies in the rock pores, which results in the formation of an oil bank. The oil bank is then forced towards the production well due to the pressure provided by the CO_2 and water. Figure 2.3 also gives an indication to how some of the injected CO_2 can be stored and sequestered within the reservoir (bottom left of diagram) and this shall be further discussed in Section 2.5.

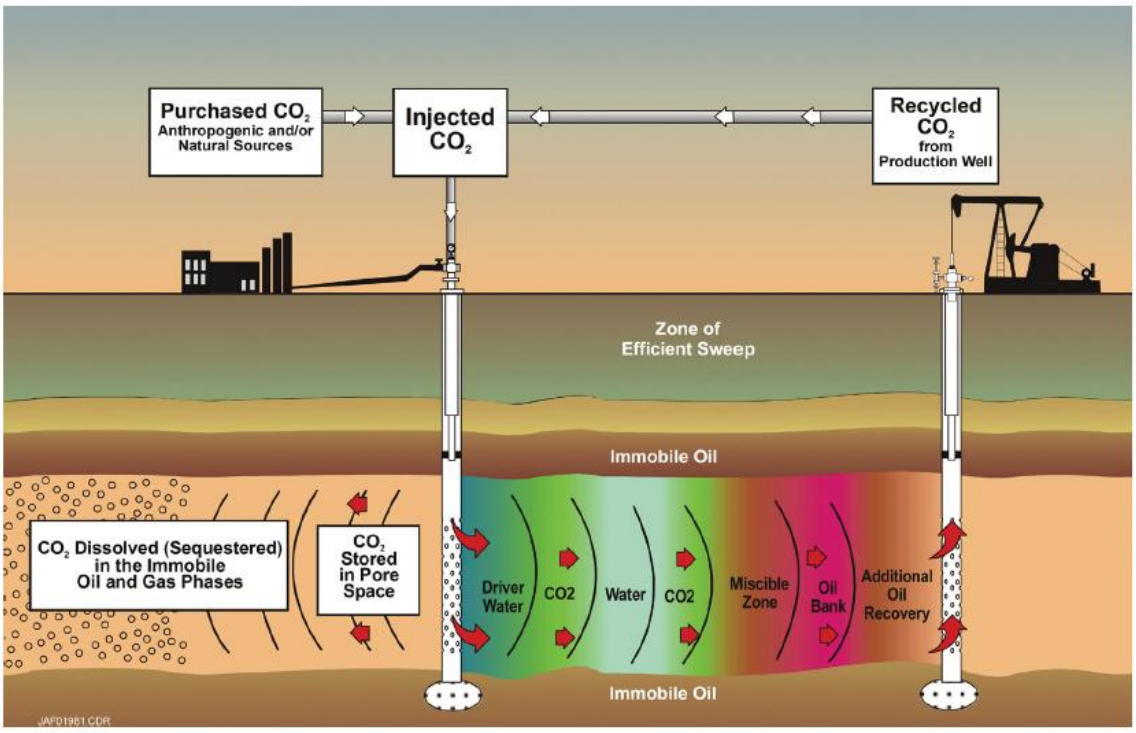

Figure 2.3: CO_2 WAG method of EOR [6]

2.3.4 Merits and drawbacks of using CO_2 for miscible flooding

The main reasons for using CO_2 as a solvent for miscible CO_2 flooding are its availability (especially in the U.S.), the fact that it can extract heavier hydrocarbon components and that its solubility in oil causes the oil to swell [35]. In addition, CO_2 has a number of other characteristics that benefit EOR, such as reducing the oil viscosity and increasing oil density. It can also extract oil by vaporisation; achieve miscibility at relativity low pressures from 10-30MPa and causes a reduction in the surface tension of both oil and water, resulting in increased displacement.

CO_2 flooding is, however, not without its drawbacks. The main problem associated with using CO_2 is its high mobility which can lead to viscous fingering and gravity segregation [48]. Viscous fingering is where finger-like intrusions develop during miscible displacement as a result of CO_2 being less viscous than oil. Gravity segregation, on the other hand, is a result of CO_2 being less dense than the oil and so only sweeps the top of the flooded area. Although these problems can reduce the efficiency of CO_2-EOR, there are ways in which to overcome them such as the aforementioned WAG process, installing well packers and shutting in production wells so as to regulate the flow [35]. In addition when CO_2 dissolves in formation water, also known as brine, its mobility decreases which in turn reduces viscous fingering and gravity segregation and therefore increases oil

displacement. As a result, CO_2 solubility in brine is an important mechanism in regards to CO_2-EOR.

CO_2 solubility in brine is an active area of research and has thus far investigated a number of factors which affect CO_2 solubility in brine, such as temperature, pressure and salinity which will be covered in Section 2.5.2 [24]. Being an active area of research, there are still aspects of the process that need to be evaluated, e.g. how the composition of the brine affects the solubility of CO_2. **By using real brine data, for instance from North Sea oil wells where CO_2-EOR may be implemented in the future, a realistic take on CO_2 solubility in brine under actual reservoir conditions can be achieved. Therefore, obtaining experimental and geochemical modelling data on how the solubility of CO_2 in brine is affected by brine composition should be an avenue for new research.**

It is clear that CO_2-EOR is one of the most effective EOR technologies and along with other EOR methods, it has the potential to significantly increase the lifetime of oil reserves. As already suggested, increasing the lifetime of remaining fossil fuel reserves is an integral part of the future of global energy security and must be a top priority. It is, however, equally important that current and increasing levels of CO_2 are appropriately dealt with. Consequently, CCS technologies are covered in the following section.

2.4 CO_2 capture and storage technologies

This section is focused on the storage of CO_2. However, a description of the CO_2 capture processes provides an additional insight into CO_2 Capture and Storage Technologies (CCS) technologies. There are three main CO_2 capture processes which include pre-combustion, post-combustion and oxy-fuel combustion [9].

2.4.1 CO_2 capture processes

Pre-combustion gas decarbonisation is a method of removing CO_2 and other pollutants during fossil fuel treatment before combustion takes place [49]. The hydrocarbon fuel undergoes gasification with oxygen which results in the production of a syngas. This syngas is mainly a mixture of carbon monoxide (CO) and hydrogen (H_2). The syngas is then used for the production of hydrogen, integrated electric power or polygeneration (which can include hydrogen, chemicals, power and heat). The CO_2 is captured using different processes depending on how the syngas is being used [49]. For hydrogen production, the CO_2 is captured via scrubbing in an absorption tower. On the other hand, during integrated power production and polygeneration the syngas is fed into a shift

converter which separates the CO_2. This process is known as water gas shift, whereby CO is reacted with steam in a catalytic reactor to produce CO_2 and H_2.

Post combustion gas scrubbing involves separating CO_2 from the exhaust gas which has been produced as a by-product of fossil fuel combustion [50]. There are a number of methods of post combustion used to separate CO_2, such as chemical and physical absorption, solid physical and chemical adsorption and membrane separation [50]. Chemical absorption involves scrubbing the exhaust gas with an absorbent in an aqueous solution, for instance potassium carbonate or an amine. Physical absorption is where CO_2 is subject to high partial pressures and low temperatures and is physically absorbed in a solvent. Solid physical adsorption involves first adsorbing CO_2 using an adsorbent to remove it from the exhaust gas, then the CO_2 undergoes desorption to separate it completely. Chemical adsorption looks to improve CO_2 adsorption by chemically modifying the surface of solid materials with inorganic metal oxides and amines. The acidic CO_2 molecules form covalent bonds with the basic active sites located on the surface of the material which promotes CO_2 adsorption [51]. Finally, membrane separation is where the exhaust gas is passed through a separation membrane which only allows the permeation of specific gases i.e. CO_2 [50].

The third CO_2 capture process is oxy-fuel combustion which involves burning the fuel in pure oxygen instead of air [9]. With the presence of nitrogen significantly reduced, the exhaust gas will be composed almost entirely of CO_2. High concentrations of CO_2 can then be recovered via condensation. The downside to this method is that due to the fuel being burnt in pure oxygen, instead of air, the flame temperature is extremely high. This means that special heat resistant combustors must be built to withstand such high temperatures and require gas recirculation.

When comparing the three processes, post-combustion is the most mature technology and is utilised in both coal and gas fired power plants, as is oxy-fuel combustion [9]. It is also considered the most cost effective method when implemented in gas-fired power plants, costing approximately \$58/t CO_2 [52]. This can be compared with using pre-combustion (\$112/t CO_2) or oxy-fuel combustion (\$102/t CO_2). Pre-combustion is generally only used in coal fired plants and is the most cost effective capture process for these plants, costing roughly \$23/t CO_2, with post-combustion and oxy-fuel combustion costing a similar amount (approximately \$34/t CO_2 and \$36/t CO_2, respectively).

2.4.2 CO_2 geological storage

Following capture, CO_2 must be transported to a storage site that will store the CO_2 in a safe and convenient manner. CO_2 can be transported by sea, by rail, and by road in tankers or can be transported via pipeline as is done in the U.S. for CO_2-EOR projects (Section 2.3.1) [7, 9]. The CO_2 is transported in either a liquid or supercritical state to maximise the CO_2 mass/volume ratio. Currently, the most economically viable means of storing CO_2 is within geological formations. There are, however, a multitude of different types of storage locations for CO_2, some of which are considerably more effective than others. For instance, the IPCC reported that as of 2005 the world's oceans had already dissolved an estimated 500Gt of the estimated 1300Gt of total anthropogenic emissions, making it an effective storage location [10]. However, there is a major concern with adding large quantities of CO_2 to the oceans and that is the effect it has on the environment. CO_2 is acidic and so alters the pH of water. This shift in pH may be small, yet even a small shift can have dire repercussions for marine biology. As a result, the injection of CO_2 into oceans is no longer considered as a viable storage method. The current, most viable means of CO_2 geological storage and their estimated storage capacities are shown in Table 2.1.

Table 2.1: Estimated storage capacity of CO_2 geological storage options [10]

Reservoir type	Storage capacity:	
	Lower estimate	Upper estimate
Oil and gas fields	675* Gt CO_2	900* Gt CO_2
Unmineable coal seams	3-15 Gt CO_2	200 Gt CO_2
Deep saline formations	1000 Gt CO_2	Uncertain, but possibly 10^4 Gt CO_2
*These numbers would increase by 25% if 'undiscovered' oil and gas fields were included in this assessment		

The storage of CO_2 in unmineable coal seams is in its infancy. This process involves injecting CO_2 into coal seams where it is adsorbed and results in the sealing of the coals capillary channels [8]. This occurs as a result of the adsorbed CO_2 causing the coal to lose its brittle nature and becoming rubbery. The original methane residing within the coal

seams has a lower affinity with the coal than the adsorbed CO_2 and is hence displaced. The methane can therefore be pumped to the surface and extracted [53]. Using CO_2 to extract methane is known as CO_2-enhanced coal bed methane (CO_2-ECBM) production. With the ability to extract natural gas and a potential storage capacity of 3-200Gt of CO_2, the use of unmineable coal seams as CO_2 storage option could become viable [10].

Another CO_2 storage method that is still being investigated is the use of CO_2 for enhanced gas recovery (EGR). This could result in increased natural gas recovery as well as the storage of CO_2 within the gas reservoirs. The cost of storing the CO_2 would likely be off-set by the income provided by the recovered natural gas. However, unlike CO_2-EOR, which is a well established technology, there have been only two known CO_2-EGR projects, namely, at the Budafa Szinfeletti Field in Hungary and at the Gaz de France K12-B Reservoir in the Netherlands [54]. The reasons for the lack of commercialisation of CO_2-EGR are likely due to CO_2 being expensive, concerns that CO_2 and methane will mix together rapidly which would degrade the gas and that CO_2 geological storage is yet to be widely practiced. That being said, simulations and laboratory tests have shown that CO_2-EGR has a lot of potential [55]. For instance, the CO_2/methane mobility ratio is favourable, as is the density of CO_2 which is two to six times higher than methane which would result in stable displacement. As a result, the use of CO_2-EGR could potentially recover 10% of the gas initially in place (GIIP). Much like the aforementioned CO_2-ECBM process, CO_2-EGR could be considered as a viable CO_2 storage option pending on future research.

Storage of CO_2 in depleted oil and gas fields as well as deep saline aquifers are deemed as the most effective CO_2 storage options. This is due to their large storage capacities, integrity and safety and that much of the infrastructure for injection is already in place as a consequence of the oil and gas industry [10]. These formations contain large volumes of porous rock that can retain the gas. Deep saline aquifers are defined as porous sedimentary rocks which are saturated with both brines and formation waters. They are located within sedimentary basins worldwide and they provide a much larger storage capacity than depleted oil and gas fields that ranges from 400-10,000Gt compared with 920Gt [11]. Before CO_2 injection can be undertaken, the aquifer must meet several standards [56]. For instance, there must be an overlying caprock that does not exhibit any fractures or contain uncompleted wells. In addition, the aquifer must be at a minimum depth of 800m meters. This is to ensure that the injected CO_2 will remain in a supercritical state. Although deep saline aquifers provide the largest CO_2 storage capacity, the

advantage of using oil and gas fields for storage is that due to the oil and gas industry these fields have been extensively mapped. In contrast, very little is known about saline aquifers.

2.4.3 CO_2 storage in the North Sea

There has been a lot of work of late looking at CO_2 storage capacities, especially in the North Sea. It has been estimated that the combination of depleted oil and gas fields along with deep saline aquifers could provide a CO_2 storage potential in the North Sea of approximately 100-300Gt [44]. A more detailed study has recently been carried out on the UKCS, called the UK Storage Appraisal Project which located and identified the risks, economics and capacities of roughly 600 CO_2 storage locations. Their findings showed that the UKCS has a theoretical storage capacity of 78Gt, of which 68Gt would be provided by saline aquifers [57]. The UK total CO_2 emissions in 2014 were approximately 422Mt, meaning that the UK theoretically has a large enough storage capacity to store its own CO_2 emissions for the foreseeable future [58]. Figure 2.4 was produced for the UK Storage Appraisal Project and shows the CO_2 storage locations in the Northern, Central and Southern North Sea along with the East Irish Sea. It also shows the proximity of the largest industrial emitters in the UK with respect to CO_2 storage locations.

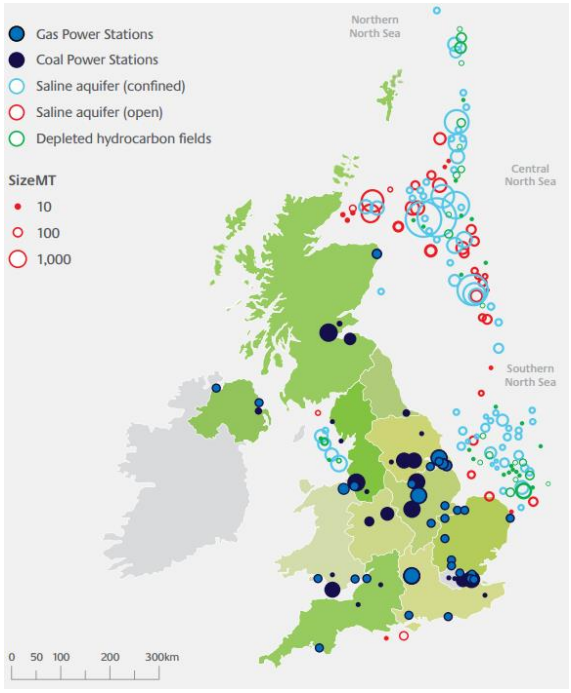

Figure 2.4: Map of CO_2 storage locations and point sources [57]

2.4.4 Carbon capture and storage by mineralisation

Arguably the safest way of storing CO_2 is via carbon capture and storage by mineralisation (CCSM), whereby insoluble carbonates are formed, that are

thermodynamically stable and hence require zero monitoring [59]. These insoluble carbonates are formed naturally through a process known as silicate weathering in which CO_2 reacts with a metal oxide. Silicate weathering, however, takes place over geological time scales and so the use of additives is required to speed up the process. Another advantage of CCSM is the abundance of raw materials, where there is estimated to be enough raw materials to sequester the total global CO_2 emissions produced from burning the remainder of our fossil fuel reserves [60]. The major downside to this technology comes in the form of slow kinetics, low efficiencies during mineral dissolution, which is necessary to extract the metal oxides and a significant energy demand associated with pre-treatment. The slow kinetics and low efficiencies can be compensated for by the use of additives but the large quantities of chemicals required makes CCSM at present, not economically viable [61].

It can, therefore, be concluded that at present the most effective means of CO_2 storage is within depleted oil and gas fields and deep saline aquifers. Once the CO_2 has been injected into these oil/gas fields and saline aquifers it can be trapped via two different mechanisms, physical trapping and geochemical trapping, which are described in the following section.

2.5 CO_2 geological storage mechanisms

When injecting CO_2 into deep geological formations, such as saline aquifers and depleted oil and gas fields, it is important to understand how the CO_2 will be trapped, namely via physical trapping and geochemical trapping [12]. The former is split into three separate mechanisms; static (structural and stratigraphic), hydrodynamic and residual gas trapping, whereas the latter consists of mineral and solubility trapping. Upon injection, CO_2 is generally trapped by physical trapping mechanisms, as geochemical trapping occurs over a considerable time period [13]. Geochemical trapping is preferred as it does not depend on the integrity of the cap rock unlike physical trapping and so is a more secure method of storage. However, geochemical trapping mechanisms can take centuries, if not millennia to come into play. As a result, when injecting CO_2 into deep geological formations it is physical trapping mechanisms that are considered as the principle means of storage which can be seen in Figure 2.5 [10].

Figure 2.5 shows both the contribution of each trapping mechanism to the storage of CO_2, as well as storage security, as a function of time. The plot does not include hydrodynamic trapping, nor does it take into account that the contribution of each trapping mechanism is dependent on the conditions of the geological formation. However, it does provide a

visual representation of how the contribution of each trapping mechanism is dependent on time and that upon injection it is physical trapping mechanisms that dominate with, the more secure geochemical trapping mechanisms reaching dominance after a geological time period i.e. in excess of 10,000 years.

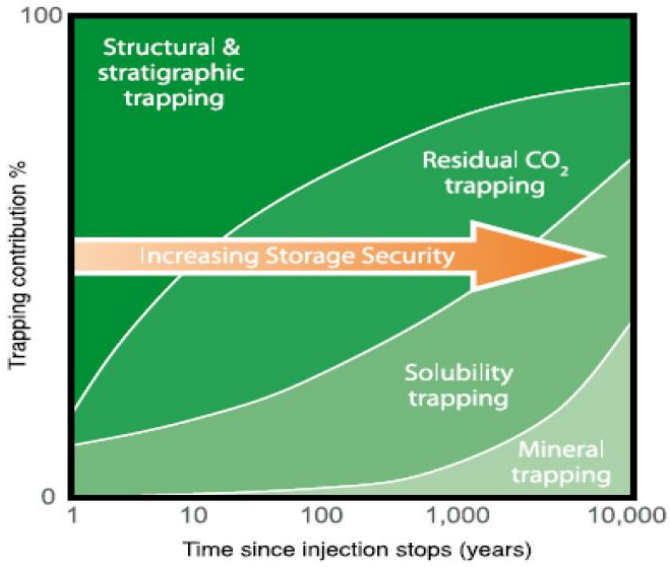

Figure 2.5: Trapping contribution and storage security of different trapping mechanisms over time [10]

2.5.1 Physical trapping mechanisms

Structural and stratigraphic trapping are known as static trapping mechanisms. During static trapping a caprock, which is a low-permeability or impermeable seal, forces the buoyant CO_2 to migrate in a lateral direction along the formation's layer of inclination [13]. The CO_2 is then either trapped by formed or folded rocks (structural trapping) or by changes in the type of rock (stratigraphic trapping). As shown in Figure 2.5, static trapping provides the largest contribution to CO_2 storage after initial injection. However, the additional pressure associated with injecting the CO_2 must be controlled, so as to avoid fracturing the caprock or causing faults to reactivate [10]. Hydrodynamic trapping is a time-dependant hydro-geological process, whereby the CO_2 is trapped as a result of the large amount of time it takes to reach the surface [10]. In fact, in a deep basin, it can take millions of years for the CO_2 to return to the surface, as it may have travelled hundreds of kilometres from where it was originally injected [56]. During hydrodynamic trapping, the CO_2 fluid forms a plume that migrates vertically along the permeable pathways until it reaches a caprock, and then the CO_2 travels buoyantly upwards towards higher structural levels located adjacent to the caprock-reservoir boundary. This is due to CO_2 being less dense than water, where under CO_2 supercritical conditions, CO_2 has a density of 436kg/m^3 compared with 998.5kg/m^3 for water [13].

The third physical mechanism discussed here is residual gas trapping. This mechanism involves CO_2 being rendered immobile within pore spaces due to interfacial tension between the local brine and the injected CO_2 [62]. The interfacial tension between the two fluids means that flow is impossible even with an available pathway. When CO_2 is injected into the reservoir a migrating stream or plume moves through the pore spaces which displaces the local brine. As the CO_2 moves out of the pore space, the displaced brine returns. This is known as an imbibition cycle, where a wetting fluid returns to a pore space after a non-wetting fluid has moved on [13]. Once the brine returns, any residual CO_2 gas bubbles that were left behind are trapped, hence the term residual gas trapping [62]. In contrast to static trapping mechanisms, residual gas trapping storage volume is time-dependant and increases as the CO_2 plume spreads and migrates [12].

2.5.2 Solubility trapping

Once the CO_2 has been physically trapped, it will start to react with the local rock and brine. It is at this point that geochemical trapping mechanisms come into play. Unlike physical trapping mechanisms, there is a particular order in which geochemical trapping mechanisms occur which can be seen from Figure 2.5. Firstly, solubility trapping takes place, whereby the CO_2 dissolves in brine, trapping it as an aqueous component [14]. The aqueous CO_2 then reacts with water to form a carbonic species. The concentration of each of the three carbonic species, H_2CO_3, HCO_3^- and CO_3^{2-}, is dependent on the brine pH which will be discussed later in the section. Equations 2.2-2.4 show the formation of each of the three carbonic species:

$$CO_2(g) \leftrightarrow CO_2(aq) \tag{2.1}$$

$$CO_2(aq) + H_2O \leftrightarrow H_2CO_3 \tag{2.2}$$

$$H_2CO_3 \leftrightarrow H^+ + HCO_3^- \tag{2.3}$$

$$HCO_3^- \leftrightarrow H^+ + CO_3^{2-} \tag{2.4}$$

Then mineral trapping occurs which involves ionic species and carbonate ions reacting with the metal cations located in the brine, forming solid insoluble carbonates. Equations 2.5-2.7 show the metal cations, Mg^{2+} and Ca^{2+} reacting with the carbonate ion, CO_3^{2-} to form magnesite (2.5), calcite (2.6) and dolomite (2.7) [14]:

$$Mg^{2+} + CO_3^{2-} \leftrightarrow MgCO_3(s) \tag{2.5}$$

$$Ca^{2+} + CO_3^{2-} \leftrightarrow CaCO_3(s) \quad (2.6)$$

$$Ca^{2+} + Mg^{2+} + 2CO_3^{2-} \leftrightarrow CaMg(CO_3)_2(s) \quad (2.7)$$

After solubility trapping, the CO_2 is no longer in a separate phase and so the CO_2 fluid is not subject to the buoyant forces that drive it upwards [15]. Hence, the CO_2 is more securely stored than with physical trapping mechanisms.

As mentioned in Section 2.3.4, the solubility of CO_2 in brine depends on a number of factors, such as pressure, temperature, and salinity [24]. Figures 2.6-2.8 show both modelling and experimental data for CO_2 solubility under pressure, temperature and salinity conditions for CO_2 storage. Figure 2.6 shows how CO_2 solubility in brine increases with pressure at a constant temperature of 323K and brine salinity of 1 mol NaCl/kg brine. This is explained by Henry's law, which states that the concentration of dissolved gas at equilibrium is directly proportional to the partial pressure of the gas [63]. The open diamonds are the results of modelling achieved using a CO_2 solubility calculator created by Duan and Sun (2003) and Duan et al. (2006), whereas the black squares are experimental measurements by Nighswander et al (1989), Li et al. (2004) and Kiepe et al. (2002) [64, 65, 66, 67, 68]. The experimental results are not consistent with one another due to different experimental procedures being employed. A critical review of the different experimental procedures that can be used to measure CO_2 solubility is presented in Section 2.6.

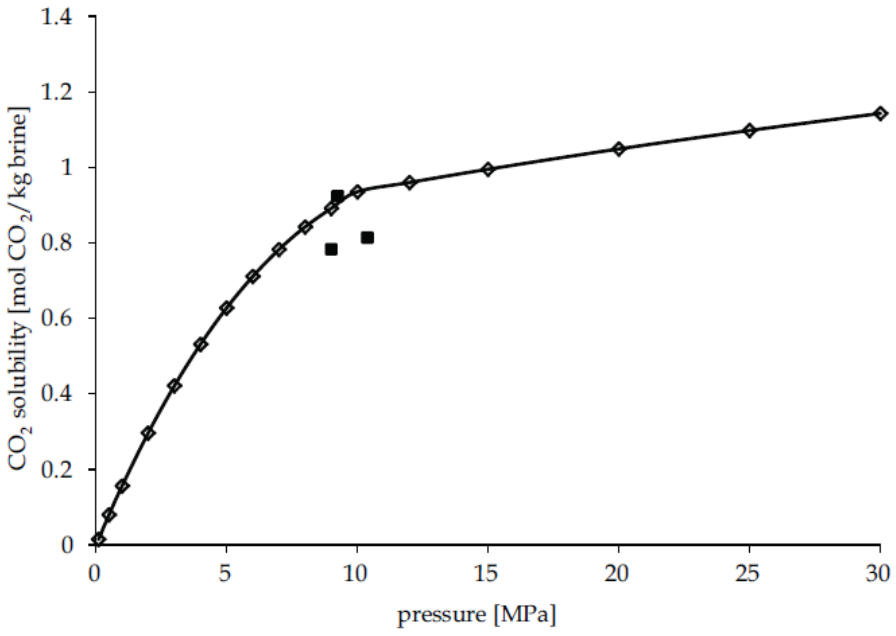

Figure 2.6: CO_2 solubility as a function of pressure at 323K and 1 mol NaCl/kg brine. Modelling and experimental data [24]

An increase in temperature has the opposite effect on brine solubility, as can be seen from Figure 2.7. When heat is added to a solution, the additional thermal energy is sufficient enough to overcome the attractive forces that exist between the solvent and the gas molecules [63]. This leads to a reduction in gas solubility and is why CO_2 solubility in water decreases with increasing temperature. Since temperature has a lesser effect on solubility than pressure, deep host rocks (800-1000m) are suitable for CO_2 storage, as the associated high pressures compensate for the increased temperatures [10]. In this case, the pressure was set to 10MPa and the salinity was once again 1 mol NaCl/kg brine [24]. As before, the modelling data is represented by the open diamonds, whereas the rest of the symbols correspond to the experimental measurements. It should be noted that the measurement by Rumpf et al. (1994) is significantly lower due to the experiment being run at high brine salinity [69].

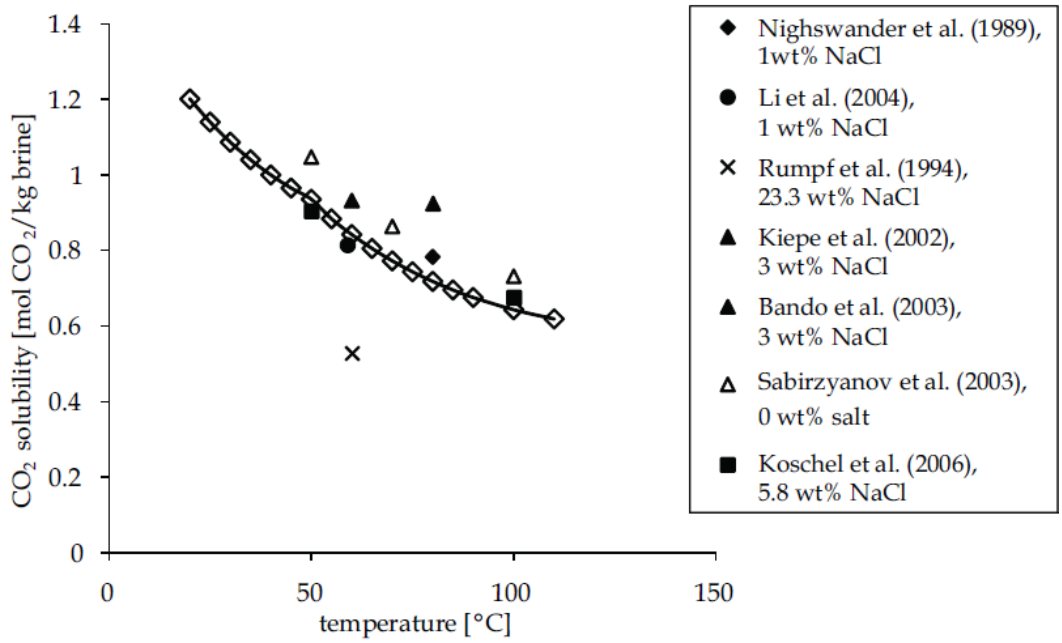

Figure 2.7: CO_2 solubility as a function of temperature at 10MPa and 1 mol NaCl/kg brine. Modelling and experimental data [24]

The results in Figure 2.8 show that, as with temperature, CO_2 solubility in brine decreases with increased brine salinity. This is a result of the salting out effect, where water can dissolve less gas due to the presence of electrolytes [70]. This is due to the water molecules being attracted to the salt ions, which reduces the number of H^+ and O^{2-} ions that can capture and disassociate gas molecules. The pressure and temperature conditions were set to 10MPa and 323K, respectively. As with both previous data sets, the modelling results are shown as open diamonds with the rest of the symbols representing experimental measurements. It is unclear why the results from Sabirzyanov et al. (2003)

and Dodds et al. (1956) are included since both sets of experiments were run at 0 wt% NaCl. Although the modelling data agrees with the experimental results, in terms of CO_2 solubility decreasing with increasing brine salinity, the CO_2 solubility calculator appears to over predict the CO_2 solubility in brine.

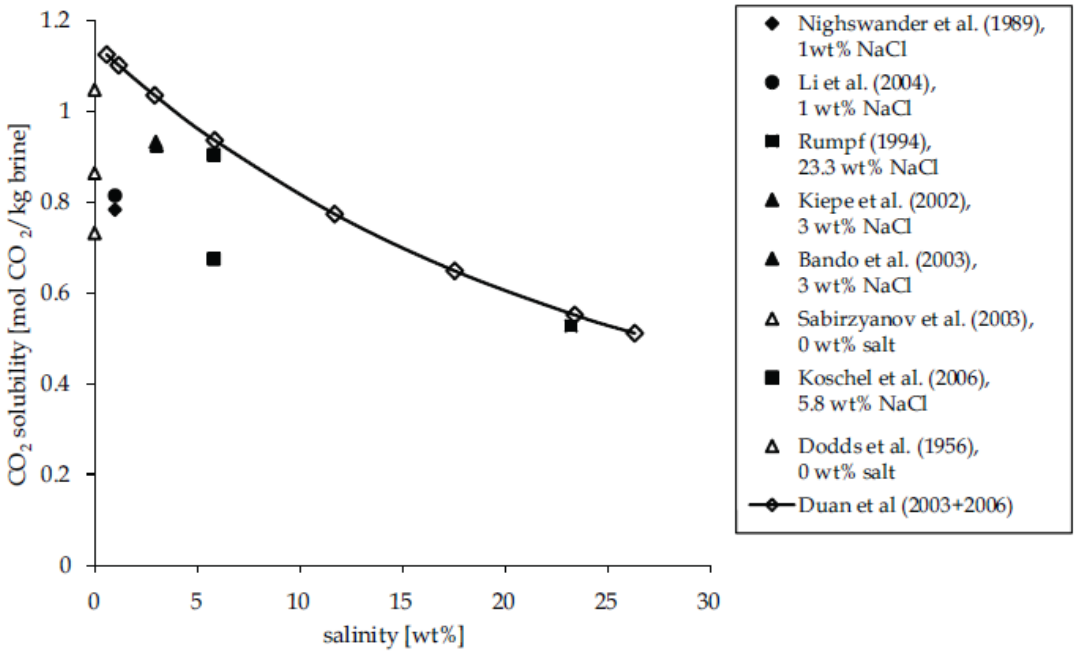

Figure 2.8: CO_2 solubility as a function of salinity at 323K and 10MPa. Modelling and experimental data [24]

The reason for the over prediction by the CO_2 solubility calculator and the large variation in results between the experimental data sets is a consequence of the difficulties of accurately measuring CO_2 solubility under reservoir conditions. These difficulties arise from the fact that much of the solubility measuring equipment cannot be used at reservoir pressures. As a result, in most cases the system has to be depressurised first, to atmospheric pressure, before measurements can be taken [71]. Depressurising the system will result in CO_2 bubbling out of the brine and so an accurate measurement of CO_2 solubility cannot be made. This is why the results from the different experimental data sets, shown in the Figures 2.6-2.8, are not consistent even under the same conditions [24].

2.5.3 Mineral trapping

Due to the formation of solid insoluble carbonates, mineral trapping is the safest and most permanent means of CO_2 geological storage. Mineral trapping in these deep formations usually takes place at temperatures between 313K and 473K and pressures ranging from 7MPa to 28MPa [16]. Previous studies have shown that higher pressure and temperature conditions result in an increase in the formation of mineral carbonates, with

temperature having a greater effect than pressure [17]. The contribution of pressure and temperature are, however, minor in comparison with the effect that brine pH has on mineral trapping [17].

The optimal pH level for the formation of mineral carbonates is over 9.0 due to the large quantity of carbonate (CO_3^{2-}) ions being present [18]. As seen from Equations 2.5-2.7, carbonate ions are needed to react with the metal cations in the brine to form insoluble carbonates. Equations (2.2-2.4), however, show that there are a number of reactions that result in different carbonic species dominating [72]. As shown in Figure 2.9, these reactions are pH dependant. For instance, at low pH (~4) Equation 2.2 dominates, producing primarily H_2CO_3. At near neutral pH (~6) the production of HCO_3^- dominates, and as previously mentioned, a pH of ~9 is needed for CO_3^{2-} to be the prevalent carbonic species. Brine pH in deep formations usually ranges from 2-7 and at the acidic end of the spectrum the formation of mineral carbonates is impossible due to too few or no carbonate ions being present [19].

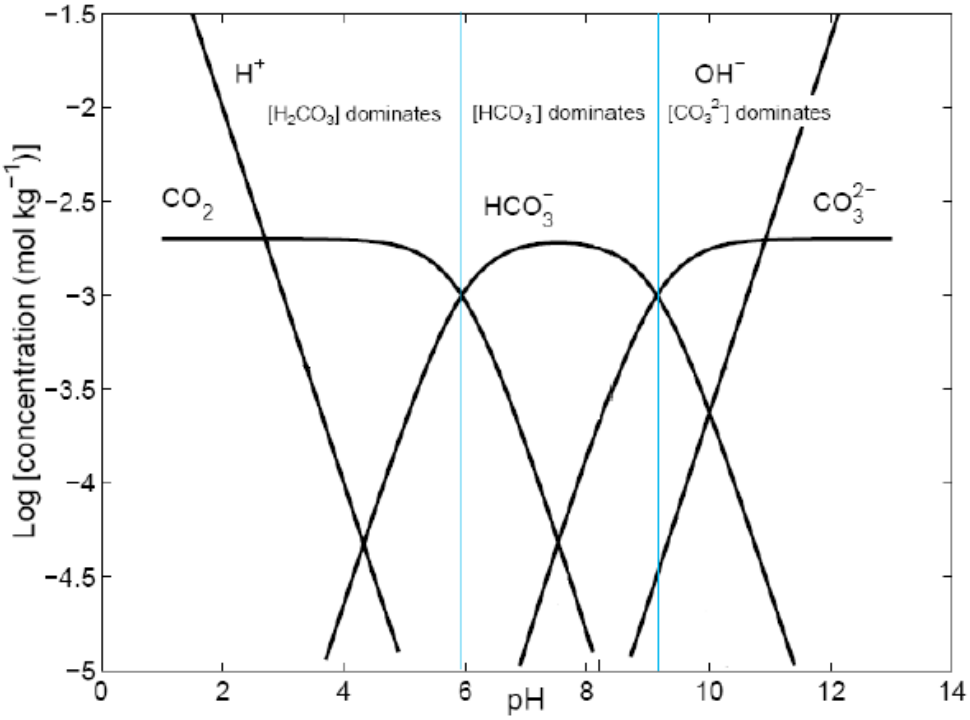

Figure 2.9: Bjerrum plot showing dissolved forms of carbonation system in seawater [72]

The brine pH, however, does increase with the injection of CO_2 due to geochemical reactions between the host rocks and the injected CO_2 [20]. When CO_2 dissolves in brine, it forms a weak acid which then reacts with calcite in the host rock to form HCO_3^- which is alkaline. This will cause the pH of the brine to increase. Therefore, as more CO_2 is injected and dissolves in the brine, the brine pH will further increase due to the increased

levels of HCO_3^- ions. A study was conducted by Rosenbauer et al. (2005) whereby CO_2 and brine were reacted in the absence and presence of arkosic sandstone and limestone. The experiments were carried out under CO_2 storage conditions at 393K and 20MPa. The arkosic sandstone increased CO_2 solubility in brine by 5% whereas the limestone increased the solubility by 6% [20]. The increased CO_2 solubility then lead to an increase in brine pH due to the formation of more HCO_3^- ions.

A further study by Matter et al. (2007) involved the injection of CO_2 saturated water, with an initial pH of 3.5, into sedimentary rock. The results of this study showed that within hours of injection, the brine pH was neutralised due to CO_2-rock-brine interactions [73]. Liu (2012) also conducted pH stability studies for a CO_2-rock-brine system whereby CO_2 was injected into brine with an initial pH of 2.6 and buffered by Oriskany rock [74]. The experiment was run under ambient conditions and the pH stabilised at around 6.3. Both studies by Matter et al. (2007) and Liu (2012) show that CO_2-rock interactions can increase brine pH to levels where HCO_3^- dominates. The production of HCO_3^- ions, and hence the increase in pH, is enhanced further if the grain size of the host rock is small as this results in a larger reactive surface area [75]. It can, therefore, be concluded that CO_2-rock-brine reactions are an important aspect of geochemical trapping as they not only increase CO_2 solubility, and hence solubility trapping, but also raise the brine pH which promotes mineral trapping via the formation of additional CO_3^{2-} ions.

It is unlikely though that the natural production of HCO_3^- ions, will be enough to raise the pH high enough for CO_3^{2-} production to dominate, and hence, additives may be required to promote the formation of mineral carbonates. These additives generally fall into the categories of biocatalysts, caustic by-products and chemical buffer solutions [74]. As with the addition of all additives, this leads to increased costs of an already expensive process and so alternative methods of increasing the effectiveness of the mineral trapping mechanism would be preferable. The brine pH is also dependant on its composition and so mineral trapping efficiencies can be affected by brine composition. Previous experimental and modelling work on brine composition and how it affects brine pH is discussed in Section 2.7.

In addition to the effect that the injected CO_2 and brine composition has on the pH of the brine, the brine pH is also affected by pressure and temperature. Although experimental studies on pH in CO_2-water systems at high pressure and temperature conditions are limited, previous work has shown that the pH of CO_2-saturated water decreases with

increasing pressure and increasing with temperature [76, 77, 78, 79]. The reason behind the limited experimental data is the difficulty in measuring pH at high pressures and temperatures. Only in recent years have pH and reference electrodes that can measure pH under high pressure and temperature conditions become commercially available and even then, great care must be taken during depressurisation so as not to cause mechanical damage to the electrodes [79]. This can occur when CO_2 diffuses into the electrodes inner compartment.

Peng et al. (2013) developed an experimental apparatus to measure the pH of CO_2-satured water up to 15.3MPa and 423.2K [79]. They obtained an Ag/AgCl reference-electrode, a zirconia pH electrode and a glass pH electrodes from Corr Instruments LLC. To prevent mechanical damage during depressurisation, a programmable back pressure regulator was installed that allowed the rate of depressurisation to be regulated. They concluded that the pH increases with temperature and decreases with increasing pressure but plateaus at higher pressures. Further discussion on how the pH was measured for this work is presented in Section 3.1.2.

2.6 CO_2 solubility measurements

Over the past decade, there has been much experimental work trying to accurately measure CO_2 solubility under reservoir conditions with varying levels of success. This section reviews this work in detail and Table 2.2 provides a summary of the different experimental procedures that are discussed here.

Table 2.2: Summary of experimental procedures and how they compare

Main Component of Apparatus	**CO_2 Solubility Measured:**	**Reference**
High Pressure Cell	Titration	Rochelle et al. (2002)
High Pressure Cell	Mass and pressure of cylinder	Bando et al. (2003)
High Pressure Cell	Gas Chromatography	Hou et al. (2013)
PVT Cell	Volume of evolved gas and mass of solution	Li et al. (2004)
PVT Cell	Adding CO_2(g) in cylinder + CO_2(g) released from cylinder + CO_2(aq) remaining in cylinder	Yan et al. (2011)
Autoclave Cell	Volume of evolved gas and mass of solution	Sabirzyanov et al. (2003)
Autoclave Cell	Coulometric Titration	Qin et al. (2008)
Autoclave Cell	Bubble point observation and masses of CO_2 and brine present	Tong et al. (2013)

2.6.1 CO_2 solubility in pure water and synthetic Utsira Porewater

In 2002, the British Geological Survey released a commissioned report on the solubility of supercritical CO_2 into pure water and synthetic Utsira porewater [80]. One of the aims of the report was to understand how much of the CO_2 injected into the Utsira formation would dissolve in the formation water. As a result, it was necessary to measure CO_2 solubility under reservoir conditions. To try and achieve this, CO_2 (at a known pressure and fixed temperature) was injected into a vessel containing brine and CO_2 in its aqueous phase was taken under experimental pressure, but at room temperature. The experimental apparatus used for this work is shown in Figure 2.10 and consisted of a CO_2 cylinder which was connected to a syringe pump that could rapidly increase the gas pressure to supercritical conditions. The supercritical CO_2 was then injected into a stainless steel

pressure vessel which contained either pure water or synthetic Utsira porewater, depending on the experiment taking place. The pressure vessel was contained within an oven to keep the temperature constant and a magnetic stirrer was used to promote dissolution of the gas. The sampling of the aqueous CO_2 was achieved via a dip tube that ensured that only the aqueous phase was sampled. When the sample was taken, it was cooled to room temperature which increased the CO_2 solubility (as solubility increases with decreasing temperature) and also reduced the chance of degassing as the aqueous solution was below the CO_2 saturation point.

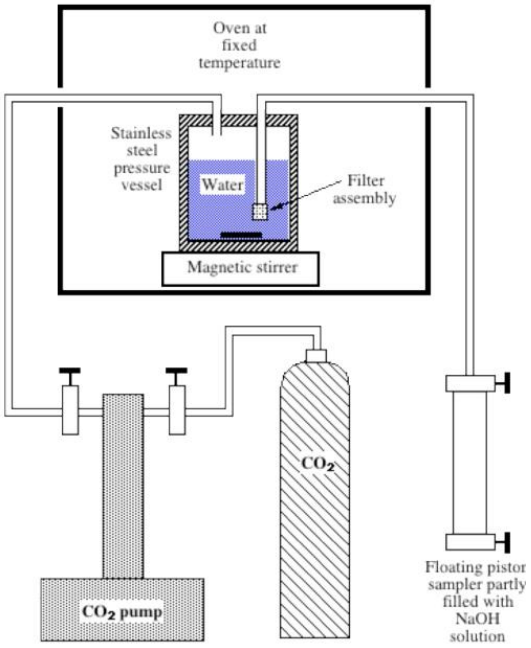

Figure 2.10: Rochelle et al. (2002) experimental setup [80]

The dissolved CO_2 was then stabilised by reacting it with 4M NaOH solution under experimental pressure and room temperature.

$$CO_{2(aq)} + NaOH = Na^+ + H^+ + CO_3^{2-} \quad (2.8)$$

All the carbonic species were converted to CO_3^{2-} due to the high pH of the solution and the CO_3^{2-} remained stable so long as the NaOH present was in excess. The solution could then be depressurised without any degassing and the CO_3^{2-} could be analysed, (using titration by a Radiometer VIT90 Video Tirtrator with ABU93 Triburette and SAM90 Sample Station) to provide a measurement of total dissolved CO_2. The addition of the NaOH solution caused dilution of the CO_2 solution and so a correction factor was needed in the form of a dilution factor which was either based on measured Na^+ content (for distilled water) or Cl^- content (for Utsira porewater).

The experimental conditions were varied from 291-353K and 80-120 bar with the majority of the data being generated under the reservoir conditions in the Utsira formation at Sleipner (310K and 100 bar). Using distilled water, the measured CO_2 solubility values were roughly 10% lower than expected. However, they did follow the general trend of previous studies [81, 82, 83]. The reasoning behind the drop in CO_2 solubility was not clear. However, the authors did not take into account compressibility and expansivity corrections as they believed that cooling the solution would have an insignificant effect on volume of the solution, and this may have caused the lower than expected results. At 310K and 100 bar, the CO_2 solubility was 5.1g of CO_2 per 100g distilled water [80]. When measuring CO_2 solubility in the synthetic Utsira porewater, the results were comparable to that of previous work and lower than the results for distilled water [84]. Under the same conditions as for the distilled water, the CO_2 solubility was 4.5g per 100g Utsira porewater [80].

2.6.2 Solubility of CO_2 in aqueous solutions of NaCl

The following year, Bando et al. (2003), studied the solubility of CO_2 in aqueous solutions of NaCl at (303.15 to 333.15) K and (100 to 200) bar [85]. The apparatus used (Figure 2.11) was made up of a high-pressure vessel (with a max pressure of 700 bar), two pressure transducers with different pressure ranges, an agitator, a pump for pressurising the water, an amplifier, a 50cm^3 sample cylinder and a CO_2 gas cylinder. Additionally, there was a gravimetric balance used to measure the mass of the samples collected. Experiments were run at temperature of 303.15K, 313.15K, 323.15K and 333.15K, pressure of 100 bar, 250 bar and 200 bar and 0, 0.0099, 0.02 and 0.03 NaCl mass fractions.

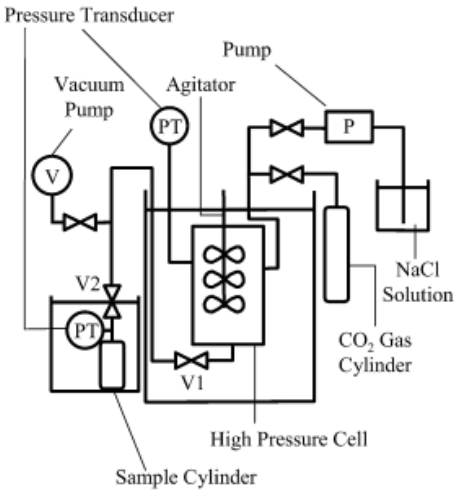

Figure 2.11: Bando et al. (2003) experimental setup [85]

Once the high-pressure vessel had been evacuated, CO_2 was injected to a pressure of approximately 10 bar. At this point, the aqueous NaCl solution was pumped into the vessel for 1 hour, while undergoing mixing by an agitator, and then left in the vessel while the temperature and pressure stabilised, which took about 2 hours. This was repeated until experimental conditions were achieved. Once the experimental conditions had been achieved, the dissolved CO_2 solution was flashed into the sample cylinder. This was done until the pressure within the sample cylinder reached 10 bar. No degassing occurred due to the pressure of the vessel remaining constant throughout the extraction procedure. Once the sample had been collected, the sample cylinder was disconnected and cooled in an ice bath until it reached 0°C. The mass and pressure of the cylinder was then measured and used to calculate the CO_2 solubility in the aqueous NaCl solution. Some of the results obtained by Bando et al. (2003) can be seen in Figures 2.7 and 2.8 [24]. According to the authors, the CO_2 solubility results obtained were in good agreement (within 0-6.4%) with previous work [86, 87, 88, 89].

2.6.3 Phase equilibria of CO_2 + H_2O + NaCl and CO_2 + H_2O + KCl

More recently, Hou et al. (2013) developed an experimental setup and procedure to measure CO_2 solubility in CO_2 + H_2O +NaCl and CO_2 + H_2O + KCl systems at temperatures ranging from 323.15K to 423.15K [90, 91]. The experimental setup consisted of several systems designed to manage circulation, sampling, injection, temperature control and pressure and temperature measurements. The circulation system was located in an oven and included two re-circulation loops and an equilibrium vessel. The liquid and vapour phases flowed through the loops via the help of a magnetic pump which allowed equilibrium to be reached in a shorter time. The purpose of the oven was to maintain a constant temperature within the vessel.

Figure 2.12 shows a schematic of the system. The system allowed for small samples (10μmol) to be withdrawn via two Rolsi samplers that were connected to the liquid and vapour loops through ports in the wall of the oven. These samples were then pushed into the gas chromatograph (GC), by the helium carrier-gas flow, where they could be analysed. Due to the transfer line to the GC being heated to roughly 473K, which resulted in vaporisation of the liquid samples, a filter had to be added to stop salt crystals from reaching the GC. At infinite dilution of volatile solutes in non-volatile solvents, the GC can be used to measure activity coefficients [92]. In addition, at infinite dilution, activity coefficients are directly related to Henry's law constants of gases. Hence, the GC can be

used to measure Henry's law constants of gases and therefore the solubility of CO_2 in brine can be calculated.

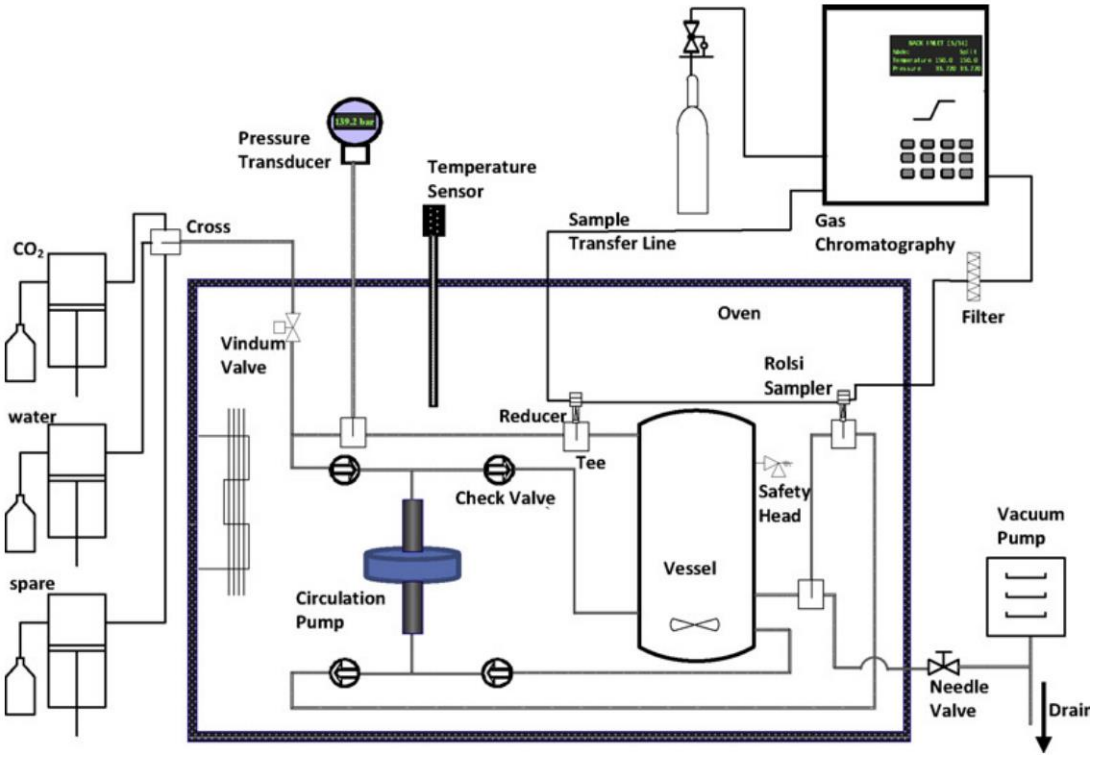

Figure 2.12: Hou et al. (2013) system [90]

CO_2 and brine were injected into the vessel via a syringe pump and equilibrium was reached after around 2 hours due to the acceleration of the process by means of the magnetic pump [91]. Upon reaching equilibrium, both the liquid and vapour samples were collected and analysed in the GC. Approximately 10 samples were taken of each phase and the average was used in the reported results. The collected samples were comparatively small (35µmol for liquid phase and 15µmol for vapour phase) compared to the total system volume of 100ml and so their withdrawal had a negligible effect on equilibrium pressure [91]. The apparatus used by Hou et al. (2013) is the first to provide coexisting liquid and vapour phase compositional data. Although not quantified, the authors state that there are some large deviations between their reported results those of previous literature. However, when tested for CO_2-water systems, the results are extremely close to those obtained more recently by Tong et al. (2013) and with the Duan et al. (2006) model, which is shown in Section 4.2.5. It is likely that the large deviations when looking at systems containing NaCl and KCl is a result of there being limited data in these cases, especially at high pressures, temperatures and salinity.

2.6.4 Solubilities for binary systems of CO_2 + water and CO_2 + brine

Unlike with Bando et al. (2003), Li et al. (2004) developed a system for measuring the solubility of CO_2 in brine [67]. Their method used apparatus (Figure 2.7) similar to that of a PVT (Pressure-Volume-Temperature) system with a 500cm^3 PVT cylinder, a high-pressure Ruska pump, a high-pressure CO_2 cylinder, a densitometer, a gasometer and a back pressure regulator (BPR), as shown in Figure 2.13. The PVT cylinder was situated in an air bath which could be rocked to accelerate the equilibrium process.

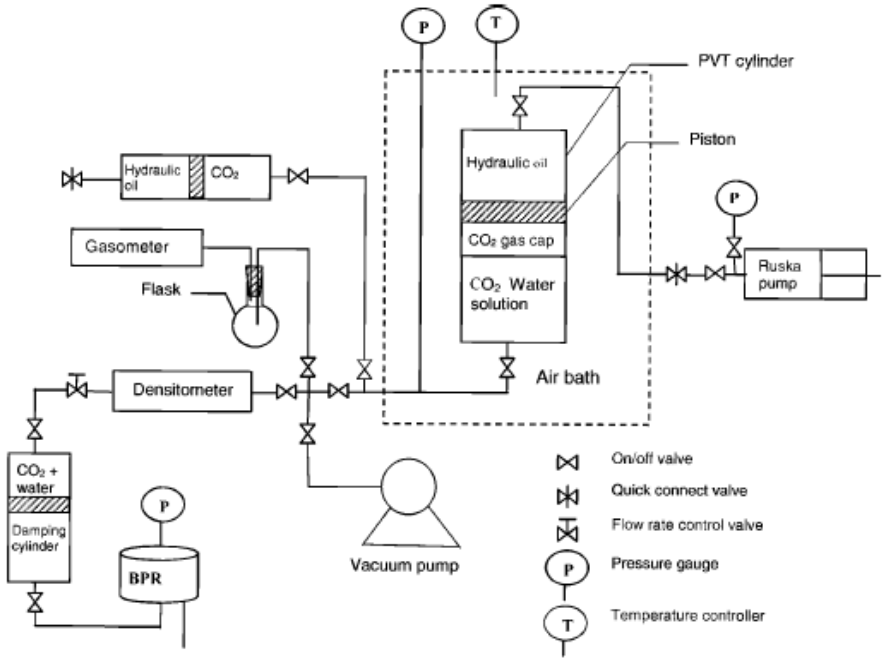

Figure 2.13: Li et al. (2004) experimental setup [67]

CO_2 was injected into the PVT cylinder, which contained a 450cm^3 sample of water. The amount of CO_2 needing to be injected was estimated by using data from Chang et al (1998). [93] An additional 30% CO_2 was injected into the PVT cylinder to ensure that there would be a gas cap at equilibrium. Once the CO_2 had been injected, the cylinder was pressurised and rocked, accelerating the equilibrium process. Equilibrium was assumed to have been reached when the pressure within the cylinder had remained constant for over 5 hours. Once equilibrium was reached, a 20cm^3 solution sample was extracted and collected in a flask. The mass of the sample was then measured and the gasometer was used to measure the CO_2 that evolved due to degassing, under ambient conditions. Using the mass of the solution and the volume of evolved CO_2, the CO_2 solubility could be calculated with the following equation:

$$R = \frac{n_g}{(m_g + m_w)/\rho_s} \qquad (2.9)$$

Where R corresponds to the solubility of CO_2(aq), m_w is the mass of water, m_g is the mass of CO_2, n_g is the number of moles of CO_2 and ρ_s is the density of CO_2(aq) in solution under saturation pressure. As with Bando et al. (2003), the results of Li et al (2003) are shown in Figures 2.7 and 2.8 [24]. The authors do state that this method of calculation is only suitable for aqueous solutions that are near neutral. In addition, Yan et al (2011) have not used these data when creating a comprehensive review of previous experimental data, as they stated that the authors did not take into account dissolved CO_2 contained within the aqueous solution at atmospheric pressure [94]. However, this should be negligible when measuring CO_2 solubility at high pressures.

2.6.5 CO_2 solubility in NaCl brine

The work by Yan et al. (2011), which included a comprehensive review of previous experimental data, measured CO_2 solubility and brine density using a modified high pressure PVT apparatus [94]. This apparatus (Figure 2.14) consisted of a DBR-JEFRI windowed equilibrium cell, an air bath, an Anton Paar high pressure density meter DMA 512, high pressure pycnometers (for sampling) and an ISCO displacement pump. The equilibrium cell was mounted upon a rocking device which accelerated the equilibrium process and also allowed for the cell to be put in the top-down and upright positions so that both heavy and light phases could be sampled. For phase sampling, the phase in question was discharged under constant pressure from the outlet located at the top of the cell.

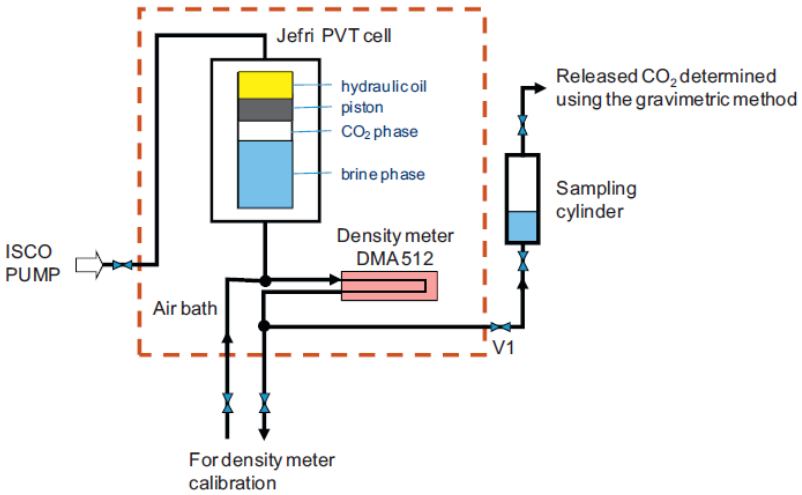

Figure 2.14: Yan et al. (2011) experimental setup [82]

The CO_2 and brine were sequentially injected into the equilibrium cell and the pressure and temperature were increased to the experimental values. The CO_2-brine mixture was then rocked for 2 hours and left overnight to reach equilibrium. Once the mixture had

reached equilibrium, a brine-phase sample was extracted, through a density meter, into a pre-weighed sampling cylinder. The single phase brine was then flashed into two phases within the sampling cylinder and cooled. The weight of the cylinder was then measured and the amount of CO_2 dissolved in the sample was determined by slowly releasing the dissolved gas from the top of the cylinder. This was done until no more gas could be released, at which point the sampling cylinder was weighed again. The total volume of dissolved CO_2 within the brine sample was calculated by adding together the amount of CO_2 in the gas phase within the cylinder, the volume of CO_2 released from the cylinder and the dissolved CO_2 remaining in the sampling cylinder under atmospheric conditions.

According to the authors, the experimental method used in this work provided CO_2 solubility measurements that were in good agreement with literature data, as can be seen in Figure 2.15, and hence, showed the merits of using this method for measuring CO_2 solubility in brine at high pressures. In the legend of Figure 2.15, "This work" corresponds to the work done by Yan et al. (2011). CO_2 solubility and the associated CO_2-saturated brine densities were measured from 50-400 bar, at 323K, 373K and 413K and 0, 1 and 5M NaCl.

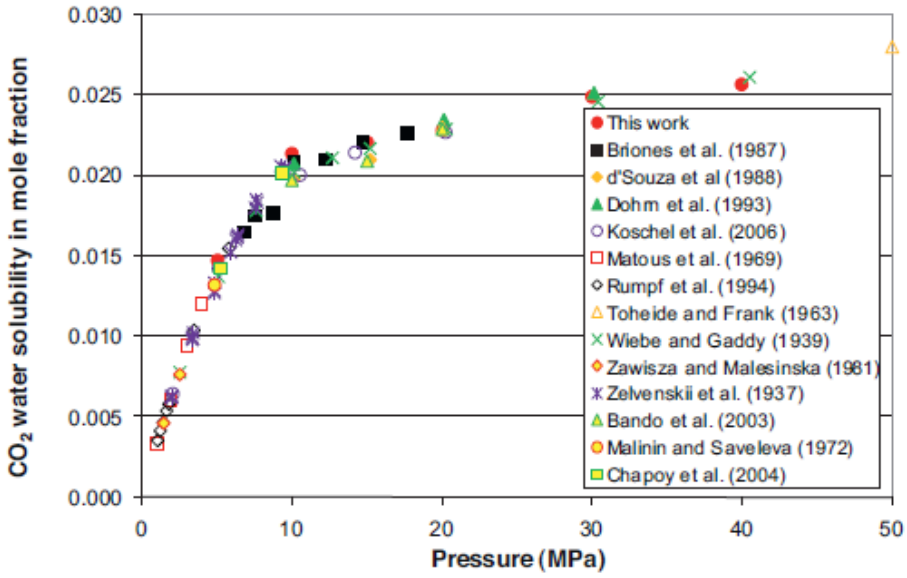

Figure 2.15: CO_2 solubility in water at 323K [94]

2.6.6 Water solubility of CO_2 under supercritical and subcritical conditions

In 2003, Sabirzyanov et al. (2003) published their experimental setup (Figure 2.16), which comprised of a gas cylinder containing the gas that would be examined, 4 high pressure valves, a deadweight gauge, a Bourdon pressure gauge, a high-pressure mercury seal, a vacuum pump, a ball, a tee and a heat-insulated high-pressure autoclave [95]. The

experimental pressure was obtained using both a hydraulic press and a hydraulic amplifier which was part of the deadweight gauge. The heat-insulated high-pressure autoclave was heated to the desired temperature using 3 Nichrome heaters. The autoclave used was a stainless steel cylinder with a sealed top cover that included a built-in high-pressure valve that could be used to isolate the vessel during agitation and equilibration. The autoclave also had a valve built in to the bottom of the vessel which was used to sample the liquid phase.

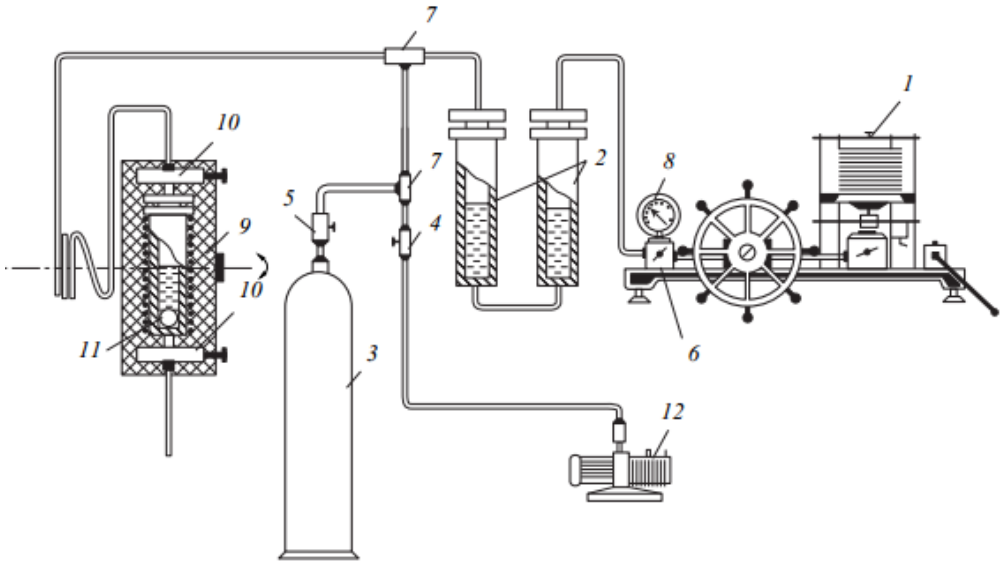

Figure 2.16: Sabirzyanov et al. (2003) experimental setup. (1) MP-2500 deadweight gage, (2) mercury seal, (3) gas cylinder, (4–6, 10) high-pressure valves, (7) tee, (8) standard pressure gage, (9) heat-insulated high-pressure autoclave, (11) ball, and (12) vacuum pump [95]

During the experiment, perfect mixing of the phases was obtained by rocking the autoclave about its horizontal axis, twice per minute, through an angle of 160°. The mixing was further promoted by the inclusion of a perforated ball which had been placed in the vessel. The equilibrium point was determined from pressure variations measured from within the vessel. Once equilibrium was reached, the vessel was held in an upright position for 1-1.5 hours. During sampling, gas was injected into the vessel from the head space of the mercury seal, to maintain constant pressure. The samples were collected in a number of weighed ampoules and the gas, which was released as the sample was throttled through the high-pressure valve, was collected and its volume measured. Taking the measured volume of gas and weight of the liquid sample, the solubility of the CO_2 in water was determined. As with Bando et al. (2003) and Li et al. (2004), the results obtained by Sabirzyanov et al. (2003) can be seen in Figures 2.7 and 2.8 [24]. The overall recorded error was reported to be 3% [95]. The authors reported that they had difficulty sampling the liquid phase from the bottom of the vessel under certain conditions due to

the CO_2 being denser than water. Their results are also reported to be within 7% of those of previous work, which is a relatively high error and brings into question the accuracy of this method [96].

2.6.7 CO_2 and CH_4 solubilities in ternary systems with water

Qin et al. (2008) developed an experimental method to calculate CO_2 and CH_4 solubility in a ternary system with water [97]. However, this method could also be used to simply measure CO_2 solubility in water and brine. The solubility experiments took place within a custom designed reaction cell which featured a 200cm^3 capacity titanium-lined autoclave. Contained within the titanium closure there were three compression fittings which accommodated a thermocouple and two titanium sampling tubes. There was also an additional thermocouple attached to the autoclave base. The reaction cell was fitted to a 180° rotating furnace, where sampling could be performed in either an inverted or upright position.

CO_2 and water were mixed within the cell at a rotation rate of 6 times per minute. Depending on the pressure and temperature, the mixture was allowed to equilibrate over a period of 8-36 hours. Once equilibrium had been reached, the rotator was turned off and left in the inverted position for roughly 30-60 minutes to allow complete separation of the liquid and vapour phases. The CO_2-water phase was extracted through a gastight syringe which contained approximately 1-2 cm^3 of 17% NaOH solution to stabilise the dissolved CO_2 and convert the carbonic species to CO_3^{2-} and HCO^{3-} and hence eliminate CO_2(aq). To prevent degassing, the experimental pressure and temperature was kept near constant during sampling. The amount of dissolved CO_2 contained within the water, and hence the CO_2 solubility, was measured through coulometric titration. This was done using a UIC Coulometric model CM5012 which was standardised by $CaCO_3$ solutions. The CO_2 solubility data obtained were validated by comparison with the Duan and Sun (2003) model [64]. The measured CO_2 solubility data at 375K were slightly lower than that contained within the Duan and Sun (2003) model, deviating by less than 4%. This was still considered, by the authors, to be in good agreement with previous results and validated their experimental method [97].

2.6.8 CO_2 solubility in aqueous solutions of $CaCl_2$ and $MgCl_2$

The most recent work on measuring CO_2 solubility under reservoir conditions was performed by Tong et al. (2013) [98]. Their method was based upon visual observation, alongside quantitative measurements of pressure, temperature and composition. This

avoided the complications associated with phase sampling and analysis, and allowed for the rapid collection of reliable data.

The experimental setup for this work is shown in Figure 2.17. CO_2 was injected into a windowed cell and allowed to reach equilibrium, at which point both the pressure and temperature were measured, so that, an equation of state (in conjunction with the known volume) could be used to calculate the mass of CO_2 present. Upon calculating the mass of CO_2 present, the brine was injected using a syringe pump, and stirred until complete dissolution was achieved. The mass of the injected brine was determined through knowledge of the initial and final volume, pressure and temperature in the pump cylinder, along with the brine density under said conditions.

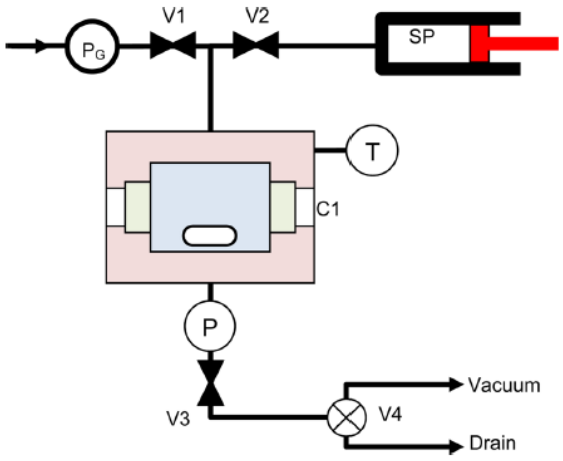

Figure 2.17: Tong et al. (2013) experimental setup [98]

The bubble point can be determined through visual observation at high pressures. Once the brine had been injected and full stabilisation had occurred within the cell, the pressure was gradually decreased until bubbles appeared. This was done by removing fresh brine, not in contact with the CO_2, from the inlet line. The phase boundary under high pressure conditions is first observed as slight temporal and spatial variations in the light passing through the solution and not through bubble formation. The reasoning behind this is that under these conditions the brine and the CO_2-rich phase densities are comparable.

Once the bubble point has been observed, the composition of the solution, which is expressed as the salt-free mole fraction of dissolved gas, can be determined through knowledge of the masses of both the brine and CO_2 present. In addition, the bubble point density of the CO_2-saturated brine can also be calculated since the cell volume is known. The results obtained through this method are in good agreement with previous work (within ±2-5%) and with the Duan et al (2006) model which can be seen in Section 4.2.5

[65, 88, 99]. This method was used to measure CO_2 solubility in aqueous solutions of $CaCl_2$ and $MgCl_2$ and successfully expanded the knowledge on how CO_2 solubility is affected by pressure, temperature and salinity in these aqueous solutions. It was found that there is a stronger salting out effect in systems containing divalent cations than those containing monovalent cations (NaCl/KCl). In addition, the solubility of CO_2 in $MgCl_2$ and $CaCl_2$ solutions of the same molality were comparable. It was therefore concluded that ion charge is considerably more important, in regards to the salting out effect, than ion size.

2.6.9 Summary

This section has reviewed the different methods published for measuring CO_2 solubility under reservoir conditions. Although all these methods follow the same trends, in terms of the effect that temperature, pressure and salinity has on CO_2 solubility, there are clearly large deviations in the results between the published datasets. Due to being in good agreement with results from previous work, as well as the Duan and Sun CO_2 solubility model, the work by Tong et al. (2013) seems to be the most accurate (in terms of how close the experimental results are to those produced through modelling) at measuring CO_2 solubility in brine under reservoir conditions. Consequently, since Hou et al. (2013) produced results almost identical to those of Tong et al. (2013) for the CO_2+water system, it can also be said to be very accurate at measuring CO_2 solubility in brine under reservoir conditions. This will be emphasised in Chapter 4 which reviews geochemical modelling of CO_2 solubility in brine and how the results obtained through modelling compare with those of the experimental work.

2.7 Previous work on brine composition

Typical brine composition (including brines found in the North Sea) consists of the following major ions [25]; Cl^-, SO_4^{2-}, Na^+, Mg^{2+}, Ca^{2+}, K^+, Fe^{3+}, Sr^{2+} and Ba^{2+}. The composition of the brine affects the formation of mineral carbonates. For instance, large quantities of metal cations such as Mg^{2+} and Ca^{2+} are preferable so as to react with CO_3^{2-} ions to form mineral carbonates. In contrast, previous studies have shown that for high carbonation efficiencies low concentrations of Fe^{3+} are necessary [17]. This is because higher concentrations of Fe^{3+} correspond to lower brine pH, which reduces the production of the required CO_3^{2-} ions. The reason for the reduction in pH is that the less stable Fe^{2+} ions, that are originally present in the brine, will easily lose an electron to form the more stable Fe^{3+} which results in the production of H^+ ions that lower the brine pH:

$$Fe^{2+} + 3H_2O \rightarrow Fe(OH)_3 + 3H^+ + e^- \quad (2.10)$$

It was, therefore, concluded that major differences in iron composition directly affects brine pH. Additional work has also been carried out on the effect of Sr^{2+} and Ba^{2+} ions on brine pH [100]. Three synthetic brines were created for the study; one without Sr^{2+}, one without Ba^{2+}, and one with both ions present. The results of this work showed that the presence of Sr^{2+} and Br^{2+} ions in brine did not lower the pH. **Considering that brine composition changes with location** [25]**. This could mean that some locations are better suited for geochemical trapping than others which would be an important factor when selecting a site for CO_2 geological storage. Hence, additional work on how brine composition changes with location and the affect it has on geochemical trapping potentials is required.**

2.8 Joint CO_2-EOR and CO_2 geological storage projects

It is clear that CO_2-EOR and CO_2 geological storage technologies will play important roles in the future of global energy security. Separately, these technologies should act as stepping stones to a renewable energy dominated future by giving renewable energy technologies enough time to mature. However, unlike CO_2-EOR, which has been established for over 40 years, CO_2 geological storage still has to overcome many barriers, the main one being the associated costs. Injecting CO_2 into deep geological formations simply for storage purposes does not generate income and unless companies are receiving large tax credits to subsidise the running of these projects then they will be unwilling to do so. A possible solution to this problem is to have joint CO_2 geological storage and CO_2-EOR projects, where the profits from the latter can be used to subsidise the former. However, there is much scepticism over whether this is a viable option.

It can be agreed upon that the practices and technologies developed over the past 40 years during CO_2-EOR can be used to the benefit of CO_2 geological storage due to the similarities in the process [101]. Moreover, since in the U.S. and Canada only 17% of CO_2 for EOR projects comes from anthropogenic sources, a percentage of the CO_2 captured for storage could be sold off to oil companies to generate income and off-set the costs of running CO_2 storage facilities [6]. This could in turn lower the price of CO_2, potentially leading to more CO_2-EOR projects being established which would have a knock on effect. Joint projects could also be established where CO_2-EOR and CO_2 storage work in tandem such as at the Dakota Gasification – Weyburn CCS project [102]. The

Weyburn project is made economically viable by the additional oil recovered through CO_2-EOR which offsets the cost of storing CO_2.

The Weyburn project is, however, the only CO_2-EOR project that incorporates CO_2 storage and the only CCS project at present that utilises CO_2-EOR. This could be due to the large infrastructure required to perform both storage and recovery. The Weyburn field for example, contains 170 CO_2 injectors alongside 320 oil production wells [102]. This can be compared with the Snøvit and Sleipner CCS projects, where CO_2 is injected via a single injector [16]. The regulations controlling CO_2 injection for geological storage compared with EOR also hinder these joint projects [103]. The reason being is that for geological storage of CO_2, all abandoned wells must be identified, located and plugged so that the caprock is not compromised. Depending on the density of wells per square mile, this could mean that dozens of abandoned wells must be sealed which would be a costly process. Also in regards to CO_2 being sold to offset running costs, there is the argument that this would only have short term benefits [101]. Once an increased number of CCS facilities have been established, the supply is likely to outweigh the demand at which point these facilities would no longer have a source of income besides any government tax credits.

There is still much debate over whether or not CO_2-EOR is key to future investment in CO_2 geological storage projects. In fact, the opposite appears to be true when considering offshore CO_2-EOR, for example in the North Sea. The main drivers for CO_2-EOR in the North Sea are funding for initial CCS demonstrations and deployment [44]. This is because CCS is considered critical to supply the required amounts of CO_2 needed for large scale CO_2-EOR in the North Sea. In addition, infrastructure associated with CCS, such as pipelines that travel from CO_2 point sources onshore to storage locations offshore could be utilised by the oil industry as well, reducing capital. Regardless, it is likely that over the next few decades the collaboration between the two industries will increase as they both continue to grow and become vital components of the global energy industry.

2.9 Summary

It is clear that over the coming decades global energy demand is only going to grow which will lead to a higher reliance on fossil fuels and increased CO_2 emissions. Renewable energy technologies have yet to develop to the point where they can take over from fossil fuels as the primary source of global energy. Consequently, alternative

strategies are needed to increase the lifetime of fossil fuel reserves and reduce CO_2 emissions. Two such strategies are CO_2-EOR and CO_2 geological storage.

CO_2-EOR is one of the most effective methods of EOR and produces 300,000 barrels of oil per day in the United States alone [7]. Consequently, EOR technologies have the potential to significantly increase the lifetime of oil reserves. Considering that oil accounted for almost a third of total primary energy supply in 2015, recovering residual oil is of huge importance [3]. The production and burning of this additional oil will in turn lead to an increase in CO_2 emissions which must be appropriately dealt with. At present, the most effective means of storing CO_2 is within deep geological formations such as depleted oil and gas fields and deep saline aquifers, which contain large volumes of porous rock [11]. Understanding the storage mechanisms of CO_2 in these formations is fundamental if both CO_2 geological storage and CO_2-EOR are to become mainstream technologies worldwide.

In terms of geological storage, geochemical trapping (solubility and mineral trapping) is key to the safe and permanent storage of CO_2. CO_2 dissolution and carbonation efficiencies are dependent on interactions with the local brine. CO_2 solubility in brine is also an important factor in CO_2-EOR as it affects oil displacement. Brine composition changes with location and there are many CO_2-brine interactions that are not fully understood.

The purpose of this study is to investigate CO_2-brine interactions using real data from North Sea oil wells, through a combination of experimental work and geochemical modelling. Several questions will be answered, such as how brine composition affects CO_2 solubility and what is currently the most effective method of experimentally measuring CO_2 solubility in brine. In addition, brine composition changes with location and this could result in certain locations being better suited for geochemical trapping and perhaps even CO_2-EOR. Therefore, compositional changes in brine as a consequence of location will also be assessed in this study. Furthermore, how CO_2-brine-rock interactions affect brine pH as well as the properties of the rock, such as porosity and permeability will also be evaluated, as this can have a direct effect on CO_2 storage security.

Chapter 3 Experimental Methodology

This chapter provides a detailed description of the experimental methodology and is presented into four distinct sections. The first section describes the preparation of the synthetic brines used throughout the experimental work, but mainly for investigating the importance of well selection (Objective 2). Section two explains how the calcite powder was prepared and the corresponding analytical techniques used to determine its properties, in order to asses calcites potential to buffer brine and promote mineral carbonation (Objective 4). The third section focuses on the experiments involving host rock cores being exposed to CO_2-saturated brine over a 9 month period and the analytical techniques used to measure their properties both before and after the experiments, to determine the effect that CO_2-saturated brine has on the permeability and porosity of local host rock (Objective 5). The final section explains the experimental setup for both the high pressure rig and the small pressure vessels, along with the corresponding experimental procedures (Objective 3).

3.1 Synthetic brine preparation

This section describes the brine compositions that were selected for the experiments focused on the importance of well selection (Objective 2). It also details the brines preparation and analytic techniques used to confirm brine composition by Inductively Coupled Plasma – Optical Emission Spectrometry (ICP-OES). Furthermore, the selection of an appropriate buffer, to increase brine pH and promote mineral carbonation, is discussed.

3.1.1 Identification of brine compositions

The brine compositions listed in Table 3.1 are taken from a database provided by the Institute of Petroleum Engineering at Heriot-Watt University, which has data related to a North Sea oil field consisting of a dozen wells, where information on brine composition has been recorded over a 12 year period, from early 2000 to late 2012. The purpose of preparing these brines is to assess how brine composition affects geochemical trapping potentials and the importance of well selection within an oil field (Objective 2).

Brine 1 is the average brine composition of the field over the 12 year period. Brines 2 and 3 correspond to the average brine composition of the lowest and highest salinity wells in the field, respectively (Objective 2). There is a noticeable variation in many of the major ion concentrations between the two brines, which is likely to lead to different dissolution and mineral trapping and could help to guide the selection of wells for CO_2 injection.

Brines 4 and 5 were prepared to evaluate the effect that seawater injection has on CO_2 dissolution and mineral trapping (Objective 2). There are no data on brine composition before seawater injection began in the field. Therefore, Brine 4 is the average of the brine compositions when the fraction of seawater injected was ≤10% and Brine 5 when fraction of seawater injected was ≥90%. Seawater injection will increase the salinity of the brine which, as previously reported, will reduce CO_2 solubility [24]. However, it will also have a significant effect on the concentration of the major ions, as seen in Table 3.1. When seawater is injected, the concentrations of Na^+ and Cl^- naturally increase, but so does the SO_4^{2-} concentration. This is important, as the SO_4^{2-} can react with the metal cations in brine such as Ca^{2+} and Sr^{2+} to form sulphates [104]. This will mean there are less metal cations available for the CO_3^{2-} ions to react with for mineral trapping. In contrast, seawater contains a lot of Mg^{2+} ions when compared to the formation water, as seen in Table 3.1, which could compensate for the loss of other metal cations and perhaps even benefit the mineral trapping process. Therefore, evaluating the effect that seawater injection has on CO_2 solubility and mineral trapping is an important aspect of this research (Objective 2).

Table 3.1: Major ion concentrations for brines and seawater (SW). N.A. = Not Available

	Na^+ (mg/l)	**K^+ (mg/l)**	**Mg^{2+} (mg/l)**	**Ca^{2+} (mg/l)**	**Sr^{2+} (mg/l)**	**Fe^{3+} (mg/l)**	**SO_4^{2-} (mg/l)**	**Salinity (mg/l)**
Brine 1 (Average)	8963	227	69	639	59	12	775	26040
Brine 2 (Low Salinity)	8386	201	146	620	88	6	154	24280
Brine 3 (High Salinity)	9480	241	2	645	41	6	1181	27450
Brine 4 (Pre-Seawater)	8056	198	118	597	84	2	119	23230
Brine 5 (Post-Seawater)	11402	360	1155	555	22	4	2288	37760
SW (Injection Water)	11000	400	1300	400	8	N.A.	2800	37370

In Table 3.1, the SW sample corresponds to the composition of the seawater injected into the wells to increase oil recovery. The brine from this field is relatively low salinity brine, which can be seen from the fact that its salinity is lower than that of the injected seawater. Using Brine 1, this low salinity brine will be compared with both seawater and a higher salinity brine from another field (see Table 3.3). The large variations in both salinity and major ion concentrations will help to understand how CO_2 solubility and mineral trapping can be affected by different locations. This may lead to some locations being better suited for CO_2 geological storage and CO_2-EOR due to the composition of the brine located there (Objective 2).

3.1.2 Preparation of synthetic brines

The ion concentrations of Brine 1 are achieved by dissolving the following seven salts, namely NaCl, KCl, $MgCl_2 \cdot 6H_2O$, $CaCl_2 \cdot 2H_2O$, $SrCl_2 \cdot 6H_2O$, $FeCl_2 \cdot 6H_2O$ and $NaHSO_4$ in distilled water. The salts are weighed using an OHAUS PA214 Pioneer Analytic Balance with an associated error of ±0.3mg and dissolved in a 2 litre beaker using ultrapure Milipore water (18.2 MΩcm) to make a 1 litre solution. Table 3.2 shows the amount of each salt that needs to be added to achieve the target ion concentrations required to produce Brine 1.

Table 3.2: Amount of each salt required to achieve target ion concentrations of Brine 1

Ion	Salt	Target (mg/l)	Amount (g)
Na^+	NaCl	8963	22.39
K^+	KCl	227	0.43
Mg^{2+}	$MgCl_2 \cdot 6H_2O$	69	0.58
Ca^{2+}	$CaCl_2 \cdot 2H_2O$	639	2.34
Sr^{2+}	$SrCl_2 \cdot 6H_2O$	59	0.18
Fe^{3+}	$FeCl_3 \cdot 6H_2O$	12	0.06
SO_4^{2-}	$NaHSO_4$	775	0.97

An example of how to calculate the amount of each individual salt required is shown below in Box 3.1. The molecular weight of the salt is divided by the molecular weight of

the target ion, multiplied by the target ion concentration and then converted to grams from mg/l. Note that the mass volume of water being added for the hydrated salts was taken into account with the calculations.

Box 3.1: Example calculation for required amount of salt

Example: Target ion concentration of K^+ = 227 mg/l

K Molecular Weight = 39.10 g/mol

KCl Molecular Weight = 74.54 g/mol

Mass of KCl needed = $\frac{74.54\ \text{g/mol}}{39.10\ \text{g/mol}} \times 227\ \text{mg/l} \times \frac{1l}{1000}$ = 0.43g

The sequence in which the salts are added is an important step of the brine preparation, where each salt is added and dissolved before the addition of the next salt. Adding the salts in the wrong order can lead to certain salts reacting with each other, forming precipitates and making the desired brine composition impossible to achieve. After several unsuccessful attempts, as described here, a clear, colourless solution was obtained, with no precipitates forming, by adding the salts in the following order; $NaHSO_4$, NaCl, KCl, $CaCl_2{\cdot}2H_2O$, $MgCl_2{\cdot}6H_2O$, $FeCl_3{\cdot}6H_2O$ and finally $SrCl_2{\cdot}6H_2O$. The $NaHSO_4$ was added and dissolved in the distilled water first as in previous attempts the SO_4^{2-} ions were reacting with the metal cations already dissolved in the water. Once the SO_4^{2-} ions were dissolved, the monovalent salts were added in order of quantity, followed by the divalent salts, leaving $SrCl_2{\cdot}6H_2O$ until last. Originally, the brine was meant to contain Ba^{2+}. However, $BaCl_2{\cdot}2H_2O$ was not added as the Ba^{2+} ions were reacting with the SO_4^{2-} ions to form $BaSO_4$. This happened regardless of the order in which the $BaCl_2{\cdot}2H_2O$ was added and is due to the saturation ratio (SR) for $BaSO_4$ being far greater than 1 (SR = 180000, see Box 3.2). The SR is used to determine whether, thermodynamically, a precipitate should form [105]. If the ratio is far greater than 1 then the formation of a precipitate is thermodynamically favourable. It is for this reason that $SrCl_2{\cdot}6H_2O$ was added last, as it was calculated that SR is 15.79 for $SrSO_4$ in Brine 1, meaning that the formation of $SrSO_4$ could be expected, but no precipitate was visible in the prepared solution.

Box 3.2: Example saturation ratio calculation for $BaSO_4$

Example: $[Ba^{2+}] = 328\text{mg/l} = 2.389\times10^{-3}\text{mol/l}$

$[SO_4^{2-}] = 775\text{mg/l} = 8.068\times10^{-3}\text{mol/l}$

Solubility product constant (Ksp) for $BaSO_4 = 1.08\times10^{-10}(\text{mol/l})^2$

SR = $\frac{[Ba2+][SO42-]}{Ksp[BaSO4]}$ = 180000 >> 1

Consequently, it was decided that all the brines would be produced without including Ba^{2+} ions. This is unfortunate, but unavoidable as either the Ba^{2+} or SO_4^{2-} ions would have to be omitted. However, previous work has already shown that the Ba^{2+} ions have no effect on the pH of the brine and so should have little effect on the mineral trapping process [100]. In contrast, the effect that seawater injection has on CO_2 solubility and mineral trapping has yet to be determined, making the inclusion of SO_4^{2-} ions in the brine necessary for the objectives of this research.

Once the salts have been added in the correct order, the top of the beaker is covered with Parafilm® and the solution is mixed thoroughly using a magnetic stirrer, for a approximately 15 minutes, until a clear solution is obtained. Once all the salts have dissolved, the pH of the brine is measured and recorded using a pH meter (Thermo Scientific Orion 3-star benchtop pH meter), with an analytical error of ±0.02. All pH measurements were performed under ambient conditions and not reservoir conditions. As discussed in section 2.5.3, the pH will change under reservoir conditions as pH decreasing with increasing pressure and increases with temperature [79]. However, to measure pH under reservoir conditions requires custom built apparatus that can accommodate pH electrodes that can operate at high pressures and temperatures, which was not available for this work. Therefore, all pH measurements had to be made under ambient conditions. However, per Peng et al. (2013), under similar experimental conditions to the experiments performed in this work (94.95°C compared with 112°C), the pH dropped from 3.97 at 60 bar to 3.23 at 154.1 bar and the pressure begins to plateau after 100 bar [79]. Section 3.1.4 discusses that excess buffer was added to increase the pH to above 10 rather than the required 9. Therefore, it is likely that the drop in pH associated with the increase in pressure with be countered by the excess buffer used.

The brine is then transferred to a 1 litre volumetric flask and distilled water is added to the graduation mark. Two samples of the brine are then taken for ICP-OES analysis to measure the major ion concentrations in the brine. Each sample is diluted with Milipore water by a factor of 10 and 2% nitric acid is added. Nitric acid keeps the ions in solution as it prevents the formation of precipitates [106]. The Milipore water is also analysed using ICP-OES to confirm that there are no contaminants present.

3.1.3 Inductively Coupled Plasma – Optical Emission Spectrometry (ICP-OES)

ICP-OES is a very effective analytical tool for determining trace metal elements at concentrations of 0.0002-1000ppm [107]. It can also be used to detect several non-

metallic elements, such as sulphur and phosphorus. An ICP-OES instrument allows for gas and liquid samples to be directly injected, whereas solid samples need to undergo acid digestion or extraction to allow for the analytes being in a solution. Once in solution, the liquid sample can be converted to an aerosol using a nebuliser (which converts liquid into a spray) [108]. This aerosol is then vaporised due to the intense temperatures within the ICP core (approximately 10,000K), liberating the analyte elements as free atoms. These free atoms are then promoted to excited states due to collisions with the plasma which imparts additional energy on to them. In addition, there is usually sufficient energy to convert the atoms to ions which are then, themselves promoted to excited states [107].

When the atoms and ions relax from their excited states, they emit a photon. Each photon has a characteristic energy determined by each atom's or ion's energy level structure. Therefore, by measuring the wavelength of the photon, the element from which it originated can be identified [107]. The concentration of each element is then determined by the total number of photons detected as the two are directly proportional.

The ICP-OES used for the analysis of the brine samples in this work is located at Edinburgh University and is a Perkin Elmer Optima 5300 DV ICP-OES [109]. The ICP-OES was selected as it can detect and measure the concentrations of SO_4^{2-} and has a relatively high total dissolved solids tolerance of 5-10%. The concentration range for this particular instrument is 0.01-1000ppm and that is why the brine samples have to be diluted by a factor of 10. For elements with concentrations less than 100ppm, the instrument was operated in axial mode, otherwise radial mode was used. Single element, 1000ppm standards were used for calibration and diluted with deionised water. In addition, VI CertiPUR® was used as a reference standard for each element. Each sample was then run three times and the standard deviation associated with each measurement was recorded. For this study, brine samples are collected upon preparation of each brine, as well as immediately after each experiment (Sections 3.4.1 and 3.4.2) and sent off for ICP-OES analysis so as to verify the precipitation of carbonates by measuring the concentration of ions present in the brine.

3.1.4 Addition of buffer

As previously mentioned in Section 2.5.3, the formation of solid insoluble carbonates is highly dependent on brine pH. The Bjerrum plot (Figure 2.9) shows that the carbonate ions (CO_3^{2-}) do not become the prevalent carbonic species until the pH increases above 9 [72]. CO_3^{2-} ions are needed to react with the metal cations such as Mg^{2+} and Ca^{2+} in the

brine to form insoluble carbonates. However, brine pH in deep formations usually ranges from 2-7 and at the acidic end of the spectrum the formation of mineral carbonates is impossible due to too few or no carbonate ions being present [19]. In this case, the pH of Brine 1 was measured to be 2.03, right at the acidic end of the scale. Therefore, without the addition of a buffer, it is extremely unlikely that any mineral carbonation will occur.

As a result, for the experiments looking at the importance of well selection (Objective 2), a buffer was used. As per previous work looking to promote mineral carbonation, 0.3M KOH was selected as the buffer [14]. As the objective of the experiments was to promote mineral carbonation, excess KOH was used to raise the pH above 10 to try and ensure the formation of mineral carbonates. In addition, the modelling software used to calculate mineral trapping potentials, PHREEQC (see Chapter 4), predicted that with the brine compositions from Table 3.1, mineral carbonation would not occur if the pH was below 10. Therefore, to be able to compare the experimental results with the predicted geochemical modelling results and to reduce the effect that increasing pressure has on the pH, the pH of each brine was increased to above 10 using 0.3M KOH buffer.

3.2 Calcite characterisation

There were three experiments conducted in the pressure vessels. For each experiment calcite powder was added to brine and then CO_2 was injected into the system under reservoir conditions (Objective 4). There were three vessels available to run the experiments and due to time restrictions the maximum runtime was 6 months. Therefore, to assess the buffering affect of calcite over time the experiments were performed over periods of 1 month, 3 months and 6 months. 6 grams of calcite was added to 60 ml of brine for a 1:10 rock/brine ratio based on previous studies [20, 74]. The pressure and temperature were set to 246 bar and 112ºC respectively, which are the reservoir conditions corresponding to the North Sea oil field brine used.

The reason for performing these experiments was that when CO_2 dissolves in brine, it forms a weak acid which will react with the calcite to produce Ca^{2+} and HCO_3^- which is alkaline [20]. This will then cause the pH of the brine to increase. The reaction can be seen in Equation 4.7 in Section 4.3.1. Therefore, as more CO_2 is injected and dissolves in the brine, the brine pH will likely further increase due to the increased levels of HCO_3^- ions. Consequently, calcite should act as a buffer and hence promote mineral carbonation. These experiments were performed to assess calcites potential to buffer the brine and promote mineral carbonation. Buffering of acid brine in chalk formations due to calcite

dissolution will be of interest in carbonate formations where there are chalk intervals overlying potential aquifer stores. In addition, the dissolution and precipitation of minerals may affect the properties of the rock such as the porosity. Changes in porosity will have a direct effect on CO_2 storage security. For example, if the porosity decreases then this will result in increased CO_2 storage security as the extent of the CO_2 migration will be reduced by the reduced flow capacity [22]. In contrast, a reduction in porosity will require greater injection pressure to displace CO_2 into the formation.

For these experiments, 1kg of calcite chips was purchased from the Geological Superstore, with a stated purity of 100%. These chips were then ground up using a pestle and mortar so that a powder was obtained (described in Section 3.2.2). This section describes how the purity of the calcite was confirmed using X-ray Diffraction (XRD). It also describes what particle size was chosen for the powder, along with how particle size distribution was used to confirm the particle size. In addition, the calcite powder was subject to Brunauer, Emmett and Teller (BET) analysis to obtain the specific surface area and the technique is also described in this section.

3.2.1 XRD

XRD is used to identify the mineral phases present and was used to confirm that the calcite chips purchased from Geological Superstore were pure, as stated by the supplier. Over 95% of solid materials have a crystalline structure and upon interaction with these structures X-rays are diffracted producing a characteristic diffraction pattern [110]. These patterns are unique to each crystalline structure and so are used for identification. Apex2 software suite can be used to create a diffraction spectrum which plots reflected intensities against detector angle. The data obtained are then compared with that from the International Centre Diffraction Data (ICDD) so as to identify what crystalline mineral phases are present. This comparison is performed to confirm that the peaks of the diffraction spectrum match and hence confirms that the sample is, in this case, calcite. If there are no other peaks presents then it also confirms that no other mineral phases or contaminants are present.

The equipment used in this work is a Bruker Nonius X8-Apex2 CCD and is located in the Chemistry Department at Heriot-Watt University. For the XRD analysis, 1g of sample was provided and the particles were ground to <75μm which is the recommended particle size for best results [111]. The XRD data was collected at room temperature using a Brucker D8 Advance powder diffractormeter. The diffractormeter was operated with Ge-

monchromated Cu $K\alpha_1$ radiation with a wavelength of 1.5406Å, along with a LynxEye linear detector, setup in reflectance mode. The data was collected over an angular range of 5-85 degrees in 2θ. XRD analysis was also performed on the solid samples collected from the mineral trapping studies to identify the crystalline mineral phases present, and hence, show whether solid insoluble carbonates had been formed.

3.2.2 Particle size distribution

Particle size has a direct and significant effect on reaction rates [112]. Reducing particle size results in increased surface area, and hence, faster reaction rates. For example, when Rahmani et al. (2014) prepared calcite from red gypsum for mineral carbonation they noted that decreasing the particle size from >200μm to <75μm, increased the Ca conversion rate from 37% to 98.8% [113]. Consequently, if the intention is to maximise reaction rates then the particle size should be as small as possible. However, it is also important that the prepared particles are within a specific size range. Otherwise, a direct comparison between different experiments cannot be made. This is where the importance of performing particle size distribution is evident.

The desired particle size for these experiments was chosen to be in the range of 45-75μm as the 45μm and 75μm sieves were the smallest available in the laboratory and the goal was to maximise reaction rates. Once the 45-75μm calcite had been prepared, a 0.5g sample was taken for particle size distribution analysis. For the particle size distribution analysis, a laser diffraction particle size analyzer (Mastersizer 3000 with a stated accuracy of ±0.6%) was used. The laser diffraction technique can be used to measure both dry and wet samples, ranging from 10nm up to 5mm [114]. The principle behind laser diffraction is that when light hits a particle, it will be scattered at an angle which is proportional to the particles size. Small particles will scatter light at wide angles, whereas large particles will scatter light at small angles. The measured intensity of the scattered light, along with the scattering angles is then used to create the particle size distribution.

The produced distribution shows the range at which most of the particles sit in and provides the user with the D [4,3] which is the mean particle size [114]. Other important values to consider are the D10, D50 and D90, which are where 10%, 50% (the median) and 90% of the distribution lies below, respectively.

3.2.3 BET analysis

A powder's specific surface area is an extremely important factor as it affects reaction rates [115]. The external surface area of a mineral can be obtained through geometric

calculation which is based upon the powder grains idealized geometry. Geometric calculation assumes that the rock framework consists of a cubic array of truncated spheres [116]. Box 3.3 shows the geometric calculation of surface area for the calcite powder, with a density of 2710kg/m^3, that was ground and sieved to a particle size of 45-75μm [117].

Box 3.3: Example geometric calculation of surface area

Example: Calcite; density = 2710kg/m^3, mean particle size = 60.3μm

Volume of 1 grain = $\frac{4}{3}\pi r^3 = \frac{4}{3}\pi \times \left(\frac{60.3}{2}\text{x}10^{-6}\right)^3 = 8.1081\times10^{-14}\text{m}^3$

Volume of 1 kg grains = $\frac{1\text{kg}}{2710\frac{\text{kg}}{\text{m}^3}} = 3.69\times10^{-4}\text{m}^3$

Number of grains in 1kg = $\frac{3.69\text{x}10^{-4}\text{m}^3}{8.1081\text{x}10^{-14}\text{m}^3} = 4.551\times10^{9}$

Surface area of 1 grain = $4\pi r^2 = 4 \times \pi \times \left(\frac{60.3}{2}\text{x}10^{-6}\right)^2 = 9.059\times10^{-9}\text{m}^2$

Surface area of Calcite = $4.551\text{x}10^{9} \times 9.059\times10^{-9} = 41.23\text{m}^2/\text{kg}$

Surface area can be calculated more accurately using the BET method. This is because it not only calculates the external surface area like with the geometric calculation, but also considers porosity. BET theory explains physical adsorption as result of multilayer adsorption [118]. The Langmuir adsorption isotherm assumed monolayer adsorption, whereby all adsorbed gas molecules would only be in contact with the surface of an adsorbent. However, the BET theory states that under high pressure and at low temperatures, multilayer adsorption occurs, whereby the adsorbent can accommodate more than one layer of gaseous molecules and that not all of these molecules would be in contact with the surface of the adsorbent.

The data collected by the machine is subject to the Brunauer, Emmett and Teller (BET) adsorption isotherm equation.

$$\frac{1}{\left[V_a\left(\frac{P_0}{P}-1\right)\right]} = \frac{C-1}{V_m C}\text{x}\frac{P}{P_0} + \frac{1}{V_m C} \qquad (3.1)$$

Where V_a (in ml) is the volume of gas adsorbed at standard temperature and pressure (STP), V_m (in ml) is the volume of gas adsorbed at STP to produce an apparent monolayer on the sample surface, P (in Pa) is the partial vapour pressure of adsorbate gas in equilibrium at the boiling point of liquid nitrogen (77.4K), P_0 (in Pa) is the saturated pressure of adsorbate gas and C is a dimensionless constant, related to the enthalpy of

adsorption of the adsorbate gas on the sample [118]. Once V_a has been measured at a minimum of 3 values of P/P_0, ranging from 0.05 to 0.3, then the BET value is plotted against P/P_0 which should produce a straight line. V_m is determined as the (slope + intercept)$^{-1}$, whereas C is (slope/intercept) + 1. Once V_m has been calculated, the specific surface area, S can be determined from the following equation.

$$S = \frac{V_m N a}{m \times 22400} \tag{3.2}$$

Where N is the Avogadro constant ($6.022 \times 10^{23} mol^{-1}$), a (in m^2) is the effective cross-sectional area of an adsorbate molecule, m (in g) is simply the mass of the powder and 22400 (in ml) corresponds to the volume occupied by a single mole of adsorbate gas at STP.

The equipment used to perform the BET analysis was a Micromeritics' Gemini VII 2390 Series Surface Area Analyzer. Before analysis can take place, the sample must undergo degassing so as to remove any vapours or gases that may have been adsorbed onto the surface. Approximately 0.4g of powder was added to a sampling tube and the overall weight was measured. The sample was placed in a heater at a temperature of 200°C and nitrogen gas was pumped through it for a period of 24 hours. After which point the sample was weighed again (noting any weight loss) and could now be used for analysis. Each analysis was run at a saturation pressure of 771.412 mmHg (millimetre of mercury), an evacuation rate of 100 mmHg/min and with a 5 second equilibration time. Each analysis took approximately 1.5 hours, recording 24 relative pressure (P/P_0) values. The BET surface area was then calculated using the P/P_0 values between 0.05 and 0.3.

The reason that the volume of gas adsorbed is recorded at 24 relative pressures is that this allows for the adsorption isotherm type to be identified. There are five isotherm types, as listed here and can be seen in Figure 3.1 [119]. The isotherm type can also be used to provide information on the type of porosity i.e. microporous, mesoporous, macroporous or nonporous [119]. Microporous, mesoporous and macroporous are defined by pore size diameter, with respective diameters of <2nm, 2-50nm and >50 nm [120]. Type I shows monolayer adsorption, uses the Langmuir model and the pores are usually microporous [119]. Type II, on the other hand has a flat region that shows monolayer adsorption but it deviates from the Langmuir model. Type III describes multilayer adsorption but excludes monolayer. Type II and Type III are typically either nonporous or macroporous. Type IV describe monolayer followed by multilayer and Type V are very similar and show

multilayer adsorption and describe the adsorption of water vapour on charcoal. Both Type IV and Type V have pore sizes ranging from 1.5-100nm i.e. microporous-macroporous [119].

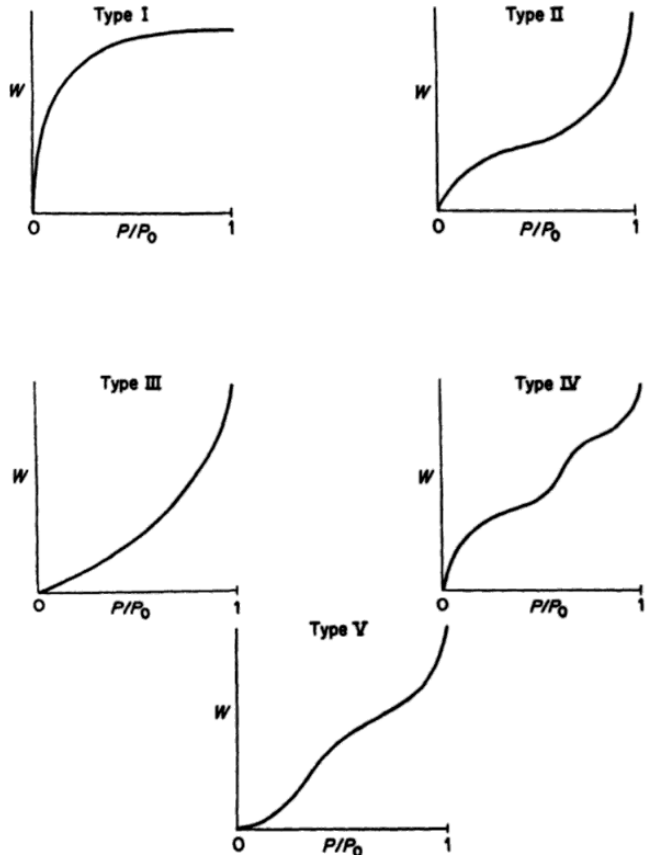

Figure 3.1: Types of adsorption isotherms [119]

3.3 Host rock samples

At present, there are no CO_2-EOR or CO_2 geological storage operations taking place in the UK sector of the North Sea. However, both Sections 2.3.2 and 2.4.3 show that there is a lot of potential for both CO_2-EOR and CO_2 geological storage in the North Sea. Therefore, it is important to understand the effect that CO_2 saturated brine has on the integrity of the local host rock (Objective 5). In this work, four core samples (size, permeability and porosity given in Section 7.1) were provided by the Institute of Petroleum Engineering from a reservoir located in the UK Continental Shelf. These cores were subject to CO_2 saturated brine under reservoir conditions (207 bar and 65°C) for time periods of 1, 3, 6 and 9 months in order to assess the effect of CO_2 saturated brine on rock integrity over time. Due to time restrictions 9 months was the maximum amount of time the experiments could be carried out over. The brine composition was taken from data on the reservoir, where the cores came from and is shown in Table 3.3. This brine was synthesised in the same way as described in Section 3.1.2.

Table 3.3: Brine composition related to host rock provide by IPE

Ion	Na^+	Ca^{2+}	Mg^{2+}	K^+	Cl^-	**Total Salinity**
Concentration (mg/l)	20803	231	96	225	32973	54328

Each core underwent characterisation both before and after the experiments, where they were exposed to CO_2-saturated brine. Firstly, the porosity and permeability of the cores was measured, then Micro-CT scans were done and finally Scanning Electron Microscopy (SEM) in conjunction with Energy Dispersive X-ray Spectrometer (EDS) was performed. It was essential to have the porosity and permeability of the cores measured both before and after the experiments as how CO_2-saturated brine affects porosity and permeability of local host rock is important when selecting a site for CO_2 injection. This is because reduction in porosity and permeability can lead to increased CO_2 storage security, as well as require greater injection pressure to displace CO_2 into the formation (see Section 3.2) [22]. Therefore, this section details how rock porosity and permeability can be determined. In addition, the concept of Micro CT scanning is explained and how it was used to produce images of the cores, both before and after the experiments, so as to provide a visual interpretation of how CO_2 saturated brine affects rock integrity. Finally, the core samples were characterised by SEM/EDS, an analytic technique which is also described in this section.

3.3.1 Porosity and permeability measurements

Porosity (Φ) of a rock is the measure of how much of the rock is open space and is defined as the pore-volume fraction.

$$\Phi = \frac{V_P}{V_T} \tag{3.3}$$

Assuming that the rock core is a cylinder (which in this case it is) then the total volume (V_T) is simply the volume of a cylinder. The pore volume (V_P), however, is more difficult to measure. The pore volume can be measured using the Inline method, whereby the core is flooded with brine (1% Na solution) dosed with 10ppm iodide and a UV spectrometer is used to measure absorbance. The UV spectrometer is set to the wavelength of the iodide (230nm) and is zeroed against the non-dosed solution i.e. brine without iodide. A pump is then used to flow the dosed solution through the core, while the UV spectrometer measures the absorbance. The scan is complete once a steady absorbance value has been obtained. The process is then repeated for a non-dosed solution. Once the scans are

complete, the resulting curves are plotted against one another and the pore volume is recorded as the area under each curve. This is shown in Figure 3.2, where D is the dosed solution, ND is the non-dosed solution and the two solutions are compared by inverting the results from the non-dosed solution (INV ND). The difference between the volume measured for the D and ND solutions should be within 0.5ml for the test to be considered successful. Finally, in order to obtain the absolute pore volume the dead volume of the system, which is the portion of internal volume out with the flow path, needs to be subtracted from the pore volume result.

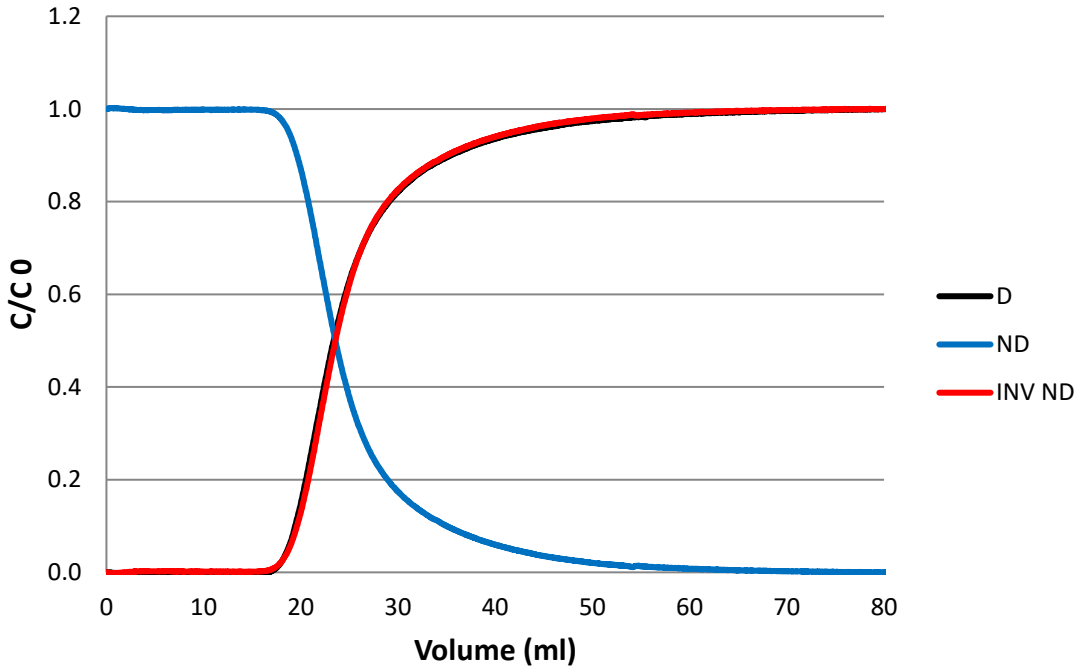

Figure 3.2: Solution concentration against volume showing both dosed and non-dosed solutions

The permeability of a rock is its ability to allow fluids to flow through it. Permeability is calculated using Darcy's Law:

$$Q = \frac{-kA}{\mu}\frac{(P_b - P_a)}{L} \tag{3.4}$$

Where Q is the flow rate (in m^3/s), *k* is the permeability (in m^2), A is the area (in m^2), μ is the viscosity (in Pa·s), (P_b-P_a) is the differential pressure (in Pa) and L is the length (m). Permeability can be measured in the lab through a flooding experimental where the rock core is at 100% water saturation. The process involves observing differential pressure and how it is affected by flow rate. Once the differential pressure is steady, the flow rate is reduced so that there is a large change in differential pressure. For example, if the original flow rate was 2.5ml/min then it should be reduced to 0.5ml/min. At this

point the flow rate is kept constant until the differential pressure is once again steady. There is then a 10-15 minute data collection period, followed by an increase in flow rate of 0.5ml/min. The flow rate is incrementally increased four times and the differential pressure is recorded until the flow rate is back to its original value at the start of the experiment. Once all the data has been collected, the flow rate is plotted against the differential pressure (Figure 3.3) and the gradient of the line is used in conjunction with Darcy's Law to calculate the permeability, k.

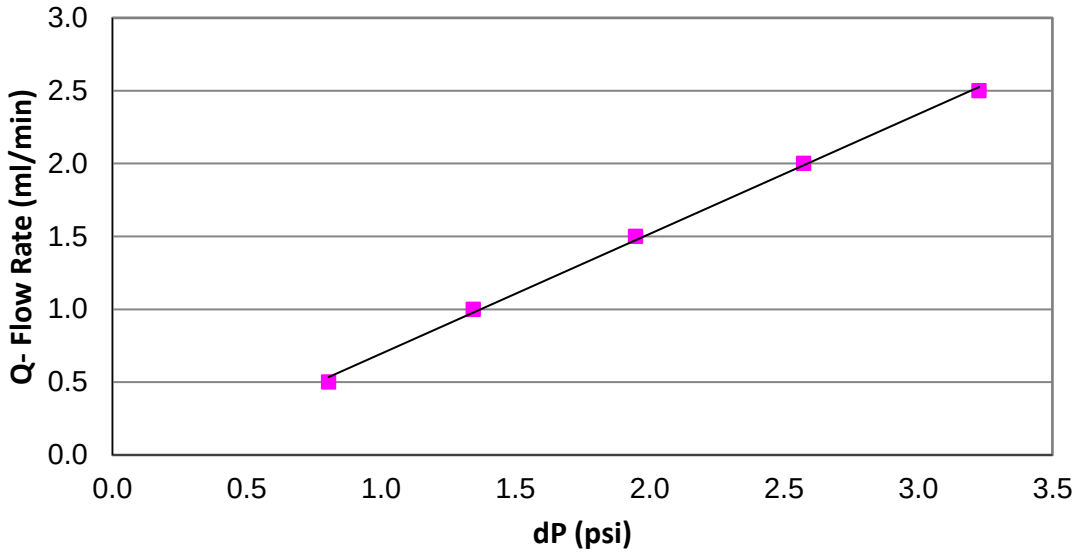

Figure 3.3: Flow rate against differential pressure and resulting gradient

For this study, the FAST group at the Institute of Petroleum Engineering at Heriot-Watt University used a bespoke coreflood rig based on a mini benchtop ambient condition coreflood rig. The differential pressure was recorded using a Validyne P51 Differential Pressure Transducer and a Camspec M501 UV/Vis Spectrometer was used to measure the iodide absorbance and determine the pore volume.

3.3.2 Micro CT scanning

Micro-CT scanning allows for the visualisation as well as the analysis of the internal structure of a material such as a rock core, without damaging the sample [121]. X-rays are generated in a similar way as with SEM, where primary electrons are emitted from the hot cathode, through thermal emission, accelerating them towards the target at the anode, which is usually a material such as tungsten [122]. This material will then emit X-rays which will be transmitted towards the sample. The X-rays emitted from the tungsten are in a conical shape which allows for a larger volume of the sample to be captured

during a single scan rotation. Higher resolution images are obtained by generating a finer electron beam as this reduces the spot size of the X-rays produced.

Micro-CT depends on two primary mechanisms of X-ray absorption; Compton scattering and the photoelectric effect [122]. When an X-ray photon collides with an outer shell electron, a portion of the photon's energy is absorbed by the electron, ejecting it from the atom. Upon collision, the photon loses energy and is deflected in a new direction. This is known as Compton scattering. The amount of scattering that occurs is dependent on both the density of the object and the energy of the photon. Therefore, higher density materials result in greater Compton scattering. When an inner shell electron absorbs all of an incident X-ray photon's energy, a secondary photon is emitted. This is the photoelectric effect and unlike Compton scattering it is dependent on the atomic weight of the material rather than the density [122]. The incident X-ray photons that have been scattered and the newly produced secondary electrons are recorded by the detector which allows for a single radiographic image to be produced. Once an image has been produced the sample is then rotated and a new image is taken [121]. This is repeated until a 360° scan has been complete.

Once all the images have been taken, powerful reconstruction software can be used to stack the images to produce a 3D virtual model of the sample [121]. The advantage of the 3D image over the 2D slices is that you can see exactly where objects (minerals in this case) are located within a sample. The reconstruction software can also be used to calculate the porosity of the cores. This is done by taking the image and adjusting the threshold. Greyscale images are made up of intensity graduations. For instance, an 8 bit image will have 2^8 intensity graduations [123]. Thresholding allows the user to separate pixels under a certain intensity value by setting a limit. Adjusting the threshold limit converts all pixels within the image that are under the threshold limit to a different colour (red is the preset colour). Therefore, allowing for objects of interest to be distinguished from the background. As the threshold is adjusted, the dark, porous spots will turn red. Once the user is confident that all porous spots have been filled the area fraction of red spots can be calculated to obtain the porosity. However, since the threshold is adjusted manually there is a tendency to overestimate the actual porosity and so it cannot be relied upon to provide accurate measurements. This is why the porosity of the cores was measured experimentally using the Inline method (Section 3.3.1).

The Micro-CT scanning of the cores before the host rock experiments took place was performed using a Micro-CT scanner located at the University of Aberdeen and was a ZEISS Xradia Versa 3D X-ray Microscope. The middle 25mm of each core was scanned using a resolution of 25 microns for a period of 4 hours. Unfortunately, due to unavailability of the equipment, upon completion of the experiments, the cores had to be scanned elsewhere. The final Micro-CT scanning was performed at the University of Edinburgh using a custom built Micro-CT scanner. Each core was scanned for a total of 30 minutes at 37 micron resolution. The scan was performed at 120kV and 12W power, using 2000 1 second exposures projections and an aluminium (0.8mm) energy filter. There is a noticeable difference in resolution between the images, as the resolution provided by the University of Edinburgh is superior. However, a comparison can still be made as seen in Chapter 7.

3.3.3 SEM/EDS

SEM involves scanning a sample using a high energy beam of primary electrons. This allows for the production of high resolution images (down to the nano-scale) of sample surface topography [124]. The primary electrons are emitted from the hot cathode, through thermal emission, accelerating them towards the anode. The hot cathode needs to be made of a material that has a high melting point and low vapour pressure, so that they can be sufficiently heated to allow thermal emissions [125]. Therefore, the cathodes are commonly made from lanthanum hexaboride (LaB_6) or tungsten. Once the primary electrons have been accelerated towards the anode, they are then focused into a very fine beam with a focal spot size between 1nm and 5nm. The beam is then deflected over the sample surface by being passed through pairs of condenser lenses. Once the primary electrons enter the sample surface, they generate a number of secondary electrons with low energy [126]. The sample surface topography governs the intensity of these secondary electrons, and therefore, by measuring the intensity of the secondary electrons as a function of the scanning electrons beams position, an image can be constructed of the sample surface.

Once the SEM scan is complete, EDS software can then be used for chemical characterisation and elemental analysis. When the sample is bombarded with primary electrons, in addition to the emission of secondary electrons, X-rays are also produced [126]. EDS software is able to analyse these X-rays to provide quantitative elemental analysis based on the principle that individual elements have unique atomic structures.

This means that it is possible to uniquely identify X-rays that correspond to a particular element's atomic structure [127]. EDS generally has an analytical accuracy of ±2% [128].

For this study, all SEM/EDS analysis were performed at the Centre for Environmental Scanning Electron Microscopy (CESEM) at the Institute of Petroleum Engineering at Heriot-Watt University. The equipment used was a Quanta FEG 650 Suite which is equipped with an Oxford Instruments X-max 150 EDX detector [129]. It is an Environmental Scanning Electron Microscope (ESEM) which is designed for the examination of microstructural and ultrastructural details of samples in their uncoated natural state. This particular suite is capable of automatic collection and stitching together of images. Montaged images that comprises of 5,000 separate frames can be constructed through software called MAPS. This suite also uses two EDS software's, Aztec and INCA. Aztec is similar to MAPS but has the ability to analyse a total area that is several square centimetres. It is however restricted to the construction of montage images that comprise of a maximum of 1,500 images. INCA is a particle analysis program, designed to indentify and analyse particulate materials. INCA can be used to analyse heavy minerals and filter papers.

SEM/EDS was not only used for rock characterisation but also to provide quantitative analysis of the elemental composition of the precipitates formed during the mineral carbonation experiments. SEM/EDS requires very little powdered sample for analysis (<1mg) and can even image and perform elemental analysis of minerals on the surface of the filter paper, which is used to separate precipitates from the aqueous solution (see Section 3.4.1). In this case what remained of the 1g sample that was prepared for XRD was subsequently used for the SEM/EDS analysis. The analysis was run at 20kV using low vacuum at a pressure of $1.1x10^{-3}$ bar and a spot size of 4.5. The working distance was 10mm and back scattered electron detector was used.

3.4 Mineral trapping studies

This section describes the experimental setup when using both the high pressure rig and the small pressure vessels (Objective 3). The high pressure rig allows for direct control over CO_2 injection rates through a Bronkhorst digital CO_2 mass flow controller, has a large capacity (600ml) and has a vessel that is highly resistant to corrosion. The high pressure rig was used to perform the experiments focused on well selection and brine composition (Objectives 2 and 3). For the CO_2-brine-calicte and the CO_2-brine-rock experiments, which would run from 1-9 months, it was more appropriate to use the small

pressure vessels (Objectives 4 and 5). Although they lack the volume of the high pressure vessel and are made from less resistant materials (stainless steel 316L instead of Hastelloy), they are more available as there is only one high pressure rig but eight small pressure vessels. This made the small pressure vessels the only viable choice to run multiple concurrent long term experiments.

3.4.1 High pressure rig setup

The high pressure rig was designed and commissioned by Dr Susana Garcia and is centred on a Parr 4544 Series High Pressure Reactor with a 600ml volume and working pressure and temperature of 345 bar and 350°C, respectively [130, 131]. The reaction vessel is made from Hastelloy C-276 which is highly resistant to corrosion [132]. The rig also contains a Parr 4843 controller for maintaining vessel temperature and stirrer speed. CO_2 injection rates are regulated through a Bronkhorst digital CO_2 mass flow controller and increased through a compressed-air driven gas booster. This allows for experimental pressures (246 bar) to be reached, as the CO_2 cylinder pressure is rated at only 30 bar. To keep the stirrer cool during the experiment and to cool the vessel during depressurisation, the rig is connected to an ATC KT1 model chiller. A photograph and schematic of the high pressure reactor are shown in Figure 3.2 and Figure 3.3, respectively [13].

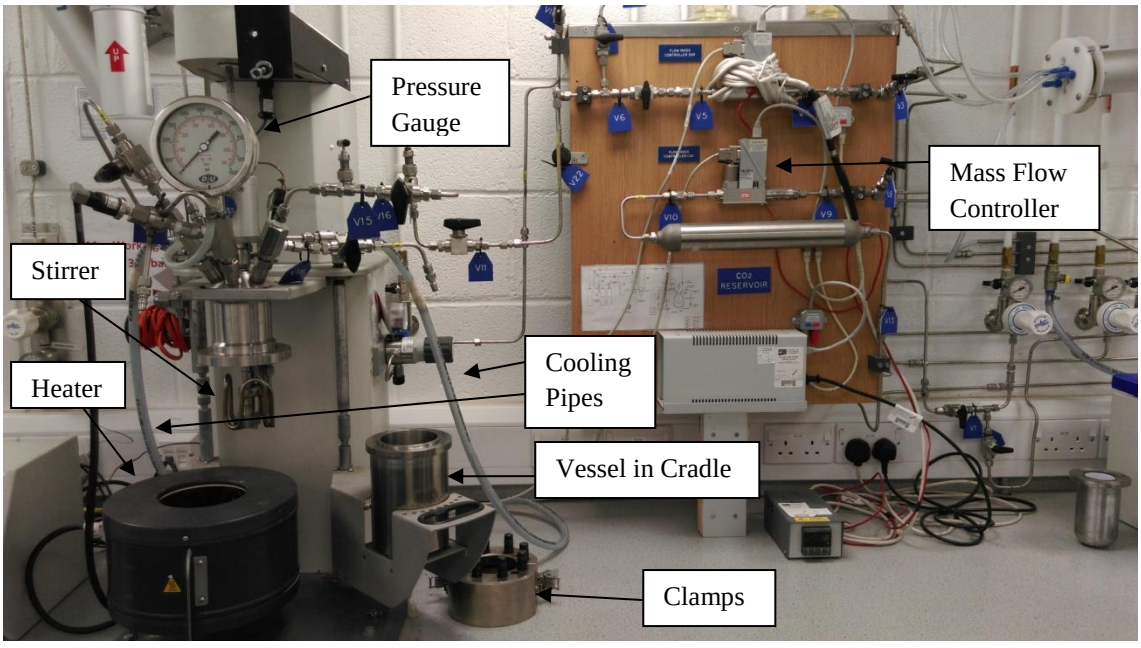

Figure 3.4: Photograph taken by author of the high pressure reactor

The experimental methodology for operating the high pressure rig is previously described by Liu (2012) who supervised the experimental setup for this work [74]. Once the sample (300ml brine + KOH buffer, amount of which is dependent on initial pH) has been added

to the reaction vessel, it is placed in the cradle and lifted up (see Figure 3.4). The clamps are then used to secure the vessel to the top of the reactor, forming a metal-to-metal seal. The bolts on the clamps are tightened in a criss-cross pattern using a torque wrench to ensure that the vessel is secure. Once the vessel is secure, the cooling water is connected to the stirrer, that is switched on and then set to 400 rpm to ensure mixing (see Figure 3.4). At this point the rig must undergo N_2 flushing so as to purge any gases from the system. As with previous work, N_2 is flushed through the system for a period of 5 minutes, after which CO_2 injection can begin [74].

The Bronkhorst mass flow controller has associated software applications which allow the user to regulate injection rates (standard rate is 10litres/min) and monitor reaction pressure and temperature. The three applications used are FlowDDE, which handles communication with the mass flow controller and relays data to the other applications, FlowView which provides readouts of parameters and FlowPlot which serves as a data logger [133, 134, 135]. CO_2 is injected into the reaction vessel by opening the gas inlet valve, V15 (see Figure 3.5) until the recorded pressure is 30 bar, which corresponds to the CO_2 gas cylinder pressure. Once 30 bar has been reached, the vessel is closed off from the system by closing V15. The heating mantle is then secured around the vessel and the heating process begins until the temperature reaches 112°C, which is the experimental temperature. Once the desired temperature has been reached, reinjection of CO_2 can commence, this time using the compressed-air driven gas booster to reach the experimental pressure of 246 bar. Once the experimental conditions have been reached, the experiment is said to have started and is run for 24 hours from this point, as per previous work by Liu (2012) [74].

Upon completion of the experiment, the vessel must undergo depressurisation. This is done by first turning off and removing the heating mantle. Then the stirrer is switched off and the cooling pipes (see Figure 3.4) are removed and placed on the cooling coil. The vessel is then allowed to cool until it reaches a temperature of approximately 35°C. At this point the CO_2 can be evacuated from the vessel by opening the gas outlet valve, V17, the pressure regulators and V21, which allows the gas to reach the gas vent (see Figure 3.5). During this part it is important to heat the evacuation line with heating tape as the CO_2 will freeze the line otherwise. Once all the gas has been evacuated, the reaction vessel is removed and the pH of the solution is measured immediately so as to reduce the amount of time it is in contact with air. To measure the pH a Thermo Scientific Orion 3-star benchtop pH meter is used. The solution is then vacuum filtered using 0.45μm glass

microfiber Whatman filter paper to separate any precipitates from the aqueous solution. A portion of the filtered solution should be transferred into a washing bottle so that it can be used to rinse out the vessel and collect any residual solids that remain inside or on the stirrer. It is important not to use distilled water for the rinsing as distilled water can potentially dissolve the precipitates that may have formed during the experiment [13]. The remainder of the filtered solution is then prepared for ICP-OES analysis, as described in Section 3.1.2. The filter paper containing the precipitates is then placed in a glass vacuum desiccation chamber for 24 hours, so that complete evaporation can occur without damaging the residue sample. The dried solids are then weighed and ground into a powder using a pestle and mortar for XRD and SEM/EDS analysis. The experimental error associated with the high pressure rig comes from the pressure transducer with an recorded error of ±1%, the temperature controller with an error of ±2°C (1.8% at 112°C) and the ICP-OES with an error of ±1% [136, 74]. Therefore, the total uncertainty from the experimental work using the high pressure rig is likely to be ±2.3%.

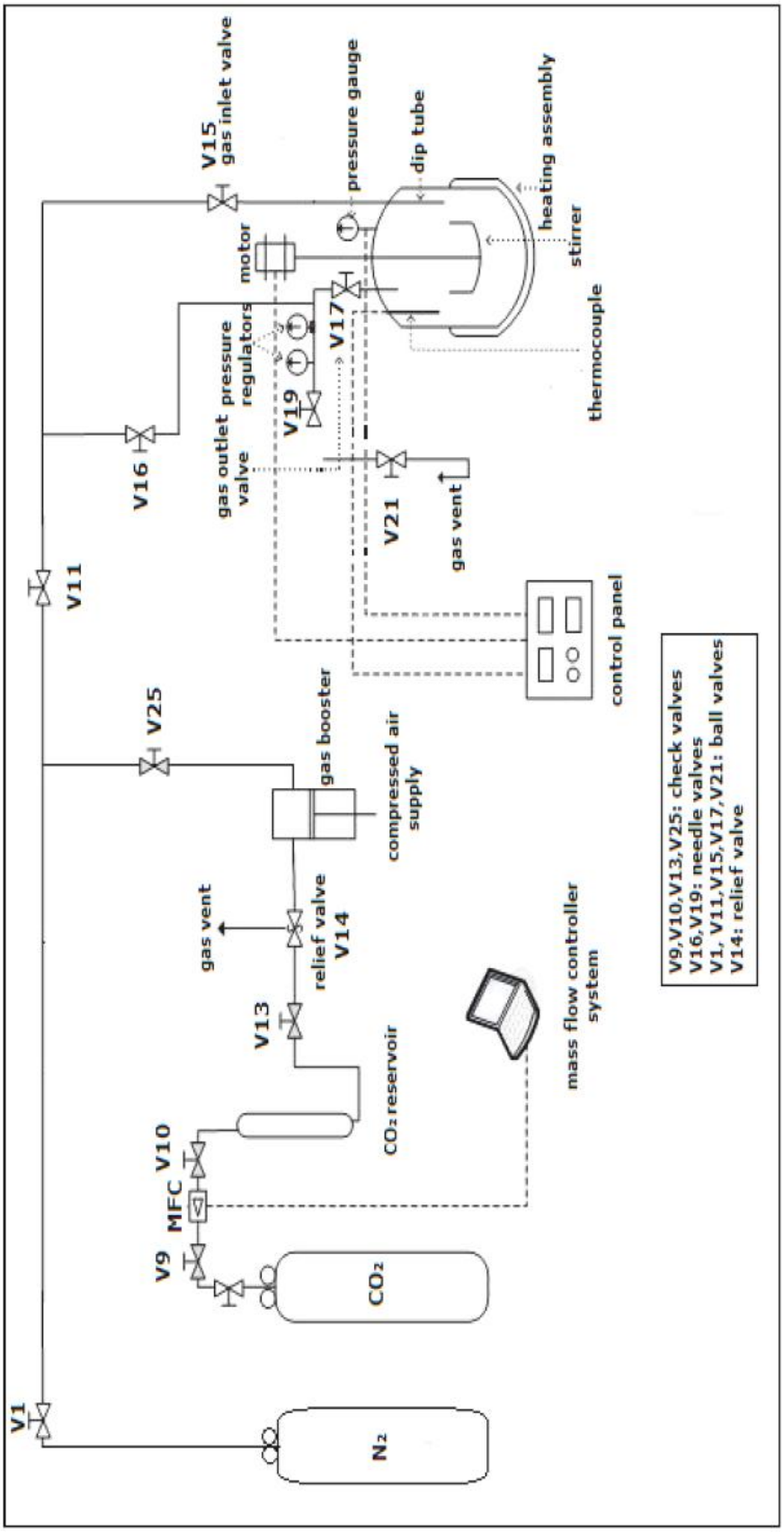

Figure 3.5: Schematic of high pressure rig [131]

3.4.2 Small pressure vessel setup

The small pressure vessel, shown in Figure 3.6, consists of a body, lid, thermocouple pocket, a Swagelok pressure relief valve (PRV) set to 275 bar, two Tedelfi needle valves rated at 1000 bar and a 400 bar pressure gauge. The body, lid and thermocouple pockets are made from 316L stainless steel which has good corrosion and heat resistance. However, it is subject to pitting and crevice corrosion when it comes into contact with water containing approximately 500mg/L of chlorides at temperatures above 60°C [137]. Therefore, for these experiments, which have conditions of 65°C and 112°C, polytetrafluoroethene (PTFE) liners were made as PTFE has a very high chemical resistance [138].

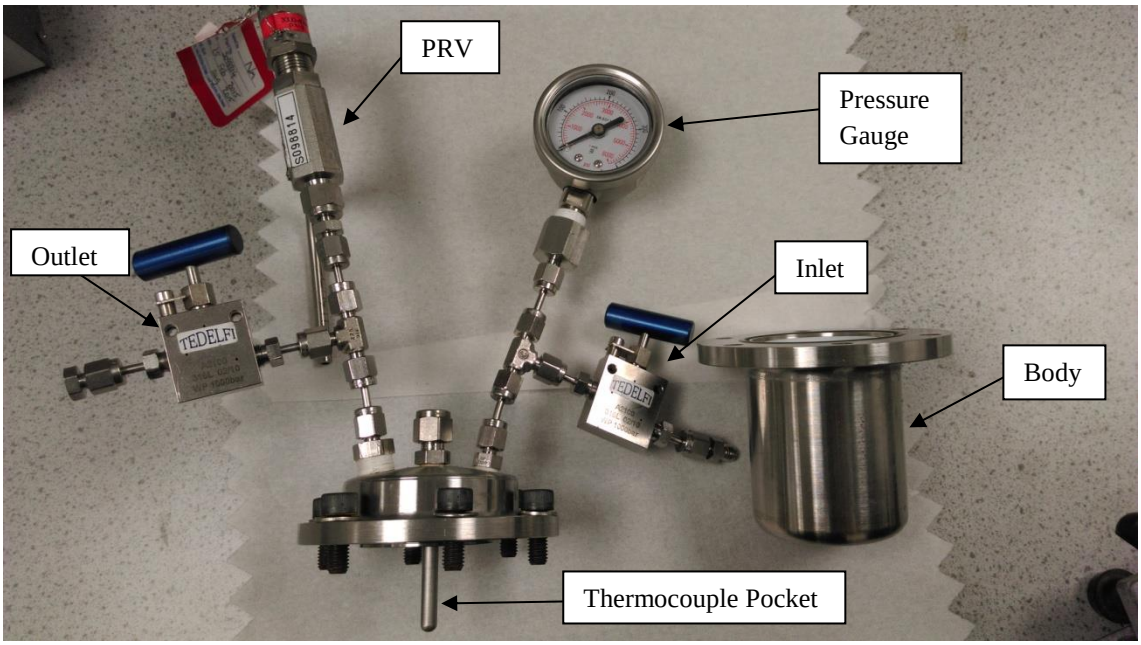

Figure 3.6: Photograph taken by author of small pressure vessel body and lid

The liners made for the host rock experiments were made thinner (1.5mm thickness) than for those experiments using calcite (3mm thickness). The reason for this is that it was important to maximise the volume so that the rock could fit in the liner and be surrounded by brine. However, due to the higher temperatures of 112°C, the liners had to be made thicker for the calcite experiments as during tests the higher temperature appeared to cause weak spots in the thin walls to fold in (explanation below). As a result, the volume of the thinner liners (1.5mm) was 110ml and the volume of the thicker liners (3mm) was 90ml. The reason for the liners folding in on themselves is inconclusive. However, the PTFE melting point is 326.8°C so it is unlikely that any melting occurred. What was observed though is that the PTFE absorbs some of the CO_2, this was noted when trying to remove the liners after the experiments. The liners fit into the body of the vessels

without incident before the experiments took place. However, after the experiments the PTFE liners were very difficult to remove as they had expanded. The higher temperature likely leads to more absorption of CO_2, and hence, more expansion. When the liner cannot expand anymore it will then fold in on itself at any available weak point.

To charge the vessels, a Teledyne ISCO Model 260D syringe pump is used. This syringe pump is designed to control pressure up to 517 bar with a flow rate of 100ml/min and a capacity of 266ml [139]. It is connected to a liquid CO_2 cylinder to supply the gas, a VWR circulating bath to keep the pump cylinder cool and a Teledyne ISCO D-Series pump controller for operation of the pump. A schematic of the syringe pump and its associated components is shown in Figure 3.7. To fill the pump cylinder to its capacity of 266ml, the CO_2 cylinder is opened, as is the inlet to the pump and the "Refill" button on the control box is pressed. This will then fill the pump to its maximum capacity and then automatically stop. The pump is connected to all of the vessels via a manifold which was built to allow the vessels to be simultaneously charged. To fill the vessels, the pressure is set using the control box, the gas outlet valve is opened, the vessel inlet is opened and the "Run" button is pressed. This will then begin filling the vessels to the desired pressure until either the set pressure is reached or the pump runs out of gas, at which point it has to be recharged. If the desired pressure is reached the "Stop" button has to be pressed. However, if the pump runs out of gas it will automatically turn off and wait to be refilled.

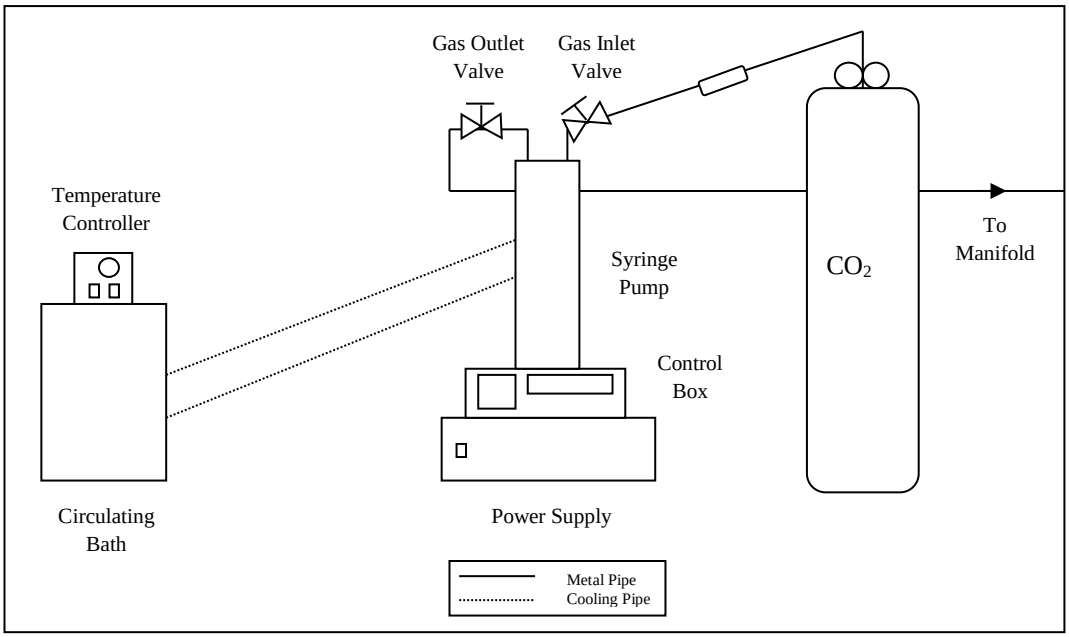

Figure 3.7: Schematic of syringe pump and components (not to scale)

To obtain the experimental temperatures, a HOTSET UK 350W heating jacket is attached to each vessel and connected to an OMEGA CN740 temperature controller, with an accuracy of ±0.1°C [140]. Rectangular metal boxes were designed that could hold two controllers each and contained warning lights to indicate if the fuse had blown. They also had ports on the back to support the connection of thermocouples. The thermocouples used were OMEGA TJ1-CASS K-type thermocouples, which when connected to the controllers allowed for a maximum temperature of 500°C [140]. In addition, these boxes were designed with solid state relays to reduce the electrical load taken by the mechanical relays on the temperature controllers. The reason for the addition of the solid state relays was that during other work (performed by another researcher) several of the mechanical relays fused shut due to the electrical load being too high, which in turn caused the temperature to continually rise, resulting in damage to the vessel and the destruction of a sample.

Before the vessels could be used for experimental purposes, they had to undergo extensive leak testing. This was conducted by adding water to the vessels and pressurising them up to 250 bar without heating them. As can be seen from Figure 3.6, the lid of each vessel contains a large number of joints where a leak may occur. A leak detector spray was used at first to go over each and every joint to check for leaks. However, after about a month it was decided that it would be easier to very carefully place the pressurised vessels in a bucket of water. This way it would be easy to identify where the leaks were coming from by looking for bubbles rising. When submerging the vessels, it was very important not to submerge either the PRV or the pressure gauge so as not to damage them. Apart from the joints, other major leak points were the valves and the seal between the lid and the base. Originally, Parker valves were used which were rated up to 345 bar. Many of these however seemed to leak back, even when the valve was closed. They were consequently replaced by Tedelfi valves and sent back to Parker for investigation. Parker stated that a few of the needles had unknown residue on them but the reason why so many of them were leaking back was inconclusive. A select few of the Tedelfi valves appear to be leaking slightly as well and so are capped after they have been closed to prevent the gas from escaping. The leaks associated with the seal between the lid and the base was caused by improper sealing. The seal couldn't be properly made due to the original O-rings, made from viton, being unsuited for use with CO_2. Therefore, DuPont Kalrez® O-rings had to be purchased, which are a perfluoroelastomer and have a chemical resistance rating of A for CO_2, which means that the elastomer should show little or no effect to its properties

when exposed to CO_2 [141]. In addition to the O-ring that made the seal between the lid and the body, there is also an O-ring in the PRV. It was noted that this O-ring had to be replaced after every depressurisation as the ring would become frayed and no longer provide a seal. Fortunately the O-rings for the PRV's, also made of viton, are low cost so this was not a major problem.

Once the leak testing is complete, the final experimental setup can begin. For the calcite experiments, 6 grams of calcite is added to 60 ml of brine for a 1:10 rock/brine ratio based on previous studies [20, 74]. This rock/brine ratio cannot be achieved for the experiments involving the host rocks since each core has a different volume. It was decided that the rock/brine ratio should be the same for all experiments. Therefore, taking the total volume that the rock + brine should occupy to be 80ml, the volume of the largest core was calculated, making the assumption that it was a cylinder. Once the volume of the core was known the value was taken away from the total volume of 80ml to give the volume of brine that should be added. The rock/brine ratio could then be determined upon knowing the volume of the rock and volume of the brine to be added. This ratio was then used to calculate how much brine should be added for each experiment. An example is shown in Box 3.4. The calculated rock/brine ratio of 1:1.7 was then used for all the core experiments.

Box 3.4: Example calculation for rock/brine ratio

Example: Height of rock = 2.598 cm, Diameter of rock = 3.81 cm

Volume of rock: $V_r = \pi r^2 h = \pi \times \left(\frac{3.81}{2}\right)^2 \times 2.598 = 29.62 cm^3 = 29.62$ ml

Volume of liquid to be added: V_l = 80ml-29.62 ml = 50.38 ml

Rock/Brine Ratio: $\frac{V_l}{V_r} = \frac{50.38}{29.62}$ = 1:1.7

Once the samples have been added and the O-ring inserted, the lid is sealed by tightening the bolts in a criss-cross pattern using a torque wrench. The heating jacket is then attached to the body of the vessel and the thermocouple is inserted into the thermocouple pocket. The vessel is then connected to the manifold and the final setup can be seen in Figure 3.8. Once the vessel is in place, the vessel inlet is opened along with the CO_2 cylinder and the pump outlet so that the vessel is charged to the cylinder pressure which is 50 bar. All valves are then closed and the vessel is heated to the experimental temperature. Once the desired temperature has been reached, the vessel is then charged to the experimental

pressure. The pump is left running after the experimental pressure has been reached to allow time (10-15 minutes) for the temperature to stabilise, as it will be affected by the large increase of pressure. Once both the pressure and temperature are stable (± 2 bar and ±0.1ºC), the inlet to the vessel is closed and the experiment is timed from this point. It is likely that after the first 24 hours the vessels will need to be recharged as a result of some of the CO_2 dissolving in the brine. When recharging the vessels it is important to first charge the manifold to the desired pressure, then open the inlet to the vessel. If the inlet of the vessel is simply opened without first charging the manifold, then the pressure within the vessel will drop dramatically which risks damaging the samples inside, especially the cores. Since the experiments are being run from 1-9 months, there will inevitably be drops in pressure due to minute leaks that are extremely difficult to detect. As a result, the vessels need to be monitored and recharged when necessary.

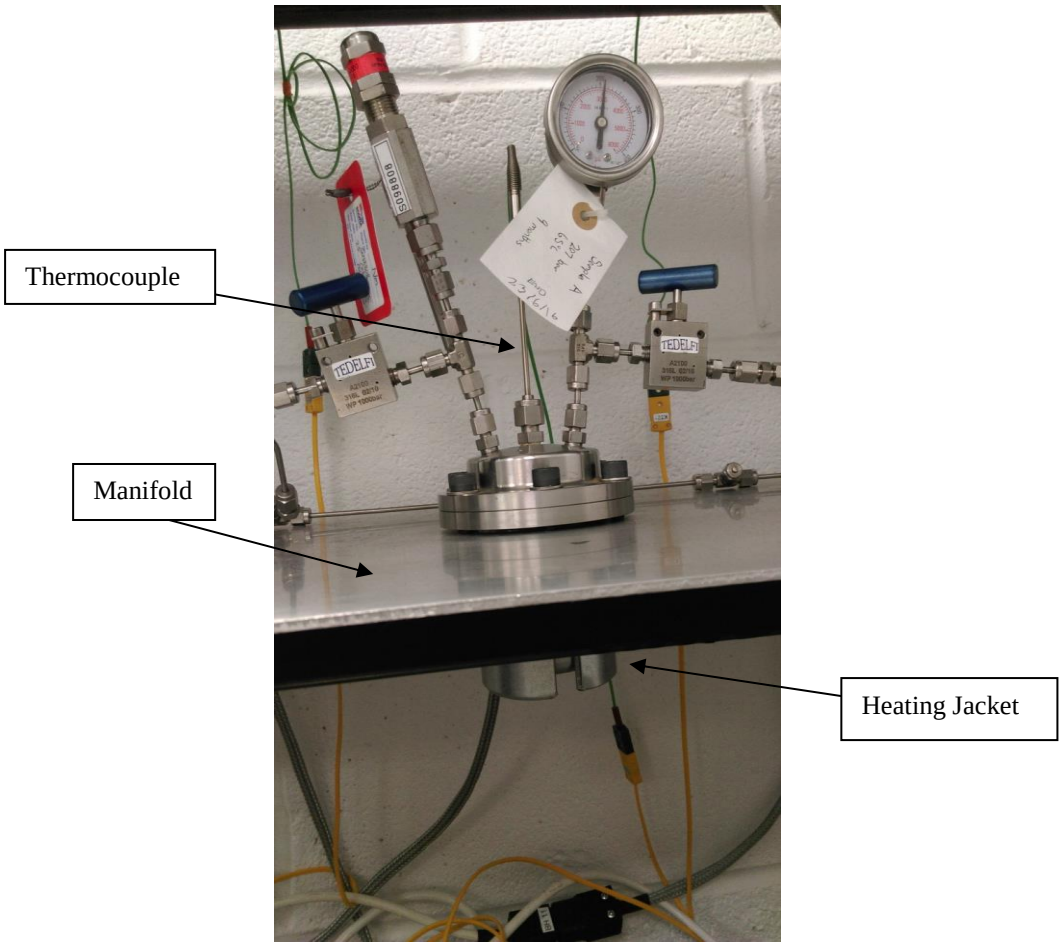

Figure 3.8: Photograph taken by author of the final setup of small pressure vessel

Upon completion of each experiment, the vessel must undergo depressurisation. This must be done carefully to avoid any explosive decompression which could damage the samples and harm the operator. Firstly, the heater is turned off and allowed time to reach

ambient temperature. This can take up to an hour depending on the experimental temperature. Once ambient temperature has been reached, the remaining pressure (pressure will have dropped due to drop in temperature) is released very slowly by only slightly opening the outlet valve. As with the temperature, this process can take up to an hour depending on the experimental pressure. However, it is preferable to letting all the gas out at once, which could be done in less than a minute. Once all the gas pressure has been released, the vessel is taken off the manifold and the lid is removed. The pH must then be measured immediately, as described in Section 3.4.1. After that, for the host rock experiments, the core is removed, placed in a container with brine and sent off for porosity and permeability measurements and then Micro-CT scanning. The liquid sample is collected, filtered and prepared for ICP-OES analysis, as described in Sections 3.4.1 and 3.1.2, respectively. As for the calcite experiments, the solution is filtered, as described in Section 3.4.1 to separate the calcite and any other precipitates from the brine. The filtered solids are then placed in the glass vacuum desiccation chamber for 24 hours and sent for XRD and SEM/EDS analysis, whereas the filtered brine is sent for ICP-OES analysis.

Chapter 4 Geochemical Modelling Methodology

This Chapter describes some of the different geochemical modelling software programs available to measure CO_2 solubility in brine as well as mineral trapping potentials (Objective 1). It then goes on to compare the modelling results with those obtained through previous experimental work, so that the appropriate software can be selected. After which, the selected modelling software is used in Chapters 5 and 6 to assess geochemical trapping mechanisms on a geological time scale and to validate the experimental results.

4.1 Geochemical modelling software packages

There are a variety of geochemical modelling software packages that can be used to calculate CO_2 solubility in brine under reservoir conditions. However, for the purposes of this study, only the three that were used to perform the geochemical modelling will be analysed, namely: (i) a general geochemical software program known as PHREEQC; (ii) HydraFLASH, an in-house software developed at Heriot-Watt University, that allows the user to change the Equation of State (EoS) used; and (iii) the previously mentioned Duan and Sun CO_2 solubility model, which is the most widely used model for calculating CO_2 solubility in brine. These software packages were chosen as they allow for CO_2 solubility to be measured in brine but do not require the user to have previous geochemical modelling experience.

4.1.1 PHREEQC

PHREEQC is a general geochemical software program that requires very little prior modelling experience and can be applied to most hydrochemical environments [142]. It is capable of saturation-index and speciation calculations as well as one-dimensional transport and batch-reaction calculations which involve reversible reactions, such as mineral gas, aqueous, surface-complexation, solid-solution and ion-exchange equilibrium. Batch-reaction calculations involving irreversible reactions are also possible, including kinetically controlled reactions, temperature changes, specified mole transfer of reactants and mixing of solutions. In addition, the software program is also capable of inverse modelling, which is used to find sets of gas and mineral mole transfers that affect water composition [143]. Previous work by Liu (2012) concluded that, in some cases, PHREEQC cannot be used to accurately predict experimental results [74]. This is because complex ion exchange models are not considered, it does not take into account uncertainties in thermodynamic constants and it makes simplified assumptions related to steady-state flow [144]. It can, however, be used to demonstrate general trends.

PHREEQC version 3 is available as freeware and can be downloaded from the United States Geological Survey website [145]. The input files used in PHREEQC are based around keyword data blocks which start with a line containing the keyword, which is followed by related lines of data [143]. It is through use of these keywords that PHREEQC version 3 models geochemical reactions. At the beginning of each a run, a database file reads the keywords and their corresponding data to define the exchange reactions, elements, mineral phases, surface complexation reactions, rate expressions and gas components. These database files are composed of thermodynamic data that has been obtained from published literature and are integral to the accuracy and quality of the geochemical modelling [146].

4.1.2 HydraFLASH

HydraFLASH is an in-house software developed by the HYDRAFACT group at Heriot-Watt University, UK. It is a PVT and thermodynamic prediction software that allows modelling of multicomponent, multiphase aqueous and hydrocarbon systems in the presence and absence of hydrates and inhibitors [147]. Although mainly used for modelling hydrocarbons for the oil and gas industry, it can also be used to calculate CO_2 solubility in brine. It is an effective tool for modelling CO_2 solubility as, unlike most geochemical models, HydraFLASH allows the user to change the EoS used. This is important as some EoS are more suited than others when calculating CO_2 solubility in brine. The EoS available are Soave-Relich-Kwong (SRK), Peng-Robinson (PR), Valderrama–Patel–Teja (VPT), Perturbed Chain form of the Statistical Associating Fluid Theory (PC-SAFT) and Simplified Cubic Plus Association (sCPA) [147].

The SRK EoS was developed in 1972 and was a modification of the Van der Waals (VdW) EoS [148]. Until this point all modifications concerning the VdW EoS looked at how the attractive parameter '$\boldsymbol{a}$' was dependant on temperature. Soave further expanded this by proposing that '$\boldsymbol{a}$' had in fact two variable dependencies, where:

$$\mathbf{a} = \mathbf{a(T, \omega)} \tag{4.1}$$

Therefore '**a**' is not only dependant on temperature, T, but also on the Pitzer acentric factor, ω, which is a measure of the sphericity (shape) and configuration of the molecule. The SRK EoS is used for predictions involving polar systems and is expressed as:

$$\left(\mathbf{P} + \frac{\mathbf{a}}{\tilde{\mathbf{v}}(\tilde{\mathbf{v}}+\mathbf{b})}\right)(\tilde{\mathbf{v}}-\mathbf{b}) = \mathbf{RT} \tag{4.2}$$

Where P is pressure, R is the ideal gas constant and T is the temperature. In addition, $\tilde{\mathbf{v}}$ is the molar volume, **a** is the attractive parameter and **b** is the repulsive parameter.

This PR EoS was developed in 1976 and is very similar to the SRK EoS [148]. In fact, in terms of performance, both EoS are of similar calibre, with the PR EoS working slightly better at the critical point. This makes the PR EoS more effective with regards to vapor-liquid equilibrium, whereas the SRK EOS works better with polar systems. The PR EoS is described as:

$$\left(\mathbf{P}+\frac{\mathbf{a}}{\tilde{\mathbf{v}}^2+\mathbf{2b}\tilde{\mathbf{v}}-\mathbf{b}^2}\right)(\tilde{\mathbf{v}}-\mathbf{b})=\mathbf{RT} \tag{4.3}$$

As with the SRK EoS, P is pressure, R is the gas constant, T is the temperature, $\tilde{\mathbf{v}}$ is the molar volume, **a** is the attractive parameter and **b** is the repulsive parameter. As can be seen from the EoS above, it retains the dependency of the attractive term on both the temperature and acentric factor, which was introduced by Soave. The only difference is that both models present different fitting parameters that are used to describe said dependency. The PR EoS is used by PHREEQC [143].

The VPT Equation of State (EoS) is a general phase equilibrium model which is based upon fugacity equality for each component in all phases [149]. The VPT EoS, used alongside non-density dependant (NDD) mixing rules, is used for modelling fluid phases. The combination of the VPT EoS and the NDD mixing rules results in an effective tool for modelling systems containing polar and non-polar compounds i.e. water and CO_2 systems. The VPT EOS is described as:

$$\mathbf{P}=\frac{\mathbf{RT}}{\mathbf{v-b}}-\frac{\mathbf{a}}{\mathbf{v(v+b)+c(v-b)}} \tag{4.4}$$

Where P is pressure, R is the gas constant and T is the temperature. Furthermore, **v** is the molar volume, **a** is the attractive parameter, **b** is the repulsive parameter and **c** is the parameter of the EoS.

The PC-SAFT EoS is an extension of the higher-order SAFT EoS that was developed by Gross and Sadowski [150, 151]. The SAFT models are based upon first-order perturbation theory proposed by Wertheim, which states that the potential energy related to relative complex molecular fluids can be described as the sum of both the potential energy of a reference fluid and a correction or perturbation term [152]. In most cases the challenge is

describing the perturbation term as the first term is generally known to a high degree of accuracy. Upon developing an appropriate perturbation term, standard thermodynamic expressions can be used to calculate the remainder of the thermodynamic properties. The perturbation term is typically a function of pressure, temperature or density and composition.

The SAFT and PC-SAFT EoS are expressed as the sum of the residual Helmholtz free energy terms that are a by-product of the different kinds of molecular interactions that occur within the system [152]. The residual Helmholtz free energy is described as the difference between the Helmholtz free energy and the Helmholtz free energy of the ideal gas (at the equivalent density and temperature). The only difference between these two EoS is that they use different reference fluids. For instance, a hard-sphere reference fluid is used for SAFT, whereas it is a hard-chain reference fluid that is used for PC-SAFT. This results in a difference in the functional forms of both models. Both EoS can be accurately used to model complex CO_2 mixtures, for example those containing ionic liquids and amines.

The sCPA is a non-cubic EoS that, like the aforementioned SAFT EoS, is based on the perturbation theory [153]. The sCPA EoS consists of two terms, the first is the SRK EoS (used to describe physical interactions) and the second is a chemical expression by Wertheim (used to model hydrogen bonding compounds). The fact that the model has both a cubic and association term is what gives the sCPA EoS its name. The sCPA EoS is most effective when used on non-polar and only slightly polar systems. It also works well for a few hydrogen bonding systems. In addition, the sCPA EoS can achieve excellent correlation for binary systems such as water/alkanes, water/methanol, methanol/alkanes and methanol (or water)/gases [154]. This results in the sCPA EoS being extremely versatile and is used in many gas processing, reservoir fluids and flow assurance studies.

4.1.3 Duan and Sun CO_2 solubility model

The Duan and Sun CO_2 solubility model is a thermodynamic model which was first developed to calculate CO_2 solubility in both pure water and NaCl(aq) solutions in the temperature range of 273K to 533K, pressure range from 0 to 2000bar and an ionic strength ranging from 0 to 4.5m [64]. This model was then improved so that it could be used to calculate CO_2 solubility in aqueous solutions which contained, N^+, K^+, Mg^{2+},

Ca^{2+}, SO^{2-}_4 and Cl^- [65]. It also improved the model's ability to calculate CO_2 solubility in pure water as well as in NaCl(aq) solutions.

The Duan and Sun model is unique in that it does not use any of the aforementioned EoS, since an EoS was developed specifically for the model [64, 65]. The EoS for CO_2 was originally developed by Duan at al. (1992) and was later used for the solubility model [155]. The EoS is described as:

$$\boldsymbol{Z} = \frac{P_r V_r}{T_r} = \mathbf{1} + \frac{a_1 + a_2/T_r^2 + a_3/T_r^3}{V_r} + \frac{a_4 + a_5/T_r^2 + a_6/T_r^3}{{V_r}^2} + \frac{a_7 + a_8/T_r^2 + a_9/T_r^3}{{V_r}^4} + \frac{a_{10} + a_{11}/T_r^2 + a_{12}/T_r^3}{{V_r}^5} + \frac{a_{13}}{T_r^3 V_r^2}\left(a_{14} + \frac{a_{15}}{V_r^2}\right) exp\left(-\frac{a_{15}}{V_r^2}\right) \quad (4.5)$$

Where $\mathbf{P_r}$, $\mathbf{V_r}$ and $\mathbf{T_r}$ are the reduced pressure, volume and temperature respectively. $\mathbf{a_1}$-$\mathbf{a_{15}}$ are specific parameters, the values of which are given in Duan and Sun (2003) [64]. Having its own EoS, specifically designed to calculate CO_2 solubility, is the reason why the model is so widely used and why the vast majority of experimental results are compared with those produced from this model. It would be more appropriate to compare experiments results with other experimental results and not rely on a model for validation, as this is bad practice. However, this is problematic, because as stated throughout the literature review, the difficulties in measuring CO_2 solubility under reservoir conditions has lead to inconsistencies in experimental data, even under the same experimental conditions (pressure/temperature/salinity). This makes validating experimental results with previous experimental results in many cases, impractical.

The Duan and Sun model is more accurate when looking at CO_2 and pure water systems, as well as CO_2-water-salt systems, which is shown in the next section. However, the model can fail at high pressures and temperatures when looking at CO_2-water-salt systems, as there is only limited data for NaCl under these conditions and no data on other salts. Furthermore, for the CO_2-brine systems, the model looks at the overall salinity of the brine rather than the actual brine composition. If the user is interested in the actual brine composition, then the updated model by Duan et al. (2006), can be used [65]. However, it only allows for the input of Na^+, K^+, Mg^{2+}, Ca^{2+}, Cl^- and SO_4^{2-} concentrations and not other common brine ions, such as Sr^{2+}, Ba^{2+} and Fe^{3+}. Therefore, if it is necessary for the complete brine composition to be considered, then geochemical software such as PHREEQC and HydraFLASH need to be used. How the geochemical models compare under different conditions is described in the following section.

4.2 Calculating CO_2 solubility in brine

This section provides a detailed description on how to use both HydraFLASH and PHREEQC to measure CO_2 solubility in brine (Objective 1). This section also discusses the impact of choosing the correct EoS and compares the experimental methods for measuring CO_2 solubility, described in Section 2.6, with those values calculated through geochemical modelling.

4.2.1 Modelling with HydraFLASH

As described in Section 4.1.2, HydraFLASH is a PVT and thermodynamic prediction software. Although it allows for complex modelling, it is very user friendly. The first step is to select VPT under the [EoS] tab. The importance of choosing the correct EoS for CO_2 solubility in brine calculations is discussed in the following section. Once the correct EoS has been selected, CO_2 has to be set as the dry fluid and the composition of the brine needs to be input. This is done under the [Composition Management] tab. The [Dry Fluid] tab is then used to select CO_2 and the [Polar Phase] tab is used to input the brine composition. This tab allows the user to select the required salts from the list and add the weight % of each salt in the water. When using HydraFLASH, the concentration of Fe^{3+} ions present in the brine cannot be taken into account, as HydraFLASH does not have any iron based salts in its database. However, as can be seen in Table 3.1 the highest Fe^{3+} concentration is in Brine 1 which is only 12 mg/l whereas the concentration in the rest of the brines ranges from 2-6 mg/l. Consequently, Fe^{3+} is unlikely to have any discernible effect on the CO_2 solubility calculations. An example of how to calculate the weight % of salt to be added is shown in Box 4.1.

Box 4.1: Example calculation for weight % of salt

Example: Target ion concentration of Ca^{2+} = 639 mg/l

Ca Molecular Weight = 40.08 g/mol

$CaCl_2$ Molecular Weight = 110.98 g/mol

Mass of $CaCl_2$ needed = $\frac{110.98\ g/mol}{40.08\ g/mol} \times 639\ mg/l \times \frac{1l}{1000} = 1.77g$

Total mass of all salts added = 26.04g

Weight % of $CaCl_2$ = $\left(\frac{1.77g}{(26.04g+1000g)}\right) \times 100 = 0.172$

Once each salt has been added, the [PVT] tab is selected followed by the [PT Flash] tab which will allow for the experimental conditions to be input and the solubility calculations

to be performed. The temperature (Kelvin) and pressure (MPa) can now be entered and the calculations are performed by pressing [Run Calculation]. The output file contains a lot of information such as the density of the vapour and polar phases, the compressibility, enthalpy and entropy etc. However, for this work the only information of concern is the polar composition which provides the user with the amount of CO_2 dissolved in the water as a fraction. This value can then be converted to mol/kg of dissolved CO_2 and furthermore into grams of dissolved CO_2 if the density of the brine is known.

However, the density of the brine increases with pressure and decreases with temperature and most experimental brine density data is available only at ambient conditions [156, 157]. This is due to the difficulties measuring brine density under reservoir conditions. Recent work by Ghafri et al. (2012) and Ghafri et al. (2013) has looked to experimentally measure densities of both aqueous solutions and synthetic brines at temperatures between 283 and 472K, pressures up to 68.5 MPa and molalities up to 6 mol/kg [156, 157]. To do this they used apparatus that consisted of a high-pressure vibrating tube densimeter that was fitted with a thermostat to control the temperature [156]. The temperature readings were verified using a second temperature sensor, located within a thermowell in the cellblock. The experimental measurements were displayed on a master instrument that was connected to the denismeter and the brine was injected using a syringe pump which had a pressure transducer installed to measure the pressure. The pump and the densimeter were connected by Hastelloy C-276 tubing which is highly chemical resistant.

Through their work the authors managed to create a model that would predict the density of synthetic brines at reservoir conditions under the assumption that at specific pressure, temperature and molality the excess molar volume of the solution was zero. Under these conditions the density of the brine is related to the densities of each of the electrolyte solutions from which it is formed by the equation:

$$\rho_m(p,T,b) = \frac{[\sum_i x_i(1+bM_i)]}{[\sum_i\{x_i(1+bM_i)/\rho_i(p,T,b)\}]} \tag{4.6}$$

where x_i, M_i, and ρ_i are the mole fraction of electrolyte i in the brine, the molar mass of the salt i and the density of the individual electrolyte solution under the pressure (p), temperature (T) and molality (b) of the brine, respectively. This equation was compared with the experimental results and it was shown that they were in agreement of ± 0.05% and hence showed the validity of the model.

In this work, the density of the brine could not be experimentally measured under reservoir conditions due to not having access to the specialised equipment required. Furthermore, Equation 4.6 could not be used either as even though the pressure, temperature and molality was known for each brine, the density of the individual electrolyte solutions could not be calculated without first knowing the period of oscillation τ which requires a densimeter to measure. Therefore, the density of each brine under reservoir conditions was extrapolated from the results for the synthetic brines in Ghafri et al. (2013) [157].

Table 5 in Ghafri et al. (2013) shows the density measurements for two different synthetic brines (one at 0.359 mol/kg and the other at 1.900 mol/kg) [157]. From the table, increases in pressure and temperature result in similar increases/decreases in brine density regardless of the molality i.e. every time the pressure is increased by 100 bar the brine density for both the 0.359 mol/kg brine and the 1.900 mol/kg increases by approximately 3-4 kg/m^3. Taking the 0.359 mol/kg brine, as it has a salinity close to the salinity of the brines in this work (24832 mg/l compared with see Table 3.1), the results from Table 5 in Ghafri et al. (2013) can be used to extrapolate the density of the brine under the reservoir conditions of this work (24.6 MPa and 385.15K).

This is done by creating graphs of both pressure versus density and temperature versus density and using the gradient of the slopes to work out the density values at 24.6 MPa and 385.15K. For example, Figure 4.1 shows the pressure versus density at 373.12K and 398.08K as well as the temperature versus density at 20.10 MPa and 30.10 MPa. From Figure 4.1 the relationships between density and both pressure and temperature are clear.

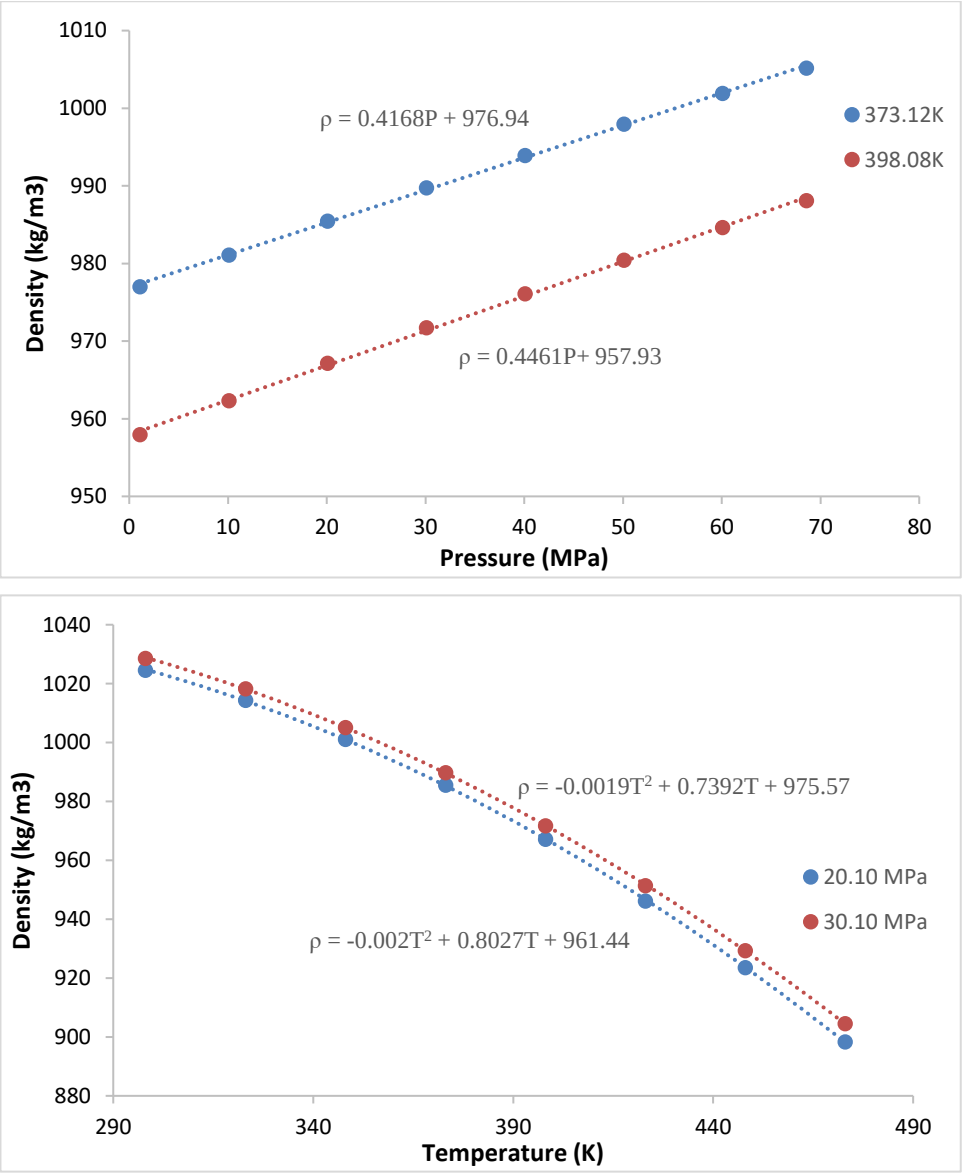

Figure 4.1: Density of brine with increasing pressure (top) and increasing temperature (bottom) [157]

Once the density has been determined at 24.6 MPa at each temperature in Table 5 of Ghafri et al. (2013), a final graph of temperature versus density can be created and the gradient of the slope can be used to determine the density at both 24.6 MPa and 385.15K (see Figure 4.2). Knowing the density of the 0.359 mol/kg brine at 24.6 MPa and 385.15K means that the density of the brines in this work under reservoir conditions can be roughly extrapolated. It should be noted that this is an estimate, which will give an indication to what the brine density will be under reservoir conditions, since the density cannot be measured experimentally or using Equation 4.6.

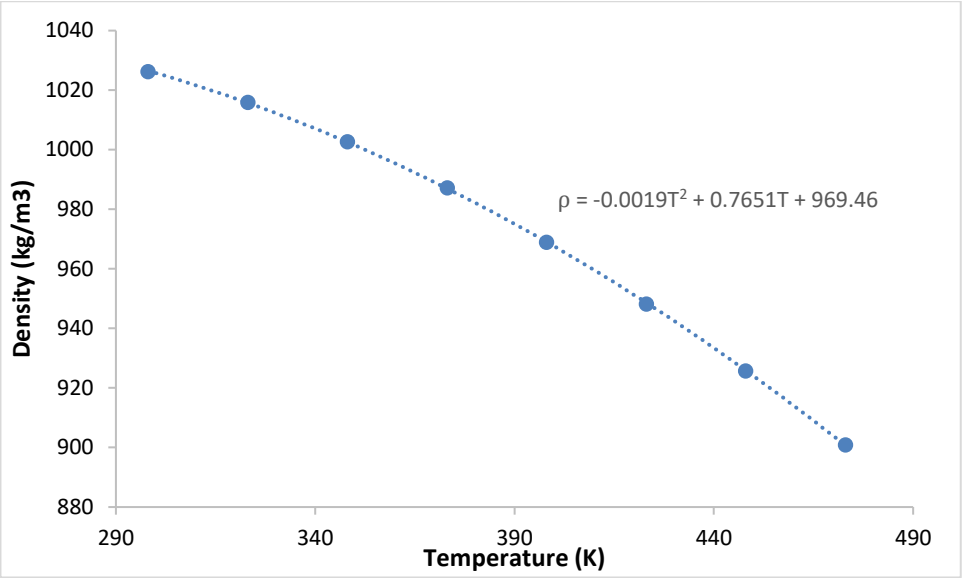

Figure 4.2: Density of brine with increasing temperature at 24.6 MPa

To do this the density of the brine is first calculated under ambient conditions by weighing the 1 litre volumetric flask without brine, using an A&D FX-2000i scale, and then weighing it again with 1 litre of brine in it. The difference between the two measurements gives the weight of the brine and hence the density under ambient conditions. The error associated with weighing the flask is ±0.02g. This value is then compared with the density of the 0.359 mol/kg brine under ambient conditions and the difference is added to the density of the 0.359 mol/kg brine under reservoir conditions. See Box 4.2 for an example of how to calculate the brine density under reservoir conditions and use it to convert the CO_2 solubility from mol/kg to g/mol.

Box 4.2: Example calculation for converting water fraction into mol/kg and grams

Example: Polar Composition: CO_2 = 0.020727, Water = 0.979273

Molecular Weight of Water = 18 g/mol

Dissolved CO_2 (mol/kg) = $\left(\frac{0.020727}{(0.979273 \text{ x } 18\text{g/mol})}\right)$ x 1000 = 1.176 mol/kg

Density of Brine 1 (STP) = 1.0153 kg/l

Density of 0.359 mol/kg brine (STP) = 1.0164 kg/l

Density of 0.359 mol/kg brine (reservoir) = 0.9823 kg/l

Density of Brine 1 (reservoir) = (1.0164 – 1.0153) + 0.9823 = 0.9834 kg/l

Molecular Weight of CO_2 = 44 g/mol

Dissolved CO_2 in 1 litre of Brine 1 = $1.176 \frac{\text{mol}}{\text{kg}} \times 0.9834 \frac{\text{kg}}{\text{l}} \times 44 \frac{\text{g}}{\text{mol}} \times 1\text{l} = 50.89\text{g}$

4.2.2 Choosing an appropriate EoS

As described in Section 4.1.2, there is a variety of EoS that HydraFLASH can use to calculate CO_2 solubility. CO_2 solubility in brine is a system containing polar and non-polar compounds [158]. Accordingly, the most appropriate EoS for systems containing polar and non-polar compounds is the VPT EoS [149]. Therefore, the VPT EoS should be the most suitable EoS for measuring CO_2 solubility in brine, when no hydrocarbons are present, which will be confirmed in this section.

Figures 4.3 and 4.4 show the results obtained when using different EoS and how they compare with the corresponding experimental work. They were produced by inputting the pressure, temperature and salinity data from Yan et al. (2011) and Li et al. (2004), described in Section 2.6, into HydraFLASH and running the software. This was done five times, for each data set, keeping all the conditions constant and only altering the EoS used.

Figure 4.1 includes the results from Yan et al. (2011), where CO_2 solubility was measured in a CO_2-H_2O-NCl (1M) system at 323.2K under varying pressures [94]. The results from the five different EoS that HydraFLASH can use are also present in the figure. The result from the Duan and Sun CO2 solubility model and PHREEQC are also included and will be discussed in Section 4.2.4. Figure 4.3 shows that at low pressures it is difficult to distinguish between the different EoS. However, as the pressure increases, the VPT results separate themselves from the rest and are comparable to the experimental results provided by Yan et al. (2011) [94]. From Equation 4.4, the VPT EoS has an additional pressure dependent ‘c’ term which the other EoS, such as the SRK (Equation 4.2) and PR (Equation 4.3), do not. This is likely why there is a larger difference between the VPT results and those from the other EoS at higher pressures.

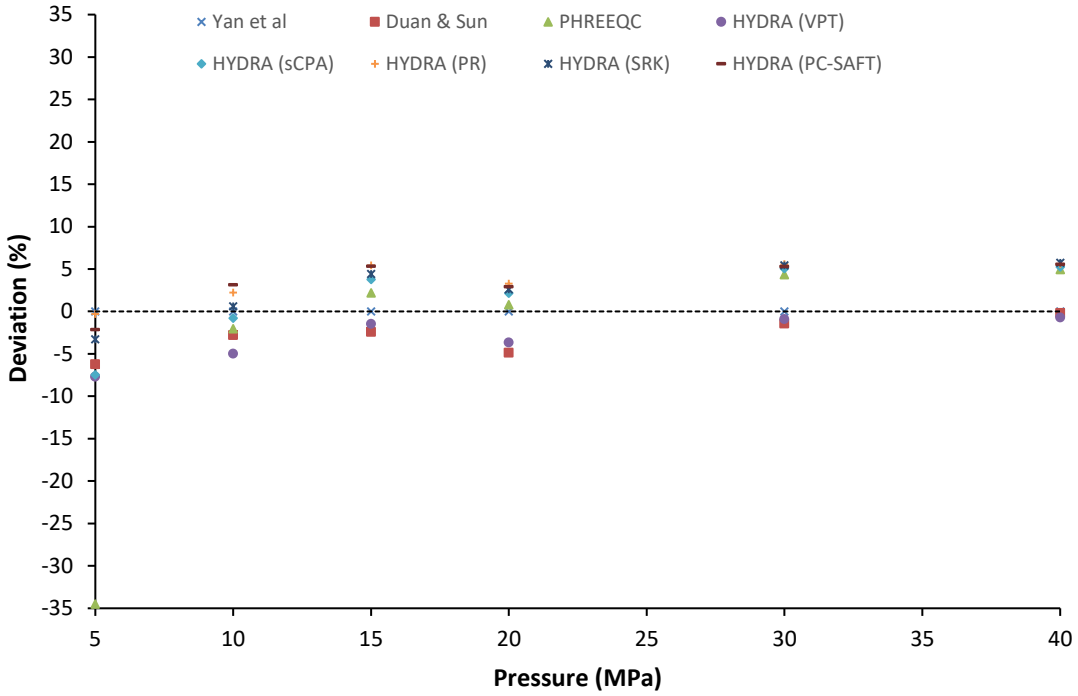

Figure 4.3: CO_2 solubility for CO_2-H_2O-NCl (1M) system at 323.2K experimental and modelling results [94]

The same trend can be seen in Figure 4.4, which compares the modelling results with those obtained by Li et al. (2004) [67]. This system included CO_2 and brine from the Weyburn reservoir in Canada. In this case, the pressure was varied under a constant temperature of 332.15K. The results from the Duan et al. (2006) CO_2 solubility model are included along with PHREEQC and will be discussed in Section 4.2.4. As with Figure 4.3, the results are difficult to distinguish between at low pressures, but as the pressure increases it is clear that the VPT results are in agreement with those from the experimental work. The results from these two figures confirm that when considering systems containing polar and non-polar compounds, such as CO_2 and brine, the VPT is the superior EoS.

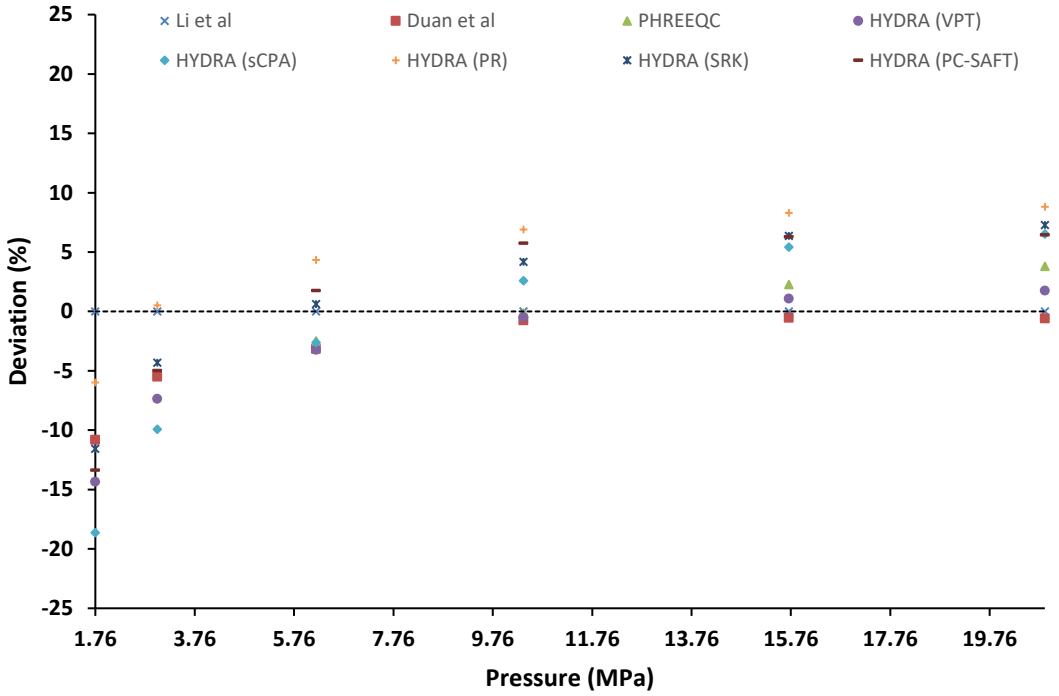

Figure 4.4: CO_2 Solubility for CO_2-Weyburn brine at 332.15K experimental and modelling results [67]

4.2.3 Modelling with PHREEQC (CO_2 solubility calculations)

For the experiments that looked at how brine composition affects geochemical trapping potentials and the importance of well selection within an oil field, the PHREEQC input files only required information on the pressure, temperature, pH and brine composition. Figure 4.5 shows the input file using Brine 1 (Table 3.1) as an example. The pressure and temperature have been set to 246 bar and 112ºC respectively, which are the reservoir conditions for the North Sea oil field in question. The concentrations of the brine ions are in ppm. The pH value of 10.77 corresponds to the pH after the KOH buffer has been added to promote mineral trapping through the production of CO_3^{2-} ions. The K (potassium) value in the input file has been corrected for the additional K added as a result of the KOH buffer.

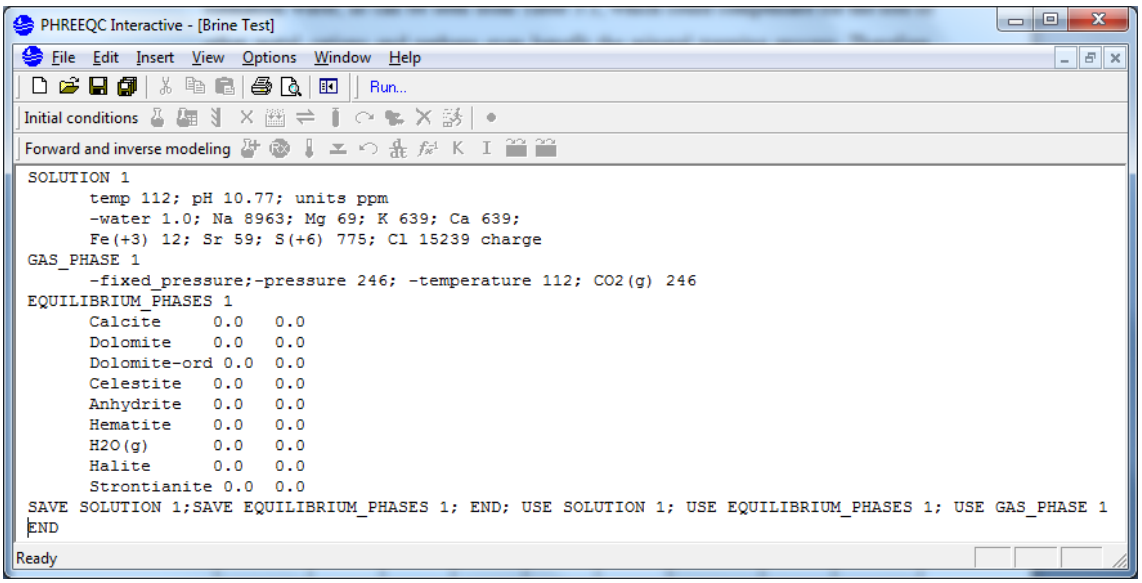

Figure 4.5: PHREEQC input file for Brine 1

The three keywords used are SOLUTION, GAS_PHASE and EQUILIBRIUM_PHASES. SOLUTION defines the chemical composition, pH and temperature of the initial solution [143]. GAS_PHASE defines the composition of a fixed volume multi-component or fixed total pressure gas phase (CO_2 for the purpose of this study). EQUILIBRIUM_PHASES relates to mineral trapping and is described in Section 4.4.1. Finally, before the calculations can be run, an appropriate database file has to be selected. In this case, the pitzer.dat database was chosen as Pitzer equations can be used to provide accurate measurements in high-ionic strength systems such as brines, unlike the Debye-Hückel and Davies equations [74].

The output files generated by PHREEQC contain information on the change in pH of the brine, the total amount of dissolved carbon and variations in the solution composition. Since mineral trapping potentials are highly dependent on brine pH it is important to record any variations in pH. The total dissolved carbon can be used to measure CO_2 solubility in brine and variations in the original solution composition can be used to measure mineral trapping potentials.

4.2.4 Comparison of the geochemical models

Section 4.1 discussed three different geochemical models that can be used to measure CO_2 solubility in brine, namely PHREEQC, HydraFLASH and the Duan and Sun CO_2 solubility model. Figures 4.3 and 4.4 also included the results from the Duan and Sun CO2 solubility model and PHREEQC to provide a comparison between the different geochemical models.

Figure 4.3 shows the experimental results of Yan et al. (2011) alongside the results from the Duan and Sun CO_2 solubility model, PHREEQC and HydraFLASH [94]. In Section 4.1.3 it was stated that since the Duan and Sun model uses an EoS specifically designed to measure CO_2 solubility, in CO_2-water and CO_2-water-salt systems, it should produce more accurate results when looking at these systems. This can be seen in Figure 4.3, as with increasing pressure, the CO_2 solubility results are in agreement with those of the experimental work. It is, however, very difficult to distinguish between the results from the Duan and Sun model and those from the HydraFLASH model, when using the VPT EoS. This shows the merits of using the HydraFLASH model when the correct EoS is selected. The results from PHREEQC on the other hand, do follow the correct trend. However, the accuracy of the results is lower than that of the other two models. This is due to the fact that not only does it use the PR EoS, which, as previously stated, is designed for gas/condensate systems, it also ignores complex ion exchange models, does not take into account uncertainties in thermodynamic constants and makes simplified assumptions related to steady-state flow [144]. Despite these challenges, PHREEQC can still be used to show trends and is useful for those who require easy to use geochemical modelling software.

The online CO_2 solubility calculator by Duan and Sun cannot be used for the Li et al. (2004) system, as it only allows for the total salinity of the brine to be inputted instead of the actual brine composition i.e. concentration of Ca^{2+}, Mg^{2+}, K^{+} ions. However, the updated model, which is based on the solubility model developed by Duan and Sun (2003), by Duan et al.(2006) can be used. As described in Section 4.1.3, the updated model can be used to input the concentrations of a limited number of brine ions. In this case, Li et al. (2004) only provided information on the concentrations of the brine ions that the Duan et al. (2006) model can use i.e. there was no information on Sr^{2+}, Ba^{2+} or Fe^{3+} concentrations. Therefore, Figure 4.4 compares the experimental results to those obtained using PHREEQC, HydraFLASH and the Duan et al.(2006) model. In this case, the gap between the PHREEQC results and those of both the other models and the experimental work is relatively small at higher pressures. Once again, the results produced by HydraFLASH and Duan et al. (2006) are very similar to the experimental results.

In this section the work by Li et al. (2004) and Yan et al. (2011) has been compared to the results obtained through geochemical modelling. Both sets of results appear to be in good agreement with those of the modelling work. However, in both methods the

experimental results do not correspond with those of the geochemical modelling at low pressures (as can be seen in Figures 4.3-4.4). Careful analysis of Figures 4.3-4.4 shows that the experimental results of Yan et al. (2011) are in better agreement with the modelling results than those of Li et al. (2004). The reason for this was provided in Section 2.6.4 where it was stated that Yan et al (2011) did not use the data produced by Li et al. (2004) when creating their review of previous experimental data, due to the authors neglecting to take into account dissolved CO_2 contained within the aqueous solution at atmospheric pressure [94]. Therefore, it can be concluded that the experimental method developed by Yan et al. (2011) is more accurate at measuring CO_2 solubility than the one developed by Li et al. (2004).

4.2.5 Experimental method performance

In the summary of Section 2.6, it was stated that the work by both Tong et al. (2013) and Hou et al. (2013) seemed to be the most accurate at measuring CO_2 solubility in brine under reservoir conditions. This is a result of the different approach that each method has taken with respect to previous work. For instance, Tong et al. (2013) looked to eliminate the complications that arise from phase sampling and analysis by employing a method based upon visual observation, alongside quantitative measurements of pressure, temperature and composition [98]. The method developed by Hou et al. (2013) on the other hand, is the first to provide coexisting liquid and vapour phase compositional data, which is likely to lead to more accurate results as all components are taken into account, not just the liquid-phase data [91]. This section reviews the results obtained by both Tong et al. (2013) and Hou et al. (2013) and how they compare with previous work and the results obtained through geochemical modelling.

Figure 4.6 shows CO_2 solubility in a CO_2-water system at 373.15K under varying pressures. The results included are those presented by both Tong et al. (2013) and Hou et al. (2013) and compared with the results obtained when the experimental conditions were input into the Duan et al. (2006) model, PHRREQC and HydraFLASH (VPT), as well as previous experimental work by Wiebe et al. (1939) and Prutton et al. (1945) [98, 90, 88, 99]. There are only two data points included for Hou et al. (2013) as those are the only data available under these conditions. However, it can be seen from Figure 4.7 that both these data points are almost identical to the results obtained by Tong et al. (2013) and so it is likely they would follow the same trend at increasing pressures. It should be noted that the work by both Tong et al. (2013) and Hou et al. (2013) are in very good agreement with the Duan and Sun solubility model, but unlike with the work by Li et al. (2004) and

Yan et al. (2011), the results by Tong et al. (2013) and Hou et al. (2013) are also in good agreement with the Duan et al. (2006) model at low pressures. Figure 4.6 also compares the results from Tong et al. (2013) with those of the three geochemical models discussed in this paper. Since this is just a CO_2-water system, although all the modelling results are in good agreement with those of the experimental work (within ±1-7%), the results from the Duan and Sun model show very little deviation (within ±1%) from those of Tong et al. (2013).

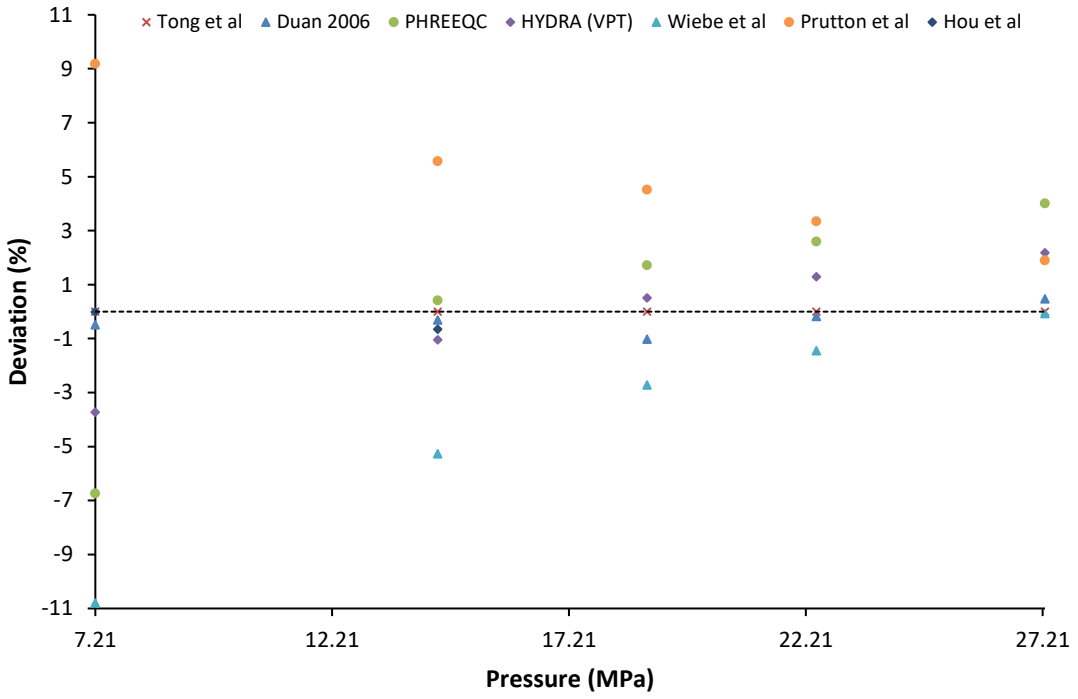

Figure 4.6: CO_2 solubility for CO_2+water system at 373.15K experimental and modelling results [98]

Section 2.6.8 described how the Tong et al. (2013) method was used to measure CO_2 solubility in aqueous solutions of $CaCl_2$ and $MgCl_2$ and successfully expanded the knowledge on how CO_2 solubility is affected by pressure, temperature and salinity in these aqueous solutions [98]. Consequently, Figure 4.7 shows the CO_2 solubility in $CaCl_2$ aqueous solution at 1M and 3M under varying pressures at 375K. The results are compared with the Duan et al. (2006) model, HydraFLASH (VPT) and PHREEQC. From Figure 4.7 it can be seen that the Duan et al. (2006) model is in very good agreement with Tong et al. (2013) at lower salinity (1M) but struggles at higher salinities (3M). This is due to the limited solubility data that the model has at higher salinities. Although HydraFLASH (VPT) deviates more from the experimental results at lower salinity more

than the Duan et al. (2006) model, when the salinity increases to 3M, the HydraFLASH results are still within 5% of Tong et al. (2013) at higher pressures.

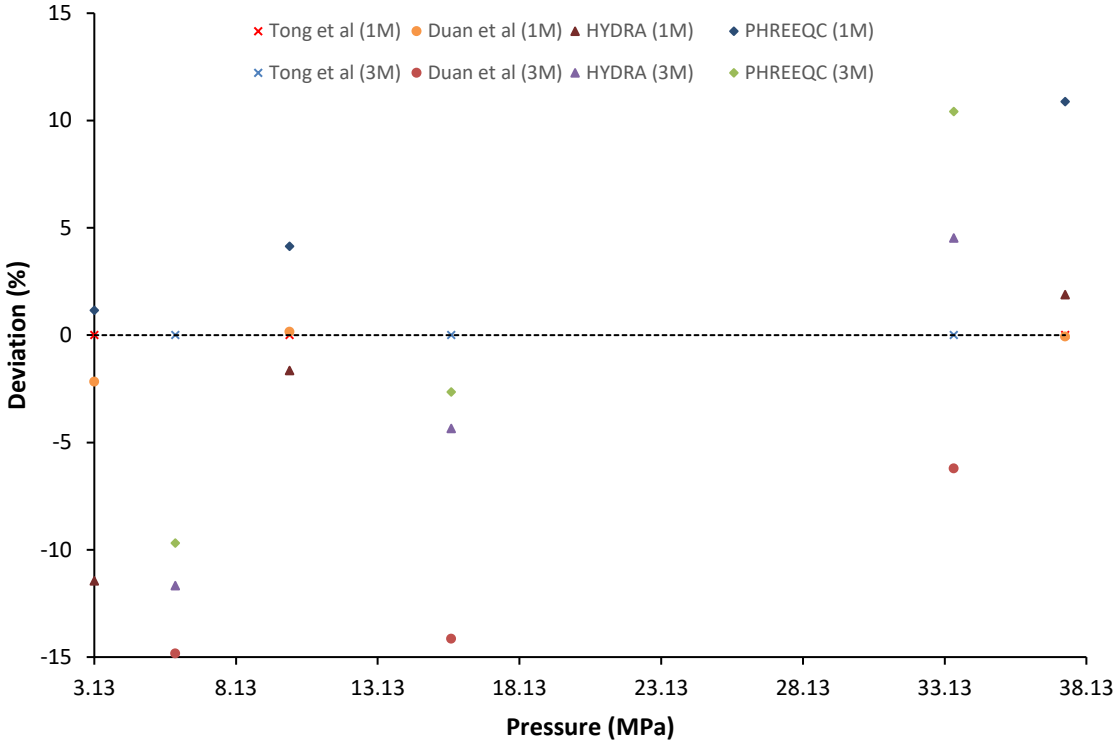

Figure 4.7: CO_2 solubility in 1M and 3M $CaCl_2$ aqueous solutions at 375K experimental and modelling results [98]

Figure 4.8 describes the CO_2 + water system at 373.15K under varying pressures, but for Hou et al. (2013), and in this case the experiments were run at different pressures and so a direct comparison with the Tong et al. (2013) data cannot be made. Once again, the experimental results are compared with those obtained through the three geochemical models discussed in this chapter. The experimental results reported by Hou et al. (2013) deviate more from the results produced through modelling, compared with those reported by Tong et al. (2013). However, the experiments performed by Hou et al. (2013) started at lower pressures (1.107MPa compared with 7.21MPa) and the difference between the experimental and modelling results decreases significantly as the pressure increases, from 13.24%, 6.99% and 26.19% at 1.107MPa, to 2.06%, 1.41% and 0.08% at 17.070MPa. These results correspond to those produced by the Duan et al. (2006) model, HydraFLASH and PHREEQC respectively. In fact, at similar pressures, the difference between the experimental results and those of the modelling is comparable for both Hou et al. (2013) and Tong et al. (2013).

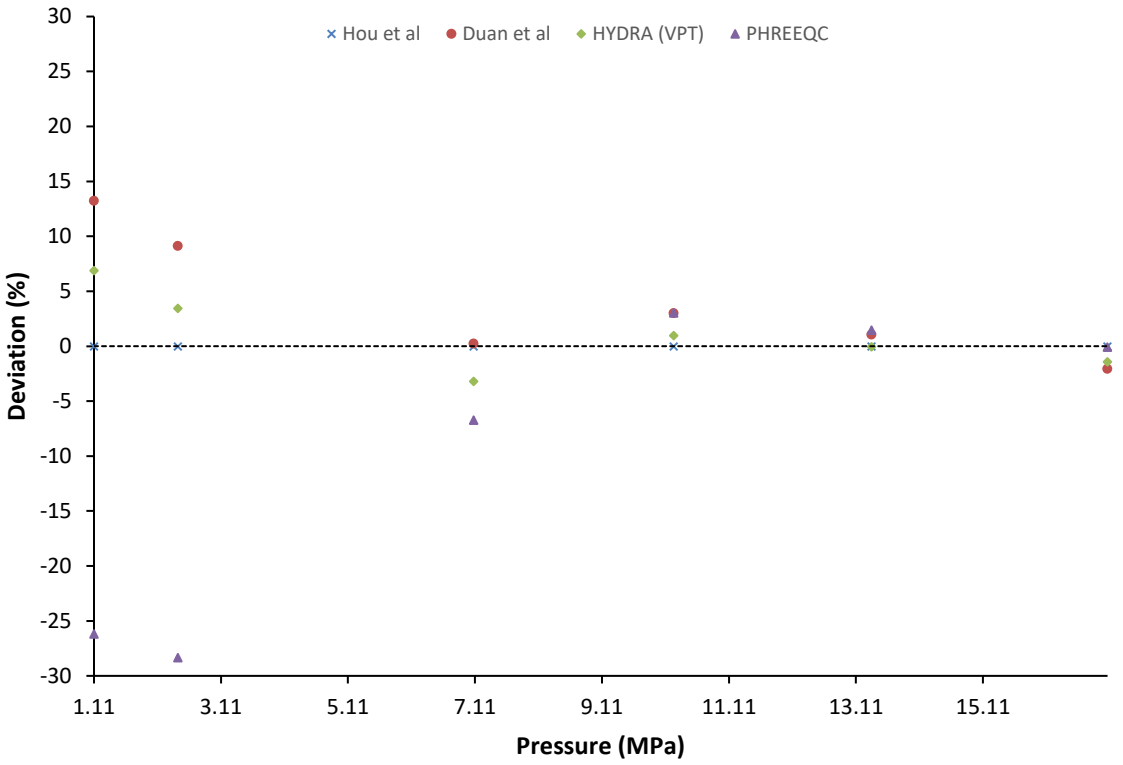

Figure 4.8: CO_2 solubility for CO_2+water system at 373.15K experimental and modelling results [91]

Furthermore, Hou et al. (2013) looked to expand the knowledge of CO_2 solubility in aqueous solutions of NaCl and KCl under varying salinities, temperatures and pressures. Figure 4.9 shows the CO_2 solubility in 2.5 M NaCl and KCl aqueous solutions under varying pressures at 423.15K. Once again, the results are compared with the Duan et al. (2006) model, HydraFLASH (VPT) and PHREEQC. In terms of how much the modelling results deviate from the experimental results, the deviations are very similar for NaCl and KCl, with the modelling results for NaCl deviating slightly less when compared with the Hou et al. (2013) results. This is likely due to there being a lot more data for the models on NaCl as there has been a lot of experimental work on CO_2 solubility in aqueous NaCl. At lower pressures the HydraFLASH (VPT) results are in better agreement with the experimental work but at higher pressures the Duan et al. (2006) model deviates by less than 5% for both NaCl and KCl.

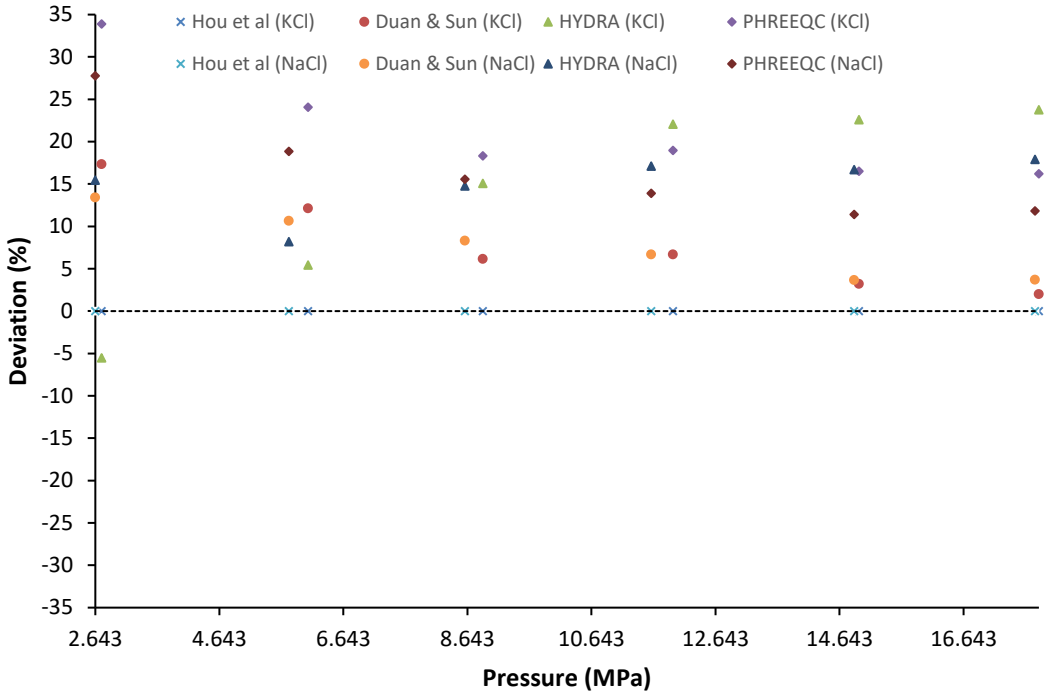

Figure 4.9: CO_2 solubility in 2.5M NaCL and KCl aqueous solutions at 423.15K experimental and modelling results [91]

It is clear that the experimental procedures developed by both Tong et al. (2013) and Hou et al. (2013) provide effective means of measuring CO_2 solubility under reservoir conditions. Not only are the results in very good agreement with those of the geochemical modelling, but unlike with some of the previous works, the results from both Tong et al. (2013) and Hou et al. (2013) are comparable with those obtained through modelling at low pressures as well. Furthermore, these methods have been used to measure CO_2 solubility in aqueous solutions of $CaCl_2$ and $MgCl_2$ (Tong et al. (2013)) as well as NaCl and KCl, at high molalities and pressures (Hou et al. (2013)), successfully expanding the knowledge on how CO_2 solubility is affected by pressure, temperature and salinity in these aqueous solutions [98, 91].

4.2.6 Software selection

In this chapter three geochemical modelling software's have been reviewed, namely PHREEQC, HydraFLASH and the Duan and Sun CO_2 solubility model. It was concluded that for systems including only CO_2 and water or CO_2, water and salt, the Duan and Sun model was the most accurate at calculating CO_2 solubility. This is mainly because it has an EoS designed specifically to perform CO_2 solubility calculations [155]. The updated version of the model, created by Duan et al. (2006) can be used to calculate CO_2 solubility in brine, but it is restricted by what ions are present. PHREEQC on the other hand is

simple to use, but it does not always accurately predict experimental results and is mainly used to show trends.

Finally, HydraFLASH was shown to be a very effective all round model, as it can match the accuracy of the Duan and Sun model in CO_2-water and CO_2-water-salt systems, and also has the ability to calculate CO_2 solubility in brine, without the restrictions of the Duan et al. (2006) model. The only requirement of HydraFLASH to produce accurate results that are in agreement with the experimental work is that the correct EoS is chosen. The importance of selecting the right EoS has also been discussed and it was concluded that for a system containing polar and non-polar compounds, such as CO_2 in water, the Valderrama–Patel–Teja EoS is the most effective [149].

Consequently, HydraFLASH was selected as the geochemical modelling software that would be used to measure CO_2 solubility in brine under reservoir conditions for this study. However, due to its inability to measure mineral trapping potentials, PHREEQC was chosen for this purpose. Although PHREEQC is mainly used to show trends, the mineral trapping potentials have already been experimentally measured, hence the results produced by PHREEQC will be sufficient as previous work has shown that it is viable for general geochemical modelling used to corroborate experimental results [74].

4.3 Calculating mineral trapping potentials

This section provides a detailed description on how to use PHREEQC to measure mineral trapping potentials in both CO_2-brine systems and CO_2-calcite-brine systems (Objective 1).

4.3.1 Modelling with PHREEQC (mineral trapping potentials)

Section 4.2.6 concluded that since HydraFLASH does not have the capability to measure mineral trapping potentials, PHREEQC will be used to corroborate the experimental results. The example input file shown in Figure 4.3 is used to measure both solubility and mineral trapping potentials. However, as stated in Section 4.2.3, the EQUILIBRIUM_PHASES keyword relates solely to mineral trapping. EQUILIBRIUM_PHASES defines the amount of pure phases that are able to react with the aqueous phase reversibly [143]. Anhydrite, calcite, celestite, dolomite, halite, hematite and strontianite were chosen as likely precipitates and by including them in the EQUILIBRIUM_PHASES keyword, it means that the output file will provide information on whether they have precipitated or not. For the purpose of calculating mineral trapping potentials, the Lawrence Livermore National Laboratory database

(llnl.dat) was chosen over pitzer.dat as it contains the most complete set of mineral species, as well as expressions used to calculate equilibrium conditions at temperatures ranging from 0-300°C [18].

When adding calcite to the system, which is required for the CO_2-brine-calcite experiments, two additional keywords are used; KINETIC and RATES. KINETIC is used to identify kinetic reactions as well as specify reaction parameters for both transport calculations and batch-reactions [143]. The rates of these kinetic reactions are then provided with mathematical expressions through the RATES keyword. Consequently, the rate law for calcite must be provided in the input file. There are three mechanisms that control the rate of dissolution of calcite and these were recognised by Plummer et al. (1978) and Rickard and Sjöberg (1983) [159, 160]. The first occurs at low pH (<3.5) and is governed by transport controlled kinetics, whereby the rate of dissolution is pH dependent but is unaffected by ionic strength. The second mechanism comes into effect at 3.5<pH<5.5, where the transitional regime is controlled by diffusion. The final mechanism (pH>5.5) is governed by surface chemical reactions and transport process and is the reverse of the first mechanism, whereby the rate of dissolution is dependent on ionic strength but pH independent.

As noted above, the dissolution and precipitation of calcite is dependent on pH and there are three reversible reactions that can take place depending on pH [74]. Equations 4.7-4.9 show these reactions and are presented below.

$$CaCO_3+H^+ \leftrightarrow Ca^{2+}+HCO_3^- \tag{4.7}$$

$$CaCO_3+H_2CO_3^* \leftrightarrow Ca^{2+}+2HCO_3^- \tag{4.8}$$

$$CaCO_3+H_2O \leftrightarrow Ca^{2+}+HCO_3^-+OH^- \tag{4.9}$$

The first reaction (4.7) occurs at pH<3.5, the second (4.8) at 3.5<pH<5.5 and the final reaction (4.9) occurs at pH>5.5 [74]. In Equation 4.8, $H_2CO_3^*$ represents the sum of the concentrations of dissolved CO_2 (aq) and carbonic acid, H_2CO_3. The rate law for calcite can be expressed as:

$$R_{calcite} \approx r_f \left(1-(SR_{calcite})^{\frac{2}{3}}\right) \times \frac{A_0}{V} \times \left(\frac{m}{m_0}\right)^{\frac{2}{3}} \tag{4.10}$$

Where SR is the saturation ratio for calcite which is defined in the PHREEQC database, A_0 is the surface area which is taken from the BET analysis of the calcite powder (m^2), V

is the volume of the brine (m^3), m is the moles of calcite at a given time and m_0 is the initial moles of calcite. Finally, r_f is the sum of the three individual rates for the reactions shown in Equations 4.7-4.9.

$$r_f = k_1[H^+] + k_2[H_2CO_3^*] + k_3[H_2O] \quad (4.11)$$

Where $[H^+]$, $[H_2CO_3^*]$ and $[H_2O]$ are the corresponding activities and k_1, k_2 and k_3 are temperature dependent (T_K) coefficients that have been previously determined by Plummer et al.(1978) and are defined below [159].

$$\log k_i = \frac{a_i}{T_K} \quad (4.12)$$

Where, i = 1,2,3 and a_1 = -443.802, a_2 = -2174.16 and a_3 = -1735.9. The rate law for calcite is included in the input file below (Figure 4.10) which shows an example using 60 ml of Brine 1 (Table 3.1) and 6g of calcite powder ground to a particle size of 75-150µm, with a measured surface area, using BET, of 1.3837m^2/g. The temperature and pressure are the same as the experimental conditions (112ºC and 246 bar) and the pH is the measured pH of the brine after the calcite is added which was 5.72.

Calcite dissolution rates have recently been measured under reservoir conditions by Peng et al. (2015) where they have shown that the dissolution rate of calcite increases with increasing pressure and temperature [161]. In addition, separate work by Peng et al. (2016) showed that under reservoir conditions, not only is the effect of high salinity on calcite dissolution kinetics small, but if the reactive surface area of the rock has been quantified, then the results obtained during studies involving pure calcite can be used to determine dissolution rates of calcite-rich minerals [162]. This is an important conclusion as the results from the CO_2-calcite-brine experiments performed in this work can be considered analogous to what could be expected when CO_2 reacts with local host rock that is rich in calcite minerals.

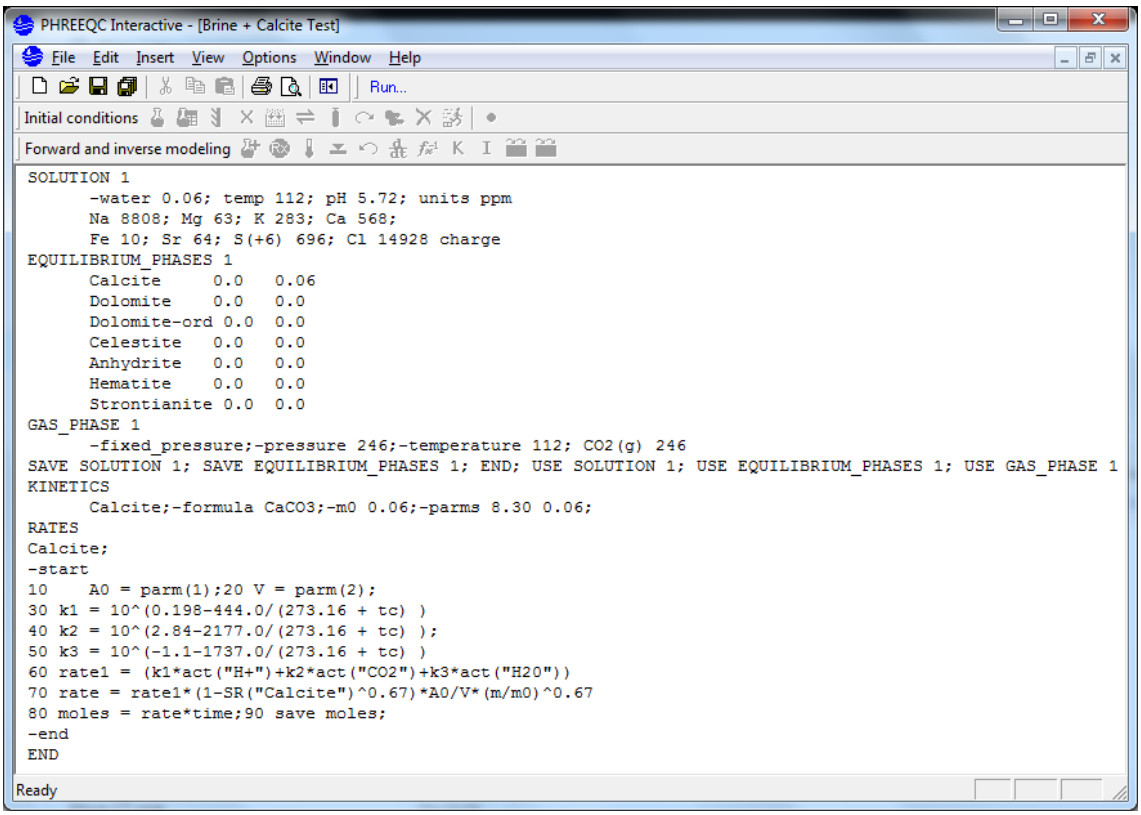

Figure 4.10: PHREEQC input file for Brine 1 + calcite

Chapter 5 Importance of Well Selection

This Chapter focuses on understanding the effect of brine composition on geochemical trapping potentials and the importance of well selection within an oil field (Objective 2). It comprises both experimental and geochemical modelling studies. Seven experiments, each involving one of the seven brines in Table 5.1, were performed over a 24 hour period and focused on CO_2-brine interactions under reservoir conditions (246 bar and 112ºC). PHREEQC and HydraFLASH were employed for the modelling work to assess geochemical trapping mechanisms (Objective 1) and a number of different analytical techniques were used to determine the brine composition both before and after the experimental work, as well as to identify any resulting solid residue.

5.1 Characterisation of synthetic brines

Each of the brines was prepared as described in Section 3.1.2. Table 5.1 shows the target concentrations of each brine ion, the actual concentration achieved and the final concentration after each of the seven experiments performed to achieve Objective 2. Additionally, the standard deviation associated with each measurement was recorded and is presented in Table 5.1 (bracketed value). Two samples of each brine were taken for ICP-OES analysis and so the results displayed are the average of the two. Consequently, the final standard deviation (SD_F) was calculated from the two standard deviations (SD_1 and SD_2) using the equation below:

$$SD_F = \sqrt{SD_1^2 + SD_2^2} \quad (5.1)$$

In several cases, such as for Brines 3 and 4, the actual value for both Ca^{2+} and SO_4^{2-} is lower than expected. This could be an error associated with the brine preparation (such as errors during weighing of salts or dilution of liquid samples) or due to masking during the ICP-OES, whereby the high relative salinity of the Na^+ can result in the measured concentrations of other ions appearing lower than they actually are. However, the SR for $CaSO_4$ in both cases was >1, so the most likely conclusion is that some of the Ca^{2+} reacted with the SO_4^{2-}, hence, forming very small amounts of anhydrite that were not visible when preparing the solution. The method to calculate the SR was described in Section 3.1.2. Lower than expected concentrations of Ca^{2+} and SO_4^{2-} seemed to consistently occur for most of the brines, and hence, was considered to have very little effect on the objective of comparing the geochemical trapping potentials of each brine.

Table 5.1: ICP-OES results comparing brine composition before and after experiment

		Na^+ (mg/l)	K^+ (mg/l)	Mg^{2+} (mg/l)	Ca^{2+} (mg/l)	Sr^{2+} (mg/l)	Fe^{3+} (mg/l)	SO_4^{2-} (mg/l)
Brine 1	Target	8963	227	69	639	59	12	775
	Actual	9096 (189.02)	224 (5.56)	68 (0.51)	689 (7.62)	74 (0.91)	12 (0.11)	802 (6.06)
	Final	**8843 (88.31)**	**622 (6.33)**	**67 (1.17)**	**622 (6.59)**	**58 (0.72)**	**4 (0.07)**	**764 (3.43)**
Brine 2	Target	8386	201	146	620	88	6	154
	Actual	8381 (77.49)	201 (4.77)	136 (1.49)	657 (5.72)	106 (0.74)	6 (0.06)	168 (2.12)
	Final	**8028 (96.62)**	**342 (6.42)**	**133 (2.19)**	**656 (7.60)**	**128 (1.45)**	**5 (0.09)**	**189 (26.29)**
Brine 3	Target	9480	241	2	645	41	6	1181
	Actual	6925 (155.51)	196 (1.86)	5 (0.02)	543 (3.27)	40 (0.32)	5 (0.02)	892 (3.81)
	Final	**7260 (181.82)**	**619 (2.46)**	**6 (0.04)**	**564 (5.00)**	**41 (0.28)**	**3 (0.03)**	**905 (6.44)**
Brine 4	Target	8056	198	118	587	84	2	119
	Actual	6184 (251.58)	176 (1.30)	100 (0.83)	521 (6.02)	88 (0.51)	1 (0.01)	114 (1.49)
	Final	**6364 (179.36)**	**241 (2.32)**	**102 (0.99)**	**539 (6.83)**	**89 (0.85)**	**2 (0.04)**	**124 (1.05)**
Brine 5	Target	11402	360	1155	555	22	5	2288
	Actual	11630 (86.95)	431 (0.41)	1128 (11.25)	557 (7.12)	32 (1.07)	4 (0.23)	2200 (24.85)
	Final	**10450**	**1421 (1.39)**	**1031 (9.04)**	**497 (3.39)**	**29 (0.43)**	**1 (0.01)**	**1979 (16.52)**
SW	Target	11000	400	1300	400	8	N.A	2800
	Actual	11170 (69.72)	456 (0.76)	1203 (9.64)	390 (4.99)	11 (0.23)	N.A	2621 (12.86)
	Final	**9571 (47.46)**	**1934 (2.16)**	**1055 (7.00)**	**332 (2.04)**	**10 (0.46)**	N.A	**2237 (15.07)**
HR	Target	20803	225	96	231	N.A	N.A	N.A
	Actual	20206	292 (0.46)	96 (2.63)	203 (3.75)	N.A	N.A	N.A
	Final	**20179**	**329 (0.44)**	**97 (1.34)**	**196 (3.75)**	N.A	N.A	N.A

5.2 Mineral trapping

Upon completion of each of the seven experiments shown in Table 5.1, two samples of brine were taken and sent for ICP-OES analysis. Any solid residue was filtered out, dried and sent for XRD and SEM/EDS analysis, as described in Sections 3.2.1 and 3.3.3, respectively. Table 5.1 displays the results of the ICP-OES analysis of the brine composition after each experiment.

5.2.1 Mineral trapping using original brine salinity

The results from Table 5.1 show that there was very little overall change in brine chemistry for all experiments. In all cases, the K^+ levels have increased but this is a result of using KOH as a buffer. Brine 1 shows a slight decrease in Ca^{2+}, Sr^{2+} and SO_4^{2-} concentrations, with Mg^{2+} remaining relatively constant. This would be consistent with the formation of anhydrite and celestite. Brine 2, on the other hand, shows very little change in any of the major ion concentrations, with SO_4^{2-} concentration appearing to increase, but this can be taken into account by the large SD. For Brines 3 and 4, the Mg^{2+} and Sr^{2+} concentrations remained relatively constant, while the Ca^{2+} and SO_4^{2-} concentrations actually increased. This increase in concentrations backs up the earlier assumption (Section 5.1) that, due to a SR>1, anhydrite was being formed during brine preparation. Under the experimental conditions, some of this anhydrite has likely dissolved which has lead to an increase in Ca^{2+} and SO_4^{2-} concentrations. Brine 5 and SW on the other hand displayed a decrease in Mg^{2+}, Ca^{2+} and SO_4^{2-} concentrations. This would be consistent with the formation of dolomite and anhydrite. Table 5.2 shows the expected formation of mineral carbonates, calculated using PHREEQC. For Brine 5 and SW, it is expected that the formation of dolomite will occur. In addition, since the pH of the brines dropped significantly in 24 hours (Table 5.3) then it is likely that the formation of anhydrite was also favourable. PHREEQC was rerun at the final experimental pH (Table 5.3) and it showed that in all cases that anhydrite would precipitate, with exception of the host rock (HR) brine as there was no SO_4^{2-} present.

Table 5.2: Formation of mineral carbonates obtained through PHREEQC modelling.

	Calcite (g/l)	**Dolomite (g/l)**	**Strontianite (g/l)**	**CO_2 Sequestered (g/l)**
Brine 1	1.34	0.53	0.10	0.87
Brine 2	0.96	1.13	0.15	1.01
Brine 3	1.64	0.02	0.07	0.75
Brine 4	1.00	0.91	0.14	0.92
Brine 5	-	2.64	0.04	1.27
SW	-	1.89	-	0.90
HR	0.18	0.76	-	0.45

Table 5.2 shows that the formation of mineral carbonates expected in each case. The PHREEQC output file provides the number of moles of each precipitate that has formed. This is then converted into grams by multiplying by the molecular weight. The total amount of CO_2 sequestered is the sum of the amount of CO_2 in each mineral. An example can be seen in Box 5.1:

Box 5.1: Example calculation for total CO_2 sequestered

Example Brine 1: Calcite 1.34 g/l, Dolomite 0.53 g/l, Strontianite 0.10 g/l

Wt% CO_2 in; Calcite (43.97%), Dolomite (47.73%), Strontianite (29.81%)

CO_2 Sequestered = (1.35 × 0.4397) + (0.53 × 0.4773) + (0.10 × 0.2981)

= 0.87 g/l

However, only for Brine 5 and SW do the ICP-OES results show evidence of the formation of mineral carbonates. This is a likely consequence of the rapid decrease in pH, as seen in Table 5.3. Table 5.3 shows the pH measured before the experiment (initial) and the pH measured after the experiment (final) and σ is the error associated with each measurement. After 24 hours the pH drops well below the required pH (>9) for the formation of CO_3^{2-} ions to be dominant [18]. Similar results were seen by Druckenmiller et al. (2006) who also used KOH as a buffer to promote mineral carbonation and recorded

that the pH dropped from 9.02 to 5.41 after 18 hours [14]. In the case of Brine 5 and SW, the initial higher overall concentrations of Ca^{2+} and Mg^{2+} allow for some very small amounts of mineral carbonates to form before the pH drops below the threshold for CO_3^{2-} production. In all other cases, it seems that the overall Ca^{2+} and Mg^{2+} concentrations are too low for precipitation to occur after 24 hours. The brines used by previous authors such as Druckenmiller et al. (2006) and Liu (2012) contained Ca^{2+} and Mg^{2+} concentrations ranging from 19570-32520mg/l and 1812-3440mg/l respectively [14, 74]. In comparison, the brines prepared for this study have relatively low concentrations of Ca^{2+} and Mg^{2+}. Therefore, not only does the pH have to be increased to promote mineral carbonation, but in the case of low concentrations of required cations the pH must also be maintained or no precipitation of mineral carbonates will occur. This conclusion is in agreement with the work performed by Liu (2012), who looked at the selection of different buffers to maintain the brine pH above 9, throughout the carbonation experiments [74].

Table 5.3: Comparison of initial and final pH obtained through experimental work

	pH Initial	**pH Final**	**σ**
Brine 1	10.77	4.15	±0.02
Brine 2	10.73	4.18	±0.02
Brine 3	10.77	4.05	±0.02
Brine 4	10.68	4.03	±0.02
Brine 5	10.68	4.58	±0.02
SW	10.46	5.15	±0.02
HR	10.78	3.90	±0.02

5.2.2 Mineral trapping using increased brine salinity

The low concentration of available ions needed to form minerals also meant that no solid residue was collected from the initial experiments. Therefore, each experiment was repeated at higher brine concentrations. To ensure the results were comparable with the original experiments, all experimental conditions, such as pressure and temperature, remained constant and each ion concentration was increased by the same factor. Oil field

brines can have salinity ranging up to saturation, which is roughly 300,000mg/l [163]. Therefore, the overall brine salinity was kept within 300,000mg/l so that it was still representative of oil field brine. In addition, the increase in ion concentrations was restricted by the SR of anhydrite. As the amount of Ca^{2+} and SO_4^{2-} increased in the brine, the SR for anhydrite became >>1 in many cases and so a clear brine solution could not be obtained due to the formation of anhydrite. For example, if the salinity of Brine 3 had been increased by a factor of 5, then the SR for anhydrite would be 113. Similarly for Brine 5, had the salinity been increased by a factor of 4, the SR would have been 121. The SR for anhydrite, therefore, had to be calculated for each brine to obtain the maximum increase in ion concentration that could be achieved without the formation of anhydrite at ambient conditions. This was done in the same way as described for $BaSO_4$ in Section 3.1.2, whereby the concentrations of each ion in the brine are multiplied together and then divided by the solubility product constant. Box 5.2 shows an example of how to calculate the SR for anhydrite using Brine 1.

Box 5.2: Example calculation of SR for anhydrite

Example: $[Ca^{2+}] = 639mg/l = 1.594\times10^{-2}mol/l$

$[SO_4^{2-}] = 775mg/l = 8.068\times10^{-3}mol/l$

Solubility product constant (Ksp) for $CaSO_4 = 4.36\times10^{-5}(mol/l)^2$

$$SR = \frac{[Ca2+][SO42-]}{Ksp[CaSO4]} = 2.95$$

The ICP-OES results for the experiments performed at increased brine salinity are shown in Table 5.4. As can be seen from Table 5.4, the reduction in major ion concentrations is much more pronounced when compared with the results in Table 5.1. As with the previous experiments (Table 5.1), the K^+ concentration has increased but this is a result of using KOH as the buffer. There was a noticeable reduction in Ca^{2+} and SO_4^{2-} concentrations after each experiment, along with the Sr^{2+} for all experiments except SW and Mg^{2+} for all experiments excluding Brine 3, both of which started with very low Sr^{2+} and Mg^{2+} concentrations respectively. The Fe^{3+} concentration also dropped significantly in all cases, likely due to the formation of hematite. Similar reductions in major ion concentrations were noted by Liu (2012) when performing CO_2-buffer-brine experiments under reservoir conditions [74]. However, the brine prepared by Liu (2012) did not contain any SO_4^{2-} and so it was concluded that the reduction in major ion concentrations was solely due to the formation of mineral carbonates (with the exception of Fe^{3+}) and

not any anhydrite or celestite as observed here. There were enough solid residues to perform XRD analysis for Brines 1-3, along with SEM/EDS. However, for the other four brines there were only enough residues to perform SEM/EDS.

Table 5.4: ICP-OES results comparing high salinity brine composition before and after experiment. 'x number' indicates the factor by which the salinity was increased

		Na^+ (mg/l)	**K+ (mg/l)**	**Mg^{2+} (mg/l)**	**Ca^{2+} (mg/l)**	**Sr^{2+} (mg/l)**	**Fe^{3+} (mg/l)**	**SO_4^{2-} (mg/l)**
Brine 1x5	Initial	32950	934	301	2810	280	46	3147
	Final	**30910**	**2413**	**273**	**2411**	**120**	**0**	**2458**
	SD	445.97	35.04	3.06	28.90	2.08	0.03	21.89
Brine 2x10	Initial	83921	2215	1345	5208	1068	46	1662
	Final	**72367**	**3326**	**1139**	**4382**	**361**	**2**	**982**
	SD	531.73	5.33	24.46	53.51	9.64	0.02	13.81
Brine 3x4	Initial	38451	1021	19	2138	185	20	4294
	Final	**32102**	**2331**	**19**	**1403**	**93**	**6**	**2594**
	SD	404	5.50	0.31	14.81	0.75	0.05	13.02
Brine 4x10	Initial	77369	2113	984	4537	932	14	1224
	Final	**68869**	**3092**	**871**	**3990**	**418**	**2**	**680**
	SD	687.82	10.02	16.13	45.17	10.71	0.04	6.18
Brine 5x3	Initial	35005	1150	3341	1319	79	9	6179
	Final	**26448**	**3041**	**2448**	**863**	**52**	**1**	**4312**
	SD	283.60	7.61	26.12	8.59	0.85	0.03	30.59
SWx3	Initial	33624	1227	3642	903	28	N/D	7387
	Final	**25061**	**3183**	**2737**	**657**	**30**	**N/D**	**5558**
	SD	188.30	4.51	71.75	5.25	0.36	N/D	29.72
HRx5	Initial	102565	1361	462	965	N/D	N/D	N/D
	Final	**94981**	**2310**	**416**	**874**	**N/D**	**N/D**	**N/D**
	SD	1679.80	6.71	5.29	4.78	N/D	N/D	N/D

Figure 5.1 shows the XRD analysis for Brine 1x5 which shows the presence of anhydrite as well as $CaMn(CO_3)_2$ and $Ca(Mn,Mg)(CO_3)_2$. These crystalline mineral phases are very similar to calcite and dolomite with the addition of small amounts of Mn. The Mn observed is a contamination from the Hastelloy vessel which contains Mn. There is a second XRD spectra in the Appendix (Figure A1) that also shows the presence of halite, which corresponds to the drop in Na^+ concentration seen in Table 5.4.

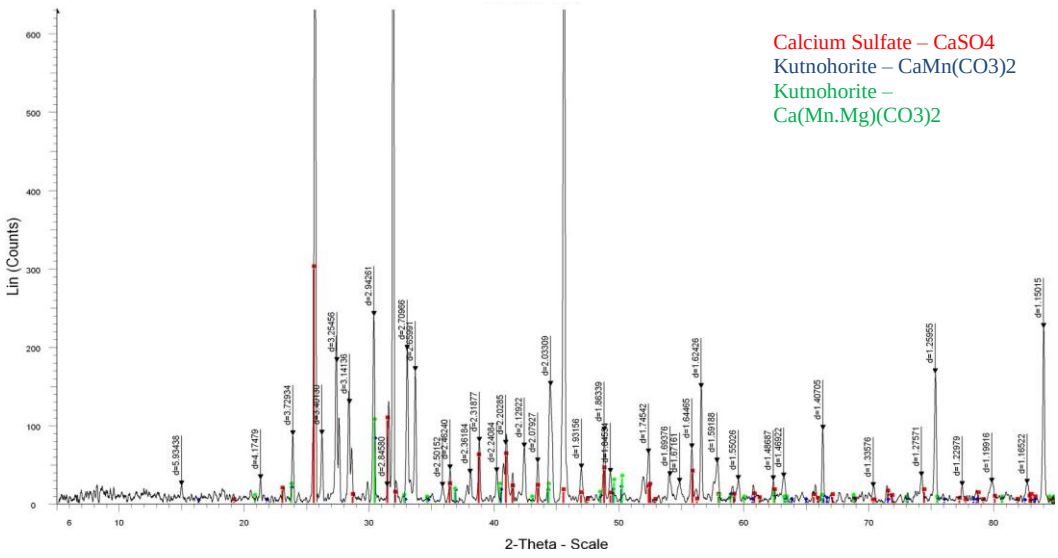

Figure 5.1: XRD analysis of Brine 1x5 solid residue

The SEM with x-ray map (Figure 5.2) also shows the presence of Ca and S as well as Sr but did not detect any Mg. PHREEQC predicts the formation of anhydrite, calcite, dolomite and celestite which is consistent with what is seen from the ICP-OES, XRD and SEM. As with the previous experiments, there was a large drop in pH from 10.72 to 5.04 in 24 hours. Consequently, it is unlikely that any dolomite actually formed due to how quickly the pH dropped and the fact that the SEM showed no Mg and the ICP showed very little change in Mg^{2+} concentration. From the XRD peaks it is quite possible that $CaMn(CO_3)_2$ was being mistaken for $Ca(Mn,Mg)(CO_3)_2$. XRD peaks can shift due to sample displacement, where the sample is not fully on the focusing circle [74]. Another factor can be flat specimen error, whereby the entirety of the surface of the sample cannot be laid flat on the focusing circle. This results in XRD measurements having an error range of approximately 2-3% [74].

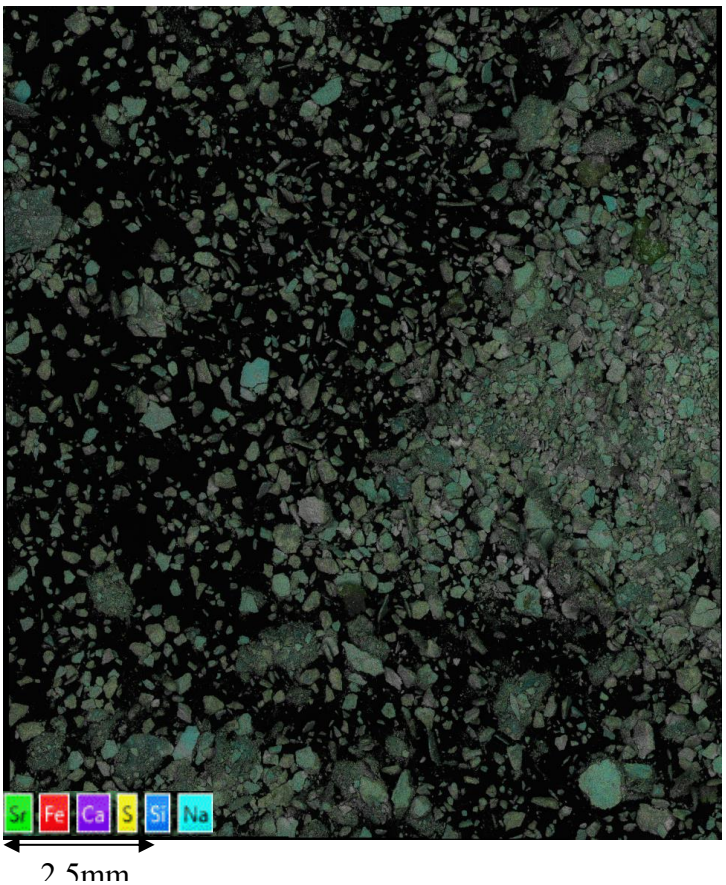

Figure 5.2: SEM image with x-ray map of Brine 1x5 solid residue

The XRD spectra for Brine 2x10 (Figure 5.3) and Brine 3x4 (Figure 5.4) can be seen below. The former shows the presence of anhydrite, halite and hematite, whereas the later shows only anhydrite and halite.

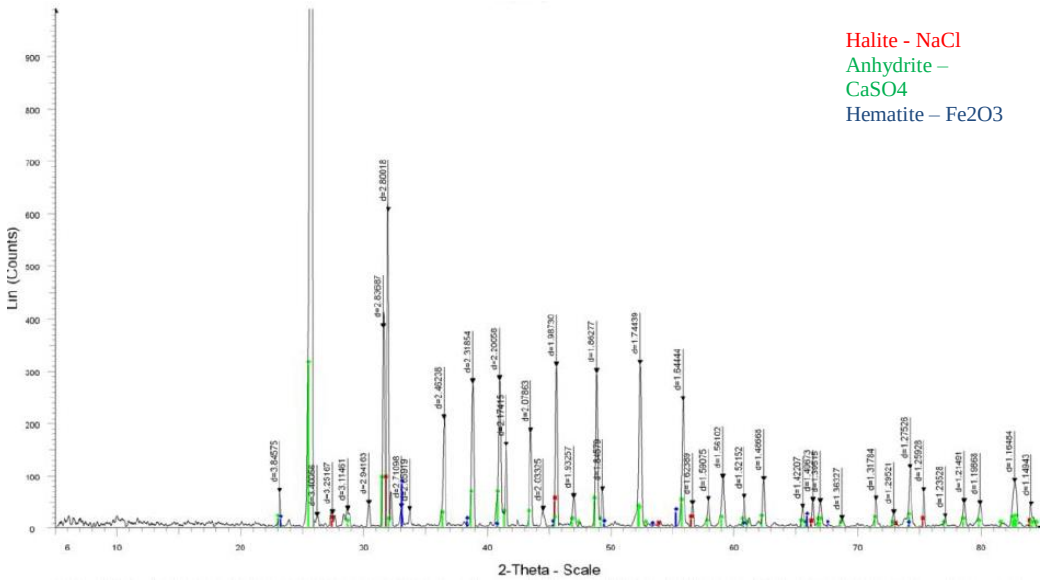

Figure 5.3: XRD analysis of Brine 2x10 solid residue

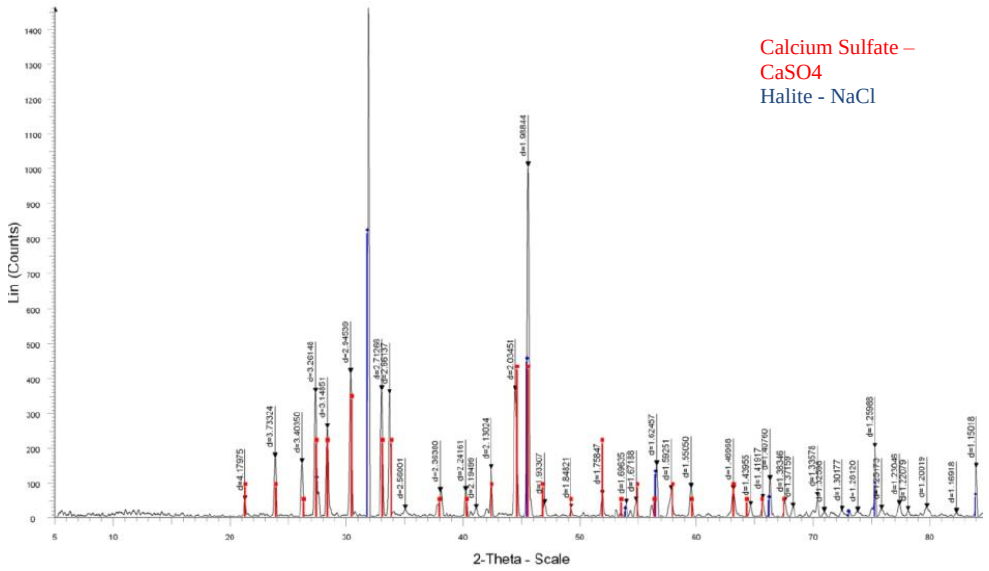

Figure 5.4: XRD analysis of Brine 3x4 solid residue

The SEM images for these brines and the images for the remaining experiments can be seen in Figure 5.5, with the EDS spectra located in the Appendix (Figures A2-20).

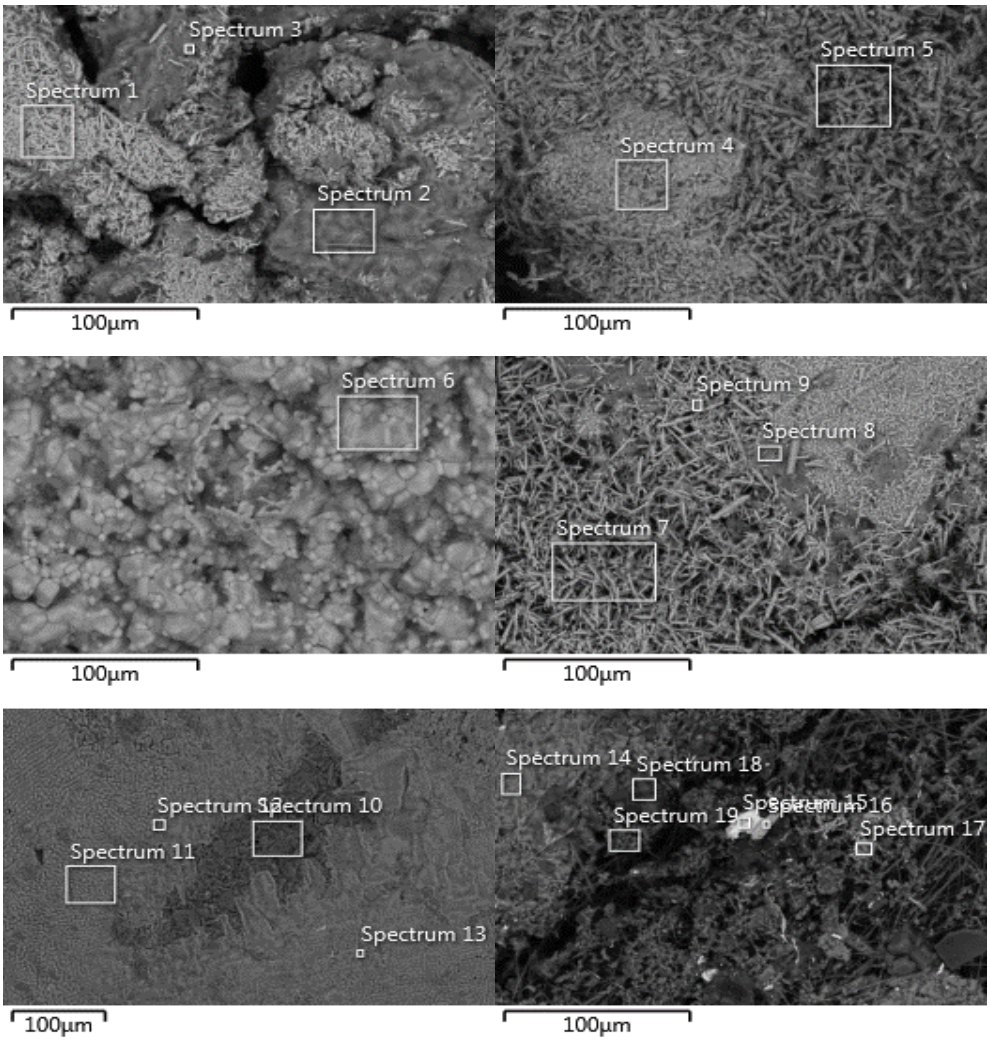

Figure 5.5: SEM images of solid residue for remaining brines

The area described as Spectrum 1 (Figure 5.5) corresponds to a large amount of Sr, S and O, indicating the presence of celestite. There is also Ca and Fe present, so it is likely that there is also anhydrite and hematite. Spectra 2 and 3 (Figure 5.5) show large amounts of sylvite (KCl) and halite, respectively. Spectra 4 and 5 (Figure 5.5) for Brine 3x4 show mainly Ca, S and O with Spectrum 5 also showing the presence of C. The area of Spectrum 4 will therefore be mostly anhydrite, whereas Spectrum 5 may also contain some calcite. The geochemical modelling for these two brines calculated that there would be anhydrite precipitation, but no calcite for Brine 2x10 and the precipitates formed from Brine 3x4 would be mostly calcite and anhydrite.

As previously stated, for the remaining four experiments there was not enough solid residue for XRD, but SEM/EDS was performed and the SEM images are shown in Figure 5.5 with the corresponding EDS spectra in the Appendix (Figures A2-20). The area corresponding to Spectrum 6 (Figure 5.5) is from the HRx5 brine and shows only halite, as indicated from the ICP-OES. PHREEQC predicts a small amount of dolomite (0.34g) but no other precipitates to form. Spectra 7-9 (Figure 5.5) are associated with Brine 4x10 and reveal large amounts of celestite (Spectrum 7-9), halite (Spectrum 8) and sylvite (Spectrum 9). There is also the presence of Ca in Spectrum 7, but it is considerably less so than S and Sr. This does agree with the ICP-OES (Table 5.4) which shows a large drop in S and Sr concentrations.

The ICP-OES for Brine 5x3 (Table 5.4) revealed a large drop in Mg^{2+}, Ca^{2+} and SO_4^{2-} concentrations. Although Spectra 10-13 (Figure 5.5) all show large amounts of halite, which can be expected from an almost 9000 mg/l drop in Na^+ concentration in the brine, there is also the presence of Mg, Ca and S. The Mg is mainly contained in the large dark area in the middle (Spectrum 10), whereas the Ca and S can be found more in the areas represented by Spectra 12 and 13. Although there is no evidence of C in the EDS spectra, PHREEQC does predict the formation of dolomite (0.49g) and anhydrite (1.24g), as seen in Table 5.2. Finally, the last SEM image is of the residue collected from the SWx3 experiment. The results are very similar to Brine 5x3, where there is Na present due to the large drop in Na^+ concentration (roughly 8500 mg/l) in the brine, along with Mg, S and some Ca. There are a few contaminations as well, where the amount of residue acquired from the experiment was very small and so there is a lot of Si detected from the filter paper. In addition, the bright piece in the centre, corresponding to Spectrum 15 (Figure 5.5), is a small piece of Hastelloy from the vessel as it contains Ni and Cr.

PHREEQC also predicted the same precipitates as for Brine 5x3 albeit in small quantities and predicted 0.99g of anhydrite and 0.19g of dolomite.

5.2.3 Summary

Although repeating the experiments at higher salinity allowed for the identification of precipitates, the same underlying problem remains. That is that the pH drops too quickly for the formation of mineral carbonates. In fact, mineral carbonates only appeared to precipitate in Brine 1x5 and Brine 3x4. These were also the only two brines that PHREEQC predicted calcite formation. In the case of Brine 5x3 and SWx3, the SEM/EDS detected the presence of Mg but no C. The Mg^{2+} could have reacted with the SO_4^{2-} to form $MgSO_4$ but according to PHREEQC, this was not thermodynamically favourable, whereas at high pH the formation of dolomite was. The main factor here is maintaining the pH>9 over time. However, it is argued that dolomite does not naturally form on its own. A process called dolomitization occurs whereby Mg^{2+} ions replace Ca^{2+} ions in already existing calcite to form dolomite [164]. Consequently, calcite must first be present. It is therefore likely that there is not enough time for calcite to form and then be converted to dolomite. Etschmann et al. (2014) looked at the experimental dolomitization of calcite marble [165]. At 200ºC under closed system conditions, there was initially no dolomite formation. However, after 4 days, only 12 wt% of calcite remained, the rest having been converted to dolomite and brucite. Therefore, for dolomitization to occur the experiments would have to be run over a longer time period. However, if dolomite is being formed through dolomitization rather than forming naturally then this will not result in more CO_2 being sequestered as pre-existing calcite (which has already sequestered CO_2) is being converted to dolomite.

Table 5.2 shows the mineral trapping potentials of each brine assuming that the pH can be maintained long enough for mineral carbonation to occur. Brine 5 can sequester the most CO_2 via mineral carbonation due to its high concentration of Mg^{2+} as well as Ca^{2+}. SW has a higher concentration of Mg^{2+} but has the second lowest amount of Ca^{2+}, which is needed to form dolomite. Therefore SW has a lower mineral trapping potential than might be expected. The HR brine has a considerably lower mineral trapping potential than the rest of the brines, as although it has a much higher overall salinity, it has far lower concentrations of the required cations needed to form mineral carbonates. The rest of the brines follow the expected trend, as the total number of available cations to form mineral carbonates (Ca^{2+}, Mg^{2+}, Sr^{2+}) is directly proportional to the amount of CO_2 sequestered via mineral trapping. This study also shows that the amount of CO_2 sequestered is

dependent on the type of mineral that precipitates, not just the total amount of precipitates. For instance, Brine 1 results in the precipitation of 1.97g of carbonates, whereas SW only results in 1.89g. However, the total amount of CO_2 sequestered is higher for SW than Brine 1 and this is because dolomite contains the largest weight % of CO_2 (47.73% compared with 43.97% for calcite and 29.81% for strontianite).

5.3 Solubility trapping potentials associated with each synthetic brine

The solubility trapping potentials of each brine were calculated using HydraFLASH and the aforementioned VPT equation of state (Chapter 4). Table 5.5 shows the CO_2 solubility measured in mol/kg calculated by HydraFLASH and the resulting amount of CO_2 that can be dissolved in one litre of brine. The mol/kg was multiplied by the molecular weight of CO_2 and the density of the brine to obtain the amount of CO_2 dissolved in 1 litre of brine in grams. The HydraFLASH (VPT) model was calibrated against the experimental work done by Tong et al. (2013) as seen in Figure 4.4 [98]. The maximum uncertainty in the modelling results is therefore ±4%.

Table 5.5: Solubility trapping potentials associated with each brine through PHREEQC modelling

	Salinity (mg/l)	**CO_2 Solubility (mol/kg)**	**CO_2 Dissolved in 1 Litre of Brine (g)**
Brine 1	26040	1.175	50.84
Brine 2	24280	1.179	51.06
Brine 3	27450	1.173	50.70
Brine 4	23230	1.181	51.19
Brine 5	37760	1.159	50.47
SW	37370	1.163	50.63
HR	54328	1.035	45.58

The solubility trapping results are as expected. The main factors affecting CO_2 solubility are temperature, pressure, salinity and ion charge [24, 98]. Since both temperature and pressure were constant for all the experiments, then that leaves the effect of salinity and

ion charge. As it can be seen from Figure 2.7, previous work by a number of authors such as Bando et al. (2003), Li et al. (2004) and Koschel et al. (2006) conclude that CO_2 solubility decreases with increasing salinity [85, 92, 166]. In addition, Tong et al. (2013) provided evidence that there is a stronger salting out effect in systems with divalaent cations ($CaCl_2$/$MgCl_2$) when compared with monovalent (NaCl/KCl) cations [98]. Therefore, the solubility of CO_2 will further decrease in systems with higher concentrations of divalent cations, when compared with monovalent cations, even at the same molality of salt.

The results in this work show that the CO_2 solubility decreases with increasing salinity, from the lowest salinity brine (Brine 4 - 23230mg/l) to the highest (HR – 54328mg/l), as would be expected. However, the difference in CO_2 solubility between Brines 1 and 2 as well as Brines 3 and 4 is lower than might be anticipated from the difference in salinity. This is because Brines 2 and 4 have a higher ratio of divalent to monovalent cations which, as mentioned above, will reduce the CO_2 solubility [98]. Therefore, when looking to maximise CO_2 dissolution in brine, even within the same field, it is important to acknowledge the brine chemistry, with wells containing low salinity brines with smaller ion charge, being preferential or wells that have not yet undergone seawater flooding. This is more difficult for EOR, as usually CO_2 is co-injected with seawater meaning that you are inadvertently reducing CO_2 solubility which will reduce sweep efficiency [8]. It may be beneficial then to inject low salinity water if possible, which would increase the CO_2 solubility.

5.4 Brine composition effect on well selection

The overall geochemical trapping potential of each brine is the sum of both the mineral trapping (Table 5.2) and the solubility trapping potentials (Table 5.5). Figure 5.6 shows the calculated geochemical trapping potentials of each brine.

Figure 5.6: Geochemical trapping potentials associated with each brine

As expected, the vast majority of the geochemical trapping potential is a result of solubility trapping. This is because CO_2 solubility in brine is dependent on pressure, temperature and salinity rather than maintaining high pH like mineral trapping [24]. In fact, from the results shown in Figure 5.6, solubility trapping accounts for roughly 97-99% of total geochemical trapping. However, the relevance of mineral trapping is that the CO_2 is permanently stored as thermodynamically stable, solid insoluble carbonates and is consequently the safest method storage [59]. Although CO_2 is considered to be permanently stored once it has dissolved in the brine and formed a carbonic species, if there was a sudden change in pressure in the reservoir, then degassing of the CO_2 could occur. Therefore, mineral trapping is preferential to solubility trapping in terms of safety and CO_2 security.

In regards to geochemical trapping, Brine 2 has the highest storage potential of 52.07g/l and Brine 4 has the second highest of 52.11g/l. Brine 2 represents the average brine composition of the lowest salinity well, whereas Brine 4 is the brine composition before seawater flooding. Brines 4 and 2 had the highest and second highest solubility trapping potentials due to having the lowest and second lowest salinities, respectively. As stated, in Section 5.3, since the pressure and temperature were constant in all experiments, changes in CO_2 solubility were a direct result of brine salinity and ion charge. In addition, they also had the second (Brine 2) and third (Brine 4) highest mineral trapping potentials, due to having high numbers of available cations to form mineral carbonates. **In conclusion, low salinity wells are always preferable to high salinity wells for geochemical trapping and this also confers to pre-seawater flooding as after seawater flooding the brine salinity will have increased.** However, seawater can

introduce additional cations such as Mg^{2+} and Ca^{2+} that are needed for mineral carbonation, which can be seen from Brine 5 having the highest mineral trapping potential as well as the third highest geochemical trapping potential.

On the other hand, seawater flooding also introduces high concentrations of SO_4^{2-}. As seen from both the geochemical modelling and the experimental residue collected from the higher salinity experiments, the formation of both anhydrite and celestite is thermodynamically favourable under reservoir conditions. Formation of anhydrite and celestite consumes much of the needed cations to form mineral carbonates. According to Egermann et al. (2005), if SO_4^{2-} is present in the brine then anhydrite will precipitate. Not only does this mean that there will be less Ca^{2+} present to react with the CO_3^{2-}, but it can also have a significant affect on the permeability of the local host rock as formation of anhydrite can result in the clogging of pore throats [104]. PHREEQC also showed that unlike with mineral carbonates, the formation of anhydrite is favourable even at lower pH, such as the final experimental pH recorded. This could be seen by the large quantities of anhydrite identified in the solid residue samples (Figure 5.3). **Consequently, this study has shown that to increase mineral trapping potentials, not only is it vital to maintain a pH greater than 9, but the concentration of SO_4^{2-} in the brine should preferably be as low as possible.**

When comparing a low salinity field with a higher salinity field in the same region, Brine 1 has a much higher geochemical trapping potential than the HR brine. In terms of solubility trapping this is expected as higher salinity leads to lower solubility trapping potential. However, for the mineral trapping, the actual brine composition is important. Brine 1 has a far lower overall salinity than the HR brine, but contains more of the required cations for mineral carbonation and hence has a higher mineral trapping potential. This shows the importance of actual brine composition. Higher brine salinity does not always infer higher concentrations of Mg^{2+}, Ca^{2+} and Sr^{2+} which are vital for mineral carbonation. **In conclusion, for maximum geochemical trapping potential, wells containing low salinity brine with relative high concentrations of Mg^{2+}, Ca^{2+} and Sr^{2+} should be selected. In addition, this study has provided new data that shows how geochemical trapping potentials can vary within the same field as a consequence of the composition of the brine present at individual wells. Hence, this study has shown the importance of well selection in regards to geochemical trapping potentials, which will prove useful when considering the long term storage and security of CO_2.**

Chapter 6 CO_2-Calcite-Brine Interactions

This Chapter focuses on investigating the potential of calcite to buffer brine and promote mineral carbonation over an extended period of time, as well as how the dissolution and precipitation of minerals can affect the properties of host rock (Objective 4). This chapter includes both experimental and geochemical modelling studies. The experiments involved calcite powder being exposed to CO_2-satured brine for periods of up to 6 months at 246 bar and 112ºC (Objective 4). PHREEQC was used for the modelling work to corroborate the experiment results and calculate the equilibrium phases (Objective 1). In addition, the brine composition was measured both before and after the experimental work using ICP-OES. A number of analytical techniques were also used to measure the properties of the calcite as well as to identify mineral phases present in the resulting solid residue.

6.1 Characterisation of brine

One litre of brine was synthesised using the method described in Section 3.1.2 and 60ml of this brine was added to each of the three pressure vessels. Two samples of the brine were taken for ICP-OES analysis and the average of the two results was calculated. Table 6.1 shows both the target and actual concentrations of each ion present in the brine, as well as the associated SD. The concentrations of Ca^{2+} and SO_4^{2-} are slightly lower than expected. As stated in Section 5.1 this could be an error associated with the brine preparation or due to masking during the ICP-OES. However, in this case the SR for $CaSO_4$ was 2.95 so it is likely that very small amounts of anhydrite formed in the solution. As this study focuses on is the comparison of the brine composition before and after the experiments, achieving the exact target composition is not imperative.

Table 6.1: ICP-OES results for brine composition

		Na^+ (ppm)	**K+ (ppm)**	**Mg^{2+} (ppm)**	**Ca^{2+} (ppm)**	**Sr^{2+} (ppm)**	**Fe^{3+} (ppm)**	**SO_4^{2-} (ppm)**
Brine	Target	8963	227	69	639	59	12	775
	Actual	**8808**	**283**	**63**	**568**	**64**	**10**	**696**
	SD	112.01	2.45	0.82	7.30	1.19	0.06	1.89

6.2 Characterisation of calcite powder

As previously stated, the calcite was ground into a powder and the target particle size was in the range 45-75µm. Figure 6.1 shows the particle size distribution measured using the Mastersizer 3000 and that the majority of the particles sit within the target range, with the mean particle size (D[4,3]) recorded as 60.3µm. The D10, D50 and D90, which describe where 10%, 50% and 90% of the particle size distribution lie below, were recorded as 10.5µm, 59.3µm and 103µm respectively.

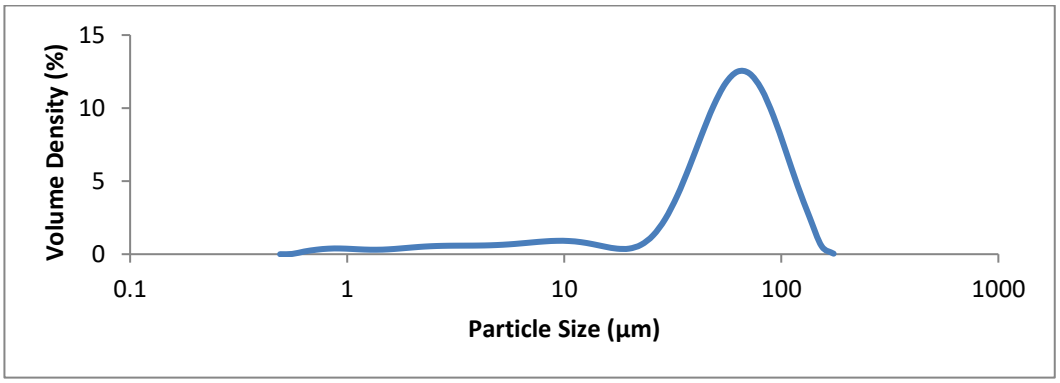

Figure 6.1: Particle size distribution of calcite powder

A sample of the calcite powder was also used for BET analysis and the measured specific surface area of the original calcite powder was 1.38 m^2/g. The XRD analysis shows that the calcite chips purchased were indeed pure calcite as can be seen from Figure 6.2.

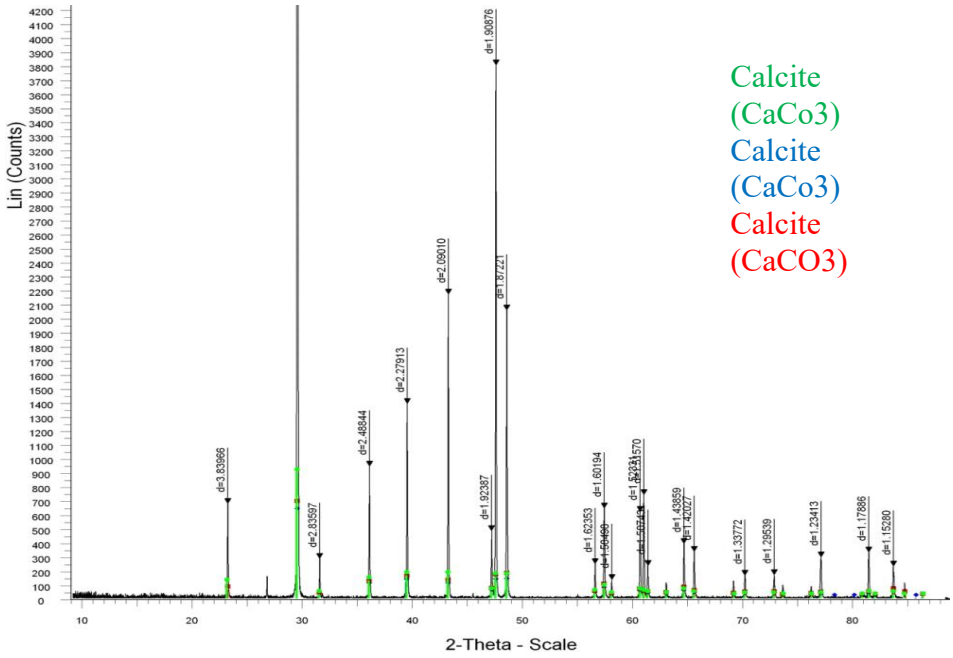

Figure 6.2: XRD of calcite powder

The SEM/EDS analysis confirms the XRD results, that the calcite was pure (Figure 6.3 and Figure 6.4). The wt% of each element in the EDS spectrum (Figure 6.4) had to be normalised and the normalised results are included in the captions below each figure.

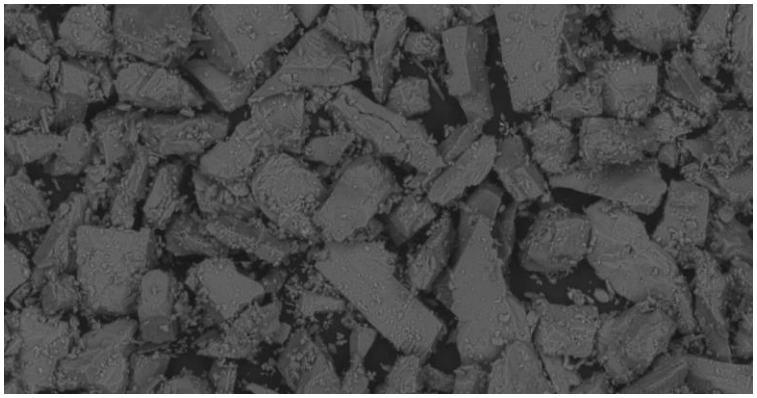

Figure 6.3: SEM image of calcite powder showing only calcite

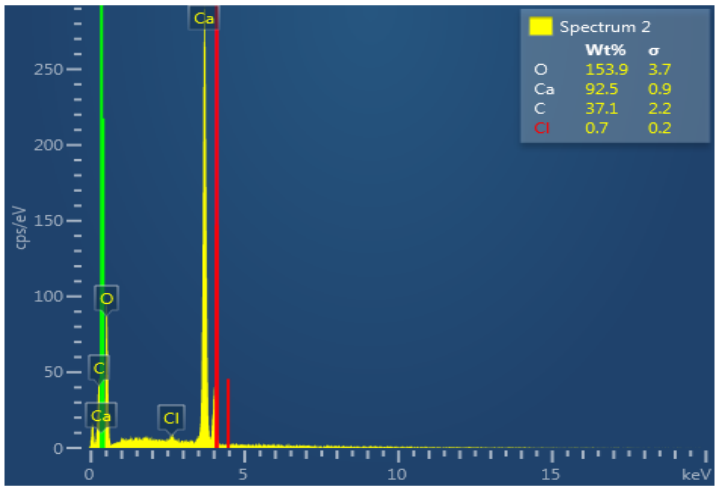

Figure 6.4: EDS spectrum for calcite powder. Normalised wt%; O – 54.2%, Ca – 32.6%, C – 13.1%, Cl – 0.3%

6.3 Buffering effect of calcite over time

One of the objectives of this study (Objective 4) was to assess the buffering effect of calcite on the brine pH. The starting pH of the brine was measured to be 2.03. Note that all pH measurements were made under ambient conditions. As previously stated, CO_2 dissolves in brine to form a weak acid which will in turn react with the calcite to produce HCO_3^-, which is alkaline [20]. This will result in an increase in brine pH. When the calcite was first added to the brine before the injection of CO_2 the pH of the brine increased to 5.72 due to the alkaline nature of the calcite. After the first month, the brine pH further increased to 5.77 due to the production of HCO_3^-.

This can be compared with a study by Matter et al. (2007) which involved the injection of CO_2 saturated water, with an initial pH of 3.5, into sedimentary rock. The experiment

by Matter et al. (2007) was run under ambient conditions. The results of this study showed that within hours of injection, the brine pH was neutralised due to CO_2-rock-brine interactions, where the rock contained 10.43 wt% CaO [73]. Liu (2012) also conducted pH stability studies for a CO_2-rock-brine system whereby CO_2 was injected into brine with an initial pH of 2.6 and buffered by Oriskany rock containing 20.07 wt% CaO [74]. The experiment was run under ambient conditions and the pH stabilised at around 6.3.

However, the increase in brine pH in this work is not enough to promote mineral trapping which requires CO_3^{2-} to be the dominant carbonic species. In addition, when the aqueous CO_2 reacts with water, it forms carbonic species based on pH. At pH below 6, H_2CO_3 dominates [72]. If the pH had increased to above 6, then it is likely that any further CO_2 dissolving in the brine would form HCO_3^- ions instead which would result in the pH remaining near neutral. However, with H_2CO_3 being the dominant species, the pH continues to drop after the first month as the CO_2 continues to dissolve in the brine. According to the PHREEQC modelling studies conducted here, the pH will stabilise at 4.43 when it reaches equilibrium. As previously stated, PHREEQC is used more to show trends than provide precise absolute results, but as can be seen from Figure 6.5, the experimental pH measurements are gradually decreasing in value toward the equilibrium pH predicted by the modelling.

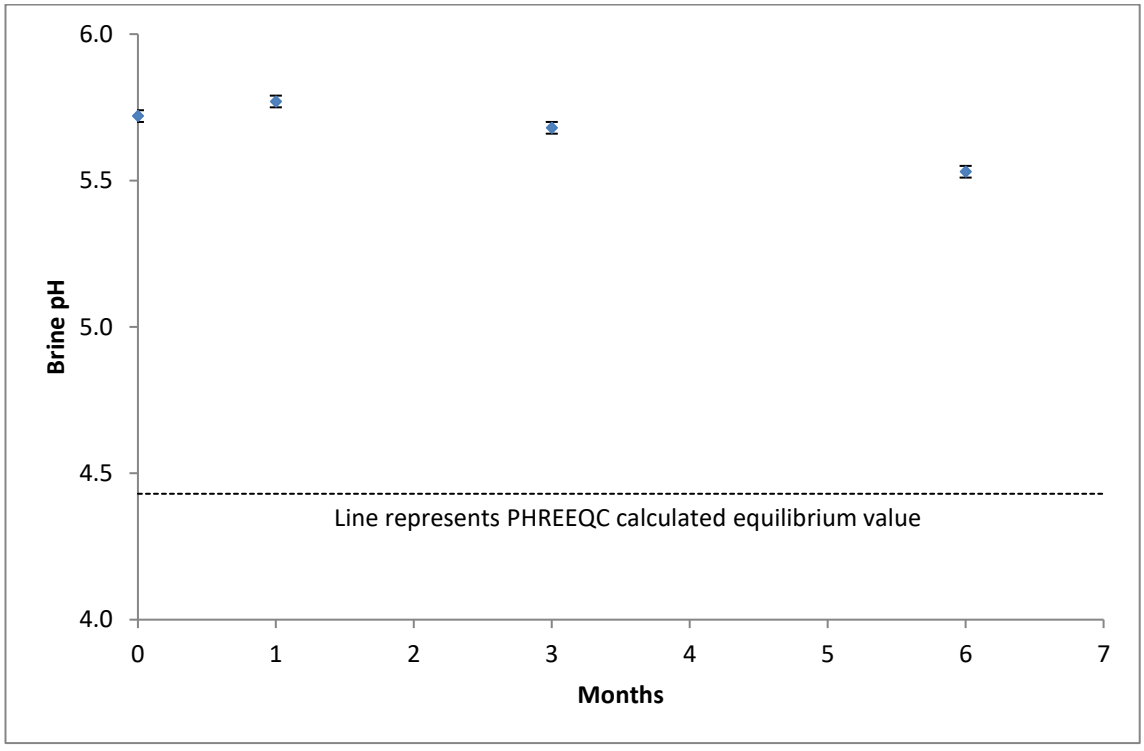

Figure 6.5: Measured brine pH after each experiment and modelled equilibrium value

6.4 Dissolution of calcite

Equation 4.7 shows how the reaction between the calcite and the H_2CO_3*, which is the sum of the concentrations of dissolved CO_2(aq) and H_2CO_3, result in the production of HCO_3^- and Ca^{2+}. Therefore, over time more Ca^{2+} will be produced and the concentration of Ca^{2+} in the brine will increase. This can be seen from Figure 6.6. At equilibrium, the calcite will reach the saturation point where it can no longer dissolve in the CO_2-saturated brine. After 6 months the concentration of Ca^{2+} ions in the brine is approaching equilibrium. This trend has been recorded in previous work by Egermann et al. (2005), where the Ca^{2+} concentration continued to increase throughout the duration of CO_2 injection from 400ppm to 1100ppm [104].

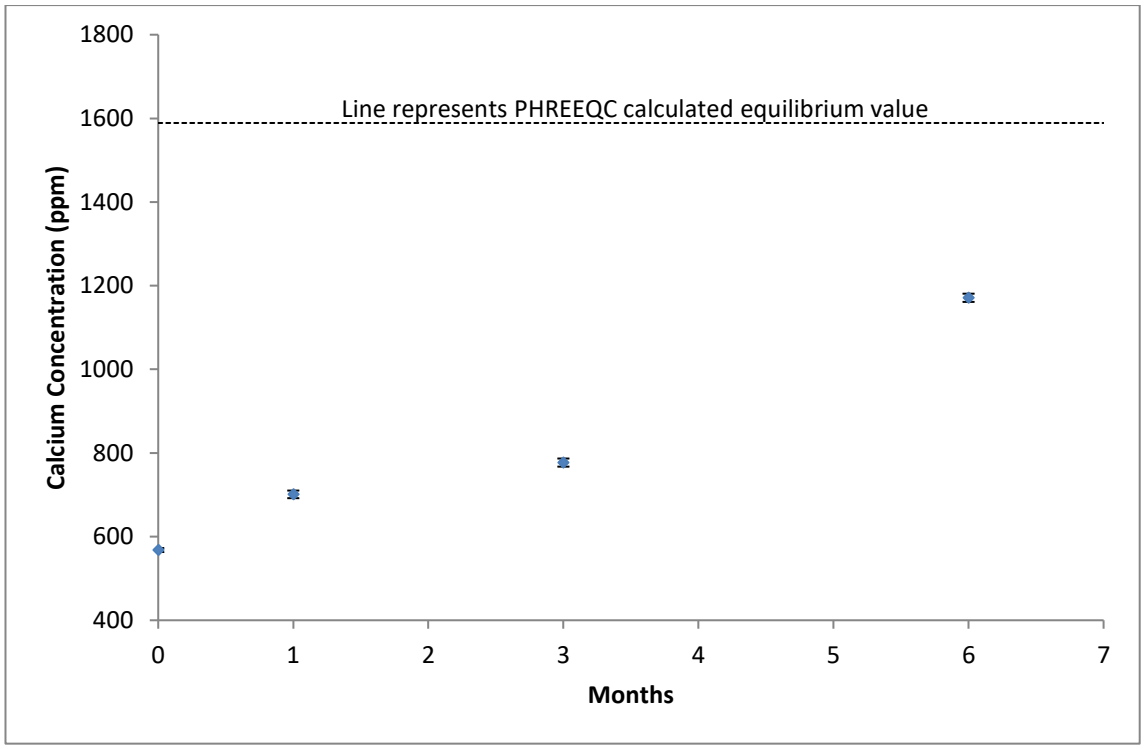

Figure 6.6: ICP-OES results showing Ca^{2+} concentrations in brine

6.5 Formation of precipitates

After the first month, apart from the increase in Ca^{2+} ion concentration in the brine due to the dissolution of calcite, there was no change in the composition of the solid residue from the original calcite sample. Both the XRD and SEM studies showed that only calcite was present (Figures 6.7 and 6.8).

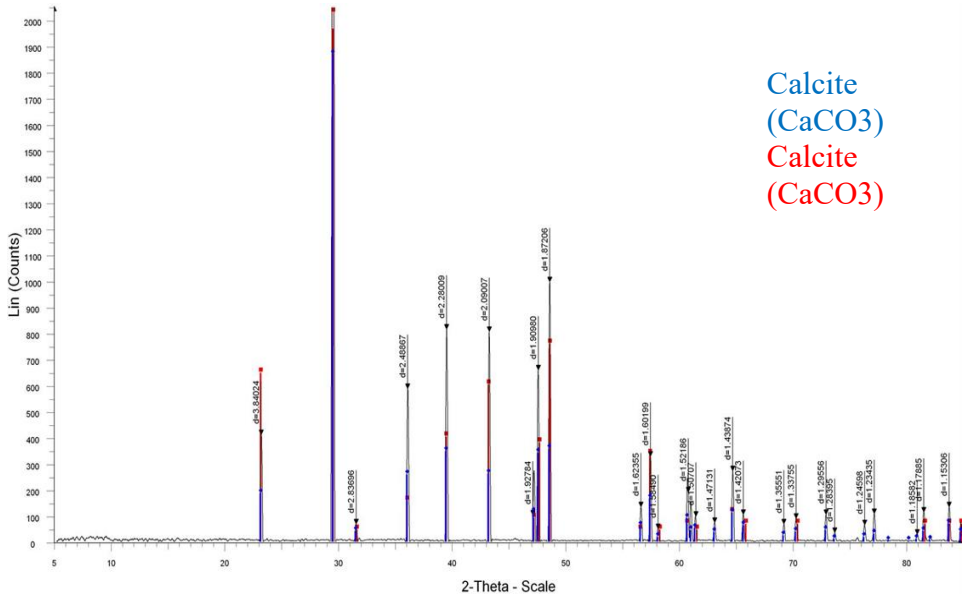

Figure 6.7: XRD of calcite after 1 month

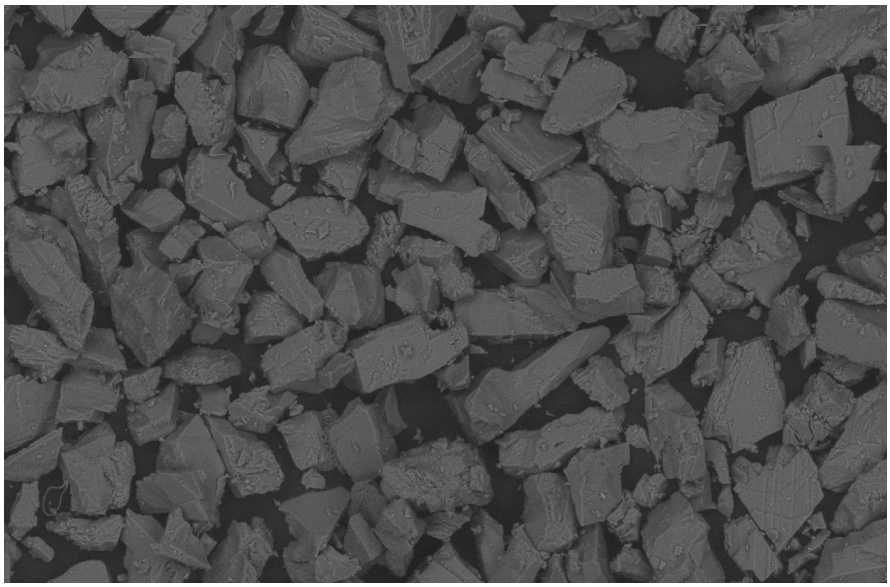

Figure 6.8: SEM image of calcite after 1 month

Once the calcite has been exposed to CO_2-saturated brine for 3 months, a very small amount of other precipitates begin to form. These precipitates are too low in quantity to show up in the XRD (Figure 6.9) which once again shows mainly calcite with some very low magnesium calcite $(Mg0.03Ca0.97)(CO_3)$. It is important to note that this is not dolomite. The EDS map did show the presence of very small amounts of Mg attached to the calcite.

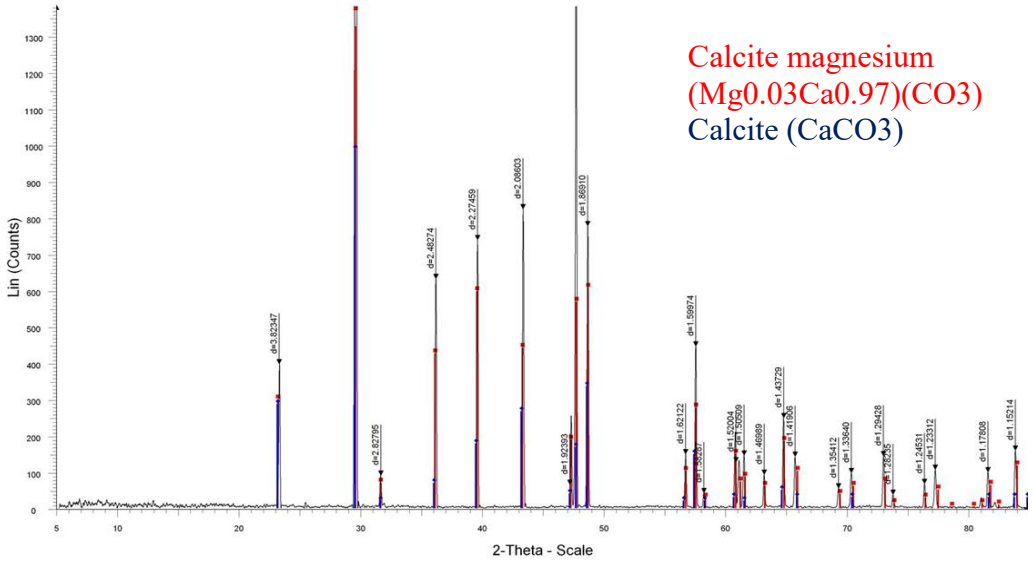

Figure 6.9: XRD of calcite after 3 months

The SEM image shows the presence of some anhydrite, hematite and a Sr mineral phase which is difficult to identify, but is most likely celestite or strontianite, as seen in Figure 6.10. According to the ICP results, there was a 37% reduction in SO_4^{2-} in solution, 64% reduction in Sr^{2+} and 98% reduction in Fe^{3+} with respect to the initial brine composition. As stated in Section 5.4, Egermann et al. (2005) concluded that if SO_4^{2-} is present in the brine then anhydrite will precipitate, which can significantly affect the permeability of the rock by clogging the pore throats [104]. Mohamed et al. (2013) confirmed that gypsum ($CaSO_4.2H_2O$) can also form, but it is only stable at temperatures lower than 40ºC; otherwise, anhydrite is the stable form [167].

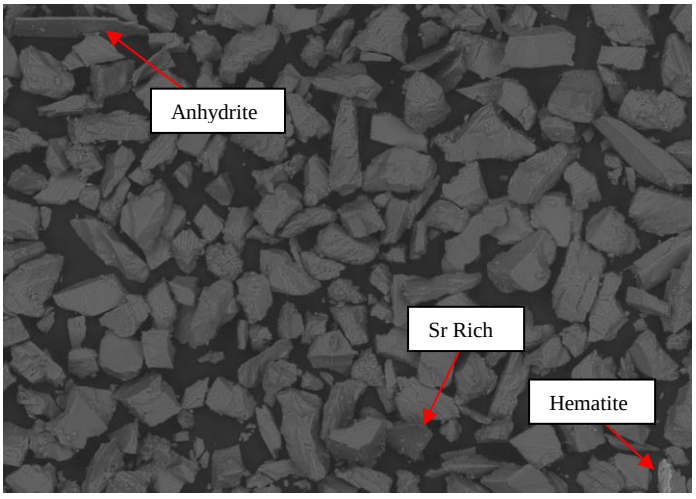

Figure 6.10: SEM image of calcite after 3 months

The EDS spectrum (Figure 6.11) confirms the presence of Sr and Fe but it did not show S. It should be noted that the EDS spectrum cannot distinguish Sr from Si and so in this case the Si identified by the spectrum is likely, Sr.

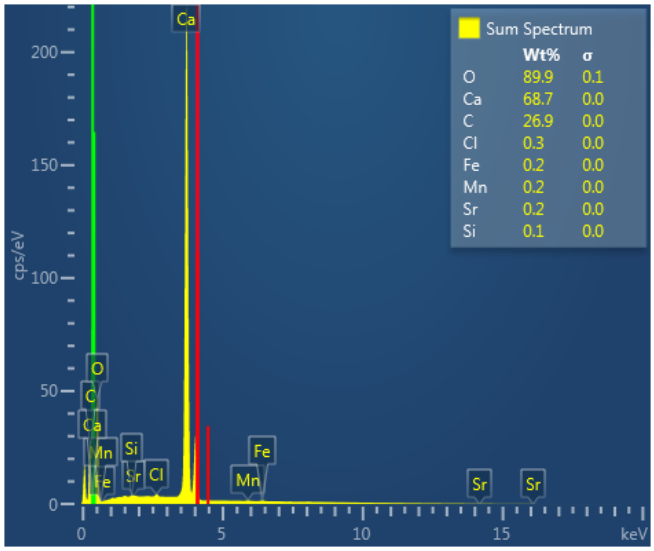

Figure 6.11: EDS spectrum of calcite after 3 months. Normalised wt%; O – 54.2%, Ca – 32.6%, C – 13.1%, Cl – 0.2%, Fe – 0.1%, Mn – 0.1%, Sr - 0.1%, Si - 0.1%

Finally, after 6 months the XRD (Figure 6.12) shows no additional changes, with respect to 3 months, identifying only calcite and low magnesium calcite.

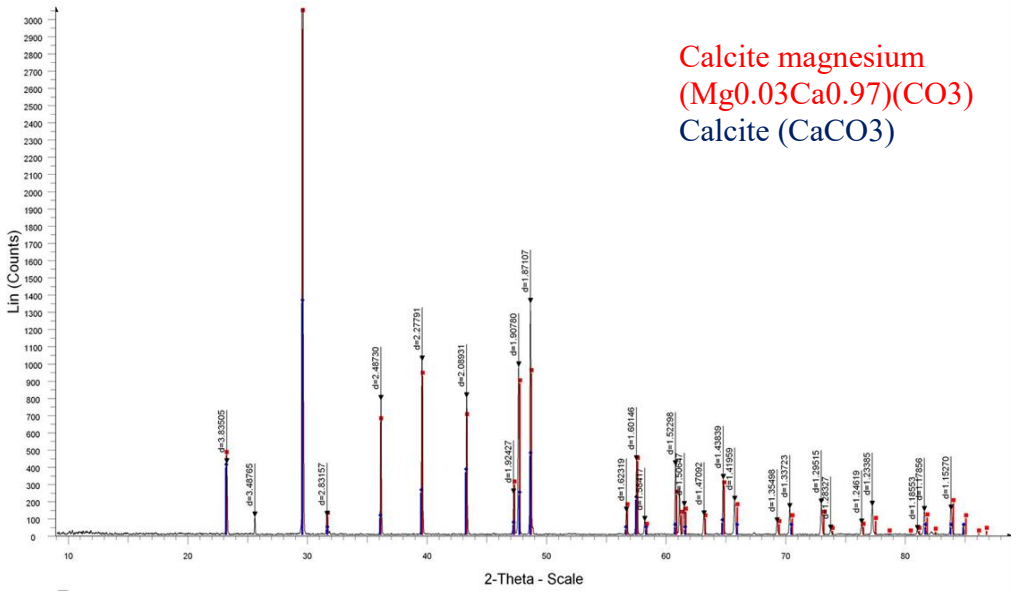

Figure 6.12: XRD of calcite after 6 months

The SEM/EDS, however, shows a larger presence of other precipitates than those recorded after 3 months. The EDS spectrum (Figure 6.13) now detects S as well as Sr and Fe. There is also NaCl present and a small amount of Mn which could have come from the 316L Stainless Steel vessels.

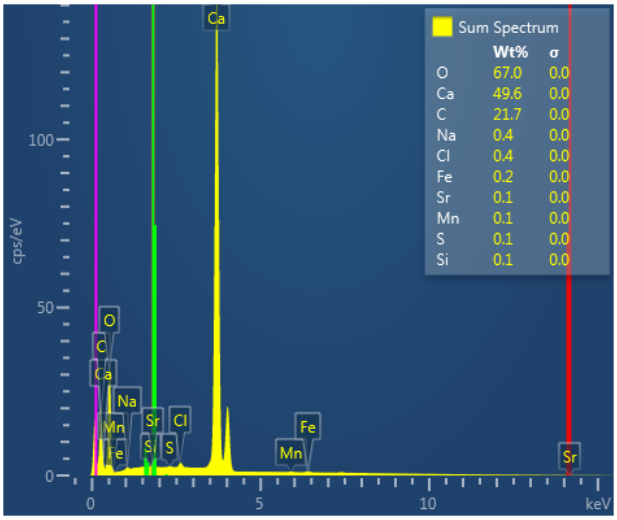

Figure 6.13: EDS spectrum of calcite after 6 months. Normalised wt%; O – 48.0%, Ca – 35.5%, C – 15.5%, Na -, 0.3%, Cl – 0.3%, Fe – 0.1%, Mn – 0.1%, Sr - 0.1%, S – 0.1%, Si - 0.1%

At this stage, there is still no dolomite present, but there is much more anhydrite and celestite, which can be seen in the SEM image (Figure 6.14). However, this SEM image was taken over a larger area when compared with the 3 month SEM image. This may have resulted in an unrepresentative quantity of precipitates being detected, as according to the ICP results the concentration of ions in solution actually increased from 3 months to 6 months. Compared with the original brine composition, there was a 26% reduction in SO_4^{2-} in solution, 39% reduction in Sr^{2+} and 82% reduction in Fe^{3+}. The brine pH dropped from 5.68 to 5.55, and therefore, it is possible that some of the precipitates that had formed after 3 months were then dissolved, which lead to an increase in SO_4^{2-}, Sr^{2+} and Fe^{3+} concentrations in the brine.

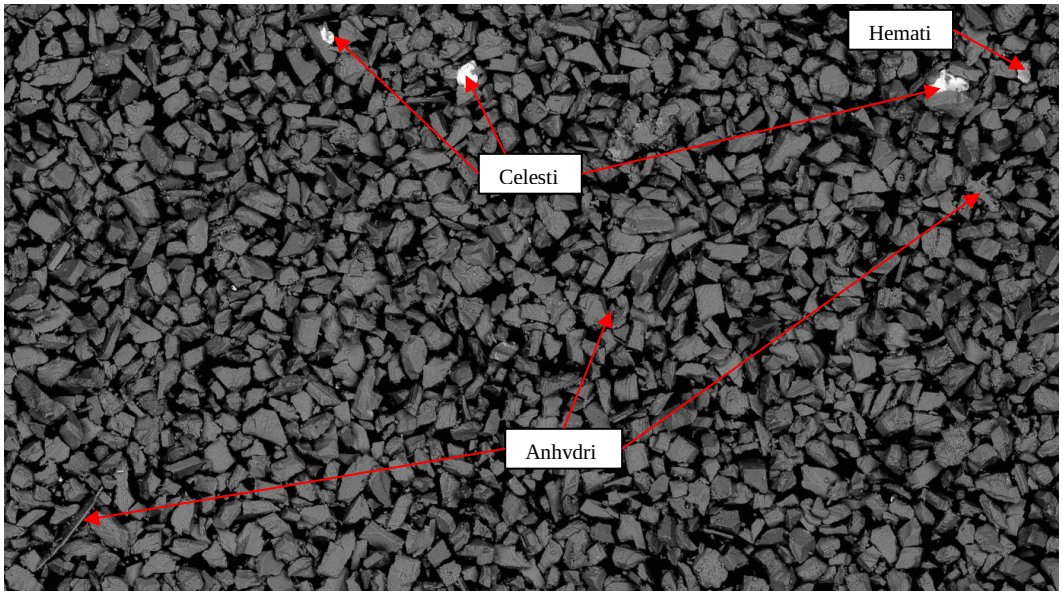

Figure 6.14: SEM image of calcite after 6 months

This trend was also predicted by the PHREEQC studies, where the final concentration of SO_4^{2-} was only 18% lower than the original concentration and there was no noticeable change in Sr^{2+} and only the slightest reduction in Fe^{3+} concentration (0.1%). Therefore, it is likely that as the pH continues to drop (until equilibrium at 4.43), many of the minerals that originally precipitated at higher pH will dissolve. As previously stated, PHREEQC cannot be used to accurately predict experimental results but can show general trends [74]. Therefore, the results from PHREEQC may not be entirely accurate but they have shown that the experimental work is following the expected trend, with respect to both brine pH and ion concentrations. In regards to the dissolution of calcite and the formation of other precipitates, PHREEQC predicts that at equilibrium there will 5.84g of calcite remaining with 0.012g of anhydrite formed and 0.013g of dolomite. The formation of the anhydrite will consume 18% of the SO_4^{2-} ions in the brine and the formation of dolomite will reduce the concentration of Mg^{2+} by 44%.

The dissolution and precipitation of different minerals can result in changes to porosity, as the mineral volume increases or decreases. For instance, as the calcite dissolves and anhydrite and dolomite precipitate then the total volume of the residue will change. If the total volume increases, the porosity will then decrease. Consequently, this may have positive impacts in regards to CO_2 storage security, as the reduced flow capacity will in turn reduce the extent of CO_2 migration [22]. Conversely, reduced porosity will mean that greater injection pressure will be needed to displace CO_2 into the formation, should the mineral changes be significant during the injection phase of the storage project.

Rosenbauer et al. (2005) studied the effect that calcite dissolution in limestone, along with anhydrite precipitation, would have on the porosity of the rock. They concluded that changes in porosity were highly dependent on the concentration of SO_4^{2-} in the original brine [20]. In the case of low SO_4^{2-} brine (454 ppm SO_4^{2-}), 10% of the original calcite in the limestone dissolved and the porosity increased by 2.6%. However, when they used a high SO_4^{2-} brine (5100 ppm SO_4^{2-}), the porosity decreased by 4.5%. The SO_4^{2-} concentration in the brine used for this study would therefore be considered low (696 ppm SO_4^{2-}).

Rosenbauer et al. (2005) used a limestone core for their experiments and used core flooding equipment to measure the porosity both before and after the experiments. In contrast, this study used a powder and thus the porosity was measured approximately by calculating any changes in mineral volume. The mineral volume can be calculated by

dividing the molecular weight by density. This value can then in turn be multiplied by the number of moles to obtain the total volume (see Box 6.1).

Box 6.1: Calculated mineral volume of anhydrite

Anhydrite: Molecular Weight = 136.14 g/mol, Density = 2.97g/cm^3

Mineral Volume = 136.16/2.97 = 45.83 cm^3/mol

Moles of Anhydrite = 0.012/136.14 = 0.000089 moles

Volume = 0.000089 × 45.83 = 0.004 cm^3

After 6 months, the overall change in volume from the original calcite sample will be a decrease of 2.3%, and consequently, will result in an increase in porosity. However, it can be said that the effect that long term exposure of CO_2-saturated brine has on porosity of calcite bearing rock is dependent on the original SO_4^{2-} concentrations. Since this brine had a relatively low concentration of SO_4^{2-}, there was less anhydrite precipitation, and consequently, the decrease in mineral volume was mainly associated with the dissolution of calcite. However, had the SO_4^{2-} concentration been high, for example 5100ppm like Rosenbauer et al. (2005), then more anhydrite would have precipitated and the total mineral volume would likely have increased. This would have lead to an increase in mineral volume, and hence, a decrease in porosity as observed by Rosenbauer et al. (2005) [20]. In addition, according to Egermann et al. (2005) the precipitation of anhydrite will also have a significant effect on permeability [104]. Formations that have been subjected to seawater injection as part of secondary oil recovery are likely to have high concentrations of SO_4^{2-} present in the brine, approaching 3,000 ppm [168, 169]. Consequently, when choosing a site for injection it is important to take into consideration the brine composition as well as the composition of the host rock.

6.6 Change in surface area

The specific surface area affects the reaction rates. It is therefore important to observe any changes in surface area. Figure 6.15 shows that after the first month the surface area of the calcite more than doubles after which point there is very little change. Although the surface area remains relatively constant, after the first month there is a slight reduction after 3 months. However, this is likely an error resulting from the BET analysis or because some precipitates have formed on the surface of a few of the calcite particles which has resulted in a reduction in surface area. In fact, from Figure 6.15 it is clear that the third measurement (3 months) is within the experimental error.

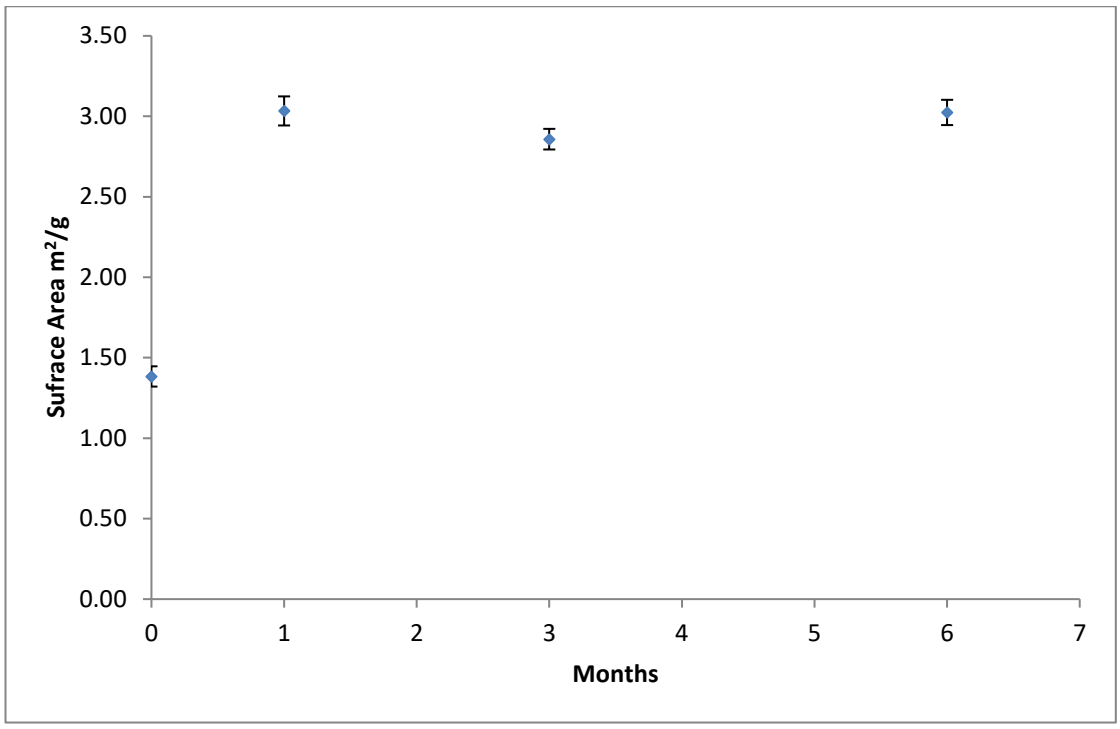

Figure 6.15: BET calculated surface area of calcite

The increase in surface area is likely due to acid etching whereby the acidic H_2CO_3 has dissolved part of the surface of the calcite particles causing small pits to form. The presence of these pits thus increases the surface area of calcite particles. Evidence of acid etching can be seen in Figure 6.16 which shows a 2500 times magnified SEM image of a calcite particle.

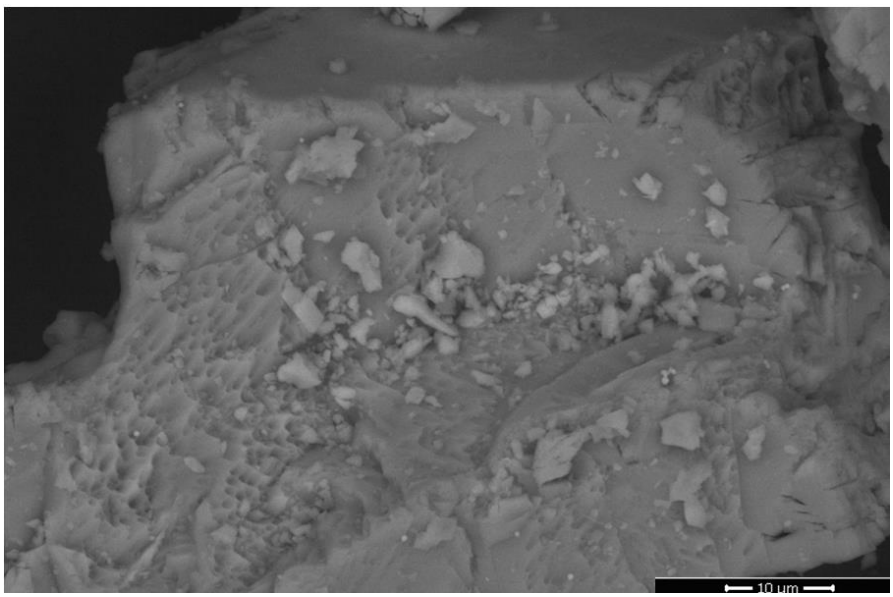

Figure 6.16: SEM image showing acid etching on calcite particle

In addition to providing the surface area, BET analysis can also provide information on the type of porosity i.e. microporous, mesoporous, macroporous or nonporous. This can

be done by identifying the isotherm type as explained in Section 3.2.3. The isotherm plot of the original calcite powder sample (pre-experiment) can be seen in Figure 6.17. It appears to be a Type II isotherm, meaning that the powder is likely nonporous or macroporous (pore size >50nm) [119].

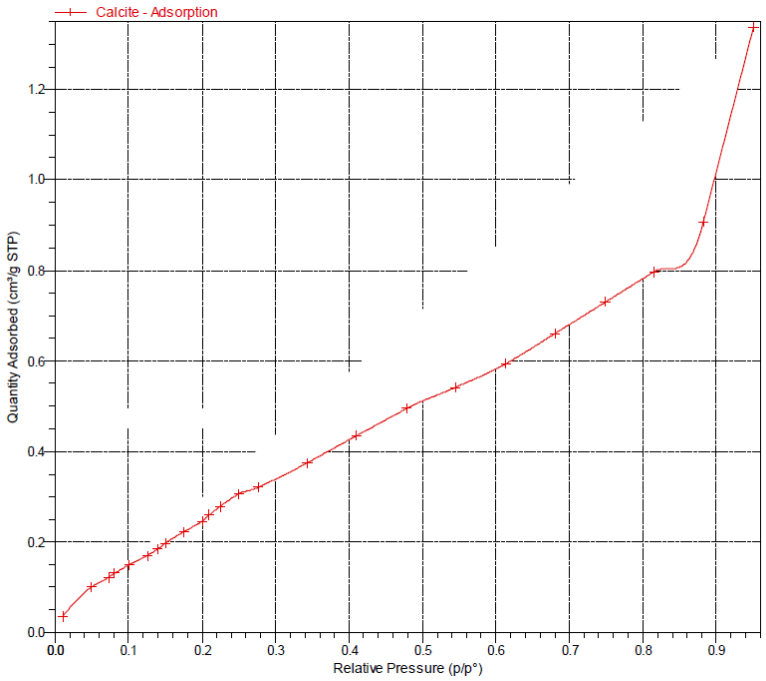

Figure 6.17: Isotherm plot for original calcite powder sample showing Type II isotherm

6.7 Summary

This chapter addressed the lack of experimental work focussing on the interactions between CO_2-saturated brine and calcite bearing host rock over extended periods of time. The objective was to assess calcite's ability to act as a buffer and promote mineral carbonation, as well as how the dissolution of calcite and precipitation of other minerals can affect the porosity of the host rock. This was achieved by performing hydrothermal experiments, involving calcite being exposed to CO_2-saturated brine, over a 6 month period.

In conclusion, the addition of calcite to the brine results in a significant increase in brine pH. However, once CO_2 has been injected, there is only a slight initial increase in pH, after which point the pH begins to drop. Even though the dissolution of calcite leads to the production of HCO_3^-, the pH does not increase above 6. As a result, H_2CO_3 is still the dominant carbonic species, resulting in a weak acid and forcing the pH to drop. **Therefore, it can be concluded that the buffering effect of calcite is not sufficient to promote mineral carbonation. Furthermore, the acidic nature of the H_2CO_3 will result in acid etching on the calcite particles, which will lead to an increase in surface**

area and faster reaction rates. However, this increase in surface area only appears to occur after the first month and after that time the surface area remains relatively constant.

With regards to dissolution and precipitation, there are noticeable deposits of anhydrite, celestite and hematite that are observed in the SEM image after 6 months, but the deposits are not large enough to appear on the XRD. However, the concentrations of SO_4^{2-}, Sr^{2+} and Fe^{3+} in the brine actually increase from 3 to 6 months, which suggests that some of the precipitates are dissolving due to the continuing drop in brine pH. This shows that even after 6 months the system has still not reached equilibrium and many reactions are still taking place. For this reason PHREEQC was used to calculate the system equilibrium.

The PHREEQC modelling studies predict that there will be 5.84g of calcite remaining at equilibrium, in addition to 0.012g of anhydrite and 0.013g of dolomite that will have precipitated. Consequently, there will be an overall decrease in mineral volume of 2.3%, which will result in an increase in porosity. **However, the significance of the change in porosity is dependent on the SO_4^{2-} concentration in the original brine, and so the brine composition needs to be considered before CO_2 injection into reservoirs containing calcite bearing rock.**

Chapter 7 Effect of CO_2-Saturated Brine on Local Host Rock

The objective of this Chapter is to understand the effect that CO_2-saturated brine has on the permeability and porosity of local host rock over an extended period of time (Objective 5). This was done by performing four experiments involving host rock cores exposed to CO_2-satured brine under reservoir conditions (207 bar and 65ºC) for time periods of 1, 3, 6 and 9 months. This Chapter also contains information on the properties of the rock, such as porosity and permeability, as well as the brine composition, both before and after the experiment. In addition, SEM/EDS was used for rock characterisation and Micro CT scans were preformed to provide a visual interpretation of how CO_2 saturated brine affects rock integrity.

7.1 Characterisation of host rock

As stated in Section 3.3, four core samples were provided by the Institute of Petroleum Engineering from a reservoir located in the UK Continental Shelf. The permeability and porosity of each core was measured both before and after the experiments by the FAST group at Heriot-Watt University, using the techniques described in Section 3.3.1 and the results are presented in Table 7.1. The porosity was calculated using Equation 3.3, where the absolute pore volume (Abs PV – Table 7.1) was divided by the volume of the core, assuming that each core was a cylinder with diameter 3.81cm and length, as presented in Table 7.1. The error in the permeability measurements is approximately 7% and the error in the absolute pore volume is ±0.5ml. This information was provided by the FAST group.

Table 7.1: Measured permeability and porosity of cores before and after experiments

	Length (cm)	**Permeability (mD)**		**Abs PV (ml)**		**Porosity (%)**	
		Before	**After**	**Before**	**After**	**Before**	**After**
Core D 1 month	1.712	196	159	6.41	4.43	32.16	22.70
Core C 3 months	1.380	131	85	5.50	3.58	32.24	22.75
Core B 6 months	2.598	144	117	9.08	6.65	30.01	22.45
Core A 9 months	2.534	152	88	9.25	6.60	31.34	22.85

After the permeability and porosity values were measured, the cores were sent for Micro-CT scans at the University of Aberdeen. These images can be found in Section 7.2 which shows a comparison of the scanned images both before and after the experiments. Each of the four cores was cut from a single plug of rock. This resulted in a small section of the plug being left over which could be analysed using SEM/EDS. This section was cut and a polished resin thin section was prepared for SEM/EDS analysis. The cores used for the experiments (A-D) could not be analysed by SEM/EDS until after the experiments had taken place, as the process requires the cores to be cut first. This was why a section of the original plug was used for the initial analysis, which will give a good indication as to what can be expected in the rest of the cores.

Figure 7.1 shows the SEM image taken of this section of the original plug. Clear areas of Ca, Mg, Fe, K, Na and Si can be seen. Using the SEM image in conjunction with EDS a phase analysis was performed which gave an indication as to what was contained within the area of thin section. The software used to perform the phase analysis was Scandium M, which detects and then uses the different greyscales in the image to identify and quantify minerals [170]. According to the phase analysis, 57.40% of the area contained quartz, 10.70% was clays (such as kaolinite) and 8.65% was feldspars, micas and calcite. The remaining 23.25% of the area, which can be seen as black spaces (see Figure 7.1), is considered to be porous by the Scandium M software. The porosity is lower than the measured porosity of the four cores before the experiments (Table 7.1). However, it only relates to the porosity of a single thin section of rock, rather than an entire core and is calculated by measuring the area occupied by black spaces between the minerals.

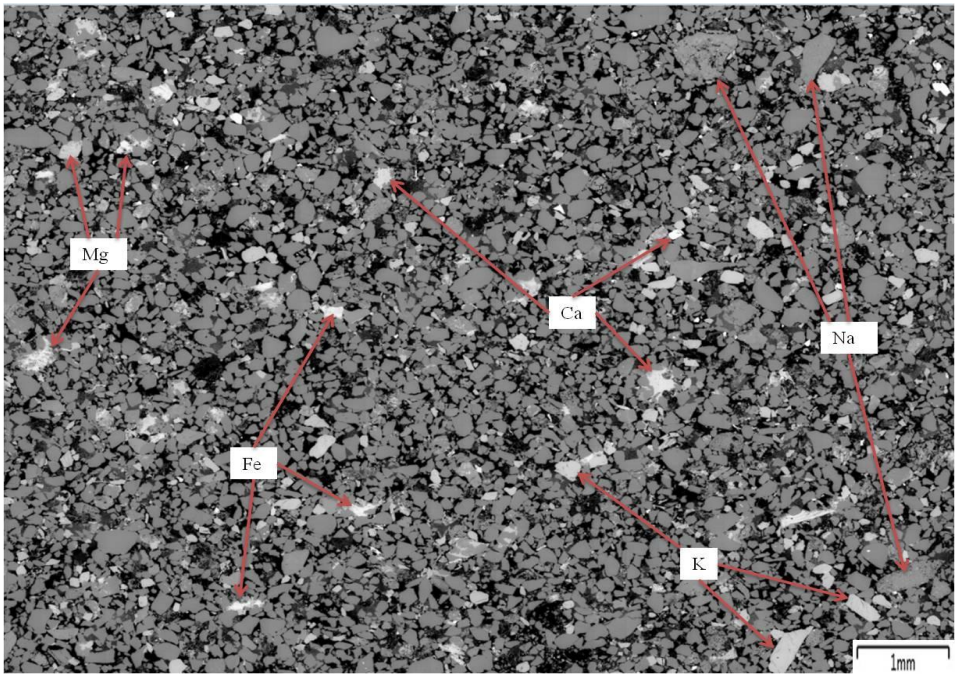

Figure 7.1: SEM image showing piece from original host rock plug

7.2 Characterisation of host rock post experiment

7.2.1 Changes in brine composition

Table 7.2 displays the initial brine composition, the final brine composition after the experiments and the SD, which is calculated using Equation 5.1. The results from Table 7.2 show large reductions in the concentration of Na^+ and K^+ ions in the brine after 1 and 3 months, which are likely due to the formation of precipitates such as halite and sylvite. Although the Na^+ and K^+ concentrations are still lower than the starting concentrations, after 6 months the concentration of these ions in the brine begins to rise again and after 9 months the K^+ concentrations are almost back to the original concentration. This could be a result of the acidic nature of the brine, where initially there is a large amount of precipitation, but over time the carbonic acid re-dissolves said precipitates.

As for the Mg^{2+} and Ca^{2+} concentrations, there is a clear trend of increasing concentration with time. The one exception is Core C where the Ca^{2+} concentration is slightly lower than for Core D and is likely due to there being less Ca present in Core C compared with Core D. Figure 7.1 showed the presence of Mg and Ca in the sample core. As previously stated, this sample core would give a good indication as to what can be expected in the rest of the cores. Consequently, as time goes on, more Mg and Ca bearing minerals will dissolve due to the acidic nature of the brine and so the Mg^{2+} and Ca^{2+} concentrations in the brine will increase, as seen in Table 7.2.

This also has a distinct effect on the brine pH, as shown in Figure 7.2. As described in Section 6.3, the acidic nature of the brine initially causes the brine pH to drop, but as time goes on the dissolution of calcite and the formation of HCO_3^- buffers the pH. The changes in brine pH directly correspond to the increase in Ca^{2+} concentrations as can be seen in Figure 7.2. After the first month there is a slight drop in brine pH as it can be assumed that the concentrations of HCO_3- is not high enough to buffer the acidic brine. As previously stated, the Ca^{2+} concentration after 3 months is actually lower than after the first month and hence the pH drops further. However, Figure 7.2 shows a large increase in Ca^{2+} concentrations after 6 and 9 months and the brine pH increases accordingly. As with the CO_2-brine-calcite experiments, all brine pH measurements were taken under ambient conditions. Following this trend and assuming there is more calcite in the rock to dissolve, it is possible that the brine pH would be further buffered to or above its initial pH before CO_2 injection.

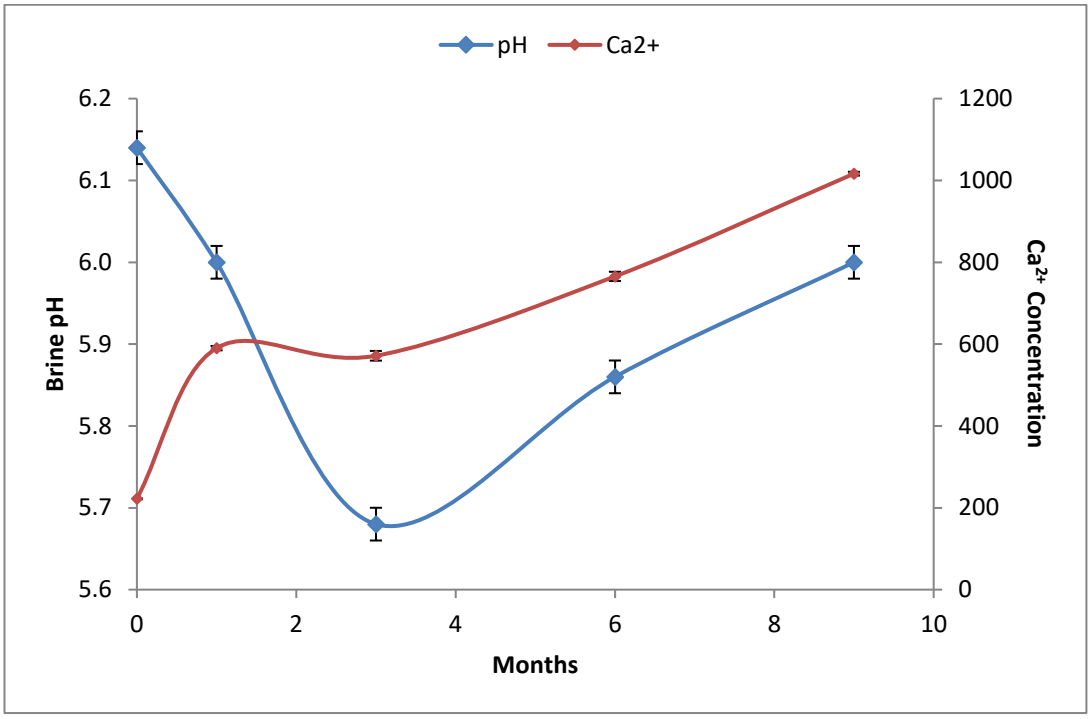

Figure 7.2: Measured brine pH and Ca^{2+} concentrations after each experiment

In addition to the increase in Mg^{2+} and Ca^{2+}, there is also an increase in Sr^{2+}, Fe^{3+} and SO_4^{2-} ions in the brines. The overall increase in Sr^{2+} is very low (no greater than 3mg/l) and in fact the SEM/EDS of the sample core did not detect any Sr present. Therefore it is likely, either a result of the dissolution of minute Sr bearing minerals or could be a possible contamination. The Fe^{3+} concentrations are equally low, except for Core A where they are slightly higher, but still only 10mg/l. Unlike with Sr^{2+}, Fe^{3+} can be accounted for from the SEM, seen in Figure 7.1. As for SO_4^{2-}, there was none detected using the

SEM/EDS. However, from Table 7.2, it is clear that sulphates have dissolved. Although the SEM/EDS did not detect any S, the presence of sulphates can be expected as they are commonly found as a cementing agent in sandstones [171].

Table 7.2: ICP-OES results showing brine composition before and after host rock experiments

		Na^+ (mg/l)	**K+ (mg/l)**	**Mg^{2+} (mg/l)**	**Ca^{2+} (mg/l)**	**Sr^{2+} (mg/l)**	**Fe^{3+} (mg/l)**	**SO_4^{2-} (mg/l)**
Core D 1 month	Initial	19248	289	88	222	0	0	0
	Final	**11781**	**162**	**220**	**590**	**2**	**>1**	**227**
	SD	158.86	1.95	2.69	5.36	0.05	0.03	2.64
Core C 3 months	Initial	19248	289	88	222	0	0	0
	Final	**11033**	**144**	**276**	**572**	**3**	**2**	**226**
	SD	37.08	0.39	3.00	11.83	0.02	0.01	3.59
Core B 6 months	Initial	19248	289	88	222	0	0	0
	Final	**12371**	**166**	**330**	**766**	**3**	**>1**	**139**
	SD	414.66	2.81	3.70	11.29	0.04	0.05	1.28
Core A 9 months	Initial	19248	289	88	222	0	0	0
	Final	**14240**	**286**	**605**	**1017**	**3**	**10**	**351**
	SD	100.64	4.25	4.88	4.65	0.04	0.02	0.89

7.2.2 Dissolution and precipitation of minerals

From the previous section, it is clear that both dissolution and precipitation of minerals has taken place after each time step. After the experiments were completed and the permeability and porosity of each core were measured and Micro-CT scans taken, polished resin thin sections of each core were prepared and analysed using SEM/EDS. As with the original sample, each SEM image was used in conjunction with EDS to produce a phase analysis. Table 7.3 shows the phase analysis performed for each image using Scandium M and Figures 7.3-7.6 show the SEM images for each core. It should be noted that the phase analysis only gives an indication as to the percentage of each mineral phase

present. This analysis is not entirely accurate, as it relies on the software distinguishing between different grey scales. However, it does allow for trends to be observed, such as overall variations in mineral phase concentrations.

The amount of quartz detected (Table 7.3) in the phase analysis will be overestimated as the software has difficulties distinguishing between Si present in quartz or in the feldspars and clays. There is a noticeable increase in clays (such as kaolinite) which will likely be a consequence of feldspar weathering [172]. The change in feldspar, mica and calcite quantity is variable. A possible explanation is that after the first 3 months (Cores D and C), Na-micas such as paragonite are forming. This is in agreement with the large decrease in Na^+ concentration seen in Table 7.2. However, as time goes on, more feldspars are transformed into clay through weathering. This weathering can be seen in Figure 7.7. This leads to an increase in Na^+ concentration in the brine (Table 7.2). In addition, the Ca^{2+} concentration in the brine also increases over time as more calcite is dissolved, which would further decrease the quantities of feldspars and calcite detected. The quantity of clay is much lower than expected after 9 months (Core A), but the amount of quartz is also a lot higher. Therefore, it is likely that the software is confusing the Si present in quartz with the Si in clay.

Table 7.3: Phase analysis of each core after experiments

	Quartz %	**Clays %**	**Feldspars, Micas and Calcite %**	**Porosity %**
Original	57.40	10.70	8.65	23.25
Core D (1 month)	62.93	15.93	9.99	9.59
Core C (3 months)	62.02	16.85	10.40	9.21
Core B (6 months)	63.42	16.45	5.91	13.41
Core A (9 months)	68.74	9.86	5.04	14.48

Figures 7.3-7.6 show the SEM images for Cores D-A (1-9 months) respectively. Just like the original sample (Figure 7.1), the presence of Na, K, Ca, Mg and Fe are detected in each image.

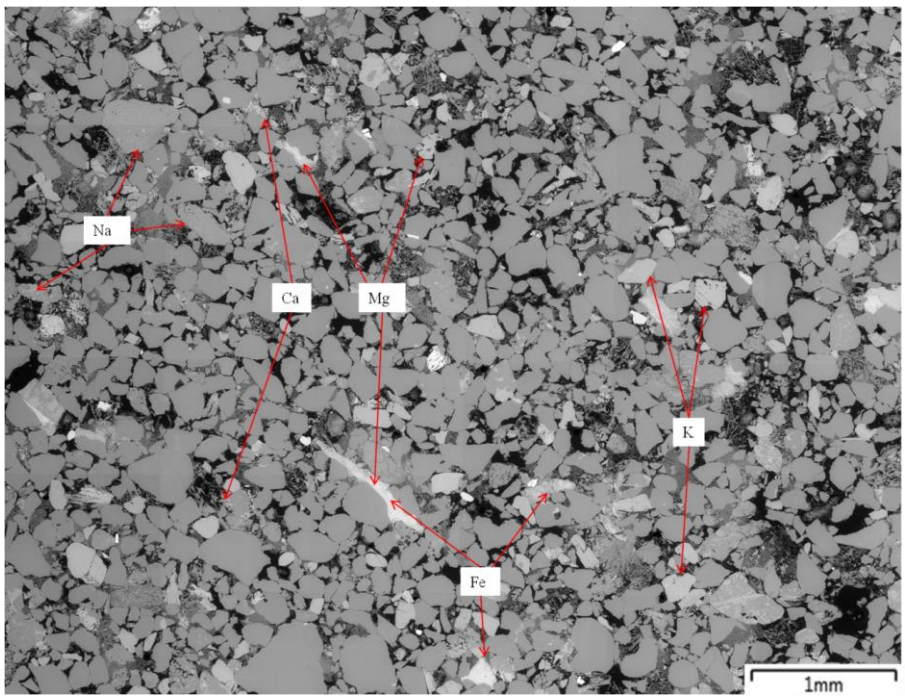

Figure 7.3: SEM image of Core D (1 month) after experiment

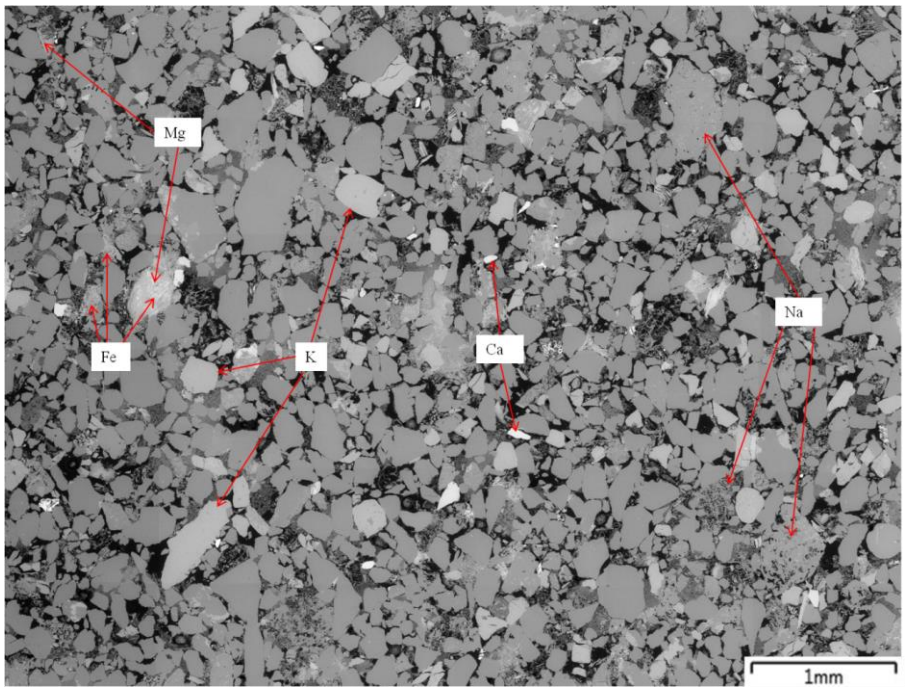

Figure 7.4: SEM image of Core C (3 months) after experiment

However, as time goes on the EDS maps show a noticeable decrease in the amount of Ca present, which corresponds with the increase in Ca^{2+} concentration in the brine (Table 7.2), as a result of the dissolution of calcite or other Ca-bearing minerals. Mg quantities are also reduced and the remaining Mg in the SEM images appears in conjunction with Fe. These minerals appear bright on the SEM and so are likely Mg-Fe rich clays.

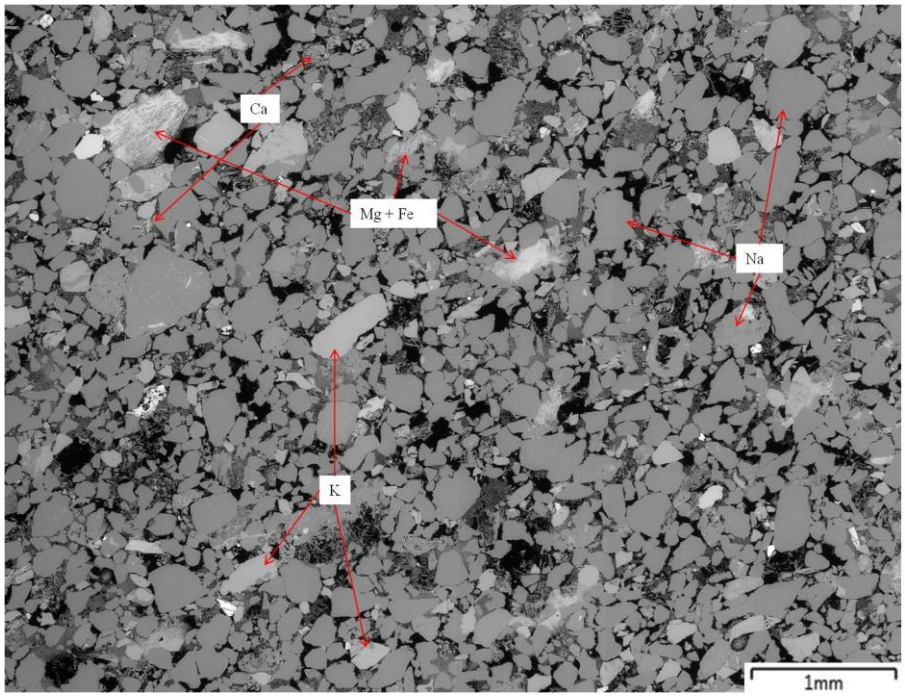

Figure 7.5: SEM image of Core B (6 months) after experiment

The presence of S was still not detected. It is likely that the quantity of S-bearing minerals is too low to be detected with the SEM at the current resolution, as a few hundred ppm (Table 7.2) is not a large amount. Increasing the resolution could lead to the detection of S but this would greatly increase the scan time which was not feasible for this work.

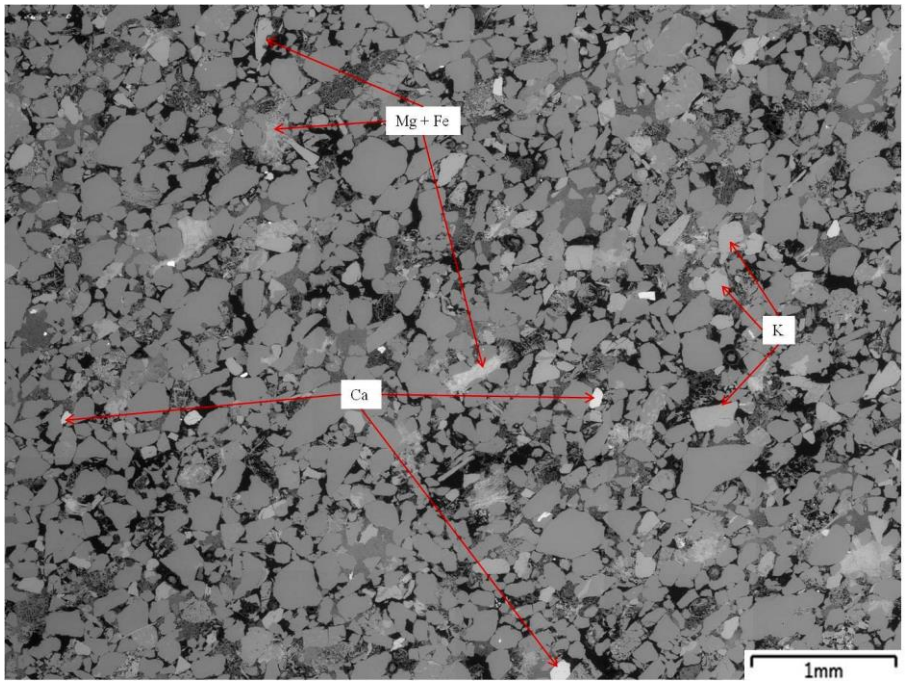

Figure 7.6: SEM image of Core A (9 months) after experiment

From the EDS map it was difficult to see any noticeable increase in Na quantities when compared with the original image (Figure 7.1). This was due to the large amount of Na

present in all cases. However, weathering of Na-bearing minerals was clear over time. Figure 7.7 shows examples of weathering after 1 month (Core D) and 6 months (Core B). The weathering effect is clearly more pronounced after 6 months, as the feldspar has been exposed to acidic brine for a longer period of time.

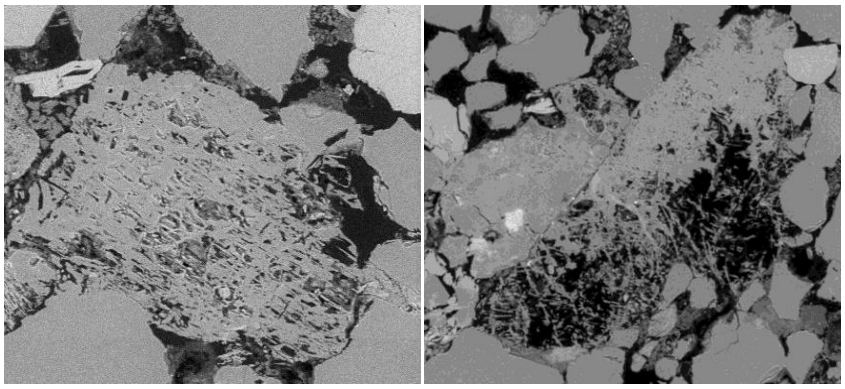

Figure 7.7: SEM images showing weather after 1 month (left) and 6 months (right)

In addition to the SEM images, physical changes in the rock can be seen from the Micro CT scans. The final scans were performed at the University of Edinburgh and even though there is a noticeable difference in resolution, a comparison can still be made with the scans performed at the University of Aberdeen. Figure 7.8 shows two images of Core D both before and after the experiment. It can be seen that there are clear markers on both the pre and post experiment images (blue circles) that show that these images are from the same section of rock and allow for the images to be compared. The red circles highlight precipitates that have formed during the experiment or where dissolution of original minerals has taken place.

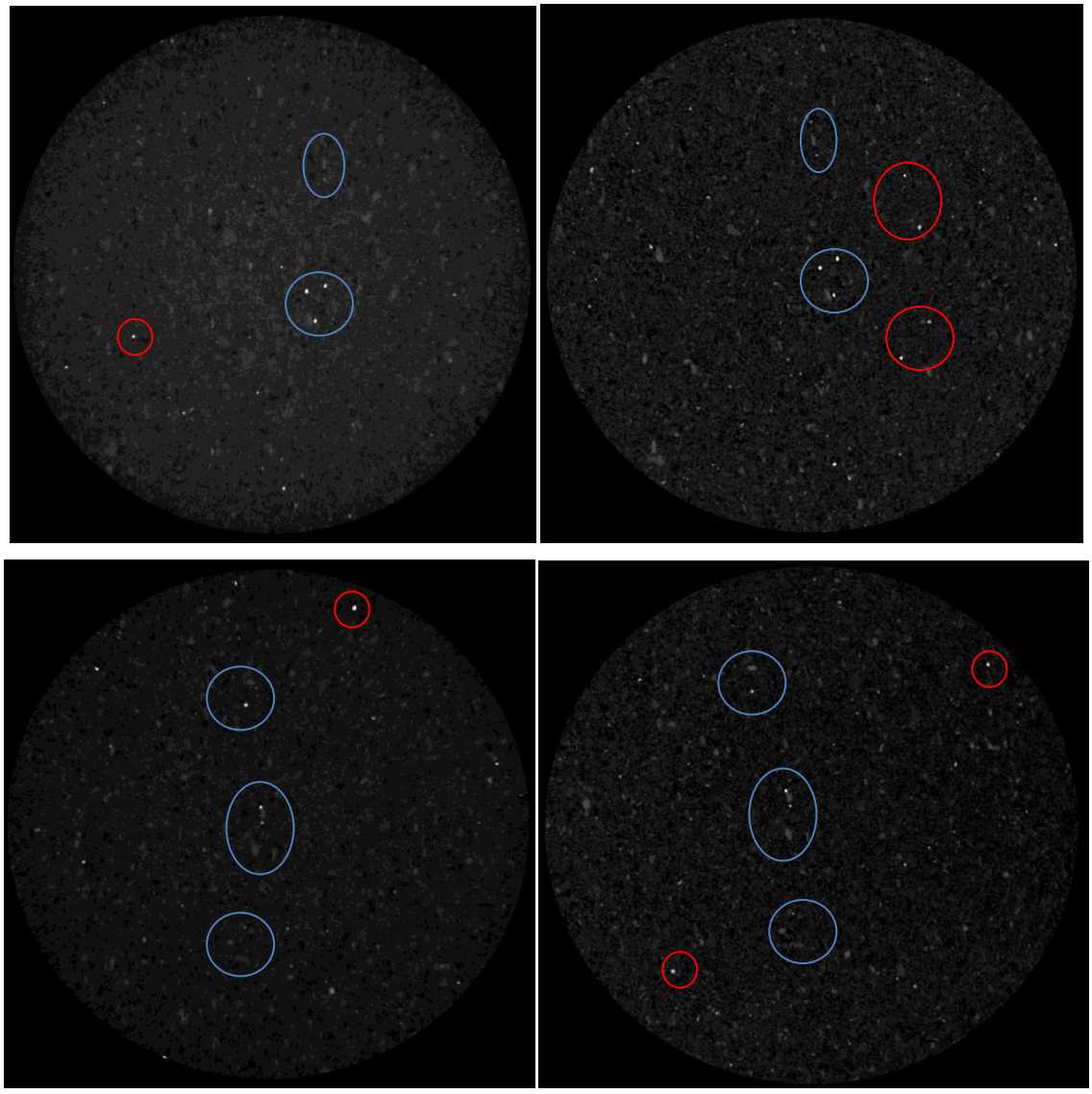

Figure 7.8: Micro CT images of Core D (1 month), before (left) and after (right) experiment

Figure 7.8 clearly shows that both dissolution and precipitation have taken place over a one month period. Although these scans are unable to provide information on what has dissolved or precipitated, they do provide a visual interpretation of how CO_2-saturated brine affects the structure of the host rock. The Micro CT images for Core C (3 months), shown in Figure 7.9, show similar results as Figure 7.8.

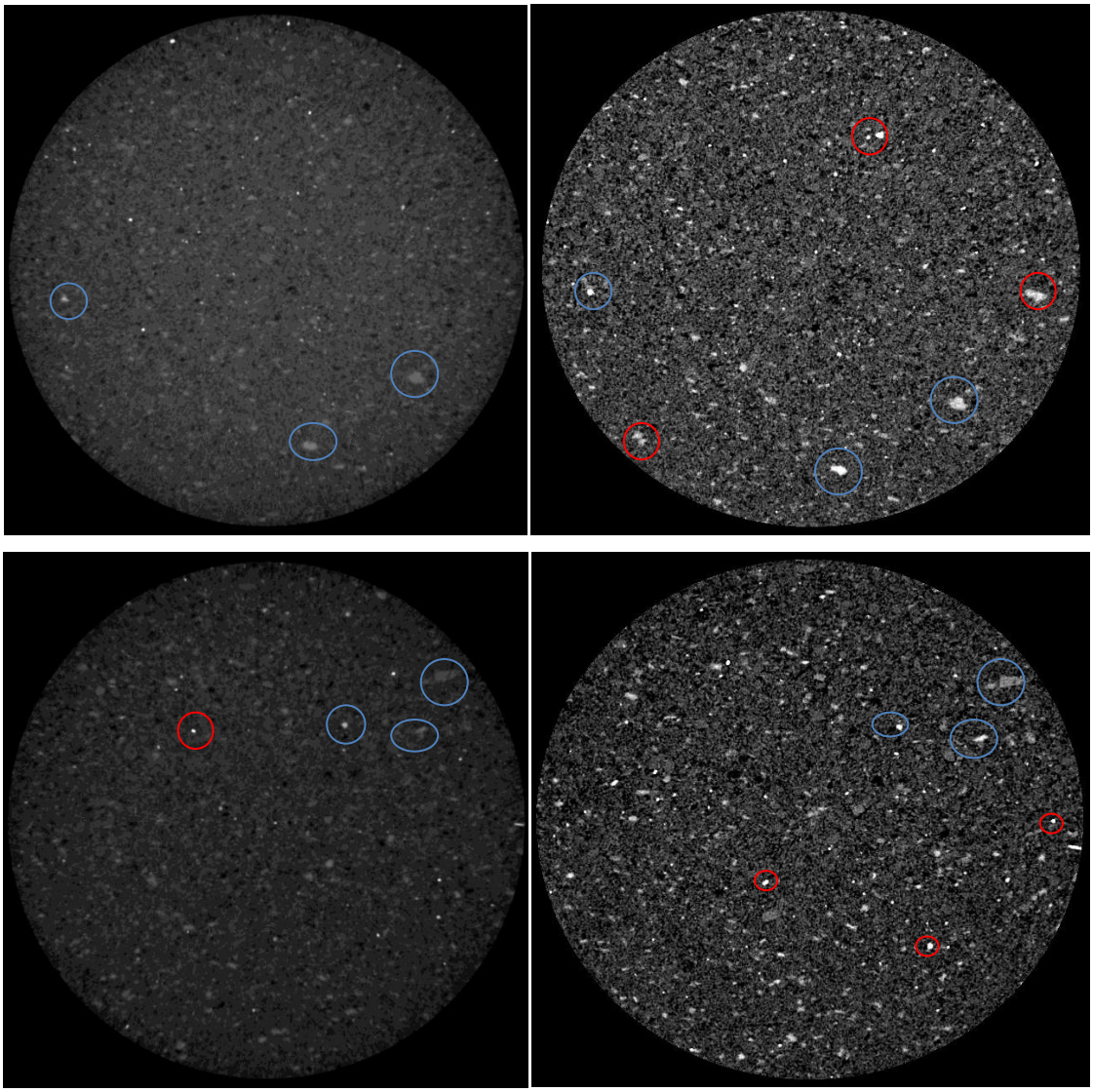

Figure 7.9: Micro CT images of Core C (3 month), before (left) and after (right) experiment

Figures 7.10 and 7.11 show the Micro CT images for both Core B (6 months) and Core A (9 months). As with the previous two figures there are noticeable formations of precipitates, as well as dissolution of minerals after the experiments. Consequently, Micro CT has been an effective tool to provide a visual interpretation of how CO_2 saturated brine affects the host rock.

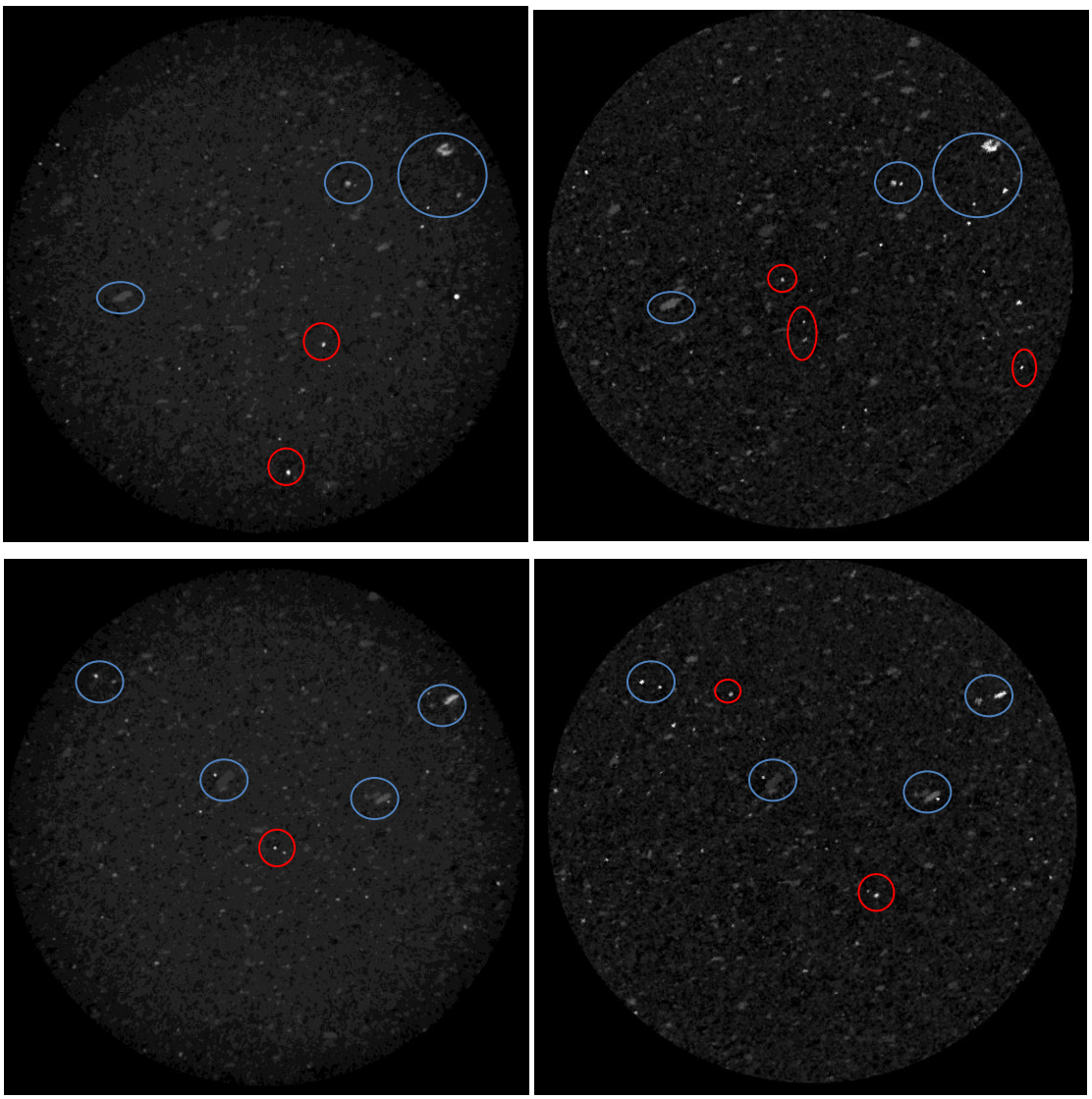

Figure 7.10: Micro CT images of Core B (6 month), before (left) and after (right) experiment

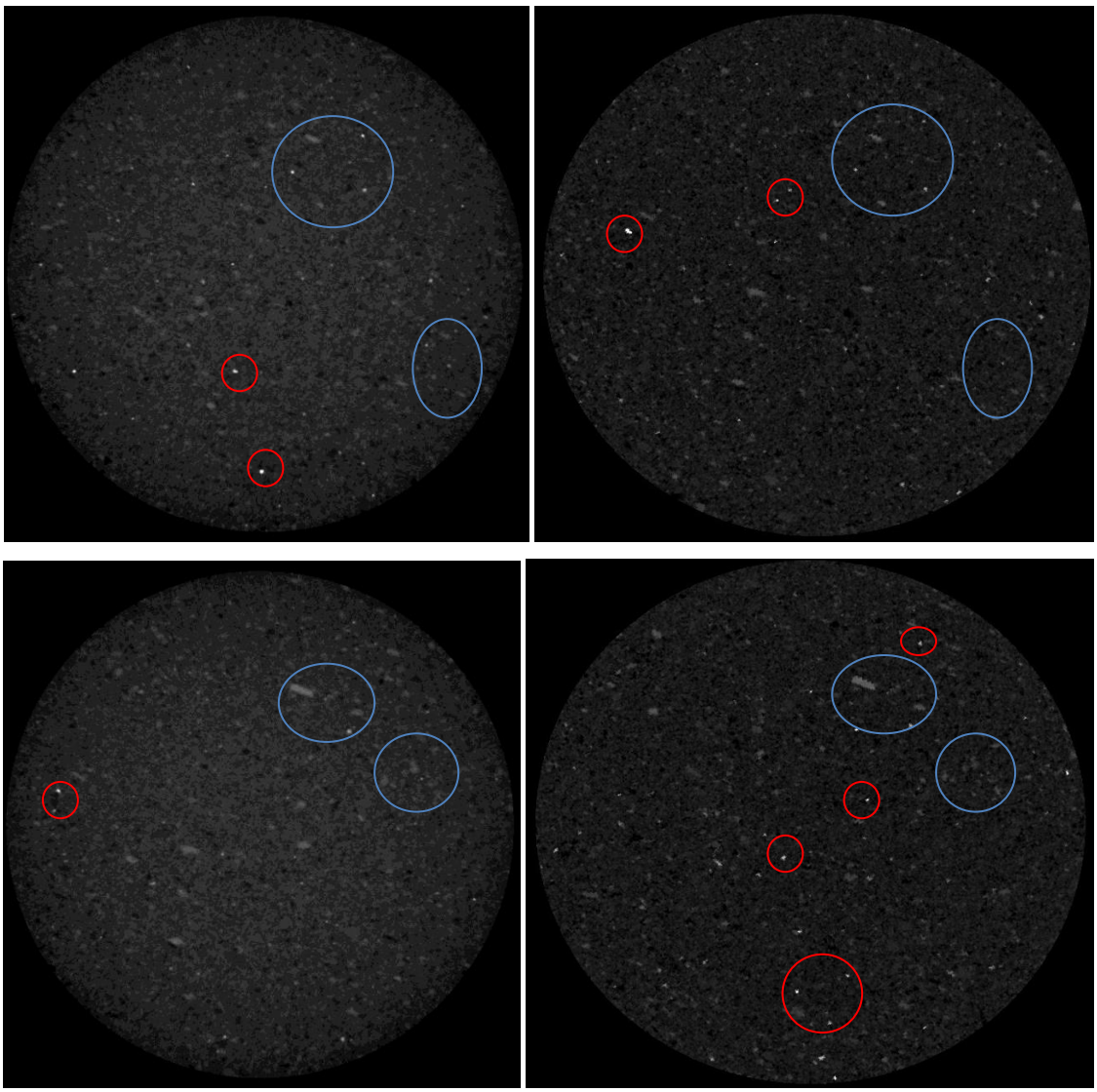

Figure 7.11: Micro CT images of Core A (9 months), before (left) and after (right) experiment

7.2.3 Changes in rock porosity and permeability

The previous two sections have highlighted the changes in both brine and rock chemistry through the precipitation and dissolution of minerals. Table 7.1 describes how these changes in rock chemistry have affected the permeability and porosity of the rock. From Table 7.1, it is clear that exposure to CO_2-saturated brine has a noticeable effect on both the permeability and porosity of local host rock.

In regards to porosity, there is a large decrease after the first month, but then remains relatively constant thereafter (Table 7.1). Changes in porosity, as well as permeability, have a distinct affect on CO_2 storage [22]. Reduction in porosity and permeability means that higher injection pressure will be needed to displace CO_2 into the formation. On the other hand, the reduced porosity and permeability will reduce the extent of the CO_2 migration, due to reduced flow capacity, which will increase storage security. The

knowledge that the there will be an initial decrease in porosity after the first month of injection, but will thereafter remain relatively constant will be very useful when considering the long term storage of CO_2. The decrease in porosity is likely a consequence of the formation of clays, as seen from Table 7.3. These clays form as a result of feldspar weathering [172]. In addition, Table 7.2 shows that the concentration of Na^+ has dropped considerably for each brine, by approximately 5,000-7,500mg/l. It was first assumed that halite formation was occurring, but there was no evidence of Cl present in the EDS maps. Therefore, the drop in Na^+ concentration in the brine is likely a result of the formation of Na-micas such as paragonite. This overall increase in the amount of mineral phases present (as observed in Table 7.3) has lead to a large decrease in porosity (Table 7.1).

The dissolution of Mg, Ca and S bearing minerals, which is evident from Table 7.2, would have the opposite affect and result in an increase in porosity and will have offset some of the porosity reduction resulting from the formation of clays and Na-bearing minerals. In relation to previous work, Lamy-Chappuis et al. (2013) injected CO_2-satured brine into sandstone where 4-5 wt% of the rock consisted of calcite [173]. They noted 5-15% increase in porosity due to the acidic carbonic acid dissolving the calcite in the sandstone. Nover et al. (2013) also noted a slight increase in rock porosity (<2%) when injecting CO_2-satured brine into sandstone due to the dissolution of minerals which was evident by the increased concentrations of Ca, Al, K and Mg in the brine after the experiment [174]. As previously stated, Table 7.2 shows that the dissolution of Mg, Ca and S bearing minerals has taken place, which would result in a relative increase in porosity which is in agreement with previous work. Therefore, the decrease in porosity seen here, which conflicts with previous work, is a direct result of the formation of clays and paragonite.

As well as porosity, the permeability of each core decreased after the experiments. Unlike with porosity, the reduction in permeability is different for each core. Just like porosity, the permeability of the porous media is affected by the dissolution and precipitation of minerals, due to changes in solid phase volume [175]. Both Lamy-Chappuis et al. (2013) and Nover et al. (2013) reported that in their experiments, the permeability increased as well as the porosity [173, 174]. However, this is not always the case. Iglauer et al. (2014), who measured the changes in permeability of sandstone due to the injection of CO_2-saturated brine, recorded a decrease in permeability [176]. The reduction in permeability was associated with the release of quartz fines and the resulting clogging of pore throats. Berrerzueta et al. (2016), also stated that pore changes can be due to detachment of quartz fines in the rock matrix [177]. This could explain why, even though the permeability

decreased like the porosity, the decrease in permeability isn't uniform. Quartz fines are not the only fines responsible for pore throat clogging. Pudlo et al. (2015) concluded that the migration of clay fines can also reduce permeability [178]. Table 7.3 showed an increase in quantities of clay present in the rock and the resulting clay fines will have likely contributed to the reduction in permeability observed.

The reduction in permeability of Core B (6 months) is noticeably lower than that of the other cores. A possible explanation is the dissolution of cements which in turn results in the release and migration of quartz fines. The SO_4^{2-} concentration in the brine after the 6 month experiment (Table 7.2) is much lower than what is observed in other experiments. As previously stated, S bearing minerals such as anhydrite can act as cements [171]. Therefore, higher dissolution of S minerals will likely lead to a larger reduction in permeability due to the release and migration of quartz fines. This would explain why the reduction in permeability, observed after 6 months, is lower than expected.

7.3 Summary

This study has shown that CO_2-saturated brine has a significant effect on the porosity and permeability of a host rock from a reservoir located in the UK Continental Shelf. In this case, four cores were subject to CO_2 saturated brine under reservoir conditions (207 bar and 65°C) for time periods of 1, 3, 6 and 9 months. In each case, the ICP-OES analysis of the brines showed that after each experiment there had been a significant reduction in Na^+ concentrations in the brine, along with increases in Ca^{2+}, Mg^{2+} and SO_4^{2-} concentrations. This is consistent with the formation of clays and Na-bearing minerals, as well as the dissolution of Ca, Mg and S bearing minerals in the rock.

In this study, the formation of clays and Na-bearing minerals (such as paragonite) has lead to a significant reduction in porosity. The permeability has also been reduced in all cases, which is likely a consequence of pore throats being clogged due to the migration of fines. Therefore, for this particular reservoir, greater injection pressure will be needed to displace CO_2 into the formation, but the migration of the CO_2 plume will also be reduced, which will increase storage security [22]**.**

Chapter 8 Conclusions and Future Work

This final Chapter provides a summary of the results and conclusions of this study, as well as how the aim and objectives of this study were achieved. In addition, Section 8.2 looks at how this work could be improved upon and expanded through future studies.

8.1 Conclusions

The aim of this study was to investigate how brine composition affects CO_2 geochemical trapping mechanisms and the effect that CO_2-saturated brine has on the permeability and porosity of host rock. This was achieved through experimental and geochemical modelling work, where real brine data from North Sea oil wells was used to produce synthetic brines. Experiments were then performed under reservoir conditions to simulate interaction between, CO_2, brine and host rock in a real reservoir. Geochemical modelling was used in conjunction with experimental work to corroborate the experimental data and calculate the equilibrium state.

8.1.1 Objective 1: Selecting geochemical modelling software

Three different geochemical modelling software programs, HydraFLASH, PHREEQC and the Dun and Sun CO_2 solubility model, available to measure CO_2 solubility in brine as well as mineral trapping potentials were assessed. This was done to determine which software would be the most appropriate to use for the geochemical modelling in this study. It was concluded that HydraFLASH was a very effective all round model, able to match the accuracy of the Duan and Sun model in CO_2-water and CO_2-water-salt systems, but could also be used to accurately calculate CO_2 solubility in brine under reservoir conditions. To produce accurate results, HydraFLASH does require the correct EoS to be chosen and it was concluded that for CO_2-brine systems, the Valderrama-Patel-Teja EoS is the most effective. As a result, HydraFLASH was selected to model CO_2 solubility in brine under reservoir conditions for this study. Unfortunately, due to its inability to measure mineral trapping potentials, PHREEQC had to be used in conjunction with the llnl.dat database to calculate the equilibrium phases. Consequently, both HydraFLASH and PHREEQC were used throughout this study to assess geochemical trapping mechanisms on a geological timescale and to validate experimental data, as per Objective 1.

8.1.2 Objectives 2 and 3: The importance of well selection using a high pressure rig

Objective 2 was to produce a number of synthetic brines using real North Sea oil field data and to measure geochemical trapping potentials through geochemical modelling and

experiments involving CO_2 and brine under reservoir conditions (Objective 3). The results were then used to ascertain the importance of well selection. It was concluded that wells containing low salinity brine with small ion charge should be selected over high salinity wells for geochemical trapping. This was due to the correlation between brine salinity, ion charge and CO_2 solubility and the fact that in this study, CO_2 solubility accounted for 97-99% of geochemical trapping. In addition, wells that have yet to undergo seawater flooding will have considerably reduced concentrations of SO_4^{2-}, and hence, more Ca^{2+} and Sr^{2+} ions will be available to form mineral carbonates rather than anhydrite or celestite which will form if SO_4^{2-} is present.

In conclusion, wells containing low salinity brine with small ion charge are always preferable to high salinity wells for geochemical trapping and this also confers to pre-seawater flooding as after seawater flooding the brine salinity will have increased. Consequently, to increase mineral trapping potentials, not only is it vital to maintain a pH greater than 9, but the concentration of SO_4^{2-} in the brine should preferably be as low as possible. Therefore, for maximum geochemical trapping potential, wells containing low salinity brine with relative high concentrations of Mg^{2+}, Ca^{2+} and Sr^{2+} should be selected. In addition, geochemical trapping potentials can vary within the same field as a consequence of the composition of the brine present at individual wells. Hence, this study has shown the importance of well selection in regards to geochemical trapping potentials.

8.1.3 Objective 4: Calcite's potential to buffer brine and promote mineral trapping

The purpose of Objective 4 was to assess calcites potential to buffer brine and promote mineral carbonation, as well as how the dissolution and precipitation of minerals can affect the properties of the host rock, such as porosity. It was determined that when calcite was added to the brine it acted as a buffer, raising the pH from 2.03 to 5.72. However, once CO_2 was injected, there was only a slight initial increase in pH to 5.77 after the first month and then the pH began to drop. After 6 months, the pH had dropped to 5.55. Therefore, it was concluded that calcite could not act as a sufficient buffer to raise the brine pH to >9 and hence promote mineral carbonation. In addition, the SEM images revealed the presence of acid etching which was due to the acidic nature of the H_2CO_3. This resulted in the surface area of the calcite powder more than doubling after the first month ($1.38 m^2/g$ to $3.03 m^2/g$) and remaining relatively constant thereafter.

The formation of anhydrite, celestite and hematite was observed after 3 months, although dissolution and precipitation were still taking place after 6 months. Subsequently, the

system had yet to reach equilibrium and so geochemical modelling using PHREEQC was performed to calculate the equilibrium state. According to the PHREEQC modelling studies, there will be 5.84g of the original 6g of calcite remaining at equilibrium with the addition of 0.012g of anhydrite and 0.013g of dolomite. This will result in an overall decrease in mineral volume of 2.3%, leading to an increase in porosity. The significance of the change in porosity is dependent on the SO_4^{2-} concentration in the original brine. Therefore, as with well selection for maximising geochemical trapping potentials, it is important to consider the brine composition before injecting CO_2 into reservoirs containing calcite bearing rock.

8.1.4 Objective 5: Effect that CO_2-satured brine has on local host rock

Objective 5 looked at the potential effect that CO_2-saturated brine has on the permeability and porosity of local host rock over a period of up to 9 months. It was observed that Ca, Mg and S-bearing minerals would dissolve over time due to the acidic nature of the carbonic acid. However, the initial decrease in brine pH would be offset due to dissolution of calcite and the formation of HCO_3^-, resulting in the pH increasing from 5.68 after 3 months to 6.00 after 9 months. The acidic nature of the brine also lead to the formation of clays as a result of feldspar weathering. This weathering was observed in the SEM images taken of the cores after the experiments. Both the formation of clays and Na-bearing micas such as paragonite lead to a decrease in porosity. The reduction in porosity was recorded for all four cores, but remained relatively constant after the first month. The migration of clay fines, along with quartz fines also resulted in a decrease in permeability in all cores, as a consequence of pore throat clogging.

This study has shown that CO_2-saturated brine has a significant effect on the porosity and permeability of local host rock. The reduction in porosity, observed here, is in conflict with previous work [173, 174]. However, this study has shown that the decrease in porosity in this case is a result of the formation of clays and Na-bearing minerals. Therefore, it cannot be assumed that in all cases the exposure of CO_2-satured brine to host rock will result in an increase in porosity, as observed in previous work. This is important as it means that individual case studies should be performed for any potential CO_2 injection site to see what affect it will have on the porosity of the local host rock. In addition, there was a recorded decrease in rock permeability after each experiment. When injecting CO_2 into a formation, a decrease in initial porosity and permeability will lead to greater injection pressures needed to displace CO_2 into the formation. On the other hand, in regards to CO_2 geological storage, there will be reduced migration of the CO_2 plume,

which will lead to increased storage security. Therefore, the information obtained in this study will be very useful when considering the long term storage of CO_2.

8.2 Future Work

Based upon the conclusions of this work, there are a number of further studies leading to new avenues of research, including:

1. To measure CO_2 solubility in brine experimentally using one of the methods described in Section 2.6, instead of solely through geochemical modelling.
2. For the mineral carbonation experiments, to identify a buffer that is able to maintain the pH above 9 for the duration of the experiments.
3. To calculate mineral equilibrium phases using more complex software programs like TOUGHREACT or EQ3/6 that consider complex ion exchange and multiphase flow, rather than PHREEQC.
4. To Perform the CO_2-brine-calcite experiments (Chapter 6) using limestone cores instead of powder, so that the porosity and permeability can be accurately measured both before and after the experiments.
5. To use a coreflood rig for the host rock experiments (Chapter 7) so that porosity and permeability measurements could be taken in-situ rather than performing batch experiments.

References

[1] IEA, “Key World Energy Statistics 2016,” 2016. [Online]. Available: https://www.iea.org/publications/freepublications/publication/KeyWorld2016.pdf. [Accessed 6 October 2016].

[2] IEA, “Key World Energy Statics 2013,” 2013. [Online]. Available: http://www.iea.org/publications/freepublications/publication/KeyWorld2013_FINAL_WEB.pdf. [Accessed 6 January 2014].

[3] BP, “BP Statistical Review of World Energy June 2016,” 2016. [Online]. Available: http://www.bp.com/content/dam/bp/pdf/energy-economics/statistical-review-2016/bp-statistical-review-of-world-energy-2016-full-report.pdf. [Accessed 22 June 2016].

[4] A. C. Todd, Reservior Engineering Lecture Notes, Edinburgh: Heriot-Watt, Institute of Petroleum Engineering, 2013.

[5] P. Geiger, “CO2-EOR and Sequestration in Wyoming,” in *4th Annual EOR Carbon Management Workshop*, Houston, 2006.

[6] National Enhanced Oil Recovery Initiative, “Carbon dioxide enhanced oil recovery: A critical domestic energy, economic and environmental opportunity,” National Enhanced Oil Recovery Initiative, 2012.

[7] V. Kuuskraa and M. Wallace, “CO2-EOR set for growth as new CO2 supplies emerge,” *Oil & Gas Journal,* vol. 112, no. 4, 2014.

[8] NETL, “Carbon Dioxide Enhanced Oil Recovery: Untapped Domenstic Energy Supply and Long Term Carbon Storage Solution,” National Energy Technology Laboratory, Morgantown, 2010.

[9] D. Y. C. Leung, G. Caramanna and M. M. Maroto-Valer, “An overview of current status of carbon dioxide capture and storage technologies,” *Renewable and Sustianable Energy Reviews,* vol. 39, pp. 426-443, 2014.

[10] IPCC, “Special report on carbon dioxide capture and storage,” Cambridge University Press, Cambridge, 2005.

[11] J. Gale, “Geological storage of CO2: What do we know, where are the gaps and what more needs to be done?,” *Energy,* vol. 29, pp. 1329-1338, 2004.

[12] S. Bachu, D. Bonijoly, J. Bradshaw, R. Burruss, S. Holloway, N. P. Christensen and O. M. Mathiassen, “CO2 storage capacity estimation: Methodology and gaps,” *International Journal of Greenhouse Gas Control 1,* pp. 430-443, 2007.

[13] S. Garcia, A. Kaminska and M. M. Maroto-Valer, “Underground carbon dioxide storage in saline formations,” *Waste and Resource Management 163,* 2010.

[14] M. L. Druckenmiller, M. M. Maroto-Valer and M. Hall, “Investigation of carbon sequestration via induced calcite formation in natural gas well brine,” *Energy & Fuels 20,* pp. 172-179, 2006.

[15] R. J. Rosenbauer and T. Koksalan, “Experimental determination of the solubility of CO2 in electrolytes: application to CO2 sequestration in deep, saline aquifers,” *The Geological Society of America 2,* p. 304, 2002.

[16] K. Michael, A. Golab, V. Shulakova, J. Ennis-King, G. Allinson, S. Sharma and T. Aiken, “Geological storage of CO2 in saline aquifers - A review of the experience from existing storage operations,” *International Journal of Greenhouse Gas Control 4,* pp. 659-667, 2010.

[17] M. L. Druckenmiller and M. M. Maroto-Valer, “Carbon sequestration using brine of adjusted pH to form mineral carbonates,” *Fuel Processing Technology 86,* pp. 1599-1614, 2005.

[18] Y. Soong, A. L. Goodman, J. R. McCarthy-Jones and J. P. Baltrus, “Experimental and simulation studies on mineral trapping of CO2 with brine,” *Energy Conversion Management 45,* pp. 1845-1859, 2004.

[19] Y. Soong, D. L. Fauth, B. H. Howard, J. R. Jones, D. K. Harrison, A. L. Goodman, M. L. Gray and E. A. Frommell, “CO2 sequestration with brine solution and fly ashes,” *Energy Conversion and Management 47,* pp. 1676-1685, 2006.

[20] R. J. Rosenbauer, T. Koksalan and J. L. Palandri, “Experiemental investigation of CO2-brine-rock interactions at elevated temperature and pressure: Implications for CO2 sequestration in deep-saline aquifers,” *Fuel Processing Technology 86,* pp. 1581-1597, 2005.

[21] C. Zhu and H. Anderson, Environmental Applications of Geochemical Modeling, Cambridge : Cambridge University Press, 2002.

[22] I. Czernichowski-Lauriol, C. Rochelle, I. Gaus, M. Azaroual, J. Pearce and P. Durst, “Geochemical Interactions Between CO2, Pore-Waters and Reservoir Rocks,” in *Advances in the Geological Storage of Carbon Dioxide* , Netherlands, Springer, 2006, pp. 157-174.

[23] L. Steel, Q. Liu, E. Mackay and M. M. Maroto-Valer, “CO2 Solubility measurements in brine under reservoir conditions: A comparison of experimental and geochemical modeling methods,” *Greenhouse Gases: Science and Technology,* vol. 6, no. 2, pp. 197-217, 2016.

[24] S. Iglauer, “Dissolution Trapping of Carbon Dioxide in Reservoir Formation Brine - A Carbon Storage Mechanism,” in *Mass Transfer - Advanced Aspects*, H. Nakajima, Ed., InTech, 2011, pp. 233-262.

[25] K. Michael, H. G. Machel and S. Bachu, “New insights into the origin and migration of brines in deep Devonian aquifers, Alberta, Canada,” *Journal of Geochemical Exploration 80,* pp. 193-219, 2003.

[26] C. Challener, “fraught fracking future,” *Chemistry and Industry 77,* pp. 20-23, 2013.

[27] United States Environmental Protection Agency, “Climate Change Indicators in the United States, 2016. Fourth Edition,” USEPA, Washington D.C., 2016.

[28] IEA, “The Global Value of Coal,” 2012. [Online]. Available: http://www.iea.org/publications/insights/insightpublications/global_value_of_coal.pdf. [Accessed 7 January 2014].

[29] W. Früh, T. Mallick, O. Crighton and A. Hunter, Renewable Energy Technologies Lecture Notes, Edinburgh: Flame, 2012.

[30] Scottish Government , “Renewable Energy,” 2010. [Online]. Available: http://www.scotland.gov.uk/Topics/Built-Environment/planning/National-Planning-Policy/themes/renewables. [Accessed 7 January 2014].

[31] Scottish Renewables , “Scottish Renewables Briefing - November 2015,” Scottish Renewables, 2015.

[32] C. F. Heuberger, I. Staffell, N. Shah and N. MacDowell, “Quantifying the value of CCS for the future electrcity system,” *Energy & Enviromental Science,* vol. 9, pp. 2497-2510, 2016.

[33] O. Edenhofer, R. Pichs-Madruga and Y. Sokona, “Climate Change 2014: Mitigation of Climate Change. Contribution of Working Group III to the Fifth Assessment Report of the Intergovernmental Panel on Climate Change: Technical Summary,” Cambridge Press, Cambridge, 2014.

[34] Energy Technology Institute LLP, “Carbon capture and storage: CCS could clear a path to the UK's carbon reduction targets,” 2014.

[35] O. M. Mathiassen, PhD Thesis, CO2 as Injection Gas for Enhanced Oil Recovery and Estimation of Potential on the Norwegian Continental Shelf, Trondheim: Norweigen University of Science and Technology, Department of Petroleum Engineering, 2003.

[36] R. Butler, Thermal Recovery of Oil and Bitumen, New Jersey: Prentice-Hall, 1991.

[37] S. Kokal and A. Al-Kaabi, “Enhanced oil recovery: challenges & opportunities,” *Global Energy Solutions,* pp. 64-69, 2010.

[38] A. Z. Abidin, T. Puspasari and W. A. Nugroho, “Polymers for Enhanced Oil Recovery Technology,” *Procedia Chemistry,* vol. 4, pp. 11-16, 2012.

[39] I. Lazar, I. G. Petrisor and T. F. Yen, “Microbial Enhanced Oil Recovery (MEOR),” *Petroleum Science and Technology,* vol. 25, no. 11, pp. 1353-1366, 2007.

[40] L. S. Melzer, *Carbon Dioxide Enhanced Oil Recovery (CO2 EOR): Factors Involved in Adding Carbon Capture, Utilization and Sotrage (CCUS) to Enhanced Oil Recovery,* Midland, Texas, 2012.

[41] J. J. Dooley, R. T. Dahowski and C. L. Davidson, “Comparing Existing Pipeline Networks with the Potential Scale of Future U.S. CO2 Pipeline Networks,” *Energy Procedia 1,* pp. 1595-1602, 2009.

[42] V. A. Kuuskraa, T. V. Leeuwen and M. Wallace, “Improving Domestic Energy Security and Lowering CO2 Emissions with “Next Generation” CO2-Enhanced Oil Recovery (CO2-EOR),” National Energy Technology Laboratory, Morgantown, 2011.

[43] U.S Energy Information Administration, “How much oil is consumed in the United States,” [Online]. Available: https://www.eia.gov/tools/faqs/faq.cfm?id=33&t=6. [Accessed 22 June 2016].

[44] H. Pershad, E. Durusut, A. Crerar, D. Black, E. Mackay and P. Olden, “Economic impacts of CO2-enhanced oil recovery for Scotland,” Scottish Enterprise, Glasgow, 2012.

[45] NETL, “CO2-EOR Offshore Resource Assessment,” National Energy Technology Laboratory, Morgantown, 2014.

[46] R. Span and W. Wagner, “A New Equation for Carbon Dioxide Covering the Fluid Region from the Triple-Point Temperature to 1100 K at Pressures up to 800 MPa,” *Journal of Physical and Chemical Reference Data,* vol. 25, no. 6, pp. 1509-1596, 1996.

[47] D. J. Dixon and K. P. Johnston, “Supercritical Fluids,” in *Encyclopedia of separation*, D. M. Ruthven, Ed., New York, John Wiley & Sons, 1997, pp. 1544-1569.

[48] F. Abbas and D. A. Rose, “Viscous Fingering and Gravity Segregation through Porous Media: Experimental Findings,” *Earth Interactions 14,* pp. 1-13, 2010.

[49] D. Jansen, M. Gazzani, G. Manzolini and E. Dijk, “Pre-combustion CO2 capture,” *International Journal of Greenhouse Gas Control,* vol. 40, pp. 167-187, 2015.

[50] D. Aaron and C. Tsouris, “Separation of CO2 from Flue Gas: A Review,” *Separation Science and Technology,* vol. 40, pp. 321-348, 2005.

[51] C.-H. Yu, C.-H. Huang and C.-S. Tan, “A Review of CO2 Capture by Absorption and Adsorption,” *Aerosol and Air Quality Research,* vol. 12, pp. 745-769, 2012.

[52] J. Gibbins and H. Chalmers, “Carbon capture and storage,” *Energy Policy,* vol. 36, no. 12, pp. 4317-4322, 2008.

[53] E. C. Gaucher, P. D. C. Deflssez, M. Bizi, D. Bonijoly, J. R. Disnar, F. Laggoun-Defarge, C. Garnier, G. Finqueneisel, T. Zimny, D. Grgic, Z. Pokryszka, S. Lafortune and S. Vidal Gilbert, “Coal laboratory characterization for CO2 geological storage,” *Energy Procedia 00,* 2010.

[54] M. T. Luu, D. Milani and A. Abbas, “Analysis of CO2 utilization for methanol synthesis integrated with enhanced gas recovery,” *Journal of Cleaner Production,* vol. 112, pp. 3540-3554, 2016.

[55] C. Khan, R. Amin and G. Madden, “Carbon dioxide injection for enhanced gas recovery and storage (reservior simulation),” *Egyptian Journal of Petroleum 22,* pp. 225-240, 2013.

[56] S. Bachu, W. D. Gunter and E. H. Perkins, “Aquifer disposal of CO2: Hydrodynamic and mienral trapping,” *Energy Conversion and Mangaement 35,* pp. 269-279, 1994.

[57] ETI, “Carbon Capture and Storage: Potential for CCS in the UK,” Energy Technologies Institute, Loughborough, 2012.

[58] UK Government, “2014 UK Greenhouse Gas Emissions, Final Figures,” Department of Energy and Climate Change, London, 2016.

[59] F. Goff and K. S. Lacknet, “Carbon dioxide sequestering using ultramfic rocks,” *Environmental Geoscience 5,* pp. 89-101, 1998.

[60] A. Sanna, M. R. Hall and M. M. Maroto-Valer, “Post-processing pathways in carbon capture and storage by mineralisation (CCSM) towards the introduction of carbon neutral materials,” *Energy Environmental Science 5,* pp. 7781-7796, 2012.

[61] X. Wang and M. M. Maroto-Valer, “Optimization of carbon dioxide capture and storage with mineralisation using recyclable ammonium salts,” *Energy 51,* pp. 431-438, 2013.

[62] S. Bachu, Chapter 2; Screening and selection criteria, and characterisation technqiues for the geological sequestration of carbon dioxde (CO2), Cambridge: Woodhead Publishing, 2008.

[63] R. Myers, The Basics of Chemistry, Westport: Greenwood Publishing Group, 2003.

[64] Z. Duan and R. Sun, “An improved model calculating CO2 solubility in pure water and aqueous NaCl solutions from 273 to 533K and from 0 to 200 bar,” *Chemical Geology 193,* pp. 257-271, 2003.

[65] Z. Duan, S. R, C. Zhu and I. M. Chou, “An improved model for the calculation of CO2 solubilities in squeous solutions containing Na+, K+, Ca2+, Mg2+, Cl- and SO42-,” *Marine Chemistry 98,* pp. 131-139, 2006.

[66] J. A. Nighswander, N. Kalogerakis and K. Mehrotra, “Solubilities of carbon dioxide in water and 1 wt% NaCl solution at pressure up to 10 MPa and temperatures from 80 to 200C,” *Journal of Chemical & Engineering Data 34,* pp. 355-360, 1989.

[67] Z. Li, M. Dong, S. Li and L. Dai, “Solubilities for binary systems of carbon dioxide + water and carbon dioxide + brine at 59C and pressure to 29 MPa,” *Journal of Chemical & Engineering Data 49,* pp. 1026-1031, 2004.

[68] J. Kiepe, S. Horstmann, K. Fischer and G. J, “Experimental determination and predicition of gas solubility data for CO2 + H20 mixtures containing NaCl or Kcl at temperatures between 313 and 393K and pressures ip to 10 MPa,” *Industrial and Engineering Chemistry Research 41,* pp. 4393-4398, 2002.

[69] B. Rumpf, H. O. C. Nicolaisen and G. Maurer, “Solubility of carbon dioxide in aqueous solutions and sodium chloride: experimental results and correlation,” *Journal of Solution Chemistry 23,* pp. 431-448, 1994.

[70] P. M. Gross, “The "Salting out" of Non-electrolytes from Aqueous Solutions,” *Chemical Reviews,* vol. 13, no. 1, August 1933.

[71] T. F. C. Lara, “PhD Thesis, Design and Testing of an Apparatus to Measure Carbon Dioxide Solubility in Liquid Foods,” University of Florida, Florida, 2008.

[72] W. Stumm and J. J. Morgan, Aquatic Chemistry, New York: John Wiley & Sons Inc., 1996.

[73] J. M. Matter, T. Takahashi and D. Goldberg, “Experimental evaluation of in situ CO2-water-rock reactions during CO2 injection in basaltic rocks: Implications for geological CO2 sequestration,” *Geochemistry Geophysics Geosystems 8,* 2007.

[74] Q. Liu, “PhD Thesis, Investigation of mineral trapping of carbon dioxide sequestration in brine,” The University of Nottingham, Nottingham, 2012.

[75] D. E. Giammar, R. G. Bruant Jr and C. A. Peters, “Forsterite dissolution and magnesite precipitation at conditions relevant for deep saine aquifer storage and sequestration of carbon dioxde,” *Chemical Geology 217,* pp. 257-276, 2005.

[76] B. Meyssami, M. O. Balaban and A. A. Teixeira, “Prediction of pH in model systems pressurized with carbon dioxide,” *Biotechnology Progress,* vol. 8, pp. 149-154, 1992.

[77] K. L. Toews, R. M. Shroll, C. M. Wai and N. G. Smart, “pH-defining equilibrium between water and supercritical CO2. Influence on SFE of organics and metal chelates,” *Analytical Chemistry,* vol. 67, pp. 4040-4043, 1995.

[78] T. Parton, S. Spilimbergo, N. Elvassore and A. Bertucco, “UV–VIS spectroscopy forthe determination of diffision coefficient and pH in aqueous solutions/SC-CO2systems,” in *High Pressure in Venice 4th International Symposium on High Pressure Process Technology and Chemical Engineering*, Venice, 2002.

[79] C. Peng, J. P. Crawshaw, G. C. Maitland, J. Trusler and D. Vega-Maza, “The pH of CO2-saturated water at temperatures between 308K and 423K at pressures up to 15MPa,” *The Journal of Supercritical Fluids,* vol. 82, pp. 129-137, 2013.

[80] C. A. Rochelle and Y. A. Moore, “The solubility of supercritical CO2 into pure water and synthetic Utsira porewater,” Keyworth, Nottingham, 2002.

[81] M. S. Kuk and J. Montagna, “Solubility of oxygenated hydrocarbons in supercritical carbon dioxide,” in *Chemical Engineering at Supercritical Conditions*, Ann Arbour, Ann Arbour Science , 1983, pp. 101-111.

[82] R. Wiebe, “The binary system carbon dioxide-water under pressure,” *Chemical Engineeering at Supercritical Fluid Conditions ,* vol. 29, no. 3, December 1941.

[83] R. Wiebe and V. L. Gaddy, “Vapour phase composition of carbon dioxide-water mixtures at various temperatures and at pressures up to 700 atmospheres,” *Journal of the American Chemical Society,* vol. 63, no. 2, February 1941.

[84] I. Czernichowski-Lauriol, S. B, C. Rochelle, K. Bateman, J. Pearce and P. Blackwell, “The underground disposal of carbon dioxide,” Keyworth, Nottingham, 1996.

[85] S. Bando, F. Takemura, M. Nishio, E. Hihara and M. Akai, “Solbulity of CO2 in aqueous solutions of NaCl at (30 to 60)C and (10 to 20) MPa,” *Journal of Chemical & Engineering Data 48,* pp. 576-579, 2003.

[86] R. D'Souza, J. R. Patrick and A. S. Teja, “High-pressure phase-equilibria in the carbon-dioxide normal-hexadecane and carbon-dioxide water-systems,” *Canadian Journal of Chemical Engineering ,* vol. 66, 1988.

[87] P. C. Gillespie and G. M. Wilson, “Vapor-Liquid and Liquid-Liquid Equilibria,” *Gas Processors Association Research Report ,* vol. 1, no. 73, 1982.

[88] R. Wiebe and V. L. Gaddy, “The solubility of carbon dioxide in water at 50, 75 and 100C, at pressures to 700 atm,” *Journal of the American Chemical Society,* vol. 61, 1939.

[89] R. Wiebe and V. L. Gaddy, “The solubility of carbon dioxide in water at various temperature from 12 to 40C and at pressures to 500 atm,” *Journal of the American Chemical Society ,* vol. 62, 1940.

[90] S. X. Hou, G. C. Maitland and M. J. P. Trusler, “Measurement and modeling of the phase behaviour of the (carbon dioxide + water) mixture at temperatures from 298.15K to 448.15K,” *The Journal of Supercritical Fluids,* vol. 73, pp. 87-96, 2013.

[91] S. X. Hou, G. C. Maitland and M. J. P. Trusler, “Phase equilibria of (CO2 + H2O + NaCl) and (CO2 + H2O + KCl): Measurments and modeling,” *The Journal of Supercritical Fluids,* vol. 78, 2013.

[92] Z. Lei, C. Dai and B. Chen, “Gas Solubility in Ionic Liquids,” *Chemical Reviews,* vol. 114, no. 2, 2014.

[93] Y. B. Change, B. K. Coats and J. S. Nolen, “A Compositional Model for CO2 Floods Including CO2 Solubility in Water,” *SPE Reservoir Evaluation & Engineering,* vol. 1, no. 2, April 1998.

[94] W. Yan, S. Huang and E. H. Stenby, “Measurement and modeling of CO2 solubility in NaCl brine and CO2–saturated,” *International Journal of Greenhouse Gas Control,* vol. 5, no. 6, September 2011.

[95] A. N. Sabirzyanov, R. A. Shagiakhmetov, F. R. Gabitov, A. A. Tarzimanov and F. M. Gumerov, “Water solubility of carbon dioxide under supercritical and subcritical conditions,” *Theorectical Foundations of Chemical Engineering 37,* pp. 51-53, 2003.

[96] M. B. King, A. Mubarak, J. D. Kim and T. R. Bott, “ The mutual solubilities of water with supercritical and lqiuid carbon dioxide,” *Journal of Supercritical Fluids,* vol. 5, no. 4, December 1992.

[97] J. Qin, R. J. Rosenbauer and Z. Duan, “Experimental Measurements of Vapor–Liquid Equilibria of the H2O + CO2 + CH4 Ternary System,” *Jounral of Chemical and Engineering Data,* vol. 53, no. 6, May 2008.

[98] D. Tong, M. J. P. Trusler and D. Vega-Maza, “Solubility of CO2 in Aqueous Solutions of CaCl2 or MgCl2 and in a Synthetic Formation Brine at Temperatures up to 423 K and Pressure up to 40 MPa,” *Jounral of Chemical and Engineering Data,* vol. 58, no. 7, May 2013.

[99] C. F. Prutton and R. L. Savage, “The solubility of carbon dioxide in calcium chloride-water solutions at 75, 100, 120 C and high pressures,” *Journal of the American Chemical Society ,* vol. 67, 1945.

[100] Q. Liu and M. M. Maroto-Valer, “Investigation of the effect of brine composition and pH buffer on CO2-Brine Sequestration,” *Energy Procedia,* vol. 4, pp. 4503-4507, 2011.

[101] J. J. Dooley, R. T. Dahowski and C. L. Davidson, “CO2-driven Enhanced Oil Recovery as a Stepping Stone to What?,” Pacific Northwest National Laboratory, Richland, 2010.

[102] L. Koottungal, “Special Report: EOR/Heavy Oil Survey,” *Worldwide EOR Survery, Oil and Gas Journal,* 2010.

[103] USEPA, “Federal Requirements Under the Underground Injection Control (UIC) Program for Carbon Dioxide (CO2) Geological Sequestration (GS) Wells,” Washington D.C., United States Environmental Protection Agency , 2010, pp. 18576-18606.

[104] P. Egermann, B. Bazin and O. Vizika, “An Experimental Investigation of Reaction-Transport Phenomena During CO2 Injection,” in *Society of Petroleum Engineers International*, Bahrain, 2005.

[105] J. E. Brady and F. Senese, Chemistry: Matter and Its Change, 4th ed., New York: John Wiley & Sons, 2004.

[106] J. T. Castro, E. C. Santos, W. P. ,. C. L. M. Santos, M. Korn, J. A. Nobrega and M. G. A. Korn, “A critical evaluation of digestion procedures for coffee samples using diluted nitric acid in closed vessels for inductively coupled plasma optical emission spectrometry,” *Talanta,* vol. 78, pp. 1378-1382, 2009.

[107] X. Hou and B. T. Jones, “Inductively Coupled Plasma/Optical Emission Spectrometry,” in *Encyclopedia of Analytical Chemistry*, R. Meyers, Ed., Chichester, John Wiley & Sons Ltd, 2000, pp. 9468-9485.

[108] J. Todoli and J. Mermet, “Pneumatic Nebulizer Design,” in *Liquid Sample Introduction in ICP Spectrometry: A Practical Guide*, Elsevier, 2008, pp. 17-76.

[109] University of Edinburgh, “ICP-OES and ICP-MS,” [Online]. Available: http://www.chem.ed.ac.uk/research/business-development/services/icp-oes-and-icp-ms. [Accessed 21 April 2014].

[110] R. Sharma, D. P. Bisen, U. Shulka and B. G. Sharma, “X-ray diffraction: a powerful method of characterizing naomaterials,” *Recent Research in Science and Technology ,* vol. 4, no. 8, pp. 77-79, 2012.

[111] V. Pecharsky and P. Zavalij, Fundamentals of Powder Diffraction and Structural Characterization of Materials, Second Edition, New York: Springer US, 2009.

[112] A. C. Lasaga, “Fundamental approaches in describing mineral dissolution and precipitation rates,” *Reviews in Mineralogy and Geochemistry,* vol. 31, pp. 23-86, 1995.

[113] O. Rahmani, M. Tyrer and R. Junin, “Calcite precipitation from by-product red gypsum in aqeous carbonation process,” *RSC Advances ,* vol. 4, no. 85, 2014.

[114] Horiba Scientific , “A Guidebook to Particle Size Analysis,” Horiba Instruments, Inc, Irvine, 2014.

[115] L. Marini, Geological Sequestration of Carbon Dioxide: Thermodynamics, Kinetics, And Reaction Path Modeling, Amsterdam: Elsevier, 2007.

[116] E. Sonnenthal, A. Ito, N. Spycher, M. Yui, J. Apps, Y. Sugita, M. Conrad and S. Kawakami, “Approaches to modeling coupled thermal, hydrological and chemical processes in the drift scale heater test at Yucca Mountain,” *International Jounral of Rock Mechanics and Mining Sciences,* vol. 42, pp. 698-719, 2005.

[117] O. K. DeFoe and A. H. Compton, “The Density of Rock Salt and Calcite,” *Physical Revieww,* vol. 25, no. 5, pp. 618-620, 1925.

[118] S. Lowell and J. ,. Shields, “Langmuir and BET theories (kinetic isotherms),” in *Powder Surface Area and Porosity*, London, Chapman & Hall, 1991, pp. 14-29.

[119] S. Lowell and J. E. Shields, “Adsorption isotherms,” in *Powder Surface Area and Porosity*, London, Chapman & Hall, 1991, pp. 11-13.

[120] G. A. A. Soler-Illia, C. Sanchez, B. Lebeau and J. Patarin, “Chemical Strategies To Design Textured Materials: from Microporous and Mesoporous Oxides to Nanonetworks and Hierarchical Structures,” *Chemical Review ,* vol. 102, pp. 4093-4138, 2002.

[121] V. Cnudde and M. N. Boone, “High-resolution X-ray computed tomography in geosciences: A review of the current technology and applications,” *Earth-Science Reviews,* vol. 123, pp. 1-17, 12 May 2013.

[122] J. R. Ashton, J. L. West and C. T. Badea, “In vivo small animal micro-CT using nanoparticle contrast agents,” *Frontiers in Pharmacology,* vol. 6, 2015.

[123] C. Grove and D. A. Jerram, “jPOR: An ImageJ macro to quantify total optical porosity from blue-stained thin sections,” *Computers & Geosciences,* vol. 37, pp. 1850-1859, 2011.

[124] H. Todokoro and M. Ezumi, “Scanning electron microscope”. United States of America Patent 733,857, 16 February 1999.

[125] M. R. Derrick, E. F. Doehne, A. E. Parker and D. C. Stulik, “Some New Analytical Techniques for use in Conservation,” *Journal of the American Institute for Conservation,* vol. 33, pp. 171-184, 1994.

[126] J. Goldstein, D. Newbury, D. Joy, C. Lyman, P. Echlin, E. Lifshin, L. Sawyer and J. Michael, Scanning Electron Microscopy and X-Ray Microanalysis Third Edition, New York: Springer US, 2003.

[127] K. Kanda, “Energy Dispersive X-ray Spectrometer”. United States of America Patent 616,249, 12 November 1991.

[128] R. A. Carlton, C. E. Lyman and J. E. Roberts, “Accuracy and precision of qunatitative energy-dispersive x-ray spectrometry in environmental scanning electron microscope,” *Scanning,* vol. 26, pp. 167-174, 2004.

[129] J. Buckman, “Centre for Environmental Scanning Electron Microscopy (CESEM),” Heriot-Watt Univeristy, [Online]. Available: http://www.hw.ac.uk/schools/energy-geoscience-infrastructure-society/about/facilities/esem.htm. [Accessed 28 October 2015].

[130] Parr Instrument Company, “Series 4540 High Pressure Reactors, 600-1200 ml,” Parr Instrument Company, 2015. [Online]. Available:

http://www.parrinst.com/products/stirred-reactors/series-4540-600-1200-ml-hp-reactors/specifications/. [Accessed 3 November 2015].

[131] S. Garcia, “PhD Thesis, Experimental and simulation studies of iron oxdies for geochemical fixation of CO2-SO2 gas mixtures,” University of Nottingham, Nottingham, 2010.

[132] Haynes International, Inc, “Hasterlloy C-276 alloy Information,” Haynes International, Inc, [Online]. Available: http://www.haynesintl.com/c276hastelloyalloy.htm. [Accessed 5 November 2015].

[133] Bronkhorst HIGH-TECH, “FlowDDE,” Bronkhorst HIGH-TECH, [Online]. Available: http://www.bronkhorst.com/en/downloads/flowware/flowware_downloads/12/flowdde. [Accessed 5 Novemeber 2015].

[134] Bronkhorst HIGH-TECH, “FlowPlot,” Bronkhorst HIGH-TECH, [Online]. Available: http://www.bronkhorst.com/en/downloads/flowware/flowware_downloads/8/flowplot. [Accessed 5 November 2015].

[135] Bronkhorst HIGH-TECH, “FlowView,” Bronkhorst HIGH-TECH, [Online]. Available: http://www.bronkhorst.com/en/downloads/flowware/flowware_downloads/11/flowview. [Accessed 5 November 2015].

[136] Parr Instrument Company, “Operating Instruction Manual for 4843 Controllers,” Parr Instrument Company, 24 May 2006. [Online]. Available: http://www.equipnet.com/mp_data/media/2lparrreactorcontroller-parr4843-operatinginstructions_2014821114611_417431_4.pdf. [Accessed 2017 April 2017].

[137] AZO Materials, “Stainless Steel - Grade 316L - Properties, Fabrication and Applications (UNS S31603),” AZO Materials, [Online]. Available: http://www.azom.com/article.aspx?ArticleID=2382. [Accessed 6 November 2015].

[138] ZEUS, “Chemical Resistance Chart - PTFE,” Cyberwoven, 2015. [Online]. Available: http://www.zeusinc.com/materials/ptfe/chemical-resistance-chart-ptfe. [Accessed 6 November 2015].

[139] TELEDYNE ISCO, “260D Syringe Pump,” Teledyne Technologies Incorporated , 2013. [Online]. Available: http://www.isco.com/products/products3.asp?PL=1051030. [Accessed 6 Novemeber 2015].

[140] OMEGA, “Temperature Controllers CN740 Series,” OMEGA Engineering Inc., 2015. [Online]. Available: http://www.omega.co.uk/pptst/CN740_Series.html. [Accessed 6 November 2015].

[141] DuPont, “Kalrez Perfluoroelastomer Parts - Chemical Resistance and Fluid Compatibility,” Parr Instrument Company, [Online]. Available:

http://www.parrinst.com/wp-content/uploads/downloads/2011/07/Parr_DuPont-Kalrez-O-ring-Materials-Corrosion-Info.pdf. [Accessed 18 January 2016].

[142] O. Gundogan, E. Mackay and A. Todd, "Comparison of numerical codes for geochemical modelling of CO2 storage in target sandstone reservoirs," *Chemical Engineering Research and Design 89,* pp. 1805-1816, 2011.

[143] D. L. Parkhurst and C. A. J. Appelo, User's guide to PHREEQC (version 2) - a computer program for speciation, batch-reaction, one-dimensional transport, and inverse geochemical calculations, Denver: U.S. Geological Survey, 1999.

[144] B. J. Merkel and B. Planer-Friedrich, Groundwater Geochemistry: A Practical Guide to Modelling of Natural and Contaminated Aquatic Systems, Berlin: Springer, 2008.

[145] USGS, "PHREEQC (Version 3)--A Computer Program for Speciation, Batch-Reaction, One-Dimensional Transport, and Inverse Geochemical Calculations," 2014. [Online]. Available: http://wwwbrr.cr.usgs.gov/projects/GWC_coupled/phreeqc/. [Accessed 24 April 2014].

[146] S. Garcia, R. J. Rosenbauer, J. Palandri and M. M. Maroto-Valer, "Sequestration of non-pure carbon dioxide streams in iron oxyhydroxide-containing saline repositories," *International Journal of Greenhouse Gas Control 7,* pp. 89-97, 2012.

[147] HYDRAFACT, 2015. [Online]. Available: http://www.hydrafact.com/index.php?page=software. [Accessed 10 March 2015].

[148] J. O. Valderrama, "The State of the Cubic Equations of State," *Industrial & Engineering Chemistry Research,* vol. 42, no. 8, pp. 1603-1618, 2003.

[149] A. Chapoy, H. Haghighi, R. Burgess and B. Tohidi, "Behavious of the Carbon Dioxide - Water Systems at Low Temperatures: Experiments and Modelling," *Journal of Chemical Thermodynamics,* vol. 47, 2012.

[150] J. Gross and G. Sadowski, "Perturbed-Chain SAFT: An Equation of State Based on a Perturbation Theory for Chain Molecules," *Industrial & Engineering Chemistry Research,* vol. 40, no. 4, January 2001.

[151] J. Gross and G. Sadowski, "Application of the Perturbed-Chain SAFT Equation of State to Associating Systems," *Industrial & Engineering Chemistry Research,* vol. 41, no. 22, October 2002.

[152] N. I. Diamantonis, G. C. Boulougouris, E. Mansoor, D. M. Tsangaris and I. G. Economou, "Evaluation of Cubic, SAFT, and PC-SAFT Equations of State for the Vapor-Liquid Equilibrium Modeling of CO2 Mixtures with Other Gases," *Industrial & Engineering Chemistry Research,* vol. 52, no. 10, February 2013.

[153] G. M. Kontogeorgis, I. V. Yakoumis and P. M. Vlamos, “Application of the sCPA equation of state for polymer solutions,” *Computational and Theorectical Polymer Science ,* vol. 10, no. 6, August 2000.

[154] G. M. Kontogeorgis, V. I. Yakoumis, H. Meijer, E. Hendriks and T. Moorwood, “Multicomponent phase equilibrium calculations for water-methanol-alkane mixtures,” *Fluid Phase Equilibria,* Vols. 158-160, June 1999.

[155] Z. Duan, N. Moller and J. H. Weare, “An equation of state for the CH4-CO2-H20 system: I. Pure systems for 0 to 1000C and 0 to 8000 bar,” *Geochimica et Cosmochimica Acta,* vol. 56, 1992.

[156] S. A. Ghafri, G. C. Maitland and M. J. P. Trusler, “Densities of Aqueous MgCl2(aq), CaCl2(aq), Kl(aq), NaCl(aq), KCl(aq), AlCl3(aq), and (0.964 NaCl + 0.136 KCl)(aq) at Temperatures Between (283 and 472) K, Pressure up to 68.5 MPa, and Molalities up to 6 mol.kg-1,” *Journal of Chemical & Engineering Data,* vol. 57, pp. 1288-1304, 2012.

[157] S. Z. A. Ghafri, G. C. Maitland and M. J. P. Trusler, “Densities of SrCl2(aq), Na2SO4(aq), NaHCO3(aq), and Two Synthetic Reservoir Brines at Temperatures between (298 and 473) K, Pressures up to 68.5 MPa, Molalities up to 3 mol.kg-1,” *Journal of Chemical & Engineering Data,* vol. 58, pp. 402-412, 2013.

[158] C. E. Manning and L. Y. Aranovich, “Brines at high pressure and temperature: Thermodynamic, petrologic and geochemical effects,” *Precambrian Research,* vol. 253, July 2014.

[159] L. N. Plummer, D. L. Parkhurst, G. W. Fleming and S. A. Dunkle, “Kinetics of calcite dissolution in CO2-water systems at 5-degrees-C to 60-degrees-C and 0.0 to 1.0 ATM CO2,” *Amiercan Journal of Science,* vol. 278, no. 2, pp. 179-216, 1978.

[160] D. Rickard and L. E. Sjoeberg, “Mixed kinetic control of calcite dissolution rates,” *Ameircan Journal of Science ,* vol. 283, pp. 815-830, 1983.

[161] C. Peng, J. P. Crawshaw, G. C. Maitland and M. J. P. Trusler, “Kinetics of calcite dissolution in CO2-saturated water at temperatures between (323 and 373) K and pressure up to 13.8 MPa,” *Chemical Geology,* vol. 403, pp. 74-85, 2015.

[162] C. Peng, B. U. Anabaraonye, J. P. Crawshaw, G. C. Maitland and J. P. M. Trusler, “Kinetics of carbonate mineral dissolution in CO2-acidified brines at storage conditions,” *Faraday Discussions,* vol. 192, no. 545-560, 2016.

[163] W. D. McCain, The Properties of Petroleum Fluids, Tulsa: PennWell Books, 1990.

[164] H. G. Machel, “Concepts and models of dolomitization: a critical reappraisal,” *Geological Society, London, Special Publications ,* vol. 235, pp. 7-63, 2004.

[165] B. Etschmann, J. Brugger, M. A. Pearce, C. Ta, D. Brautigan, M. Jung and P. A, “Grain boundaries as microreactors during reactive fluid flow: experimental dolomitization of calcite marble,” *Contributions to Mineralogy and Petrology,* vol. 168, no. 1045, 2014.

[166] D. Koschel, J. Y. Coxam, L. Rodier and V. Majer, “Enthalpy and solubility data of CO2 in water and NaCl(aq) at conditions of interest for geological sequestration,” *Fluid Equilibria 247,* pp. 107-120, 2006.

[167] I. Mohamed, J. He and H. A. Nasr-El-Din, “Effect of Brine Composition on CO2/Limestone Rock Interactions during CO2 Sequestration,” *Journal of Petroleum Science Research,* vol. 2, no. 1, 2013.

[168] E. J. Mackay, “Prediciting In-Situ Sulphate Scale Deposition and the Impact on Produced Ion Concentrations,” *Chemical Engineering Research and Design,* vol. 81, no. 3, pp. 326-332, 2003.

[169] Y. Hu, O. Ishkov, E. J. Mackay and A. Strachan, “Predicted and Observed Evolution of Produced Brine Compositions, and Implications for Scale Management,” in *SPE Production and Operations*, Aberdeen, 2016.

[170] ResAlta Research Technologies, “Scandium M - entry level software for SEM and portable SEM,” ResAlta Research Technologies, [Online]. Available: http://www.resaltatech.com/scandium_m_main.htm. [Accessed 26 September 2016].

[171] F. J. Pettijohn, P. E. Potter and R. Siever, Sand and Sandstones, New York: Springer, 1987.

[172] A. Oberlin and R. Couty, “Conditions of kaolinite formation during alteration of some silicates by water at 200°C,” *Clays and Clay Minerals,* vol. 18, pp. 347-356, 1970.

[173] B. Lamy-Chappius, D. Angus, Q. Fisher, C. Grattoni and B. W. D. Yardley, “Rapid porosity and permeability changes of calcareous sandstone due to CO2-enriched brine injection,” *Geophysical Research Letters,* vol. 41, 2014.

[174] G. Nover, J. Gonna, S. Heikamp and J. Koster, “Changes of petrophysical properties of sandstones due to interaction with supercritical carbon dioxide - a labortatory study,” *European Journal of Mineralogy,* vol. 25, no. 3, 2013.

[175] L. Andre, P. Audigane, M. Azaroual and A. Menjoz, “Numerical modelling of fluid-rock chemical interactions at the supercritical CO2-liquid interface during CO2 injection into a carbonate reservoir, the Dogger aquifer (Paris Basin, France),” *Energy Conversion and Management,* vol. 48, pp. 1772-1797, 2007.

[176] S. Iglauer, M. Sarmadivaleh, A. Al-Yaseri and M. Lebedev, “Permeability evolution in sandstone due to injection of CO2-saturated brine or supercritical CO2 at reservoir conditions,” *Energy Procedia,* vol. 63, pp. 3051-3059, 2014.

[177] E. Berrerzueta, B. Ordonez-Casado and L. Quintana, “Qualitative and quantitative changes in detrital reservoir rocks caused by CO2-brine-rock interactions during first injection phases (Utrillas sandstones, northern Spain),” *Solid Earth,* vol. 7, pp. 37-53, 2016.

[178] D. Pudlo, S. Henkel, V. Reitenbach, D. Albrecht, F. Enzmann, K. P. G. Heister, L. Ganzer and R. Gaupp, “The chemical dissolution and physical migration of minerals induced during CO2 labarotory experiments: their relevance for reservoir quaility,” *Enviromental Earth Sciences,* vol. 73, no. 11, pp. 7029-7042, 2015.

[179] J. A. Briones, J. C. Mullins, M. C. Thies and B. U. Kim, “Ternary phase equilibria for acetic acid-water mixtures with supercritical carbon dioxide,” *Fluid Phase Quilibria,* vol. 36, 1987.

[180] R. Dohrn, A. P. Bunz, F. Devlieghere and D. Thelen, “Experimental measurements of phase equilibria for ternary and quaternary systems of glucose, water, CO2 and ethanol with a novel apparatus,” *Fluid Phase Equilibria,* vol. 83, 1993.

[181] J. Matous, J. Sobr, J. P. Novak and J. Pick, “Solubility of carbon dioxide in water at pressures up to 40atm,” *Collection of Czechoslovak Chemical Communications ,* vol. 34, 1969.

[182] K. Todheide and E. U. Franck, “Das Zweiphasengebiet und die kritische Kurve im System Kohlendioxid-Wasser bis zu drucken von 3500 bar,” *Zeitschrift fur Physikalische Chemie ,* vol. 37, 1963.

[183] A. Zawisza and B. Malesinska, “Solubility of carbon dioxide in liquid water,” *Journal of Chemical & Engineering Data,* vol. 26, 1981.

[184] Y. D. Zelvenskii, “The solubility of carbon dioxide in water under pressure,” *Journal of Chemical Industry (USSR),* vol. 14, 1937.

[185] S. D. Malinin and N. I. Savel'eva, “Experimental investigations of CO2 solubility in NaCl and CaCl2 solutions at 25, 50 and 75C and elevated CO2 pressure,” *Geokhimiva ,* vol. 6, 1972.

[186] A. Chapoy, A. H. Mohammadi, A. Chareton, B. Tohidi and D. Richon, “Measurement and modeling of gas solubility and literature review of the properties for the carbon dioxide-water system,” *Industrial & Engineering Chemistry Research,* vol. 43, 2004.

[187] J. Kaszuba, B. Yardley and M. Andreani, “Experimental perspectivies of mineral dissolution and precipitation due to carbon dioxide-water-rock interactions,” *Reviews in Mineralogy and Geochemistry ,* vol. 77, no. 1, pp. 153-188, 2013.

[188] Y. Farzin, “The impact of oil prices additions to US proven reserves,” *Resource and Energy Economics,* vol. 23, pp. 271-291, 2001.

[189] K. M. Krupka, K. J. Cantrell and B. P. McGrail, “Thermodynamic Data for Geochemical Modeling of Carbonate Reactions Associated with CO2 Sequestration - Literature Review,” Pacific Northwest National Laboratory, Richland, 2010.

Appendix

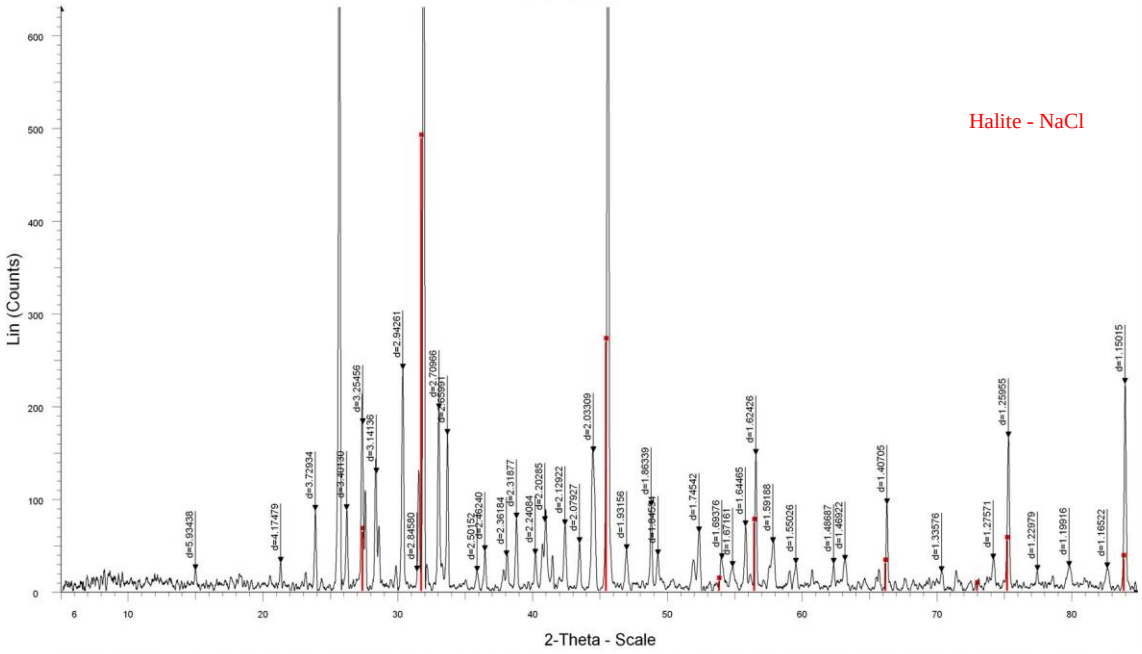

Figure A1: XRD analysis of Brine 1x5 solid residue showing halite

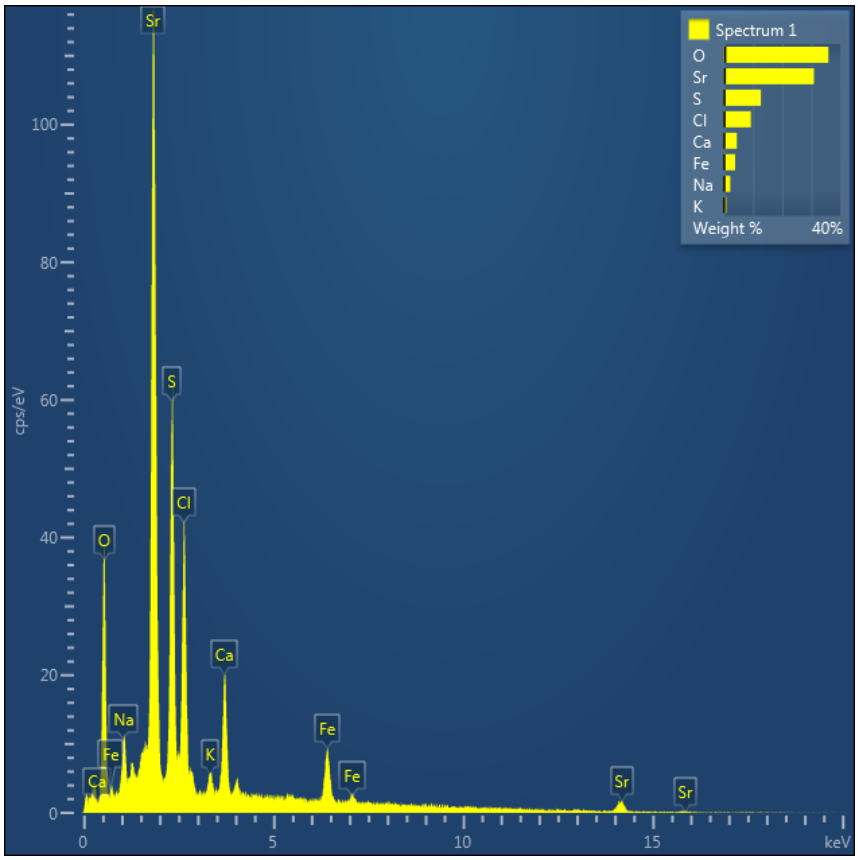

Figure A2: EDS Spectrum 1

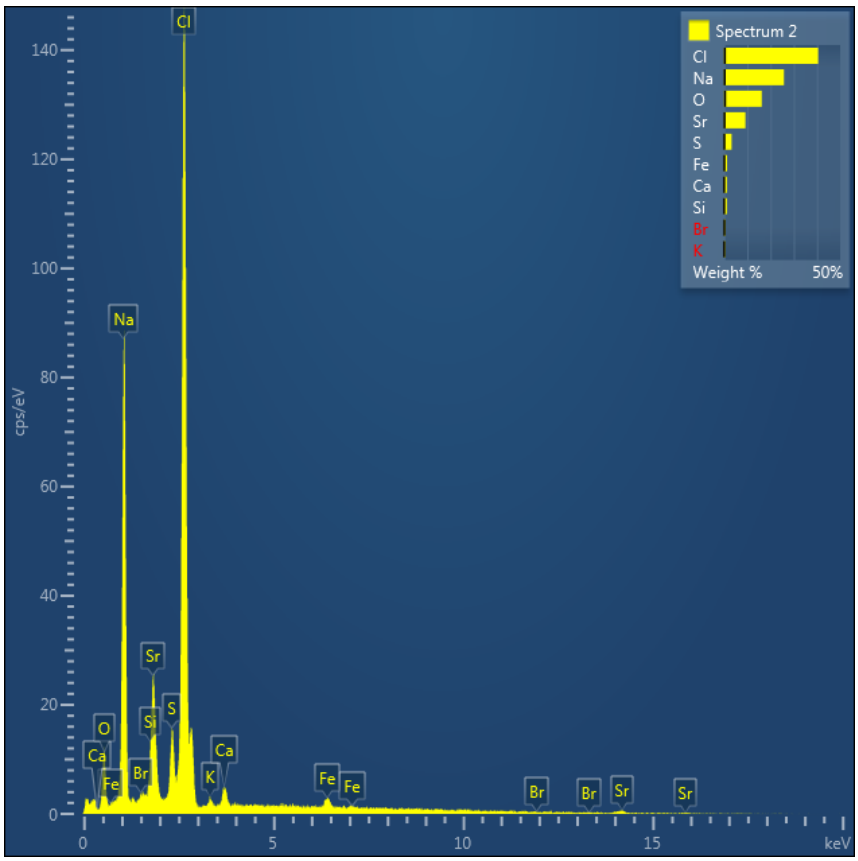

Figure A3: EDS Spectrum 2

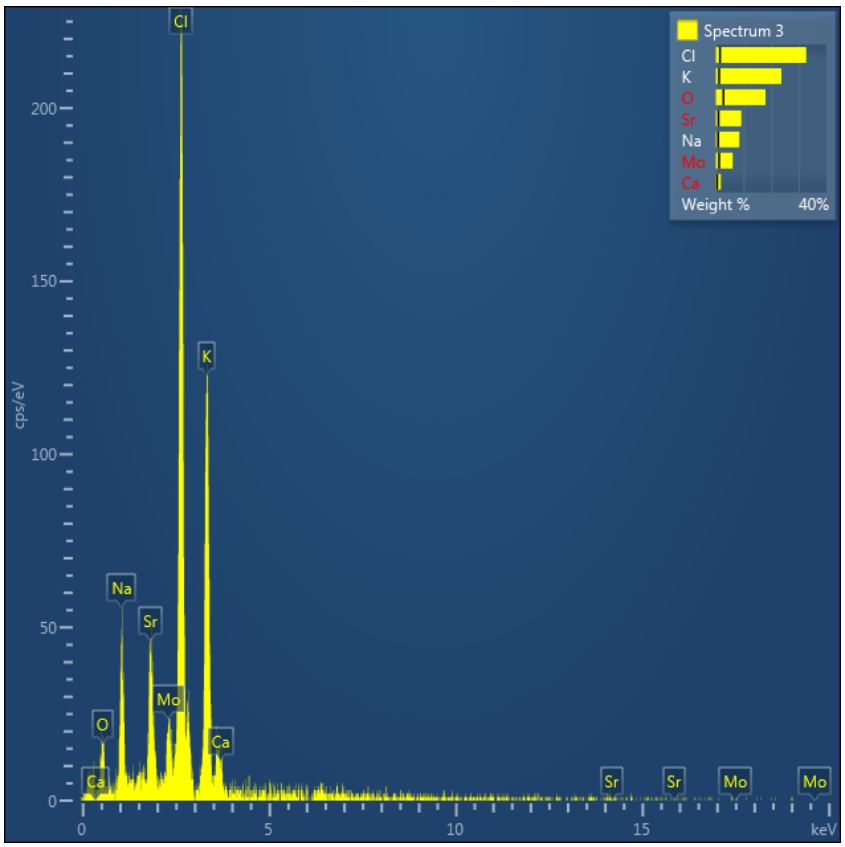

Figure A4: EDS Spectrum 3

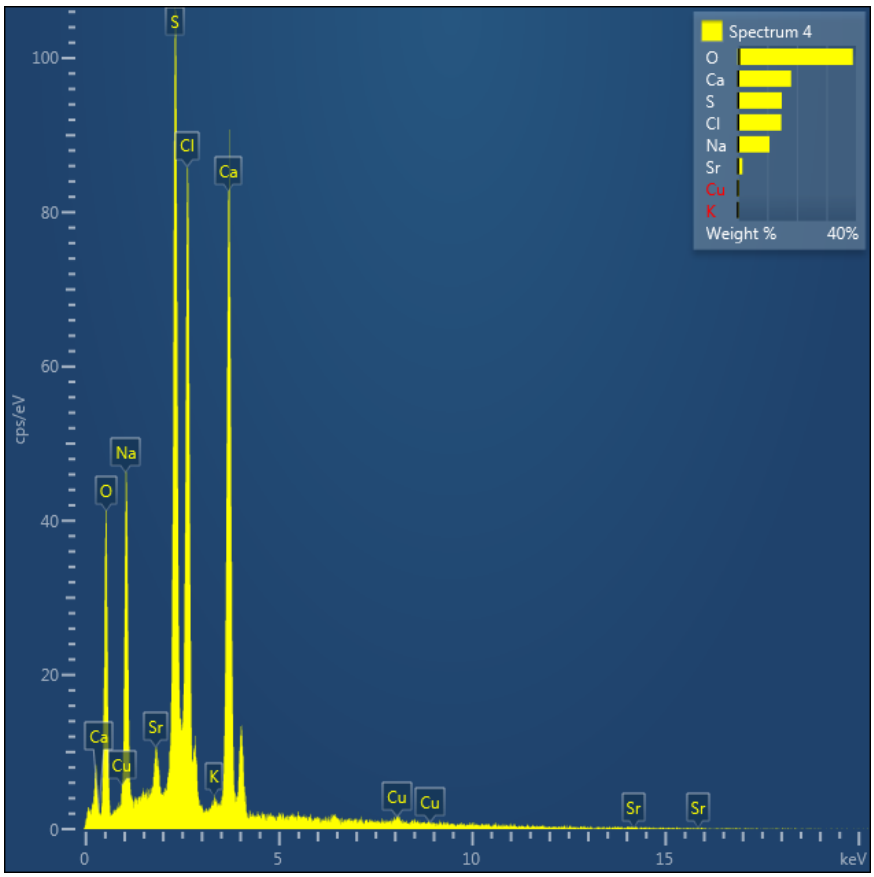

Figure A5: EDS Spectrum 4

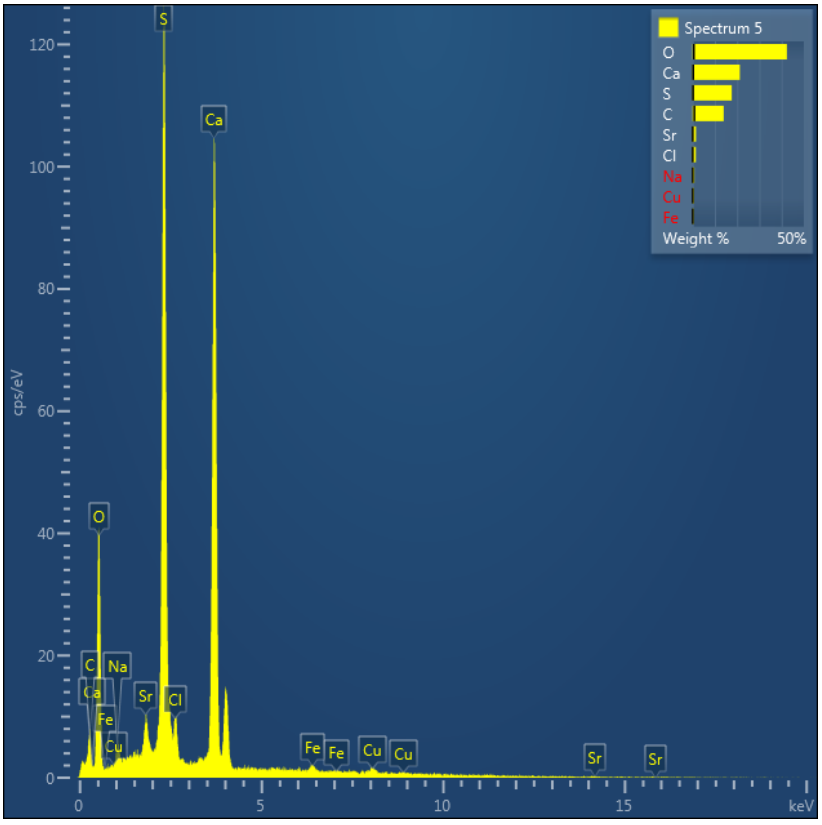

Figure A6: EDS Spectrum 5

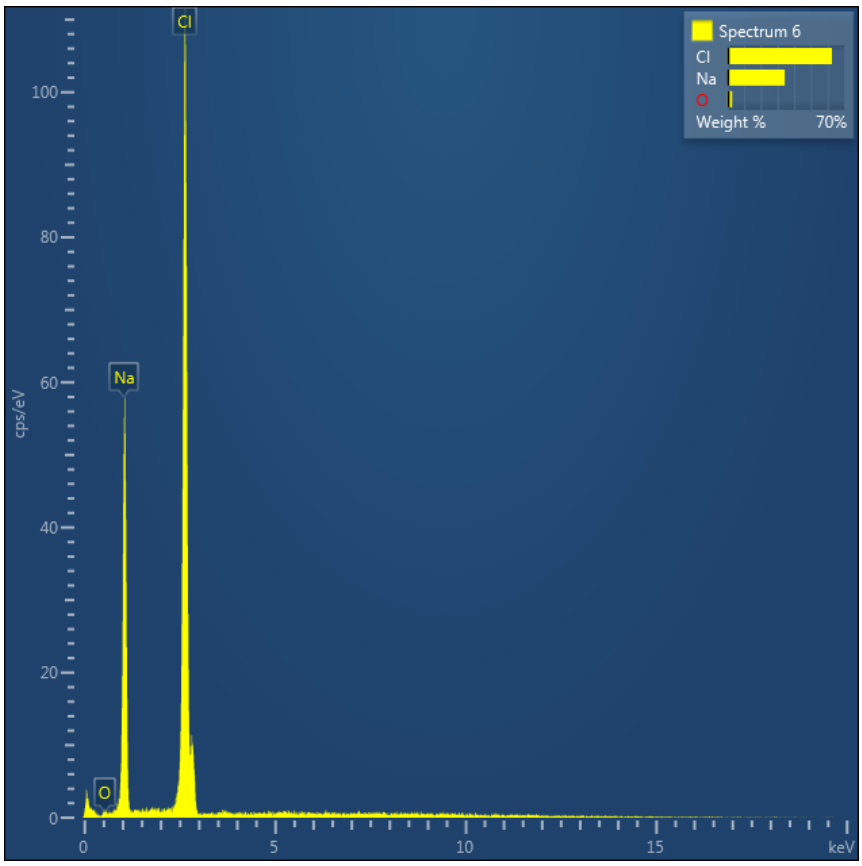

Figure A7: EDS Spectrum 6

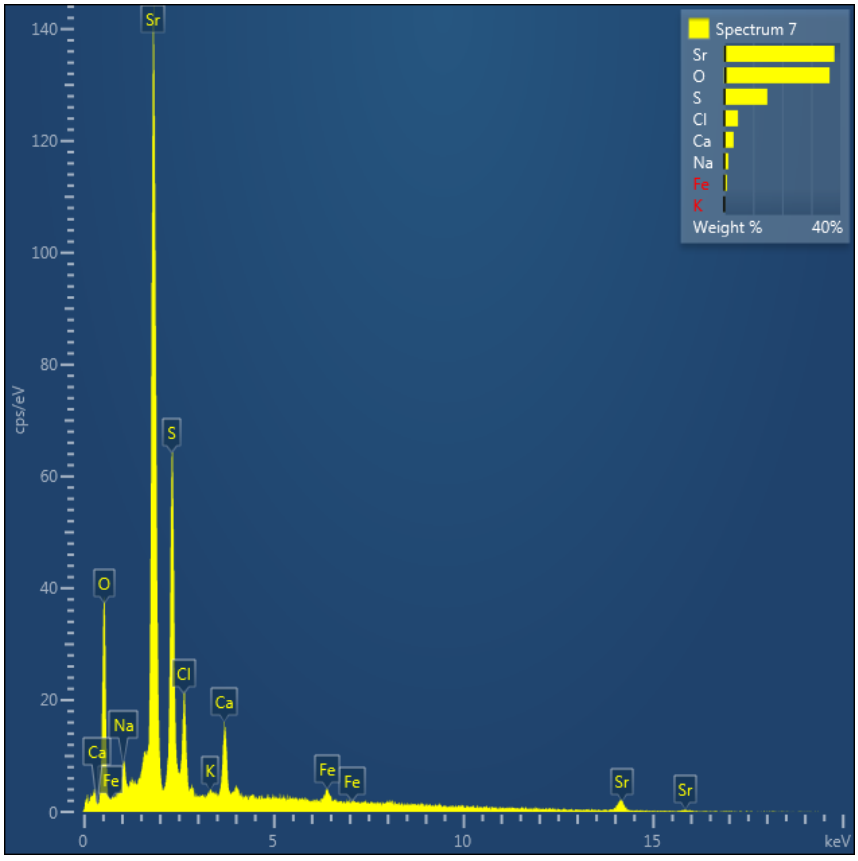

Figure A8: EDS Spectrum 7

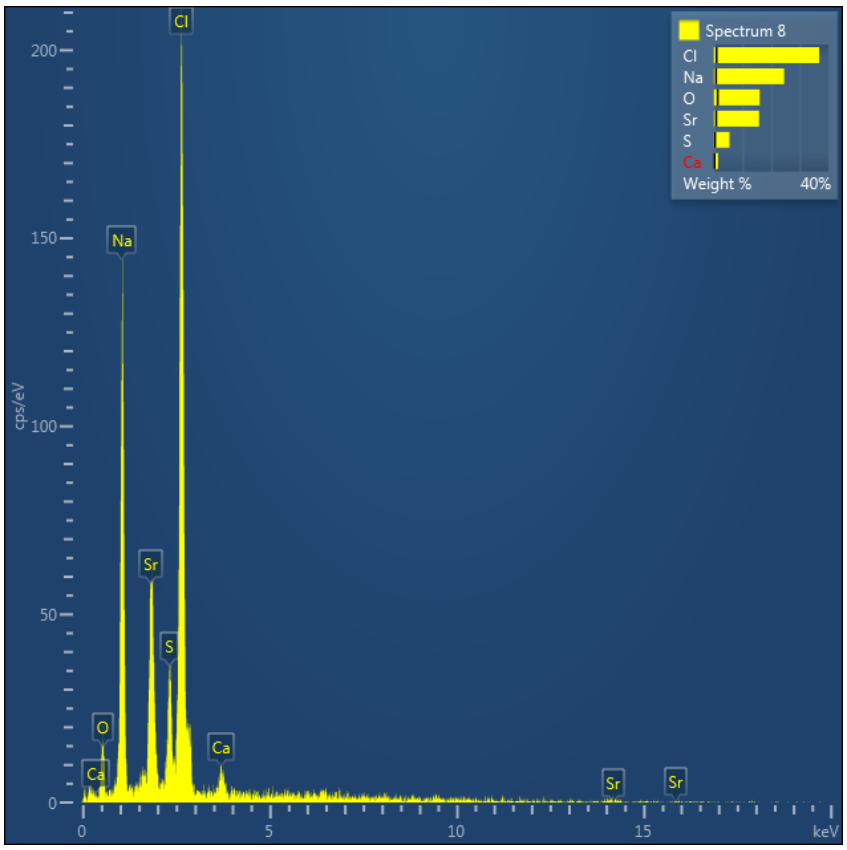

Figure A9: EDS Spectrum 8

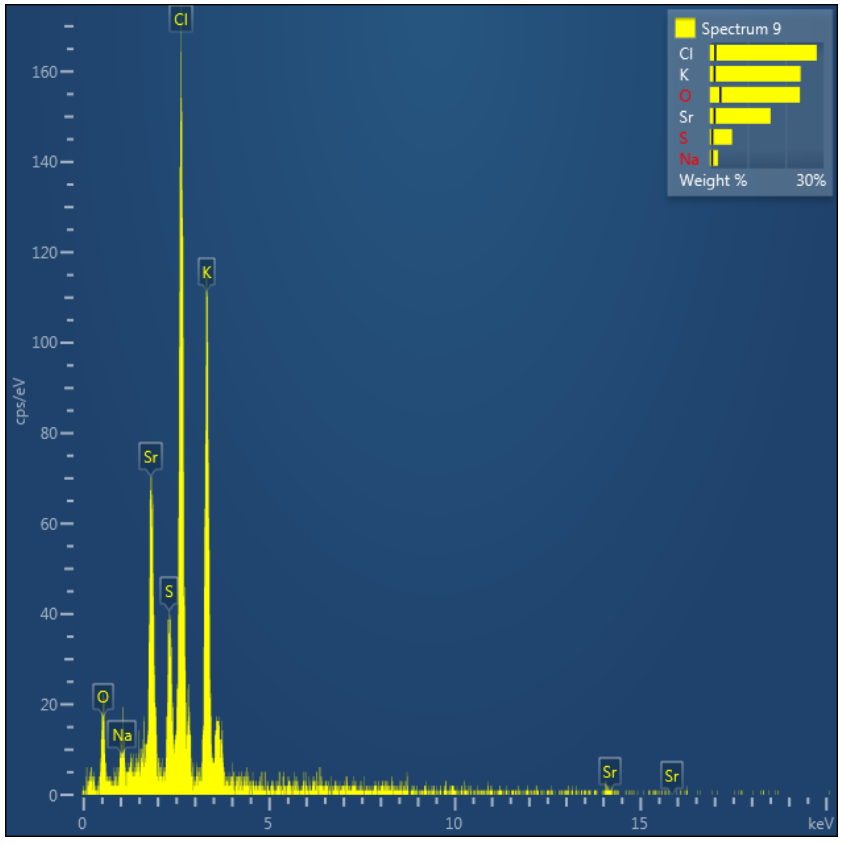

Figure A10: EDS Spectrum 9

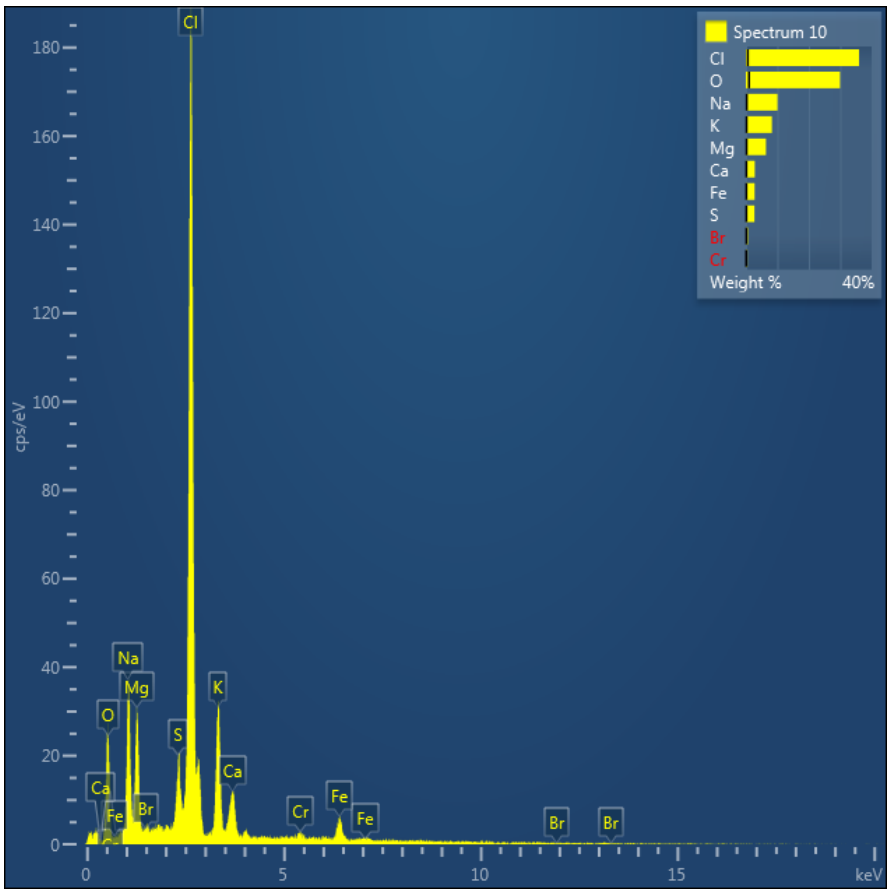

Figure A11: EDS Spectrum 10

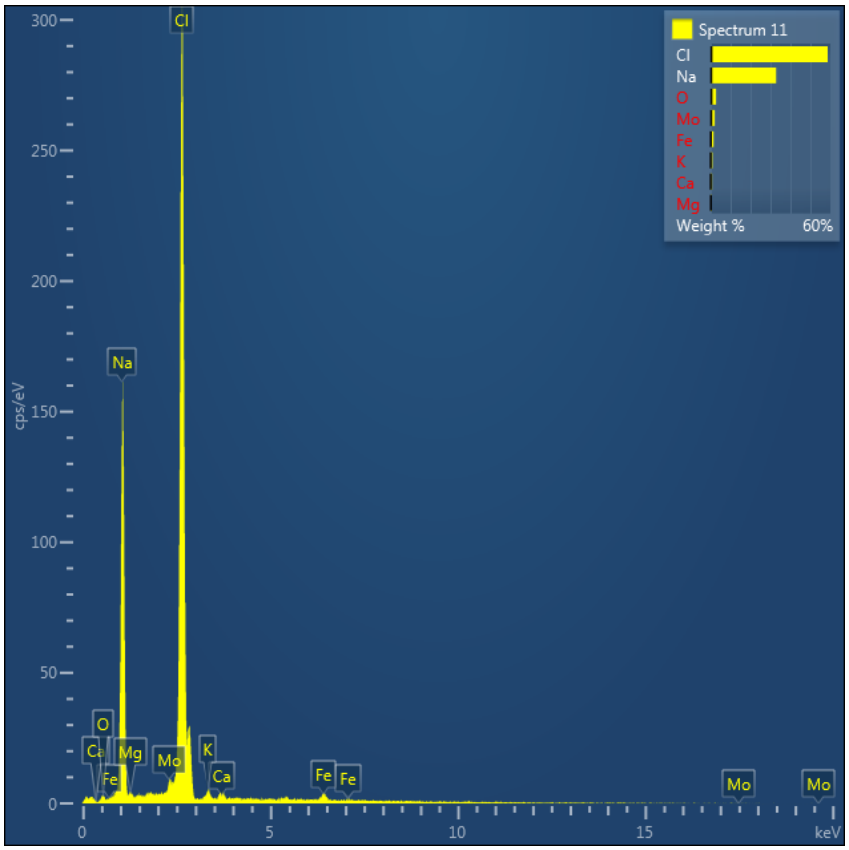

Figure A12: EDS Spectrum 11

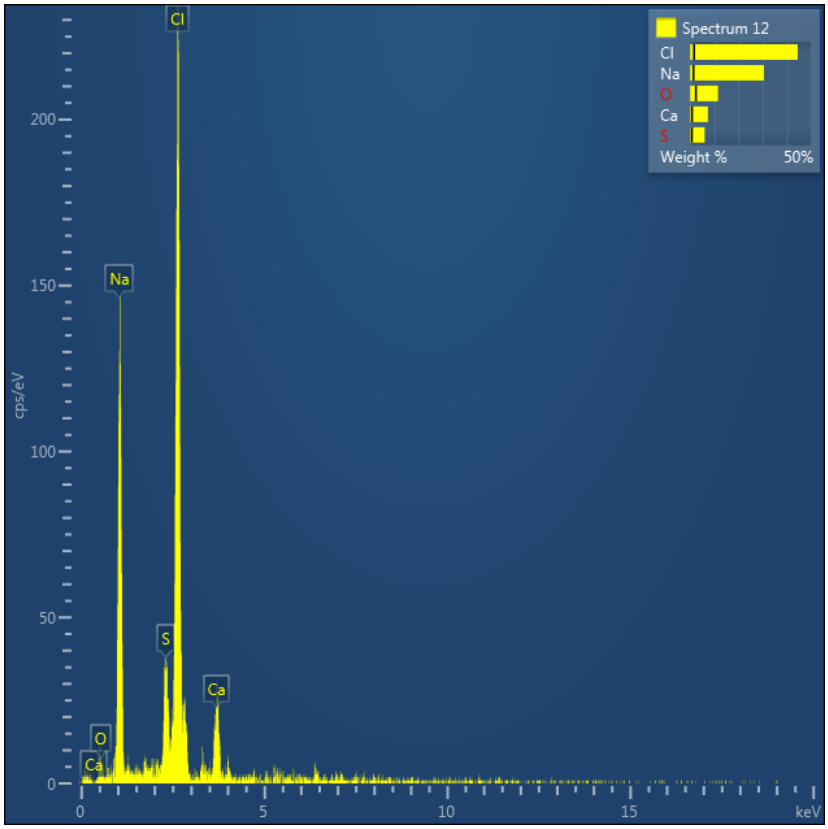

Figure A13: EDS Spectrum 12

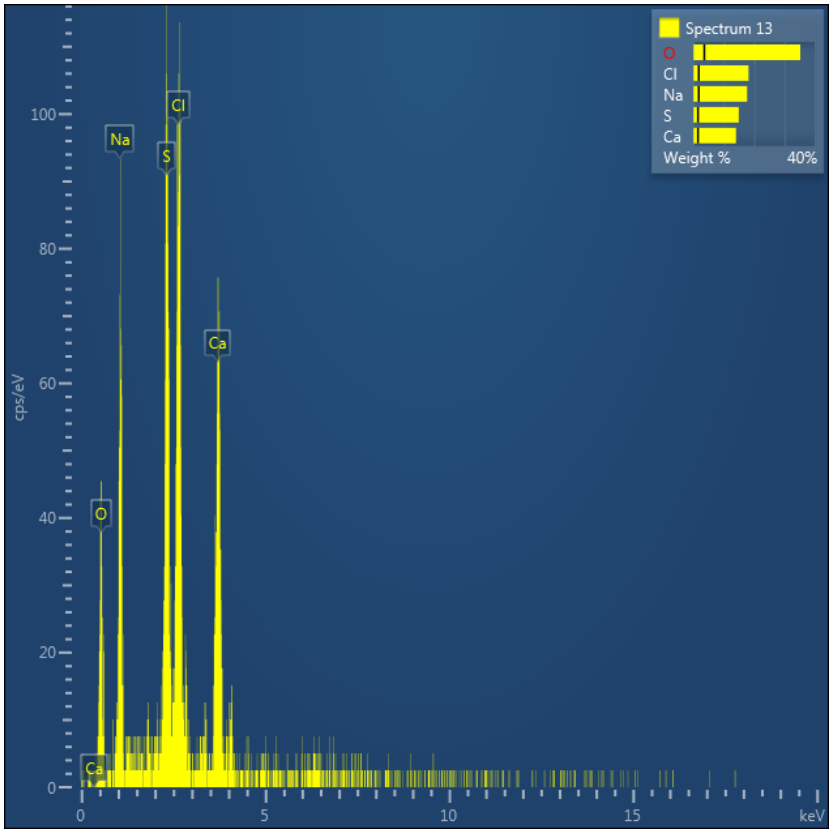

Figure A14: EDS Spectrum 13

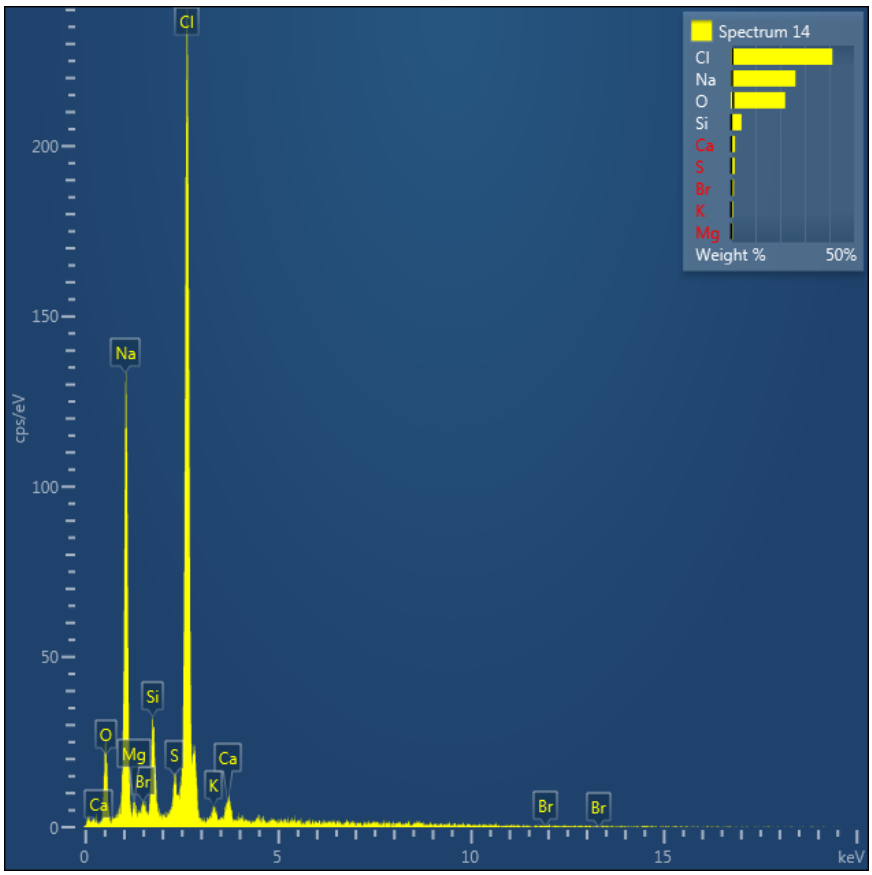

Figure A15: EDS Spectrum 14

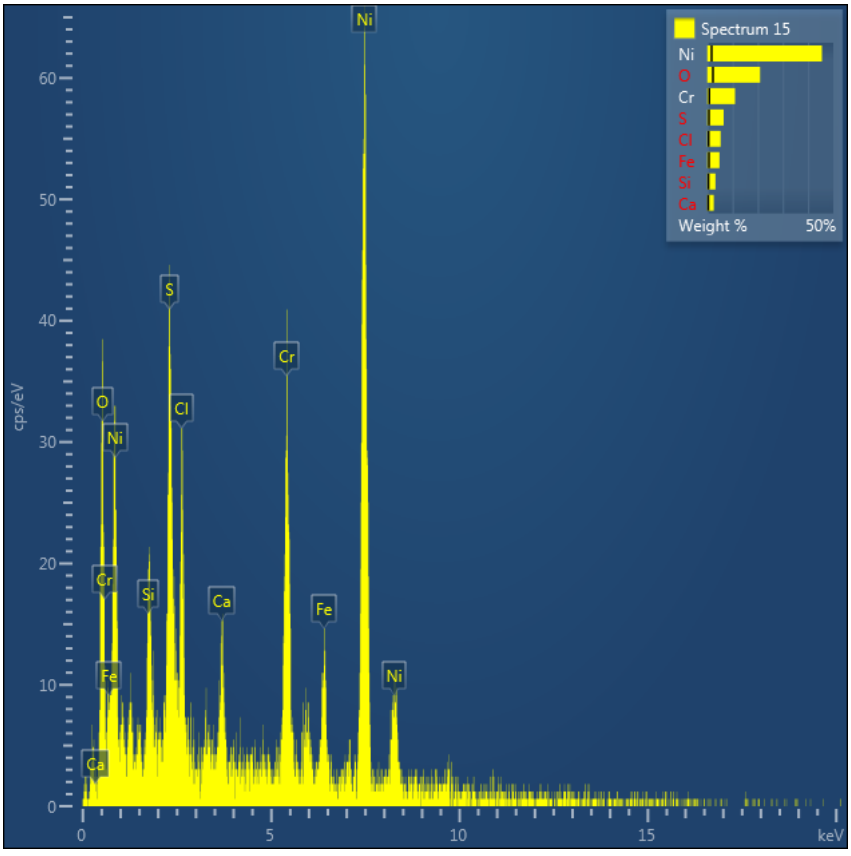

Figure A16: EDS Spectrum 15

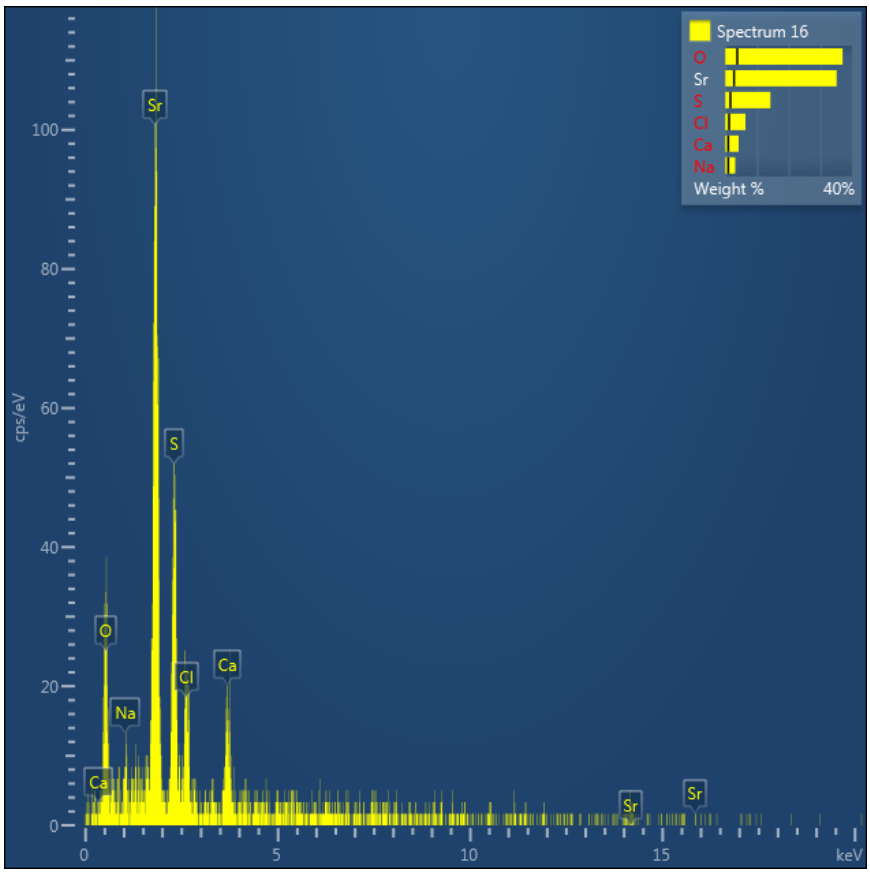

Figure A17: EDS Spectrum 16

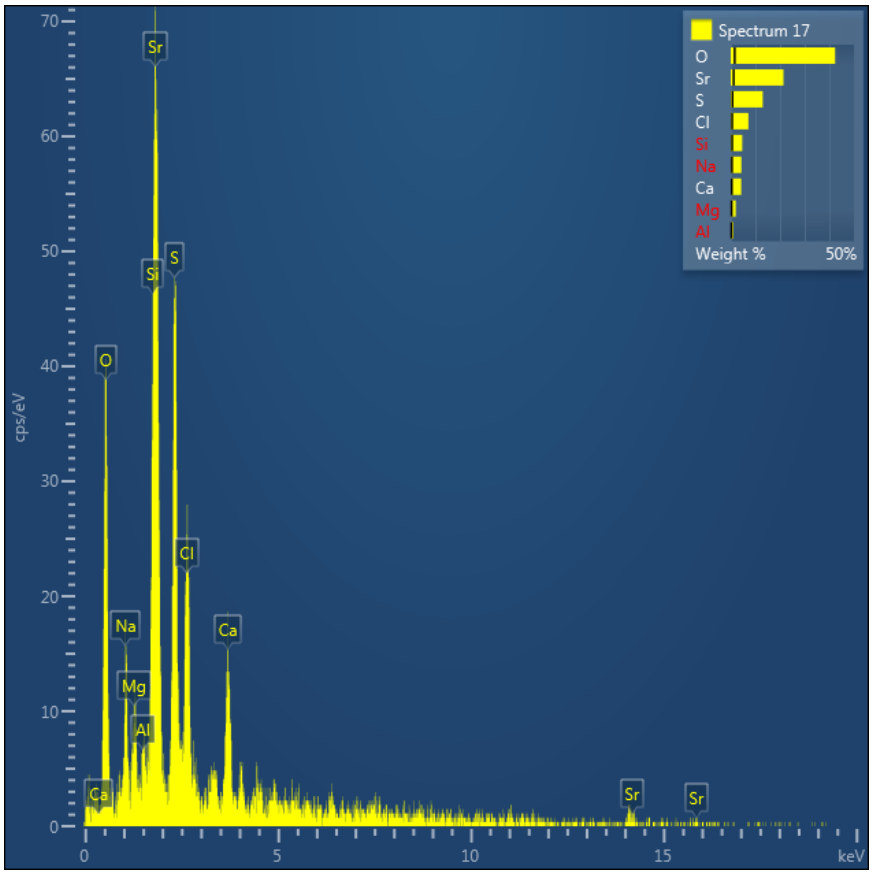

Figure A18: EDS Spectrum 17

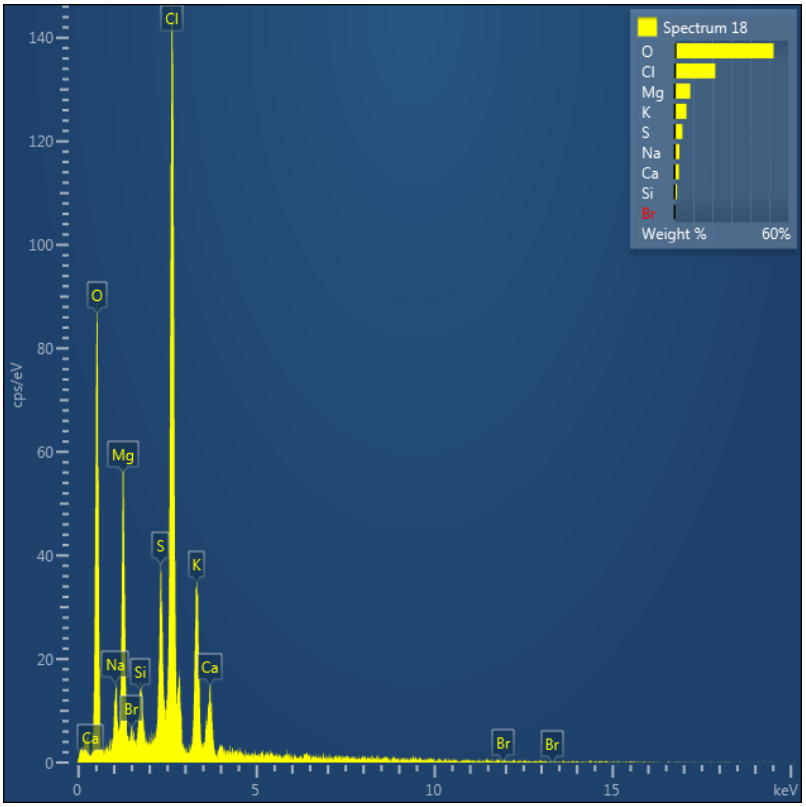

Figure A19: EDS Spectrum 18

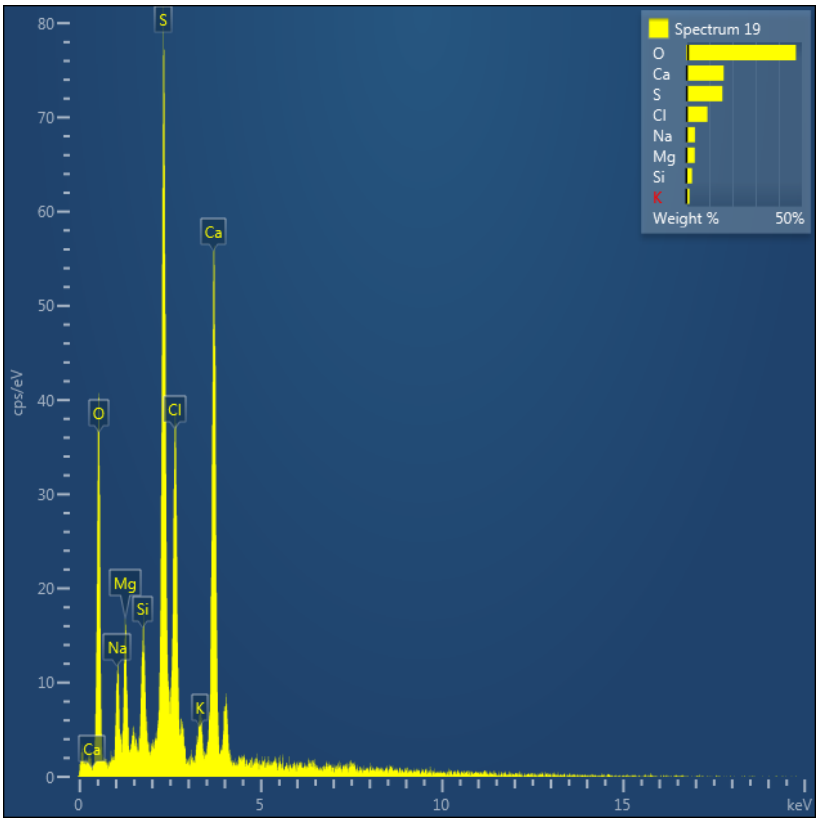

Figure A20: EDS Spectrum 19